

Summer 8-13-2019

# Monitoring Subcellular Calcium by Designed Calcium Sensors and the Calcium Sensing Receptor Structure and Function

Cassandra Miller

Follow this and additional works at: [https://scholarworks.gsu.edu/chemistry\\_diss](https://scholarworks.gsu.edu/chemistry_diss)

---

## Recommended Citation

Miller, Cassandra, "Monitoring Subcellular Calcium by Designed Calcium Sensors and the Calcium Sensing Receptor Structure and Function." Dissertation, Georgia State University, 2019.  
[https://scholarworks.gsu.edu/chemistry\\_diss/171](https://scholarworks.gsu.edu/chemistry_diss/171)

This Dissertation is brought to you for free and open access by the Department of Chemistry at ScholarWorks @ Georgia State University. It has been accepted for inclusion in Chemistry Dissertations by an authorized administrator of ScholarWorks @ Georgia State University. For more information, please contact [scholarworks@gsu.edu](mailto:scholarworks@gsu.edu).

MONITORING SUBCELLULAR CALCIUM BY DESIGNED CALCIUM SENSORS AND  
THE CALCIUM SENSING RECEPTOR STRUCTURE AND FUNCTION

by

CASSANDRA LYNN MILLER

Under the Direction of Jenny J. Yang, Ph.D.

ABSTRACT

Calcium ( $\text{Ca}^{2+}$ ) regulates various biological and pathological functions via calcium dynamics and interacting with key calcium binding proteins such as the calcium sensing receptor (CaSR). In this dissertation, the first X-ray structure of the extracellular domain of CaSR was determined by engineering mammalian expression systems. The revealed  $\text{Ca}^{2+}/\text{Mg}^{2+}$  and Trp derivative L-1,2,3,4-tetrahydronorharman-3-carboxylic acid (TNCA) binding sites and key determinants contribute to the functional cooperativity of CaSR in cells. Magnesium ( $\text{Mg}^{2+}$ ) acts as a heterotropic cooperative co-agonist with calcium to co-activate the function of CaSR, including calcium oscillations. TNCA potentiates CaSR co-activation and recovers a loss of function caused by mutation at the dimer interface calcium binding site. Several mutations of the main  $\text{Ca}^{2+}/\text{TNCA}$  binding site at the hinge region eliminate CaSR activity. Mutations S272A and D216N at the hinge region lead to a loss of  $\text{Ca}^{2+}$  binding and complete loss of cooperative binding for  $\text{Tb}^{3+}$  using

bacterially expressed protein and Trp-sensitized FRET assay. Efforts in the development of new CaSR therapeutics using structure-based drug design were also explored.

Next, we aimed to monitor endoplasmic/sarcoplasmic reticulum (ER/SR) mediated subcellular  $\text{Ca}^{2+}$  dynamics using our designed calcium sensors CatchER<sup>+</sup> and CatchER<sup>+</sup>-JP45. Using highly inclined laminated optical (HILO) microscopy, we report calcium dynamics in the ER/SR with differential calcium responses to 4-cmc for release and recovery indicating differential  $\text{Ca}^{2+}$  signaling from  $\text{Ca}^{2+}$  and protein expression subcellular microdomains. We find  $\text{Ca}^{2+}$  dynamic differences between the localized high  $\text{Ca}^{2+}$  release region of the junctional SR for E-C coupling with targeted CatchER<sup>+</sup>-JP45 to ryanodine receptor over the global  $\text{Ca}^{2+}$  ER/SR regulation of CatchER<sup>+</sup> sensor. To understand ER  $\text{Ca}^{2+}$  dynamics in neurons, we utilized our sensor CatchER<sup>+</sup> and high-resolution HILO imaging to show that 100  $\mu\text{M}$  DHPG induced mGluR1/5 activation leads to IP<sub>3</sub>R  $\text{Ca}^{2+}$  release as well as  $\text{Ca}^{2+}$  uptake throughout the soma and dendrites. The differential release and uptake for the ER  $\text{Ca}^{2+}$  dynamics in response to DHPG indicates subcellular microdomains throughout the neurons as well. These sensors will significantly impact  $\text{Ca}^{2+}$  dynamics research and molecular basis of ER  $\text{Ca}^{2+}$  related diseases by exposing  $\text{Ca}^{2+}$  dynamics, function, mobility, and trafficking in the ER/SR.

**INDEX WORDS:** Calcium sensing receptor, CaSR, G-protein coupled receptor, GPCR, Genetically encoded calcium indicator, GECl, Calcium, Green fluorescence protein, GFP, CatchER, CatchER<sup>+</sup>, Calcium signaling, Protein crystallization, ER, SR, HILO, JP45, CatchER<sup>+</sup>-JP45, STORM, Calcium dynamics

MONITORING SUBCELLULAR CALCIUM BY DESIGNED CALCIUM SENSORS AND  
THE CALCIUM SENSING RECEPTOR STRUCTURE AND FUNCTION

by

CASSANDRA LYNN MILLER

A Dissertation Submitted in Partial Fulfillment of the Requirements for the Degree of

Doctor of Philosophy

in the College of Arts and Sciences

Georgia State University

2019



Copyright by  
Cassandra Lynn Miller  
2019

MONITORING SUBCELLULAR CALCIUM BY DESIGNED CALCIUM SENSORS AND  
THE CALCIUM SENSING RECEPTOR STRUCTURE AND FUNCTION

by

CASSANDRA LYNN MILLER

Committee Chair: Jenny J. Yang

Committee: Ning Fang

Ming Luo

Angela Mabb

Electronic Version Approved:

Office of Graduate Studies

College of Arts and Sciences

Georgia State University

July 2019

## DEDICATION

I want to dedicate this dissertation to my family and friends who have supported and loved me throughout this arduous but rewarding journey.

I could not have become the person I am today and achieved all of these accomplishments without my family. My mom who never gave up on us and did everything she could to give us a better life, even when times were hard, she made life a fun adventure and gave us all the love and support in the world without restraint. My dad who came into my life later but who has been a much better father than anyone could ever wish for, I appreciate how much he loves us all and what a great man he is every day. My sister and brother, who have also supported me throughout life during the good times and the bad, having siblings is like having friends your whole life.

My friends helped to support me throughout this journey and give me joy and laughter each day. I enjoyed all of the great times we have had and will have and am grateful for all of my friends; without you this would have been much harder and near impossible. The love all my friends have shown me encouraged me to succeed. Thank you all for the support, love, guidance, and camaraderie you have shown me through the years, I am always grateful.

I would also like to mention the unconditional love, support, and calming stress relief my pets have given me throughout this journey. My cat Cleos who was with me in the beginning and who left too soon from renal failure and my dog Nefi who helped me through that pain as well as providing love and joy.

## ACKNOWLEDGMENTS

I would like to first and foremost express my most profound appreciation and admiration for my research mentor, advisor, and dissertation committee chair Dr. Jenny J. Yang. She has continually conveyed her passion and spirit for research which motivated and encouraged my scientific growth. Her patience, motivation, enthusiasm, guidance, and immense knowledge helped me in all the time of research, presentation preparation, and in writing of this dissertation. I could not have imagined having a better advisor and mentor for my PhD study, and without her guidance and persistent help this dissertation would not have been possible.

I would also like to thank the rest of my committee Dr. Ning Fang, Dr. Ming Luo, and Dr. Angela Mabb for their encouragement, insightful comments, and discerning questions. They assisted me not only on my progress for my defense and dissertation but were also collaborators and mentors whom I could turn to for assistance and guidance in my research and scientific pursuits.

I also could not have completed this research without the scientific collaborations on multiple fronts. Dr. Ed Brown who discovered CaSR and helped to guide and mentor our CaSR research. Dr. Kelley Moremen for his guidance and mammalian protein purification expertise. Dr. Jian Hu for his crystallography knowledge, performing CaSR X-Ray crystal diffraction and his precise feedback. Dr. Binghe Wang and Mengyuan Zhu for their organic synthesis aptitude and lead drug design assistance with LADI software and Sybyl binding studies of CaSR. Dr. Ning Fang and Dr. Bin Dong for their imaging methodology prowess, utilizing their HILO and STORM imaging systems, and Ca<sup>2+</sup> sensor project insights. Dr. Angela Mabb and Amin Ghane for their collaboration for neuronal imaging using the CatchER+ sensor, as well as expertise, and advice

for the  $\text{Ca}^{2+}$  sensor project. Dr. Francesco Zorzato for his collaboration designing the CatchER<sup>+</sup>-JP45 sensor, myotubule transfection efficiency and  $\text{Ca}^{2+}$  sensor project assistance.

I also give my sincerest gratitude to my mentors in the Yang lab, my first being the person who initially trained me in the lab and taught me how to be a bench scientist to the fullest, Dr. Chen Alice Zhang. I enjoyed all of our fun times together and the friendship we developed, which made every day a joy. Additionally, my mentor for the sensor project Dr. Florence Reddish who was my friend in the lab before she became my mentor later.

I also want to thank the two scientists who went along this whole journey with me since we all three joined at the same time in the Yang lab for our PhDs, Dr. Rakshya Gorkhali and Dr. Shanshan Tan, it was a great relief to have you both these past years to go through this process together and support one another.

I also want to thank my mentee Xiaonan Shawn Deng, who showed me how to be a thorough mentor myself and pushed me with his questions. Of course, I could not have made this journey either without the support and family that the Yang lab members provide. Over these past six years people have graduated and joined the lab as well been in this journey with me. I will never forget or take for granted the time that we all shared. We really are a supportive unit which helps one another and are brought together through working in the Yang lab. I could never have had a better research group and advisor to be a part of.

Finally, I would like to thank the funding sources for supporting this research the National Institute of Health, the Brains and Behavior fellowship, and the American Heart Association.

## TABLE OF CONTENTS

<b>DEDICATION.....</b>	<b>X</b>
<b>ACKNOWLEDGMENTS .....</b>	<b>XI</b>
<b>LIST OF TABLES .....</b>	<b>XIX</b>
<b>LIST OF FIGURES .....</b>	<b>XX</b>
<b>LIST OF ABBREVIATIONS .....</b>	<b>XXV</b>
<b>1 INTRODUCTION .....</b>	<b>1</b>
<b>1.1 Calcium as a Critical Physiological Ion .....</b>	<b>1</b>
<b>1.2 Calcium Dynamics and Cellular Signaling .....</b>	<b>2</b>
<b>1.3 Ca<sup>2+</sup> Binding Proteins .....</b>	<b>6</b>
<b>1.4 Family C G-protein Coupled Receptors (GPCRs) .....</b>	<b>8</b>
<b>1.5 The Calcium Sensing Receptor .....</b>	<b>9</b>
<i>1.5.1 The CaSR induced intracellular calcium oscillation and signaling .....</i>	<i>11</i>
<i>1.5.2 Diseases of CaSR and mutation .....</i>	<i>12</i>
<i>1.5.3 Challenges in studying the CaSR.....</i>	<i>13</i>
<b>1.6 Calcium Related Disorders.....</b>	<b>14</b>
<i>1.6.4 Differential expression of key CaBPs and ER/SR related disorders .....</i>	<i>14</i>
<i>1.6.5 Neurological calcium diseases.....</i>	<i>18</i>
<b>1.7 Unmet Need to Design Calcium Sensors .....</b>	<b>18</b>
<b>1.8 Fluorescent Proteins.....</b>	<b>19</b>

1.9	Fluorescent Ca <sup>2+</sup> Dyes .....	21
1.10	Fluorescent Ca <sup>2+</sup> Sensor Proteins .....	25
1.11	Research Objectives and Questions to be Addressed .....	27
2	STRUCTURAL DETERMINATION OF CASR ECD.....	30
2.1	Introduction .....	30
2.2	Results .....	34
2.2.1	<i>Mammalian Expressed CaSR Optimization</i> .....	34
2.2.2	<i>CaSR Determined Structures</i> .....	36
2.2.3	<i>Structure Analysis</i> .....	42
2.2.4	<i>Trp Compound Analysis and Uncovering TNCA</i> .....	46
2.2.5	<i>Molecular Regulation of CaSR by Co-activators Mg<sup>2+</sup>, Ca<sup>2+</sup>, and TNCA</i> .....	48
2.3	Discussion.....	57
2.4	Materials and Methods .....	63
2.4.6	<i>Computational prediction</i> .....	63
2.4.7	<i>mCaSR ECD expression</i> .....	63
2.4.8	<i>mCaSR ECD purification</i> .....	63
2.4.9	<i>Crystallization, data collection, and structure determination</i> .....	64
2.4.10	<i>High-resolution LC-ESI-MS and identification of TNCA</i> .....	65
2.4.11	<i>Immunohistochemistry antibody staining</i> .....	67
2.4.12	<i>SDS-PAGE gels and western blot</i> .....	67

2.4.13	<i>Cell culture and transfection</i> .....	68
2.4.14	<i>Cell imaging</i> .....	68
2.4.15	<i>Measurement of <math>[Ca^{2+}]_i</math> changes by <math>[Mg^{2+}]_o</math> in single CaSR-transfected cells</i> ...	69
2.4.16	<i>Intracellular calcium concentration in cell population by fluorimetry</i> .....	69
2.4.17	<i>BSA standard and protein analysis</i> .....	71
<b>3</b>	<b>UNDERSTANDING MOLECULAR BASIS OF CASR RELATED DISEASES</b> .....	<b>72</b>
3.1	<b>Introduction</b> .....	<b>72</b>
3.2	<b>Results</b> .....	<b>74</b>
3.2.1	<i>bCaSR Expression Development</i> .....	74
3.2.2	<i>Disease Related Mutations of CaSR</i> .....	77
3.2.3	<i>Expression and Purification of bCaSR</i> .....	79
3.2.4	<i>Biophysical Studies of CaSR</i> .....	82
3.2.5	<i>Circular dichroism</i> .....	82
3.2.6	<i>Trp fluorescence spectroscopy</i> .....	83
3.2.7	<i>ANS binding fluorescence spectroscopy</i> .....	88
3.2.8	<i>Terbium/Trp FRET and <math>Ca^{2+}</math> competition</i> .....	93
3.3	<b>Discussion</b> .....	<b>100</b>
3.4	<b>Materials and Methods</b> .....	<b>105</b>
3.4.9	<i>Plasmid extraction</i> .....	105
3.4.10	<i>Primer construction</i> .....	105



3.4.11	<i>Polymerase chain reaction (PCR)</i> .....	106
3.4.12	<i>Agarose gel electrophoresis</i> .....	106
3.4.13	<i>Inoculation and expression</i> .....	106
3.4.14	<i>CaSR ECD purification</i> .....	107
3.4.15	<i>SDS-PAGE and western blot</i> .....	107
3.4.16	<i>Circular dichroism spectroscopy</i> .....	108
3.4.17	<i>Intrinsic tryptophan fluorescence spectroscopy</i> .....	108
3.4.18	<i>Terbium FRET spectroscopy</i> .....	108
3.4.19	<i>ANS-binding spectroscopy</i> .....	109
<b>4</b>	<b>STRUCTURE BASED DRUG DESIGN</b> .....	<b>110</b>
4.1	<b>Introduction</b> .....	<b>110</b>
4.2	<b>Results</b> .....	<b>111</b>
4.2.1	<i>Lead Drug Compound Design</i> .....	<i>111</i>
4.2.2	<i>TNCA and Determined Related Compounds Optical Properties</i> .....	<i>117</i>
4.2.3	<i>Determining Drug Effectiveness Using Single Cell Imaging</i> .....	<i>121</i>
4.2.4	<i>Screening Potential Drugs Using Cell Population Assay</i> .....	<i>123</i>
4.3	<b>Discussion</b> .....	<b>127</b>
4.4	<b>Materials and Methods</b> .....	<b>129</b>
4.4.5	<i>Cell culture and transfection</i> .....	<i>129</i>
4.4.6	<i>Measurement of <math>[Ca^{2+}]_i</math> changes in single CaSR-transfected cells</i> .....	<i>129</i>

4.4.7	<i>Intracellular calcium concentration in cell population by fluorimetry .....</i>	<i>130</i>
<b>5</b>	<b>VISUALIZING SUBCELLULAR CA<sup>2+</sup> DYNAMICS USING DESIGNED CA<sup>2+</sup> SENSORS .....</b>	<b>132</b>
5.1	<b>Introduction .....</b>	<b>132</b>
5.2	<b>Results .....</b>	<b>137</b>
5.2.1	<i>Using Epifluorescence Imaging to Analyze CatchER<sup>+</sup> Function.....</i>	<i>137</i>
5.2.2	<i>Highly Inclined and Laminated Optical Sheet (HILO) Microscopy.....</i>	<i>140</i>
5.2.3	<i>Examining Microdomains using CatchER<sup>+</sup> and HILO Imaging .....</i>	<i>147</i>
5.2.4	<i>Confocal Imaging of Global CatchER<sup>+</sup>, RyR, and SERCA Distribution .....</i>	<i>150</i>
5.2.5	<i>Comparison of Localized CatchER<sup>+</sup>-JP45 vs. Global CatchER<sup>+</sup> Sensors.....</i>	<i>155</i>
5.3	<b>Discussion.....</b>	<b>164</b>
5.4	<b>Materials and Methods .....</b>	<b>168</b>
5.4.6	<i>Cloning of CatchER<sup>+</sup> .....</i>	<i>168</i>
5.4.7	<i>Cell culture and transfection of CatchER<sup>+</sup> .....</i>	<i>168</i>
5.4.8	<i>Confocal imaging of CatchER<sup>+</sup>.....</i>	<i>169</i>
5.4.9	<i>Epifluorescence imaging of CatchER<sup>+</sup> .....</i>	<i>169</i>
5.4.10	<i>HILO imaging of CatchER<sup>+</sup>.....</i>	<i>170</i>
5.4.11	<i>Preparing cells for STORM imaging .....</i>	<i>170</i>
<b>6</b>	<b>NEURONAL APPLICATION OF CATCHER<sup>+</sup> .....</b>	<b>171</b>
6.1	<b>Introduction .....</b>	<b>171</b>

<b>6.2</b>	<b>Results .....</b>	<b>177</b>
6.2.1	<i>CatchER<sup>+</sup> HILO Imaging in Neurons .....</i>	<i>177</i>
<b>6.3</b>	<b>Discussion.....</b>	<b>183</b>
<b>6.4</b>	<b>Materials and Methods .....</b>	<b>186</b>
6.4.2	<i>Generation of primary hippocampal neuron cultures and transfection.....</i>	<i>186</i>
6.4.3	<i>Epifluorescence imaging of CatchER<sup>+</sup> .....</i>	<i>186</i>
6.4.4	<i>HILO imaging of CatchER<sup>+</sup> .....</i>	<i>187</i>
<b>7</b>	<b>MAJOR CONCLUSIONS AND SIGNIFICANCE .....</b>	<b>188</b>
7.1	<b>CaSR Significance and Conclusions .....</b>	<b>188</b>
7.2	<b>Calcium Sensors Significance and Conclusions .....</b>	<b>192</b>
<b>8</b>	<b>APPENDICES.....</b>	<b>196</b>
	<b>Appendix A – Optimizations .....</b>	<b>196</b>
	<i>Removal of TNCA from mCaSR.....</i>	<i>196</i>
	<i>Identifying CaSR Disease Mutations.....</i>	<i>198</i>
	<i>PCR of CaSR Mutations.....</i>	<i>233</i>
	<i>Perifusion Drug Treatment Over Small Volume Diffusion Method .....</i>	<i>242</i>
	<i>Neuron Imaging.....</i>	<i>244</i>
	<i>CatchER<sup>+</sup> STORM Imaging in Neurons .....</i>	<i>254</i>
	<b>Appendix B – ArcKR Neuron Mutation .....</b>	<b>260</b>
	<b>REFERENCES.....</b>	<b>267</b>

## LIST OF TABLES

Table 1.1 – ER/SR protein diseases related to calcium signaling.....	15
Table 1.2 – Current calcium indicators on the market.....	22
Table 2.1 – EC <sub>50</sub> of [Mg <sup>2+</sup> ] <sub>o</sub> for stimulation of [Ca <sup>2+</sup> ] <sub>i</sub> signaling in the presence of different co-activators and TNCA. ....	51
Table 2.2 – EC <sub>50</sub> of [Mg <sup>2+</sup> ] <sub>o</sub> for stimulation of [Ca <sup>2+</sup> ] <sub>i</sub> signaling with or without TNCA. ....	56
Table 2.3 – Comparison of the binding sites between CaSR structures. ....	58
Table 3.1 – CaSR disease mutations. ....	79
Table 3.2 – Summary of bCaSR WT binding titrations.....	99
Table 4.1 – Compounds of CaSR agonists (calcimimetics) or antagonists (calcilytics). ....	112
Table 4.2 – Lead drug design templates based on TNCA structure. ....	113
Table 4.3 – Specs compounds ordered for CaSR targeting after computational evaluation of Specs library.....	116
Table 5.1 – Expression of ER/SR proteins in different cell lines. ....	134
Table 5.2 – Epifluorescence $\Delta F/F_0$ responses in each cell type to 4-cmc, CPA, and ATP. ....	139
Table 5.3 – Epifluorescence and HILO CatchER <sup>+</sup> $\Delta F/F_0$ for each cell and drug type using. ....	146
Table 6.1 – ER/SR related diseases. ....	174
Table 8.1 – CaSR disease mutations using CaSRdb and COSMIC.....	198
Table 8.2 – hCaSR disease mutation primers designed.....	236
Table 8.3 – bCaSR ECD disease mutation primers designed.....	238
Table 8.4 – bCaSR and hCaSR ECD disease mutations and primers made. ....	240
Table 8.5 –hCaSR ECD disease mutation made by Geng et al. and observations. ....	241
Table 8.6 – Components of NEUROBASAL medium. ....	249

## LIST OF FIGURES

Figure 1.1 – Calcium oscillations signal processes inside the cell. ....	1
Figure 1.2 – Calcium signaling inside the cell.....	4
Figure 1.3 – A diagram of the CaSR signaling pathway. ....	12
Figure 2.1 – CaSR proposed Ca <sup>2+</sup> binding sites. ....	31
Figure 2.2 – CaSR modeled structure. ....	33
Figure 2.3 – History of mCaSR expression optimization. ....	35
Figure 2.4 – Three separate mCaSR expression batches under GF purification. ....	36
Figure 2.5 – Science Advances CaSR structures ....	38
Figure 2.6 – Metal binding at the acidic patch.....	39
Figure 2.7 – Binding sites of Mg <sup>2+</sup> /Ca <sup>2+</sup> /TNCA/Bicarbonate in CaSR ECD.....	40
Figure 2.8 – Comparison of our CaSR 5FBK (green) and the modeled CaSR (orange).....	43
Figure 2.9 – Key determinants for the molecular basis of disease-associated mutations and regulation. ....	44
Figure 2.10 – A positively charged pocket for loop 1 association.....	45
Figure 2.11 – Identification and characterization of a tryptophan derivative bound to hCaSR-ECD as a novel high-affinity co-agonist of CaSR. ....	47
Figure 2.12 – Cell imaging using the novel hCaSR agonist TNCA. ....	50
Figure 2.13 – Cell population using the novel hCaSR agonist TNCA. ....	50
Figure 2.14 – Disease-related mutations on CaSR ECD. ....	52
Figure 2.15 – Complete loss of function hinge CaSR mutations.....	53
Figure 2.16 – Determining TNCA binding capability to hCaSR-ECD. ....	54
Figure 2.17 – CaSR mutation E228I representative oscillations. ....	55

Figure 2.18 – Working model of CaSR binding and activity. ....	57
Figure 2.19 – Comparison of our CaSR 5FBK and the Geng et al. CaSR 5K5S <sup>[284]</sup> . ....	59
Figure 2.20 – Comparison of our CaSR 5FBK and the Geng et al. CaSR 5K5T <sup>[284]</sup> . ....	60
Figure 3.1 – CaSR mutations made for functional studies in cells. ....	73
Figure 3.2 – bCaSR WT versus bCaSR deletions using Rosetta-gami. ....	75
Figure 3.3 – CaSR sequence. ....	76
Figure 3.4 – The difference of SHuffle compared to Rosetta-gami. ....	77
Figure 3.5 – CaSR disease mutations for ECD. ....	78
Figure 3.6 – Coomassie blue SDS-PAGE gel of bCaSR WT and mutants expression. ....	80
Figure 3.7 – bCaSR WT and representative mutant purification from SHuffle cells. ....	80
Figure 3.8 – Western blot gel ADD antibody for bCaSR WT and mutants purification. ....	81
Figure 3.9 – Circular dichroism Ca <sup>2+</sup> titration on bCaSR ECD WT. ....	83
Figure 3.10 – Trp residues in CaSR ECD. ....	84
Figure 3.11 – Trp fluorescence Ca <sup>2+</sup> titration on 2 μM bCaSR ECD WT. ....	85
Figure 3.12 – Trp fluorescence Ca <sup>2+</sup> and PO <sub>4</sub> titration on 2 μM bCaSR ECD WT. ....	86
Figure 3.13 – Trp fluorescence Ca <sup>2+</sup> titration on bCaSR WT, S272A, and D216N. ....	87
Figure 3.14 – ANS binding Ca <sup>2+</sup> titration of mCaSR ECD WT. ....	89
Figure 3.15 – ANS binding Ca <sup>2+</sup> titration on 2 μM bCaSR ECD WT. ....	90
Figure 3.16 – ANS binding TNCA titration on 2 μM bCaSR ECD WT. ....	91
Figure 3.17 – ANS binding PO <sub>4</sub> and Ca <sup>2+</sup> titration on 2 μM bCaSR ECD WT. ....	92
Figure 3.18 – Tb <sup>3+</sup> /Trp FRET diagram for CaSR. ....	94
Figure 3.19 – Tb <sup>3+</sup> /Trp FRET with Tb <sup>3+</sup> titration on 2 μM bCaSR ECD WT. ....	95
Figure 3.20 – Tb <sup>3+</sup> /Trp FRET with Ca <sup>2+</sup> competition titration on bCaSR ECD WT. ....	96

Figure 3.21 – Tb <sup>3+</sup> /Trp FRET with Tb <sup>3+</sup> titration on 2 μM bCaSR WT and S272A. ....	97
Figure 3.22 – Tb <sup>3+</sup> /Trp FRET with Tb <sup>3+</sup> titration of CaSR ECD subdomains <sup>[269]</sup> .....	98
Figure 4.1 – CSR-101 to 106 compound structures and molecular weights. ....	113
Figure 4.2 – LADI program and R group replacements. ....	114
Figure 4.3 – LADI and Sybyl compound results for a lead compound for CaSR. ....	114
Figure 4.4 – Specs compounds bound to CaSR. ....	115
Figure 4.5 – TNCA optical properties. ....	118
Figure 4.6 – CSR-107 to CSR-115 absorbance properties. ....	119
Figure 4.7 – CSR-107 to CSR-115 excitation and emission properties. ....	120
Figure 4.8 – TNCA live-cell imaging with hCaSR in HEK293 cells. ....	121
Figure 4.9 – Ca <sup>2+</sup> and TNCA live-cell imaging with hCaSR in HEK293 cells. ....	122
Figure 4.10 – Ca <sup>2+</sup> and CSR-101 live-cell imaging with hCaSR in HEK293 cells. ....	122
Figure 4.11 – Representative cell population data for WT hCaSR. ....	124
Figure 4.12 – EC <sub>50</sub> cell population data for WT hCaSR with control compounds. ....	125
Figure 4.13 – EC <sub>50</sub> for WT hCaSR with possible lead compounds. ....	126
Figure 5.1 – ER/SR calcium signaling inside the cell. ....	133
Figure 5.2 – CatchER <sup>+</sup> sensor design and improvement process. ....	136
Figure 5.3 – CatchER <sup>+</sup> confocal imaging in C2C12 with ER Tracker. ....	136
Figure 5.4 – CatchER <sup>+</sup> epifluorescence in response to 4-cmc, CPA, and ATP. ....	138
Figure 5.5 – CatchER <sup>+</sup> captures a highly defined ER-network pattern using HILO. ....	141
Figure 5.6 – Epifluorescence and HILO imaging comparison. ....	142
Figure 5.7 – Epifluorescence and HILO cross-sectional 3D response comparison. ....	143
Figure 5.8 – CatchER <sup>+</sup> HILO in response to 4-cmc, CPA, and ATP. ....	144

Figure 5.9 – CatchER <sup>+</sup> HILO imaging in C2C12 in response to 1 mM 4-cmc. ....	148
Figure 5.10 – Analyzing subcellular microdomains using CatchER <sup>+</sup> and HILO imaging. ....	149
Figure 5.11 – CatchER <sup>+</sup> HILO imaging in C2C12 with different normalization. ....	150
Figure 5.12 – CatchER <sup>+</sup> confocal imaging in C2C12 with ER Tracker. ....	151
Figure 5.13 – CatchER <sup>+</sup> confocal imaging in C2C12 with RyR antibody. ....	152
Figure 5.14 – RyR confocal imaging in C2C12. ....	153
Figure 5.15 – SERCA1 and SERCA2 confocal imaging in C2C12. ....	154
Figure 5.16 – CatchER <sup>+</sup> -JP45 sensor design and SR expression.....	156
Figure 5.17 – CatchER <sup>+</sup> and CatchER <sup>+</sup> -JP45 in myoblasts of C2C12 cells with 4-cmc. ....	157
Figure 5.18 – CatchER <sup>+</sup> and CatchER <sup>+</sup> -JP45 in myoblasts of C2C12 cells with CPA. ....	158
Figure 5.19 – CatchER <sup>+</sup> and CatchER <sup>+</sup> -JP45 HILO imaging in C2C12 tubule cells. ....	159
Figure 5.20 – CatchER <sup>+</sup> and CatchER <sup>+</sup> -JP45 FDB fiber analysis. ....	160
Figure 5.21 – CatchER <sup>+</sup> STORM imaging in C2C12 mouse muscle cells.....	162
Figure 5.22 – CatchER <sup>+</sup> -JP45 STORM imaging in C2C12 mouse muscle cells.....	163
Figure 5.23 – CatchER <sup>+</sup> -JP45 STORM imaging in C2C12 mouse muscle cells.....	163
Figure 6.1 – Calcium dynamics in neurons. ....	171
Figure 6.2 – GFP control representative response in mouse hippocampal neuron.....	177
Figure 6.3 – DHPG and 4-cmc representative response in hippocampal neurons.....	179
Figure 6.4 – DHPG and 4-cmc representative response in mouse cortical neurons.....	181
Figure 6.5 – DHPG and CPA representative response in mouse hippocampal neurons. ....	182
Figure 8.1 – TOF MS of mCaSR TNCA peak being competed out by Phe. ....	196
Figure 8.2 – Expression and purification of mCaSR using Phe wash. ....	197
Figure 8.3– CaSR disease mutations for ECD.....	234



Figure 8.4 -CatchER <sup>+</sup> in Cos-7 cells small volume versus perfusion systems. ....	243
Figure 8.5 – CatchER <sup>+</sup> in mouse hippocampal neurons. ....	245
Figure 8.6 – CatchER <sup>+</sup> in mouse hippocampal neurons. ....	247
Figure 8.7 – GFP in mouse hippocampal neurons. ....	248
Figure 8.8 – ACSF buffer on mouse hippocampal neurons. ....	252
Figure 8.9 – Confocal imaging of hippocampal neurons with mGluR1 and CatchER <sup>+</sup> . ....	255
Figure 8.10 – STORM imaging of mouse hippocampal neurons with CatchER <sup>+</sup> . ....	257
Figure 8.11 – STORM imaging of neurons with mGluR1/5 and CatchER <sup>+</sup> . ....	258
Figure 8.12 – STORM imaging of mouse hippocampal neurons with IP <sub>3</sub> R and CatchER <sup>+</sup> . ....	259
Figure 8.13 – ArcKR and WT mouse hippocampal neurons 4-cmc responses. ....	262
Figure 8.14 – WT mouse hippocampal neurons DHPG representative responses. ....	263
Figure 8.15 – ArcKR neurons DHPG responses for trials 3, 4, 6, and 8. ....	264
Figure 8.16 – ArcKR neurons DHPG representative responses for trials 9 and 11-13. ....	265

**LIST OF ABBREVIATIONS**

$[Ca^{2+}]_i$	Intracellular calcium concentration
$[Ca^{2+}]_o$	Extracellular calcium concentration
$[Mg^{2+}]_o$	Extracellular magnesium concentration
AA	Amino acids
ACSF	Artificial cerebrospinal fluid
AD	Alzheimer's disease
ADH	Autosomal dominant hypocalcemia
aGPCR	Family A G-protein coupled receptors
AhpC	Alkyl hydroperoxide reductase subunit C
AKV	Acrokeratosis verruciformis
ALS	Amyotrophic lateral sclerosis
AM	Acetoxymethyl
AMPA	$\alpha$ -amino-3-hydroxy-5-methyl-4-isoxazolepropionic acid receptor
ANHD	Dann-Epstein-Sohar syndrome
ANS	8-anilino-1-naphthalenesulfonic acid
ARVD	Arrhythmogenic right ventricular dysplasia
ATCC	American Type Culture Collection
ATP	Adenosine triphosphate
bCaSR	Bacterial expressed calcium sensing receptor
BFP	Blue fluorescence protein
bGPCR	Family B G-protein coupled receptors
BPD	Bipolar disorder

BRM	Brody myopathy
BS 1-5	Binding sites 1-5
Ca <sup>2+</sup>	Calcium
CaBPs	Calcium binding proteins
CaM	Calmodulin
CaSQ	Calsequestrin
CaSR	Calcium sensing receptor
CaSRLs	CaSR ligands
CatchER	Calcium sensor for detecting high concentration in the ER
CCD	Central core disease of muscle
CD	Circular dichroism
CFP	Cyan fluorescence protein
cGPCR	Family C G-protein coupled receptors
CICR	Calcium induced calcium release
CLSM	Confocal laser scanning microscopy
CNS	Central nervous system
cpV	YFP Venus in circularly permuted form
CPVT	Catecholaminergic polymorphic ventricular tachycardia
CRD	Cys rich domain
Cy5	Cyanine dye
DAG	Diacylglycerol
DAPI	4',6-diamidino-2-phenylindole
DD	Darier disease

DHPG	Dihydroxyphenylglycine
DHPR	Dihydropyridine receptor
DMEM	Dulbecco's modified Eagle's medium
dSTORM	Direct STORM
EBFP	Enhanced blue fluorescence protein
E-C coupling	Excitation-contraction coupling
EC <sub>50</sub>	Effective concentration at 50%
ECD	Extracellular N-terminus domain
ECFP	Enhanced cyan fluorescence protein
ECL1-3	Extracellular loops 1-3
EGFP	Enhanced green fluorescence protein
ER	Endoplasmic reticulum
ER/SR	Endoplasmic/sarcoplasmic reticulum
ERK1/2	Extracellular signal-regulated kinase 1 and 2
EYFP	Enhanced yellow fluorescence protein
FBS	Fetal bovine serum
FDA	Food and Drug Administration
FDB	Flexor digitorum brevis muscle
FHH	Familial hypocalciuric hypercalcemia
FP	Fluorescent proteins
FRET	Förster/fluorescence resonance energy transfer
FXS	Fragile X syndrome
GA	Glutaraldehyde

GABAB	Gamma-amino-butyric acid type B receptors
GECI	Genetically encoded calcium indicators
GECO	Genetically encoded $\text{Ca}^{2+}$ indicators for optical imaging
GFP	Green fluorescence protein
gor	Glutathione reductase
GPCR	G-protein coupled receptors
Grx1	Glutaredoxin 1
H1R	Histamine receptor
HCX	Hydrogen-calcium exchanger
HD	Huntington's disease
HILO	Highly inclined laminated optical microscopy
ICD	C-terminal intracellular domain
ICL 1-3	Intracellular loops 1-3
IP <sub>3</sub>	Inositol trisphosphate
IP <sub>3</sub> R	Inositol (1,4,5)-trisphosphate receptor
IPTG	Isopropyl $\beta$ -D-1-thiogalactopyranoside
JP45	Junctional protein 45
LC-ESI-MS	Liquid chromatography–electrospray ionization–mass spectrometry
LTD	Long-term depression
LTP	Long-term potentiation
m/z	Mass/charge ratio
mCaSR	Mammalian expression of CaSR
MCU	Mitochondrial calcium uniporter

Mg <sup>2+</sup>	Magnesium
mGluR	Metabotropic glutamate receptors
MH	Malignant hyperthermia
MMDO	Multiminicore disease with external ophthalmoplegia
mRFP1	Monomeric red fluorescent protein
MUG	MULTiple Geometries
MW	Molecular weight
nAChR	Nicotinic acetylcholine receptors
NCKX	Potassium-dependent sodium-calcium exchanger
NCX	Sodium-calcium exchanger
NMDAR	N-methyl-D-aspartate receptor
NSHPT	Neonatal severe hyperparathyroidism
P2YR	Purinergic receptors
PBS	Phosphate-buffered saline
PCC	Pearson's correlation coefficient
PCR	Polymerase chain reaction
PD	Parkinson's disease
PDB	Protein data bank
PFA	Paraformaldehyde
PIP <sub>2</sub>	Phosphatidylinositol bisphosphate
PKC	Protein kinase C
PLC $\beta$	Phospholipase C
PMCA	Plasma membrane Ca <sup>2+</sup> ATPase

PTH	Parathyroid hormone
RFP	Red fluorescence protein
ROC	Receptor-operated channels
ROI	Regions of interest
RyR	Ryanodine receptor
S/N	Signal to noise ratio
SCA15/29	Spinocerebellar ataxia 15 and 29
SERCA	Sarco/endoplasmic reticulum calcium-ATPase
SOC	Store-operated channels
sp	Signal peptide region
SPCA	Secretory pathway $\text{Ca}^{2+}$ -ATPase
SR	Sarcoplasmic reticulum
STORM	Stochastic optical reconstruction microscopy
T1R	Taste receptors
TED	Targeted-esterase-induced dye loading
TIRF	Total Internal Reflection Fluorescence
TnC	Troponin C
TNCA	L-1,2,3,4-tetrahydronorharman-3-carboxylic acid
TRP	Transient receptor potential channels
trxB	Thioredoxin reductase
VGCC/VDCC	Voltage-gated/voltage-dependent calcium channel
VOC	Voltage-operated channels
WT	Wild type

## 1 Introduction

### 1.1 Calcium as a Critical Physiological Ion

Calcium ( $\text{Ca}^{2+}$ ) is the most prevalent metal ion in the human body.  $\text{Ca}^{2+}$  is a critical ion for cell function and signaling, not only for complex eukaryotic multicellular organisms, but also in unicellular organisms as  $\text{Ca}^{2+}$  is the messenger for life and death<sup>[1, 2]</sup>.  $\text{Ca}^{2+}$  is a first messenger binding to proteins on the plasma membrane such as the calcium sensing receptor (CaSR) in order to induce intracellular  $\text{Ca}^{2+}$  release from the ER in oscillations.  $\text{Ca}^{2+}$  oscillations with different frequencies communicate many biological functions<sup>[1]</sup>.

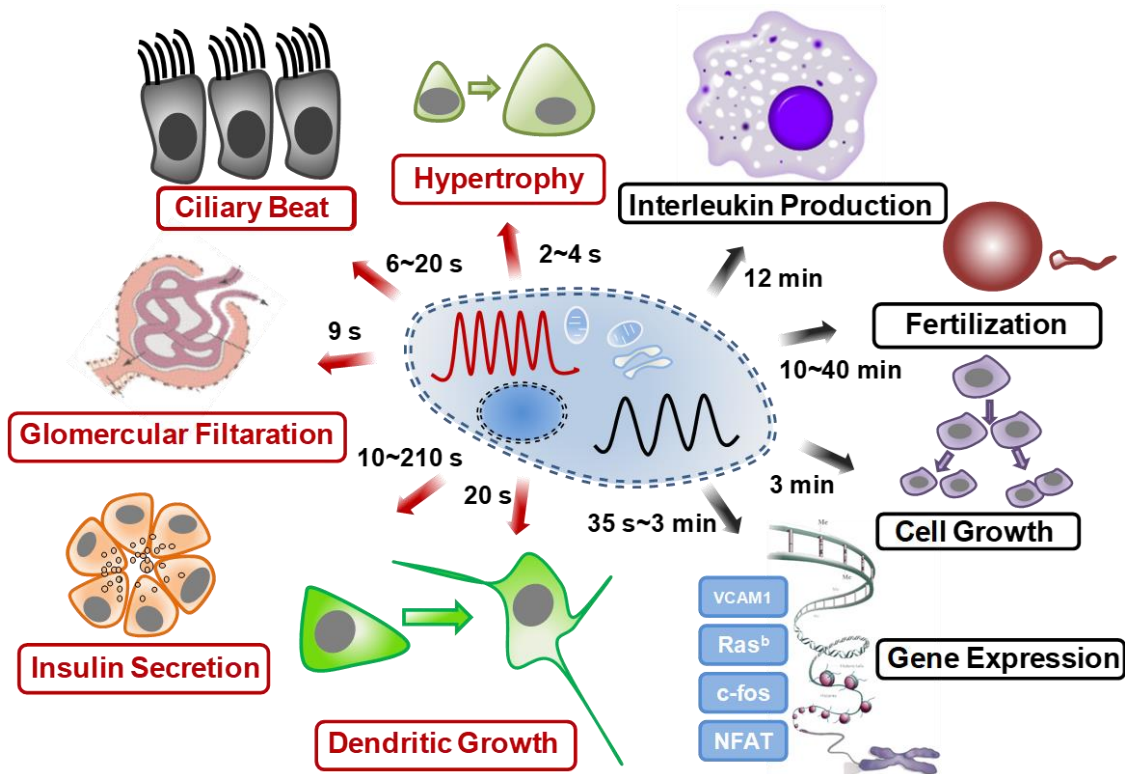


**Figure 1.1 – Calcium oscillations signal processes inside the cell.**  $\text{Ca}^{2+}$  oscillations inside the cell relate to the function of cell-based oscillation frequency where high frequency oscillations (red) do fast processes, and slower frequency oscillations (black) do slower processes.



The rate of  $\text{Ca}^{2+}$  oscillations depends on cell type and expressed proteins present (Figure 1.1). Low frequency intracellular  $\text{Ca}^{2+}$  oscillations signal slower processes such as fertilization or cell growth and fast processes such as dendritic growth or insulin secretion are signaled by fast frequency intracellular  $\text{Ca}^{2+}$  oscillations (Figure 1.1). The dynamics of  $\text{Ca}^{2+}$  from extracellularly to intracellularly and to cellular organelles is an intricate and complex system.

## 1.2 Calcium Dynamics and Cellular Signaling

Calcium is a critical ion in the body for a plethora of cellular functions such as muscle contraction, fertilization, activating of enzymes, and gene regulation. A fluctuation in cell concentrations may also have dire consequences where high  $\text{Ca}^{2+}$  levels in the cell are toxic and results in apoptosis. Intracellular calcium concentration,  $[\text{Ca}^{2+}]_i$ , is found at low levels  $\sim 100$  nM, whereas extracellular calcium concentration,  $[\text{Ca}^{2+}]_o$ , is much higher at 1.1-1.8 mM, and even up to 40 mM in the bone environment. Organelle  $\text{Ca}^{2+}$  concentration can vary with the endoplasmic/sarcoplasmic reticulum (ER/SR) being the major intracellular  $\text{Ca}^{2+}$  storage organelle with ER  $[\text{Ca}^{2+}]$  at 0.5-1.0 mM  $\text{Ca}^{2+}$  concentrations vary throughout the whole cell system. Extracellular calcium changes from 1.1 to 1.8 mM, intracellular calcium fluctuates from 0.1  $\mu\text{M}$  to 10  $\mu\text{M}$  depending on if in the resting or excited states, respectively (Figure 1.2).

Since  $\text{Ca}^{2+}$  is such a critical cellular messenger, the  $[\text{Ca}^{2+}]$  extracellularly, intracellularly, and in organelles is tightly regulated. Changes in  $[\text{Ca}^{2+}]$  from 1.1-1.8 mM to 2-3 mM can trigger intracellular and extracellular signaling cascades and as such the  $\text{Ca}^{2+}$  homeostasis within the cell is tightly regulated. While these are the general  $[\text{Ca}^{2+}]$  found in most cell types, there is differential  $[\text{Ca}^{2+}]$  found in specific cell types, such as cells in the bone have  $[\text{Ca}^{2+}]_o$  up to 40 mM and  $[\text{Ca}^{2+}]_{\text{SR}}$  of skeletal muscle cells have up to 50 mM stores<sup>[3]</sup>. These levels initially came in to play when

$\text{Ca}^{2+}$  was naturally selected as a critical cellular messenger and phosphate became the energy standard. The formation of insoluble  $\text{Ca}^{2+}$  phosphate reduces the bioavailability of phosphate and calcium for intracellular signaling. Cytosolic  $[\text{Ca}^{2+}]$  is kept in the  $\mu\text{M}$  range, or lower<sup>[2]</sup>, and fluctuations outside of these concentrations can lead to an increased  $[\text{Ca}^{2+}]_i$  which will lead to apoptosis<sup>[1]</sup>.

$\text{Ca}^{2+}$  binds to various types of calcium binding proteins (CaBPs) including calsequestrin (CaSQ), to buffer  $\text{Ca}^{2+}$  concentration, or the  $\text{Ca}^{2+}$  sensing receptor (CaSR) to read the changes in  $[\text{Ca}^{2+}]_o$  to initiate downstream intracellular signaling cascades. The  $\text{Ca}^{2+}$  levels within the cellular organelles also vary dramatically. The ER/SR is the major intracellular  $\text{Ca}^{2+}$  store and is critical for protein synthesis and muscle contraction.

The intricate intracellular regulation of  $\text{Ca}^{2+}$  levels involves  $\text{Ca}^{2+}$  trigger proteins such as calmodulin (CaM), channels such as inositol (1,4,5)-trisphosphate receptor ( $\text{IP}_3\text{R}$ ) and the ryanodine receptor (RyR), and pumps such as sarco/endoplasmic reticulum calcium-ATPase (SERCA). It also involves various buffer proteins such as calbindin in the cytosol and calsequestrin in the ER. Specific organelle  $\text{Ca}^{2+}$  concentrations also fluctuate, with the highest concentrations of  $\text{Ca}^{2+}$  being in the ER/SR, often referred to as the  $\text{Ca}^{2+}$  storage of the cell.

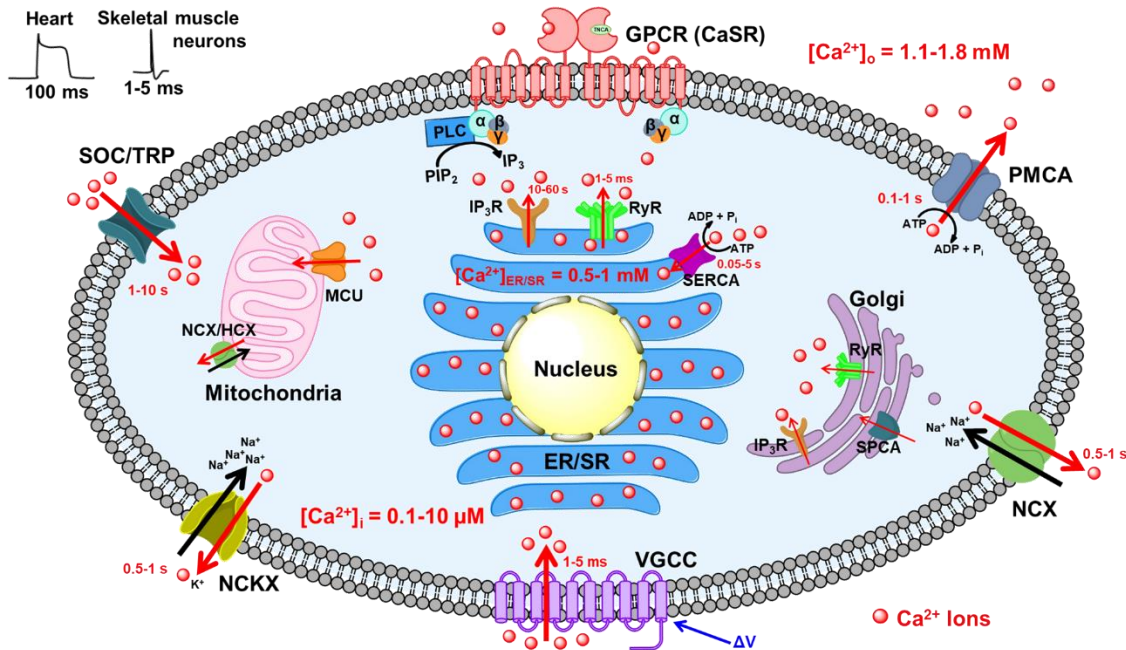


**Figure 1.2 – Calcium signaling inside the cell.**

$\text{Ca}^{2+}$  signaling dynamics in the cell to communicate the  $\text{Ca}^{2+}$  homeostasis between the high  $[\text{Ca}^{2+}]_o$  extracellularly in the mM range and the low  $[\text{Ca}^{2+}]_i$  intracellularly in the  $\mu\text{M}$  range is regulated by a multitude of proteins as well as by the internal organelle  $\text{Ca}^{2+}$  storage in the ER/SR in the mM range. These proteins operate in a variety of differing rates of  $\text{Ca}^{2+}$  transport from the millisecond (ms) to seconds (s) range. On the plasma membrane are channels that either remove  $\text{Ca}^{2+}$  from the cytosol to maintain the  $\mu\text{M}$   $[\text{Ca}^{2+}]_i$  or that bring  $\text{Ca}^{2+}$  back into the cytosol from the  $[\text{Ca}^{2+}]_o$ . The plasma membrane  $\text{Ca}^{2+}$  ATPase (PMCA), the sodium-calcium exchanger (NCX), and the potassium-dependent sodium-calcium exchanger (NCKX) are just a few proteins which pump  $\text{Ca}^{2+}$  out of the cell in exchange for energy (ATP) or gradient transfer ( $\text{Na}^+/\text{K}^+$ ). On the other hand, proteins such as store-operated channels (SOCs), transient receptor potential (TRP) channels, and voltage-gated calcium channels (VGCCs) deliver  $\text{Ca}^{2+}$  from the extracellular into the cytosol.  $[\text{Ca}^{2+}]_i$  concentration is also further regulated by ER proteins such as the  $\text{IP}_3\text{R}$ , RyR, and SERCA pump with either release  $\text{Ca}^{2+}$  from the ER/SR into the cytosol or pump  $\text{Ca}^{2+}$  back into the ER/SR, respectively. Additionally, GPCRs such as CaSR can sense  $[\text{Ca}^{2+}]_o$  and lead to a production of  $\text{IP}_3$ , which then binds the  $\text{IP}_3\text{R}$  and release ER/SR  $[\text{Ca}^{2+}]_i$  into the cytosol. The  $[\text{Ca}^{2+}]_i$  is also regulated by the mitochondria by the mitochondrial calcium uniporter (MCU) and the NCX/hydrogen-calcium exchanger (HCX) whereas the Golgi is regulated by  $\text{IP}_3\text{R}$ , RyR and secretory pathway  $\text{Ca}^{2+}$ -ATPase (SPCA).

$\text{Ca}^{2+}$  oscillations and transients also regulate cellular function through their frequency and amplitude, where the rate of frequency or the time frame of  $\text{Ca}^{2+}$  signaling can indicate to the cell

the appropriate response. A quick and rapid frequency, of a few seconds or milliseconds, can initiate muscle contraction in muscle cells while a slower and measured frequency, of 10-20 hours, can lead to cell division response<sup>[1]</sup>.  $\text{Ca}^{2+}$  can regulate the cell through transients or oscillations,  $\text{Ca}^{2+}$  sparks or whole cell  $\text{Ca}^{2+}$  waves, which can also pass intracellularly between cells for such processes as wound healing or insulin secretion<sup>[1]</sup>.

The amplitude and release kinetics of  $\text{Ca}^{2+}$  from the ER/SR via protein channels such as the RyR and  $\text{IP}_3\text{R}$  can indicate a vast variety of functional roles, such as excitation-contraction (E-C) coupling during muscle contraction<sup>[4]</sup> (Figure 1.2). The mitochondria, as the energy production center of the cell, keeps a  $\text{Ca}^{2+}$  store in the low micromolar range. This  $\text{Ca}^{2+}$  store in the mitochondria to communicate with the plasma membrane and ER/SR by controlling its release kinetics of  $\text{Ca}^{2+}$  stores<sup>[5]</sup>. The ER/SR and mitochondria have a role in regulating  $\text{Ca}^{2+}$  homeostasis by directly communicating with each other through electrostatic connections in a microdomain. This homeostatic regulation is done by regulation of  $\text{Ca}^{2+}$  increases in the mitochondrial matrix, which in turn activated several enzymes necessary for energy production. This leads to increased ATP production in the mitochondria, further showing how the mitochondria are the powerhouse of the cell. In contrast, having prolonged increased  $\text{Ca}^{2+}$  concentration can lead to cell death via apoptosis<sup>[6]</sup>. Such temporal and spatial regulation of  $[\text{Ca}^{2+}]$  and signaling is partially regulated by CaBPs, which can vary by having different  $\text{Ca}^{2+}$  binding affinities depending on their cellular environments. For instance, calmodulin, an indispensable cytosolic CaBP with four helix-loop-helix  $\text{Ca}^{2+}$  binding motifs (EF-hand), can respond to  $[\text{Ca}^{2+}]_i$  with a large  $\text{Ca}^{2+}$  induced conformational change, this change then can regulate many target proteins through binding<sup>[7]</sup>.  $\text{Ca}^{2+}$  signaling is monitored by extracellular and internal  $\text{Ca}^{2+}$  stores. The calcium sensing receptor (CaSR) is a transmembrane protein which binds extracellular  $\text{Ca}^{2+}$  and signals ER  $[\text{Ca}^{2+}]$  release

into the  $[Ca^{2+}]_i$  or inhibition to regulate overall  $Ca^{2+}$  homeostasis. Therefore, understanding CaSR mediated disease through the structure,  $Ca^{2+}$  binding, and functional signaling can help to understand the  $Ca^{2+}$  mediated molecular basis for disease regulated by CaSR  $Ca^{2+}$  dynamics. Extracellular  $Ca^{2+}$  enters the cell through receptor-operated channels (ROCs), store-operated channels (SOCs), and voltage-operated channels (VOCs). The majority of  $Ca^{2+}$  signaling is generated by internal  $Ca^{2+}$  stores, such as the ER/SR through release channels RyR and  $IP_3R$ <sup>[8]</sup>. A collapse in the communication of  $Ca^{2+}$  signaling, channel function modification by mutations, or hyperactivity of the system has been linked to various diseases and conditions, such as heart failure<sup>[9],[10]</sup>. Additionally, the divergent nature of the ER/SR with variable expression of the smooth ER, rough ER, and the SR depending on the cell types leads to the conclusion that the ER/SR does not uniformly store or signal  $Ca^{2+}$ . Thus, there is an unmet need for a methodology and targeted  $Ca^{2+}$  sensors to study the ER/SR  $Ca^{2+}$  dynamics of these subcellular microdomains to confirm their existence in cells, skeletal muscles, and neurons and be able to investigate the effects these microdomains have on the cellular system in normal and disease states.

### 1.3 $Ca^{2+}$ Binding Proteins

$Ca^{2+}$  has an ionic radius of 0.99 Å. The binding geometry of  $Ca^{2+}$  can vary from 3 to 8, but most predominately prefers a 7-coordination geometry of pentagonal bipyramidal<sup>[2, 11]</sup>.  $Ca^{2+}$  binding proteins read subtle  $Ca^{2+}$  changes and communicate these variations to other proteins, organelles, and cells.  $Ca^{2+}$  sensor proteins include calmodulin, CaSR, synaptotagmin, S-100, troponin C, annexins, STIM, etc.  $Ca^{2+}$  buffering proteins includes calreticulin, calsequestrin, parvalbumin, etc.<sup>[2]</sup>.

The most common calcium binding proteins bind calcium with a helix-loop-helix calcium binding motif called the EF-hand motif<sup>[12]</sup>. There are more than 50 EF-hand subfamilies including CTER (Calmodulin, Troponin C, and Essential Regulatory light chain proteins), CPR (Calcineurin B, p22, Recoverin proteins), the S100 subfamily, and other common proteins such as parvalbumin and aequorin<sup>[13]</sup>. EF-hand proteins can be composed of multiple EF-hand motifs, Calmodulin (CaM) is made up of four EF-hands in order to bind up to four  $\text{Ca}^{2+}$ . While most EF-hand binding proteins consist of EF-hand pairs, there are instances where there is an odd number of EF-hands, but it is much less occurrence. Troponin C (TnC) is very similar to CaM since they are in the same EF-hand family CTER which both have 4 EF-hand motifs. Although their structures are incredibly similar, these two CaBPs have very different functions. Where CaM modulates a variety of functions, the only purpose for TnC is to bring together troponin I and T for excitation-contraction (E-C) coupling in muscles for muscle contraction. The calcium binding ability and cooperativity of the  $\text{Ca}^{2+}$  binding EF-hand motifs in a multitude of CaBPs are essential for their differential cellular functions<sup>[14]</sup>.

CaBPs also contains calcium binding sites formed by discontinuous calcium ligand residues for a variety of regulatory and functional purposes.  $\text{Ca}^{2+}$  ATPases bind  $\text{Ca}^{2+}$  in exchange for ATP dephosphorylation in order to pump  $\text{Ca}^{2+}$  against the  $\text{Ca}^{2+}$  gradient.  $\text{Ca}^{2+}$  ATPases pump  $\text{Ca}^{2+}$  either outside of the cell through the plasma membrane or into the ER/SR. The most prevalent  $\text{Ca}^{2+}$  ATPases are the sarco/endoplasmic reticulum  $\text{Ca}^{2+}$ -ATPase (SERCA) pump and plasma membrane  $\text{Ca}^{2+}$  ATPase (PMCA). Maintaining the  $\text{Ca}^{2+}$  homeostasis and gradients is important to be able to utilize cellular signaling with  $\text{Ca}^{2+}$ . Annexins are another large CaBP type which does not utilize the EF-hand domain and has 16 subfamilies A1-A16<sup>[15]</sup>. Annexins interact with proteins on the cytosolic plasma membrane as well as inside of the cytosol, even including CaBPs

such as S100<sup>[3]</sup>. C2 domains, e.g., synaptotagmin and copines, are another type of CaBP with over 100 sequences. These proteins interact with membranes and proteins and are commonly found binding to enzymatic domains<sup>[3]</sup>.

There are also CaBPs specific for the endoplasmic and sarcoplasmic reticulum (ER/SR) such as the Ca<sup>2+</sup> buffering protein calsequestrin (CaSQ) found in the SR as well as the chaperone proteins calnexin and calreticulin in the ER to specify proteins for retention or degradation. Together calnexin and calreticulin help to regulate the correct protein folding as well as glycoprotein quality control. The SR can hold up to 50 mM Ca<sup>2+</sup> for the necessary rapid Ca<sup>2+</sup> release and refilling required for muscle contraction and release in skeletal and cardiac muscle, but a majority of this Ca<sup>2+</sup> is bound to CaSQ<sup>[3]</sup>. In order to regulate such a high concentration of Ca<sup>2+</sup> in the ER/SR, the calreticulin and CaSQ CaBPs are present to bind Ca<sup>2+</sup> and hold it until ready for release through the RyR. CaSQ Ca<sup>2+</sup> buffering keeps the SR free Ca<sup>2+</sup> concentration closer to 1 mM similar to ER but with the extra Ca<sup>2+</sup> bound to CaSQ, whereas the ER has Ca<sup>2+</sup> bound to calreticulin<sup>[3]</sup>. Additionally, in order to keep the low cytosolic Ca<sup>2+</sup> levels, the internal cell organelles have personal Ca<sup>2+</sup> stores. Organelles such as the ER/SR have one of the largest stores at 0.1-1 mM range, while the mitochondria also have its own store for energy production at nM to μM range. Cellular signaling can be highly dependent on CaBPs, and Ca<sup>2+</sup> gradients and fluctuations in these gradients, as well as CaBPs functionality disruption, can cause relevant physiological diseases.

#### **1.4 Family C G-protein Coupled Receptors (GPCRs)**

G-protein coupled receptors (GPCRs) are the largest family of membrane bound proteins. These proteins are known for their seven transmembrane helices (7TM) which all sub-families of the GPCR superfamily contain this signature trait. Additionally, all GPCRs have an N-terminal

extracellular domain (ECD), a C-terminal intracellular domain (ICD), as well as three extracellular loops (ECL1-3) and three intracellular loops (ICL1-3) which connect the 7TM helices. Currently, over 800 GPCRs have been discovered, but the exact size of the GPCR superfamily is still not known<sup>[16, 17]</sup>. Half of these known GPCRs have been found to regulate sensory functions such as olfactory, pheromones, taste, and light perception while the other half of the GPCRs have been shown to mediate cellular signaling through activation of ligands varying from small ions to small compounds, peptides, and even other proteins<sup>[16, 17]</sup>. In humans, there are three major classes of GPCRs, family A the Rhodopsin-like class, family B the Secretin receptor class, and family C the glutamate class. Family A GPCRs (aGPCR) is the largest group and the most thoroughly studied classified by its 7TM domain and shorter ECD and ICD regions. aGPCRs have 19 sub-families which include such proteins as chemokine receptors, angiotensin receptors, opioid receptors, melatonin receptors, P2 purinergic receptors (P2YR), cannabinoid receptors, rhodopsin receptors, dopamine receptors, and histamine receptors (H1R) to name a few<sup>[18]</sup>. Family B GPCRs (bGPCR) have a moderated ECD domain and three sub-families with such proteins as the calcitonin receptor, the parathyroid hormone receptor, secretin receptor, GPR56 orphan receptor, and diuretic hormone receptor<sup>[19]</sup>. Family C GPCRs (cGPCR) include metabotropic glutamate receptors (mGluRs), the calcium-sensing receptor (CaSR), the gamma-amino-butyric acid type B (GABAB) receptors, as well as three taste type 1 receptors<sup>[20]</sup>. The cGPCRs are classified by their large ECD where ligand binding occurs.

### **1.5 The Calcium Sensing Receptor**

The calcium-sensing receptor (CaSR/CaR) belongs to the superfamily class C from the G-coupled protein receptor family, cGPCR<sup>[21]</sup>. Before the discovery of CaSR, Ca<sup>2+</sup> was mainly considered



as a crucial second messenger thought to only regulate function through rapid, yet efficient, alterations in the intracellular calcium. After the discovery of CaSR in 1993 by Dr. Edward M. Brown who had cloned the receptor that is primarily responsible for this type of regulation from bovine parathyroid gland<sup>[22]</sup>, it was realized that  $\text{Ca}^{2+}$  could also act as a first messenger. When  $\text{Ca}^{2+}$  plays a role as the first messenger for the CaSR, it integrates calcium signaling from changes in the extracellular  $\text{Ca}^{2+}$  concentration ( $[\text{Ca}^{2+}]_o$ ) to intracellular signaling networks that are critically important for many physiological processes by cooperatively responding to small changes in  $[\text{Ca}^{2+}]_o$  to activate multiple signaling pathways. The CaSR has a topology of a dominantly large extracellular N-terminus domain (ECD), seven transmembrane helices, and an intracellular C-terminus. The CaSR regulates the narrow fluctuations allowable in calcium balance through the parathyroid glands and the production of the parathyroid hormone (PTH). This protein is a potential target for such diseases as hyperparathyroidism, hypoparathyroidism, bone diseases, tetany, osteoporosis, kidney stones, kidney failure, etc. The CaSR binds calcium, in addition to other drug targets, other metals, and amino acids<sup>[23, 24]</sup>. The GPCR class C family of proteins has been shown to function similarly while the specific end goals may differ.  $\text{Ca}^{2+}$  homeostasis between the intracellular and extracellular, as well as through the whole body, is mainly regulated by the CaSR. CaSR is a family C G-protein coupled receptor (cGPCR) which binds  $\text{Ca}^{2+}$  extracellularly and then initiates its coupled G-protein to cause a downstream production of inositol trisphosphate ( $\text{IP}_3$ ) which binds the  $\text{IP}_3$  receptor ( $\text{IP}_3\text{R}$ ) releasing  $\text{Ca}^{2+}$  from the ER in oscillations. The activation of CaSR leads to a release of  $\text{Ca}^{2+}$  from the ER which then induces the inhibition the parathyroid hormone (PTH), while inhibition of CaSR leads to a decrease in serum  $\text{Ca}^{2+}$  levels and this induces PTH production. PTH production activate the kidneys to reabsorb more  $\text{Ca}^{2+}$  and producing active vitamin-D which prompts the intestines to uptake more

$\text{Ca}^{2+}$ , in severe cases  $\text{Ca}^{2+}$  will also be absorbed from the bone engendering osteoporosis, all of this raises  $\text{Ca}^{2+}$  blood serum levels prompting the activation of CaSR and inhibition of PTH stopping these reactions until the blood  $\text{Ca}^{2+}$  levels drop again.

### ***1.5.1 The CaSR induced intracellular calcium oscillation and signaling***

The GPCR class C family of proteins has been shown to function similarly while the specific downstream signaling responses differ (Figure 1.3). The CaSR is activated on the extracellular N-terminus end of the heptahelical transmembrane protein by binding of activators such as calcium, magnesium, glutamate, amino acids, drugs, etc. This activated protein then associates with the alpha, beta, gamma complex to break off the G protein  $G_q$ , alpha-q in Figure 1.3, to activate phospholipase C ( $\text{PLC}\beta$ ).  $\text{PLC}\beta$  then converts phosphatidylinositol bisphosphate ( $\text{PIP}_2$ ) into diacylglycerol (DAG) and inositol trisphosphate ( $\text{IP}_3$ ). DAG activates protein kinase C (PKC) and downstream effectors while  $\text{IP}_3$  activates the release of  $\text{Ca}^{2+}$  from the ER by binding to the  $\text{IP}_3\text{R}$ . The  $\text{IP}_3\text{R}$  releases  $\text{Ca}^{2+}$  from the ER in an oscillation pattern, where the frequency of oscillation can affect the function of the cell for fast processes such as insulin secretion in the seconds range or slow processes such as fertilization in the minute range<sup>[25-28]</sup>. In addition to the  $G_q$  pathway GPCRs and CaSR can be activated through the  $G_i$  pathway for cAMP inhibition and the  $G_s$  pathway for increased cAMP production, although the G-protein pathway utilized by CaSR can depend on ECD binding partners or cell type for G-proteins present<sup>[29]</sup>.

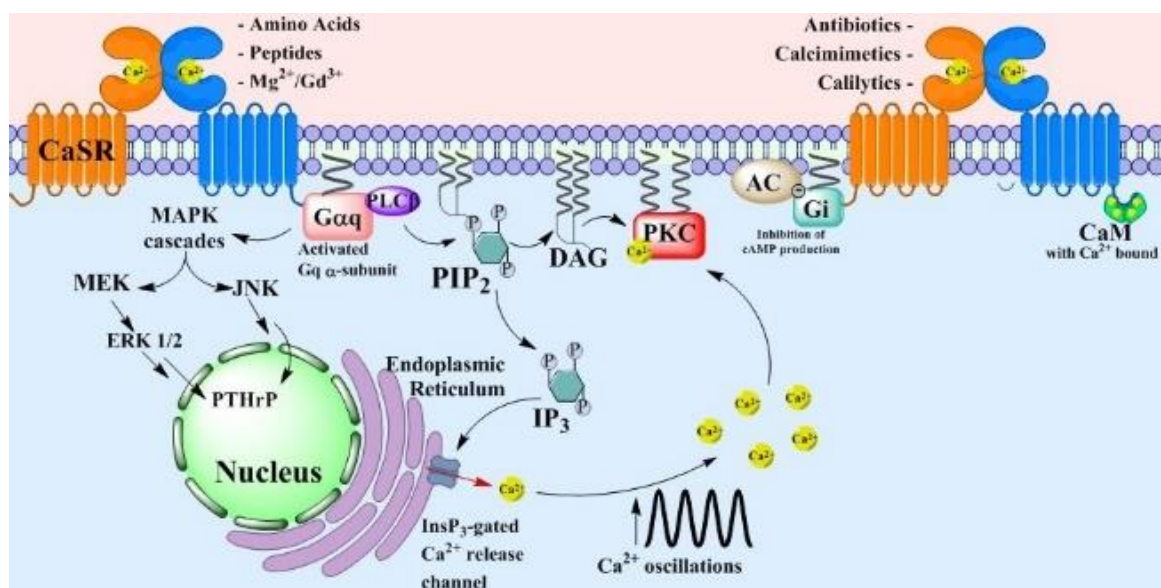


**Figure 1.3 – A diagram of the CaSR signaling pathway.**

The CaSR is shown in the VFT domain in dimer form bound to calcium in the hinge region and with other agonists/antagonists. This shows the general pathway for GPCR superfamily C proteins. After binding to an agonist, this activated protein then associates with the alpha, beta, gamma complex to break off the G protein Gq, alpha-q in the image below, to activate phospholipase C, PLC $\beta$ . PLC $\beta$  then converts phosphatidylinositol bisphosphate, PIP<sub>2</sub>, into diacylglycerol, DAG, and IP<sub>3</sub>. DAG activates PKC and downstream effectors while IP<sub>3</sub> activates the release of Ca<sup>2+</sup> from the ER.

### *1.5.2 Diseases of CaSR and mutation*

Unlike other families of GPCRs, the majority of cGPCRs size and functionality resides in the large ECD. Over 390 mutations on CaSR that have been found in disease states such as familial hypocalciuric hypercalcemia (FHH) and neonatal severe hyperparathyroidism (NSHPT) which reduce CaSR's sensitivity to [Ca<sup>2+</sup>]<sub>o</sub>, whereas activating mutations of autosomal dominant hypocalcemia (ADH) as well as carcinomas. Of the 390 mutations over 225 mutations are in the ECD alone, accounting for over 57% of the disease-causing mutations for CaSR. Since the Ca<sup>2+</sup> binding to CaSR has long been shown through binding assays and mutation studies to bind in the ECD, it comes as no surprise that many disease mutations occur in this critical domain of the receptor. Additionally, if looking at the diseases associated directly with dysfunction in the Ca<sup>2+</sup>

homeostasis from CaSR mutations (FHH, ADH, and NSHPT) there are 216 mutations for CaSR and 134 mutations in the ECD alone, accounting for 62% of the mutations. Due to the lack of a determined CaSR crystal structure, the location of drug binding is still unknown. Thus, although there are several drugs which target CaSR and one which is FDA approved, cinacalcet, no studies have been able to show where these compounds definitively bind and can only be done with mutational studies on the proposed binding regions based on computational binding studies.

### *1.5.3 Challenges in studying the CaSR*

The challenges in studying the CaSR are diverse and in multitudes. First, the CaSR is a membrane protein, so the challenges associated with membrane proteins may also occur to the CaSR. Membrane proteins are difficult to separate from the cells due to their hydrophobic transmembrane domain. Also, heating may cause aggregation and thus reduce the solubility of the protein. Secondly, X-ray crystallography has been used as one of the major tools to study the structure of proteins, but in a glycosylated protein, such as the CaSR, it is difficult at best. Like other glycosylated proteins, the complex form of the glycans on the CaSR can prevent the crystallization of this protein because they usually inhibit crystallization. Moreover, the selectivity of the CaSR for different amino acids is not apparent and the interaction between amino acids and the CaSR are relatively weak, in the mM range.

Currently, methods for direct measurement of  $\text{Ca}^{2+}$  and amino acid binding to the CaSR have not yet been well established, nor are there methods for directly monitoring ligand-induced conformational changes of the proteins. Approaches for addressing these questions rely on indirect measurements of calcium-induced intracellular signaling changes in living cells or utilizing the Fluorescence Resonance Energy Transfer (FRET) assay for monitoring ligand generated

fluorescence changes in isolated proteins. Last, but not least, the large size of the protein, extracellular domain 612 amino acids; whole protein 1078 amino acids, and the fact that the CaSR functions as a dimer, contribute to the difficulties in studying the protein.

## **1.6 Calcium Related Disorders**

The disruption in  $\text{Ca}^{2+}$  homeostasis can lead to a host of issues since  $\text{Ca}^{2+}$  is necessary for such functions as muscle contraction, cardiac function, and bone formation. Here,  $\text{Ca}^{2+}$  disease states regulated by the major  $\text{Ca}^{2+}$  storage organelle the ER/SR and neurodegenerative diseases will be discussed. Dysregulation of  $\text{Ca}^{2+}$  leads to many disease states, homeostasis disease states by the  $\text{Ca}^{2+}$  homeostasis regulator CaSR is outlined more specifically in Chapter 2 and 3.

### ***1.6.4 Differential expression of key CaBPs and ER/SR related disorders***

There are three major membrane proteins on the surface of the ER/SR which regulate the  $\text{Ca}^{2+}$  homeostasis of the ER  $\text{Ca}^{2+}$  store. These three proteins are the ryanodine receptor (RyR), the inositol triphosphate receptor ( $\text{IP}_3\text{R}$ ), and the sarco/endoplasmic reticulum  $\text{Ca}^{2+}$ -ATPase (SERCA) pump. The RyR and  $\text{IP}_3\text{R}$  both release  $\text{Ca}^{2+}$  from the ER/SR into the cytosol while the SERCA pump brings  $\text{Ca}^{2+}$  back into the ER/SR. Each of these ER/SR membrane proteins have different isoforms for differential expression in varying tissue types for  $\text{Ca}^{2+}$  regulation (Table 1.1).

RyR1 is expressed in skeletal muscle, brain cerebellum, and hippocampus<sup>[30]</sup>. RyR2 is expressed in the heart muscle, brain cerebellum, and hippocampus, as well as in the placenta<sup>[9, 30, 31]</sup>. RyR3 is expressed more broadly than RyR1 and RyR2, having been found in such regions as liver, kidney, brain, placenta, and skeletal muscle. RyR3 in the brain is found to be most highly expressed in regions such as the hippocampus, cerebellum, caudate nucleus, amygdala, and lower

expression in the thalamus, corpus callosum, and substantia nigra<sup>[30, 32]</sup>. The IP<sub>3</sub>R also has three isoforms called IP<sub>3</sub>R type 1-3. Further, SERCA pumps also present with three primary genes encoding SERCA type 1-3. Table 5.1 outlines the differential cellular expression of the RyR, IP<sub>3</sub>R, and SERCA pump isoforms. SERCA1 has two characterized additional isoforms from alternative splicing referred to as SERCA1a and SERCA1b. SERCA1 is mainly expressed in skeletal muscle and fast-twitch muscle fibers<sup>[33]</sup>. For the isoforms SERCA1a is the dominant form found in adult skeletal muscle while SERCA1b is found in fetal skeletal muscles<sup>[34, 35]</sup>. SERCA2 is expressed in all tissue types with its isoforms being distributed in differing tissue types. SERCA2a isoform is found mainly in slow-twitch skeletal muscle, cardiac muscle, and slightly in smooth muscle<sup>[36-40]</sup>. The SERCA2b isoform is found at low levels throughout all tissue types including smooth muscle and non-muscle tissues such as the liver, pancreas, brain, and kidneys<sup>[36-38, 41-43]</sup>. The isoform SERCA2c is also found in cardiac and cardiomyocytes, hematopoietic, kidney, liver, lung, and epithelial cells<sup>[36-38]</sup>. SERCA3 is found mainly in non-muscle cells with minor expression in muscle cells<sup>[44-47]</sup>. There are seven known SERCA3 isoforms named SERCA3a to SERCA3g, with SERCA3a, SERCA3b, and SERCA3c being the most thoroughly studied of the known isoforms<sup>[46-50]</sup>. Based on the discovery of differential expression of isoforms at different locations, it has been hypothesized that calcium dynamics at microdomains close to the essential proteins could be very different. Alteration of the differential expression of their isoforms by mutations leads to a multitude of disease states (Table 1.1). However, such calcium subcellular microdomain dynamics have yet to be reported before.

**Table 1.1 – ER/SR protein diseases related to calcium signaling.**

Inositol trisphosphate receptor (IP <sub>3</sub> R)	Ryanodine receptor (RyR)	Sarco/endoplasmic reticulum Ca <sup>2+</sup> -ATPase (SERCA) pump
Alzheimer's disease (AD)	Alzheimer's disease (AD)	Brody disease
Bipolar disorder (BPD)	Malignant hyperthermia (MH)	Darier disease (DD)
Spinocerebellar ataxia 15 and 29 (SCA15/29)	Catecholaminergic polymorphic ventricular tachycardia (CPVT)	Type II diabetes
Huntington's disease	Central core disease (CCD) myopathy	Acrokeratosis verruciformis (AKV)
Schizophrenia	Cardiac arrhythmia	
Amyotrophic lateral sclerosis (ALS)	Multiminicore disease with external ophthalmoplegia (MMDO)	
Epilepsy		

Malignant hyperthermia (MH) is associated with RyR1 since MH is an autosomal dominant disease associated with skeletal muscle where the RyR1 is highly expressed. 100 naturally occurring RyR1 mutations have been found in relation to MH<sup>[51-94]</sup>. MH is a severe reaction to anesthetic drugs resulting in muscle rigidity, fever, acidosis, and if not treated immediately, death. Central core disease of muscle (CCD) is another disease mainly affected by the 48 point mutations and one deletion associated with the RyR1<sup>[51, 59, 69, 72, 89, 92, 93, 95-113]</sup>. CCD is marked by skeletal muscle weakness that can be mild to severe since this disease is related to the RyR dysfunction many also simultaneously have MH. CCD can cause delayed development of motor skills and cause scoliosis. Multiminicore disease with external ophthalmoplegia (MMDO) is attributed by five mutations on RyR1<sup>[114-116]</sup>. MMDO is a heterogeneous neuromuscular disease that affects muscle fibers, specifically skeletal muscles like CCD, and many also present with MH too. MMDO can also cause issues with respiratory failure when the muscles required for breathing are affected.

Catecholaminergic polymorphic ventricular tachycardia (CPVT) is a disease caused by mutations in RyR2 or CaSQ. There are 40 mutations to RyR2 known to cause CPVT<sup>[117-130]</sup>. CPVT affects the muscles in the heart where activity or stress can trigger arrhythmia, and in untreated or severe cases lead to cardiac arrest. Additionally, one RyR2 mutation has been shown to cause arrhythmogenic right ventricular dysplasia (ARVD)<sup>[131]</sup>. ARVD leads to a steady break down of

the heart wall muscle called the myocardium, this weakening can lead to arrhythmias and cardiac arrest. Disease-related mutations in RyR3 has been less studied than the RyR1 and RyR2 isoforms, and as such has not currently reported disease-related mutations.

Similarly, to RyRs, differing mutations of IP<sub>3</sub>Rs leads to a variance of disease states. The IP<sub>3</sub>R1 has three associated disease with mutations occurring on IP<sub>3</sub>R1. One mutation on IP<sub>3</sub>R1 causes spinocerebellar ataxia 15 (SCA15) and two more mutations cause spinocerebellar ataxia 29 (SCA29), SCA is a disease of cerebellum leading to slow degradation of motor functions <sup>[132-135]</sup>. Additionally, four more IP<sub>3</sub>R mutations lead to another neurological disorder Gillespie syndrome<sup>[136, 137]</sup>. Gillespie syndrome causes underdevelopment of the cerebellum leading to slight intelligence deficiency, aniridia, balance issues, and speech delay from mouth muscle dysfunction.

Only one mutation has been found so far on IP<sub>3</sub>R2 relating to a disease state, this mutation is a loss of function mutation leading to anhidrosis, isolated, with normal sweat glands (ANHD) which is also known by Dann-Epstein-Sohar syndrome which disrupts the body's ability to sweat normally<sup>[138]</sup>. So far, there are no IP<sub>3</sub>R3 related disease mutations found.

SERCA1 has only one disease mutation related to Brody myopathy (BRM), a disease which affects the skeletal muscles and causes muscles stiffness and cramping especially after exercising and in cold weather, this disorder also causes an overproduction of myoglobin from the muscle tissue damage<sup>[139]</sup>. SERCA2 has two associated diseases, acrokeratosis verruciformis (AKV) and Darier disease (DD). AKV is associated with one point mutation of P602L while DD has 44 point mutation and three segment deletions leading to the disease state<sup>[138, 140-145]</sup>. AKV and DD are both disorders affecting the skin and causing lesions to appear, which can be crusty or pus filled. These



lesions can be aggravated by stress, clothing, or the environment. SERCA3 currently has no known disease mutations.

Primarily due to limitations of imaging techniques and lack of calcium sensors that are able to report the local calcium responses with required kinetics and calcium binding affinity, this work is mostly unexplored. Chapter 5 will report our effort in visualizations of calcium dynamics at microdomains using our designed calcium sensors.

### ***1.6.5 Neurological calcium diseases***

There are two types of neurotransmitters which are classified by their signaling functions as either excitatory or inhibitory neurotransmitters.  $\text{Ca}^{2+}$  functions in neuron physiology by overseeing the secretion as well as the synthesis of neurotransmitters. Release of neurotransmitters is regulated by the  $[\text{Ca}^{2+}]_i$  and also affects the postsynaptic action potential capabilities.  $\text{Ca}^{2+}$  signaling has been shown to affect a multitude of processes throughout the body and also in learning, memory, neuron excitability, dendrite development, and synaptic transmissions.  $\text{Ca}^{2+}$  dysfunction through mGluRs, RyR, IP<sub>3</sub>R, and the SERCA pump have been linked to many neurodegenerative disorders including Alzheimer's disease (AD), bipolar disorder (BPD), amyotrophic lateral sclerosis (ALS), Huntington's disease (HD), schizophrenia, spinocerebellar ataxias, Parkinson's disease (PD), epilepsy, and fragile X syndrome (FXS) (Table 1.1)<sup>[146-172]</sup>. The damage of  $\text{Ca}^{2+}$  activity-dependent proteins is associated with the development and evolution of several neurodegenerative diseases.

## **1.7 Unmet Need to Design Calcium Sensors**

There is a lack of  $\text{Ca}^{2+}$  sensors for targeting to the ER/SR accurately, at the high  $\text{Ca}^{2+}$  environment of 1 mM, and with appropriate rapid kinetics to monitor quick responses. Currently,  $\text{Ca}^{2+}$  ER dyes cannot be targeted accurately to specific organelles especially for subcellular environments and

other protein-based  $\text{Ca}^{2+}$  ER sensors have slow kinetics related to their multiple  $\text{Ca}^{2+}$  binding sites and the  $\text{Ca}^{2+}$  induced large conformational change to induce fluorescence changes. There is a need for a sensor that can avoid common imaging pitfalls such as photobleaching and methodologies to combat the cell movement/shape change in response to reagents. Fast dynamic measurements in the ER/SR using current protein-based fluorophores on the market is not adequate since either their kinetics are either too slow or their  $K_d$  is too low for the high ER [ $\text{Ca}^{2+}$ ]. Also, there is a lack of having an imaging methodology capable of imaging fast kinetics and in subcellular location differences with high resolution of the ER network. Using an improved targeted designed sensor, we could more accurately investigate the heterogeneous distribution of ER/SR pumps and channels.

## 1.8 Fluorescent Proteins

The discovery of fluorescent proteins (FPs) in 1962 allowed for the field of genetically encoded calcium indicators to flourish by utilizing these FPs. The first discovered FP was green FP (GFP) by Shimomura et al. from the jellyfish *Aequorea victoria* as a side product of purifying aequorin protein<sup>[173]</sup>. With the first cloning and expression of GFP in the early 1990s, the protein was demonstrated to be able to retain its fluorescence in other systems of expression besides the species it was extracted from<sup>[174-176]</sup>. Upon solving the GFP crystal structure in 1996, the studies of altering GFP for the creation of genetically encoded indicators took off<sup>[177, 178]</sup>. GFP structure is marked by a  $\beta$ -barrel motif with the fluorescence from the central chromophore within the  $\beta$ -barrel center. This chromophore is a three amino acid aromatic sequence from the transcription of GFP itself, comprised of Ser65, Tyr66, and Gly67. The first significant improvement of GFP to utilize the protein for further development as a fluorescent probe was the mutation of WT GFP into enhanced

GFP (EGFP) which showed brighter fluorescence at 488 nm and enhanced expression at 37°C<sup>[179]</sup>. In order to broaden the fluorescence color spectrum, mutations were made directly or indirectly to the chromophore of GFP to make blue FP (BFP) with the best mutation being Tyr66 in the chromophore into a His changing the excitation/emission wavelength from 488/510 nm for GFP to 382/448 nm for BFP, respectively<sup>[180]</sup>. Additionally, when the Y66 chromophore amino acid was mutated to tryptophan, instead of histidine, a cyan FP (CFP) was formed instead with an excitation/emission of 436/485 nm, respectively. Via further mutating the GFP to Y66H and Y145F double mutation led to an even better BFP with fluorescence intensity and production comparable to the WT GFP<sup>[181]</sup> and adding the third mutation F64L led to an enhanced BFP (EBFP)<sup>[182-184]</sup>. Further mutagenesis of CFP led to a group of mutations called W7 (Y66W, N146I, M153T, V163A, and N212K) which shifted the excitation/emission to 434/476 nm, respectively, making an enhanced CFP (ECFP)<sup>[181-183]</sup>. Another variant of GFP was made by mutations T203Y, S65G, V68L, and S72A that shifted GFP to yellow FP (YFP)<sup>[177, 185]</sup>. Furthermore, an enhanced version EYFP was also developed with increased pH sensitivity compared to EGFP, increasing the pKa from 6.15 to 7.1<sup>[186]</sup>. These early YFP variants had issues relating to photobleaching and chloride sensitivity, thus after several rounds of more mutations improved YFPs were developed called Citrine, from V68L and Q69M, and Venus, from F46L, F64L, M153T, V163A, and S175G. These new variants Citrine and Venus had not only removed their chloride sensitivity but also improved the pH sensitivity and reduced the photobleaching effects<sup>[187, 188]</sup>.

There was a pressing need to design FPs with other wavelengths within the full light spectrum, but mutation studies upon GFP were on ever able to extend past 529 nm thus precluding red fluorescent proteins from being designed<sup>[182]</sup>. Therefore, focus turned to find naturally occurring other color variants of FPs similarly to how GFP was discovered in the jellyfish *Aequorea victoria*. Matz et

al. were able to identify and clone six FPs from fluorescent coral species, with the most hopeful being the one derived from *Discosoma* sp. “red” mushroom anemone, drFP583 or DsRed as it is now referred to<sup>[189]</sup>. Unfortunately, DsRed itself was not ideal for studies since it oligomerized, leading to aggregation, toxicity, and activating other proteins which are affected by oligomerization. While DsRed did present with these caveats, there were benefits of being insensitive to pH, having little photobleaching, and being able to be mutated to even longer wavelengths, thus still making DsRed a good starting point for further optimization studies<sup>[190]</sup>. Just three years later in 2002 was discovered the first monomeric version of DsRed termed mRFP1 (monomeric red fluorescent protein)<sup>[191]</sup>. It took 33 mutations on DsRed to create mRFP1 and with these mutations come faster maturation time and a shift in fluorescence of 25 nm to 584 and 607 nm. Unfortunately, the mRFP1 does have more sensitivity to photobleaching as well as a decreased quantum yield and extinction coefficient<sup>[191]</sup>. This first step in producing a stable RFP allowed for further mutation studies to be performed which was able to produce a wider variety of FPs from excitation of 487 to 587 and with emission from 537 to 610, respectively. These newly designed monomeric (m) and dimeric (d/td) FPs are mHoneydew (Ex 487/504, Em 537/562 nm), mBanana (Ex 540/Em 553 nm), mOrange (Ex 548/Em 562 nm), dTomato (Ex 554/Em 581 nm), tdTomato (Ex 554/Em 581 nm), mTangerine (Ex 568/Em 585 nm), mApple (Ex 568/Em 592 nm), mStrawberry (Ex 574/Em 596 nm), and mCherry (Ex 587/Em 610 nm)<sup>[192, 193]</sup>.

## 1.9 Fluorescent Ca<sup>2+</sup> Dyes

Ca<sup>2+</sup> is a critical intracellular messenger and imaging these cytosolic Ca<sup>2+</sup> changes were necessary not only to understand Ca<sup>2+</sup> signaling and dynamics but also to see the effects diseases or drugs have upon these Ca<sup>2+</sup> signaling cascades. Many previous Ca<sup>2+</sup> probes initially were not cell-

permeable, and thus the cell had to be permeabilized to allow the indicator to enter the cell, which changes the signaling responses as well as allows for the probes to potentially be washed away. Thus, designing  $\text{Ca}^{2+}$  indicators which were cell-permeable became the goal for many. In 1980  $\text{Ca}^{2+}$  indicators were designed based on  $\text{Ca}^{2+}$  chelator BAPTA, which is derived from EGTA, to create several indicators, with the ideal being Quin-2<sup>[194]</sup>. There was still the issue of the probe not being cell-permeable, which was brilliantly circumvented in 1981 by adding acetoxymethyl groups onto each oxygen group ( $\text{COO}^-$ ) creating a hydrophobic indicator which was able to pass through the plasma membrane and then be de-esterified by naturally occurring esterase within the cell cytosol and therefore cleaved into the active Quin-2  $\text{Ca}^{2+}$  indicator<sup>[195]</sup>. Quin-2 continued to be improved upon by making other BAPTA derivatives, and six new  $\text{Ca}^{2+}$  indicators were designed in 1985, stil-1, stil-2, indo-1, fura-1, fura-2, and fura-3<sup>[196]</sup>. Fura-2 and Indo-1 immediately became famous for their new properties of being ratiometric. Fura-2 has dual excitation peaks (340/380 nm) which are ratiometrically  $\text{Ca}^{2+}$  dependent and a single emission peak (510 nm). Indo-1, on the other hand, has dual emission peaks (400/475 nm) and a single excitation peak (350 nm)<sup>[196]</sup>. Currently, there are over 30  $\text{Ca}^{2+}$  indicators on the market for  $\text{Ca}^{2+}$  imaging with single or ratiometric fluorescence properties, excitation wavelengths from 340-615 nm, and  $K_d$  values for  $\text{Ca}^{2+}$  between 60 nM and 320  $\mu\text{M}$ .

**Table 1.2 – Current calcium indicators on the market.**

Indicator	$K_d$ for $\text{Ca}^{2+}$ ( $\mu\text{M}$ )	Excitation (nm)	Emission (nm)	References
Calcium Green-1	0.19	490	530	[197, 198]
Calcium Orange	0.19	550	575	[197]
Calcium Crimson	0.19	590	615	[197]

Fluo-3	0.33	505	525	[199, 200]
Fluo-4	0.35	494	520	[201-203]
Fluo-4FF	9.7	494	520	[204, 205]
Fluo-5F	2.3	494	520	[206, 207]
Fluo-5N	90	494	520	[208, 209]
Fura-2	0.15	340/380	510	[196, 197, 210-213]
Fura-4F	0.77	340/380	510	[214]
Fura-6F	5.3	340/380	510	[214, 215]
Fura-FF	5.5	340/380	510	[214, 216, 217]
Fura Red	0.14	420/480	650	[218, 219]
Indo-1	0.23	488	405/485	[196]
Mag-fluo-4	22	490	520	[220]
Mag-fura-2	25	340/380	510	[221-223]
Mag-indo-1	35	350	405/485	[224]
Magnesium Green	6		530	[225]
Oregon Green 488 BAPTA-1	0.17	488	520	[226]
Oregon Green 488 BAPTA-5N	20	494	520	[215]
Oregon Green 488 BAPTA-6F	3	494	520	[227, 228]
Quin-2	0.06	350	495	[194]
Rhod-2	0.57	552	580	[229, 230]
Rhod-FF	19	522	580	[231, 232]
X-rhod-1	0.7	580	600	[233, 234]
X-rhod-5F	1.6	580	600	[233, 235]

---

While  $\text{Ca}^{2+}$  sensing dyes have proliferated the market, they do have certain advantages and limitations. Calcium dyes are highly conjugated species found as salts, dextran conjugates, or acetoxymethyl esters. The commonly used synthetic dyes are suitable due to the wide variety of binding affinities available as well as the quick introduction to the cell.  $\text{Ca}^{2+}$  dyes are mainly targeted to the cytosol and are incubated with the cells to allow permeabilization of the dye into the cytosol, this incubation is easier on the cells than protein transfection and expression. Additionally, chemical  $\text{Ca}^{2+}$  indicators come in a broad range of  $\text{Ca}^{2+}$  affinities for a multitude of uses cellularly. Unfortunately, while  $\text{Ca}^{2+}$  dyes have been targeted to other cellular organelles, their small compound chemistry prevents accurate organelle targeting and instead is a pseudo-targeting by a recombinant targeting of the esterase that cleaves the AM form of the  $\text{Ca}^{2+}$  dyes and thus cleaves them into the organelle the esterase is targeted to<sup>[236, 237]</sup>. This targeting method, targeted-esterase-induced dye loading (TED), is shown to have residual  $\text{Ca}^{2+}$  dye in the cytosol and other regions, but by using a low affinity dye such as Fluo-5N mitigates this incomplete targeting by having the ER signal be larger than the cytosolic signal, while this method does work it is not entirely accurate since there is dye in the cytosol as well as the organelle and removes the advantage of having a wide array of affinity dyes to choose from<sup>[236, 237]</sup>. Additionally, extended experiments can have an issue in that the chemical  $\text{Ca}^{2+}$  dyes are eventually compartmentalized and removed from the cells<sup>[238]</sup>. The setbacks are that these dyes cannot easily be targeted to specific organelles and often are compartmentalized and thus diffuse out of the cell after a prolonged time, commonly seen in longer experimental procedures. Attempts to remedy this compartmentalization have proven successful with large dextran tags, but this method also made the dyes too large for the easy loading. Thus, a protein  $\text{Ca}^{2+}$  sensor with appropriate protein

retention sequences would be ideal for sensor targeting to organelles and having a stable  $\text{Ca}^{2+}$  sensor for different experiment conditions throughout the cell.

### **1.10 Fluorescent $\text{Ca}^{2+}$ Sensor Proteins**

$\text{Ca}^{2+}$  has an essential role in biological functions and influences a multitude of diseases such as osteoporosis, cancers, heart disease, and Alzheimer's. This regulation of diseases creates a dire need for intracellular  $\text{Ca}^{2+}$  probes to measure the dynamics of  $\text{Ca}^{2+}$  in vivo. When FPs were first discovered, they were always planned to be used for fluorescence usage whether they would be tagged to organelles/proteins for investigation or to be used as direct binding sensors. The first genetically encoded calcium indicators (GECIs), designed from fluorescent proteins (FPs), were the cameleon (CaMeleon) series in 1997, getting its name from their CaBP being CaM and their Förster resonance energy transfer (FRET) color change giving the idea to name their series after the color-changing animal the chameleon<sup>[239]</sup>. This discovery was made possible by earlier work investigating CaM and M13 a synthetic peptide derived from the CaM binding domain on the light chain of the myosin motor protein<sup>[240]</sup>. Porumb et al. found if they connected CaM and the M13 peptide by a glycyglycine linker that after CaM binds  $\text{Ca}^{2+}$  then it can further bind the attached M13 domain, this  $\text{Ca}^{2+}$  dependent binding through a linker opened up the possibility of fluorescent proteins having FRET interactions when brought together attached to this CaM/M13 interaction<sup>[239, 240]</sup>. The cameleon series was made with initially seven FRET sensors with different combinations of FPs as well as retention sequences for organelle targeting. These first seven were cameleon-2 (EBFP/EGFP), cameleon-2nu (nucleus EBFP/EGFP), cameleon-3er (ER EBFP/EGFP and E104Q), yellow cameleon-2 (ECFP/EYFP), yellow cameleon-3er (ER ECFP/EYFP and



E104Q), yellow cameleon-4er (ER ECFP/EYFP and E31Q), and ECFP-CaM and M13-EYFP separated domains<sup>[239]</sup>.

Just two years later a new class of GECIs were introduced using a technique of circular permutation of a single FP leading to a removal of the necessity of FRET between two FPs and allowing the direct CaBP being attached to the single FP<sup>[241]</sup>. This new class of GECIs was named camgaroos since they had a direct CaM CaBP inserted between residues 145/146 leading to the idea that the CaM was being carried by the GFP/YFP in a pouch position similar to kangaroos<sup>[241]</sup>. When Ca<sup>2+</sup> binds to the CaM in camgaroos the FP is able to become fluorescent through conformational change<sup>[241]</sup>. In 2001 pericams and GCaMPs were simultaneously developed by combining the split FP concept from camgaroos with the CaM/M13 binding partners from the cameleon sensors<sup>[242, 243]</sup>. The pericams have CaM on one half of the EYFP and M13 on the other half, so when Ca<sup>2+</sup> binds to CaM then the bound form of CaM can bind M13 and either bring the FP halves together or separate them through conformational change and resulting in a fluorescence signal gain or loss, respectively. Pericams come in different forms and organelle targeting such as pericam, flash pericam, inverse pericam, ratiometric-pericam, ratiometric-pericam-mt (mitochondria), ratiometric-pericam-nu (nucleus), and split-pericam<sup>[242]</sup>. GCaMPs were developed from the EGFP instead of EYFP and did not have any inverse forms, so they only gain fluorescence upon Ca<sup>2+</sup>/CaM/M13 binding<sup>[243]</sup>. GCaMP was the initially engineered EGFP variant but was later used as a steppingstone for production of a plethora of further CaMP variants with different colors as well as targeting, which are still being further improved to date.

Improvements were then made on the original cameleon series of sensors in 2006 designing a series of sensors based on the newly engineered YFP Venus in circularly permuted (cpV) form and CFP<sup>[244]</sup>. Additionally, they made three different computationally directed mutations on the

M13 peptide in order to reduce perturbation of the sensors by naturally occurring CaM in the cell<sup>[244]</sup>. The change of the FP to cpV led to a 3-5-fold increase in the dynamic range, and the modified M13 led to higher Ca<sup>2+</sup> sensitivity of the sensors. Three different M13 modifications were made leading to three sensors D2cpv (A13I), D3cpv (I14F), and D4cpv (V11W)<sup>[244]</sup>. Furthermore, targeted versions were made to target the plasma membrane and the mitochondria<sup>[244]</sup>.

GCaMPs were being further modified for improvements and in 2006 GCaMP2 was designed, which was able to do cell imaging since it was more stable at body temperatures<sup>[245]</sup>. Subsequently, GCaMP3 was designed in 2009 from GCaMP2 with a 3-fold increase dynamic range and 1.3-fold increased Ca<sup>2+</sup> sensitivity. Zhao et al. then began working in 2011 on large scale random mutations of GCaMP3 in order to elucidate improved and variant GCaMPs across the FP color spectrum<sup>[246]</sup>. These new indicators were termed genetically encoded Ca<sup>2+</sup> indicators for optical imaging (GECOs)<sup>[246]</sup>. This led to the development of G-GECO series (GFP), R-GECO series (RFP mApple), B-GECO series (BFP), GEM-GECO series (blue-green FP), and GEX-GECO series (ratiometric GFP)<sup>[246]</sup>.

### **1.11 Research Objectives and Questions to be Addressed**

The overall goal of our research is to understand the Ca<sup>2+</sup>-mediated molecular basis for disease in high Ca<sup>2+</sup> environments of extracellular and ER/SR. We committed to investigating this quandary by looking at the calcium sensing receptor (CaSR) for the sensing of high extracellular Ca<sup>2+</sup> to signal intracellular Ca<sup>2+</sup> function through the ER oscillatory Ca<sup>2+</sup> release through the IP<sub>3</sub>R. In order to understand the ER high Ca<sup>2+</sup> dynamics relationship, we designed an ER Ca<sup>2+</sup> sensor capable of fast kinetics and able to investigate subcellular microdomain changes. The overall

question of what is the  $\text{Ca}^{2+}$ -mediated molecular basis for disease in high  $\text{Ca}^{2+}$  environments of extracellular and ER/SR is addressed in our research. We address this wide-ranging question by delving into the CaSR and ER/SR targeted  $\text{Ca}^{2+}$  sensors projects.

Chapter I provides an overview of the background related to calcium regulation by calcium binding proteins, especially calcium sensing receptor and related diseases. Calcium dynamics and the need for design calcium sensor in subcellular calcium. Objectives and questions will be addressed in this dissertation are provided.

In Chapter 2, we accomplished this goal by elucidating the first CaSR crystal structure of the ECD domain using purified protein from a mammalian expression system. After determining the first crystal structure of CaSR ECD, we investigated the effect and functionality of cations and/or CaSR binding ligands on WT CaSR and disease-related mutations in order to understand the mechanisms of how CaSR integrates the  $\text{Ca}^{2+}$ -mediated signaling and to probe the molecular basis for diseases resulting from alterations in  $\text{Ca}^{2+}$  homeostasis.

In Chapter 3 we were then interested in if we could correlate the changes between the WT CaSR and disease-related mutations using bacterially expressed CaSR for structural information in comparison to functional and signaling information gained from cellular CaSR studies in order to expand our understanding in disease-mediated function differences.

In Chapter 4, we also used TNCA as a potential lead compound for therapeutic CaSR drug screening and structure-based drug design in order to discover a new and improved therapeutic for CaSR either as a calcimimetic or calcilytic.

In Chapter 5, we then turned to look at the relation of ER/SR  $\text{Ca}^{2+}$  dynamics in global and localized microdomain regions for the understanding of the regulation of cellular  $\text{Ca}^{2+}$  dynamics. First, we designed an ER/SR sensor with the capability to detect high ER  $[\text{Ca}^{2+}]$  with fast kinetics for

variable  $\text{Ca}^{2+}$  dynamics called CatchER<sup>+</sup>. We were then interested in if CatchER<sup>+</sup> able to function in the ER/SR under live-cell imaging and monitor the global and the local ER/SR subcellular changes of  $\text{Ca}^{2+}$  dynamics through activation of RyR, IP<sub>3</sub>R, and SERCA pumps and were able to use new imaging modalities of HILO and STORM imaging. In order to further investigate these microdomain localized to these subcellular locations of the ER/SR, we designed a targeted sensor to the skeletal muscle RyR co-localizing junctional protein 45 (JP45) at a local microdomain called CatchER<sup>+</sup>-JP45 in order to observe local versus global  $\text{Ca}^{2+}$  dynamics.

In Chapter 6 we were also interested in the microdomains through the variable ER expression of neuronal systems, so we applied CatchER<sup>+</sup> in hippocampal neurons to see the differential subcellular signaling in response to DHPG activation of mGluR1/5 to potentiate LTD.

In Chapter 7, we review the significance of our work as well as encompassing the major findings from this research. We also go into future routes of research to continue progressing these significant findings.

## 2 Structural Determination of CaSR ECD

### 2.1 Introduction

CaSR is a part of the family C of GPCR superfamily with a large ECD, a cys rich domain (CRD), a 7TM domain, and an ICD<sup>[21]</sup>. The CaSR primary function is to regulate Ca<sup>2+</sup> homeostasis and is predominantly expressed in the parathyroid, thyroid, and kidney cells for the modulation of parathyroid hormone (PTH) secretion and reabsorption in the renal system.<sup>[22, 247, 248]</sup> CaSR plays critical functional roles in biological and pathological regulation and is extensively expressed throughout the body in the skin, gastrointestinal, the central nervous system (CNS), cardiovascular, in bone, kidney, breast, and the parathyroid tissues<sup>[249-252]</sup>. The main agonist for CaSR is Ca<sup>2+</sup> in regulation of Ca<sup>2+</sup> homeostasis but has been shown to respond to various other cations such as Mg<sup>2+</sup>, Gd<sup>3+</sup>, and Tb<sup>3+</sup>, while Mg<sup>2+</sup> is found natively in the body at higher concentrations than Ca<sup>2+</sup> it has not been shown to induce the same oscillatory effect as seen with Ca<sup>2+</sup> activation of CaSR<sup>[22, 253, 254]</sup>. In addition to cations, L-amino acids such as L-Phe as well as polypeptides and polyamines have been shown to be CaSR binders. L-Phe has been shown to enhance the CaSR activity with Ca<sup>2+</sup> as a co-agonist and improving activation on WT and loss of function mutations<sup>[23, 24]</sup>. Additionally, several drugs have been designed which affect CaSR function with cinacalcet and AMG-416 as examples of agonist calcimimetics and NPS-2143 as an antagonist calcilytic, where only cinacalcet has been FDA approved<sup>[255-258]</sup>. Determination of the CaSR crystal structure of the ECD domain using purified protein from a mammalian expression system in order to garner more critical structural and functional information for drug and signaling studies. We are also curious on the actual ion binding sites to investigate the effect and functionality of cations and/or CaSR binding ligands on WT CaSR and disease-related mutations in order to understand the

mechanisms of how CaSR integrates the  $\text{Ca}^{2+}$ -mediated signaling and to probe the molecular basis for diseases resulting from alterations in  $\text{Ca}^{2+}$  homeostasis.

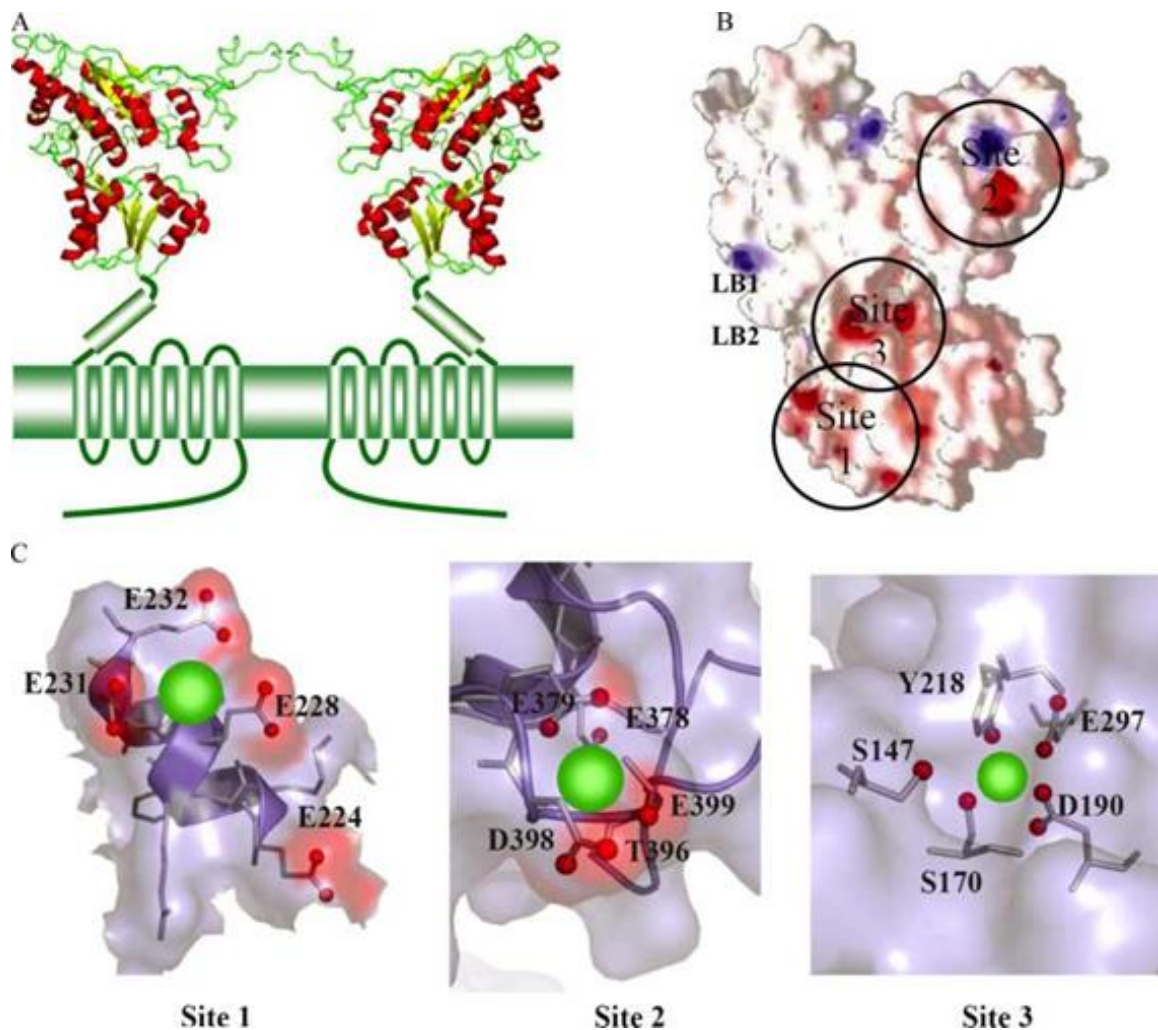


**Figure 2.1 – CaSR proposed  $\text{Ca}^{2+}$  binding sites.**

**A – The overall dimer binding of two CaSR proteins. B – Based off of electronegativity the proposed calcium binding sites. C – The residues shown of the proposed calcium binding sites from B<sup>[259]</sup>.**

With the challenges surrounding GPCR purification, our lab looked at other methods of analyzing CaSR structure and function while simultaneously optimizing CaSR ECD expression and purification. The amino acid sequence of CaSR was known and using that information we did sequence alignment with ClustalW program and other cGPCRs to find that mGluR1 had the highest sequence homology<sup>[260]</sup>. Since mGluR1 had two structures determined, 1EWT and 1ISR,

we were able to utilize these structures and WISS-MODEL and MODELLER<sup>[261-263]</sup> software to create a preliminary CaSR model structure in 2007 with which to investigate potential Ca<sup>2+</sup> binding sites using the program MetalFinder<sup>[264]</sup> which was an initial version of our developed prediction algorithm MUG (MULTiple Geometries)<sup>[265-268]</sup>. Using this methodology, we were able to initially determine three Ca<sup>2+</sup> binding sites on CaSR ECD which were the hinge binding site, the dimer binding site, and another near the top of the ECD as outlined in Figure 2.1. We were then able to do grafting of these binding sites onto a non-CaBP CD2 to see if Ca<sup>2+</sup> was able to bind to these proposed residues and confirmed they were able to produce Ca<sup>2+</sup> binding sites and that mutation of these grafted residues led to a decrease or loss of binding activity<sup>[259]</sup>.

We further were able to create an even better CaSR modeled structure using three mGluR1 determined structures (1EWK, 1EWT, 1ISR). We choose mGluR1 as the template for CaSR structure modeling since mGluR1 and CaSR are in the same family C of GPCRs and share the most sequence similarity to each other as compared to other family C GPCRs. In order to conserve time and resources, we were only able to computationally model the CaSR structure of the ECD in monomer form, not dimer form, since the ECD is where Ca<sup>2+</sup> binding is hypothesized to occur. After computation modeling was performed, we were able to obtain a hypothetical CaSR structure model (Figure 2.2). Using this structure model, we were able to apply our calcium binding site program MUG in order to identify possible Ca<sup>2+</sup> binding sites in the ECD of the CaSR<sup>[265-268]</sup>. MUG was able to identify five potential binding sites (BS). Binding site 1 (BS1), previously named binding site 3, was in the hinge region of the ECD with residues S147, S170, D190, Y218, and E297 (Figure 2.1). This binding site correlates most closely with the primary binding site in the hinge region of the ECD of mGluR1 for glutamate. BS2 was identified as residues D215, L242, S244, D248, and E253. BS3, previously called binding site 1, was identified as residues

E224, E228, E229, E231, and E232 and was near the back of the CaSR model and most likely for dimerization stability (Figure 2.1). BS4 was identified as residues E350, E353, E354, N386, and S38.

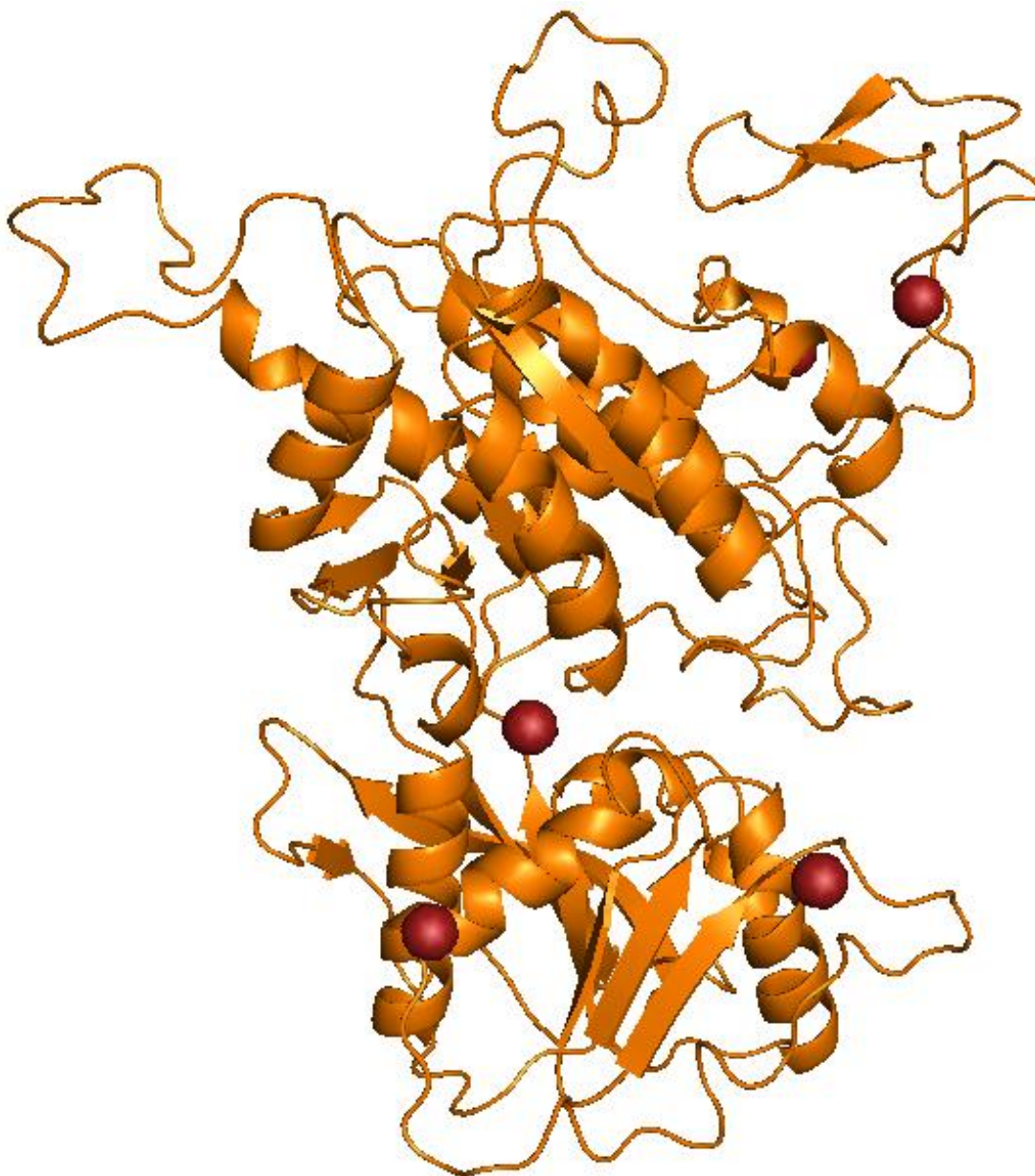


**Figure 2.2 – CaSR modeled structure.**  
Based off of mGluR1 structures (1EWK, 1EWT, 1ISR). Potential Ca<sup>2+</sup> brick red spheres. 1EWK bound with Glu and Mg<sup>2+</sup>, 1EWT Apo form, 1ISR bound with Glu and Gd<sup>3+</sup>.



Lastly, BS5, previously called binding site 2, was identified as residues T396, D398, E399, E378, and E379 (Figure 2.1). With these new binding sites identified, as well as confirmation of previously found binding sites and in conjunction with our improving CaSR expression, we were able to express subdomains of the CaSR ECD in order to look at  $\text{Ca}^{2+}$  binding in each purified subdomain and examine the cooperative binding of the  $\text{Ca}^{2+}$  binding sites<sup>[269]</sup>. These three subdomains were subdomain 1 with amino acids (AA) 132–300 containing BS1-3, subdomain 2 with AA 185 to 324 containing BS 2-3, and subdomain 3 with AA 340–445 containing BS 4-5<sup>[269]</sup>. Using mutations of these binding sites, and these three different subdomains being investigated, we found that the hinge site BS1 and the dimer site BS3 are critical for binding and cooperativity<sup>[269]</sup>. We next optimized the purification of full CaSR ECD from bacterial and mammalian expression systems and were able to look at full CaSR ECD binding, cooperativity, and reaction to amino acids as well as  $\text{Ca}^{2+}$  binding and found that L-Phe acts as a co-activator of CaSR with  $\text{Ca}^{2+}$  and using modeling and mutation studies is thought to bind with  $\text{Ca}^{2+}$  in the hinge region BS1<sup>[23, 24]</sup>.

## 2.2 Results

### 2.2.1 Mammalian Expressed CaSR Optimization

In addition to expression CaSR in a bacterial system, we also expressed CaSR ECD in a mammalian host system for X-Ray Crystallization and binding studies. Bacterial and mammalian vectors expressing human CaSR, bCaSR and mCaSR, respectively, are done utilizing the CaSR ECD. We use mammalian expression for the correct folding of the protein and post-translation modifications. We have improved upon previous expression and purification techniques by using Dr. Moremen's Lec1 cells to express CaSR, which prevents complex glycosylation from forming

on the nine potential N-linked glycosylation sites on the CaSR ECD. This is beneficial because then only high mannose glycans can bind which are readily cleaved by Endo F1, whereas complex glycans are not as wholly cleaved. For binding studies using mCaSR the glycans are not cleaved and high mannose glycosylation are still present. Deglycosylated mCaSR is not as stable as glycosylated mCaSR and tends to aggregate before binding studies can be performed (Figure 2.3).

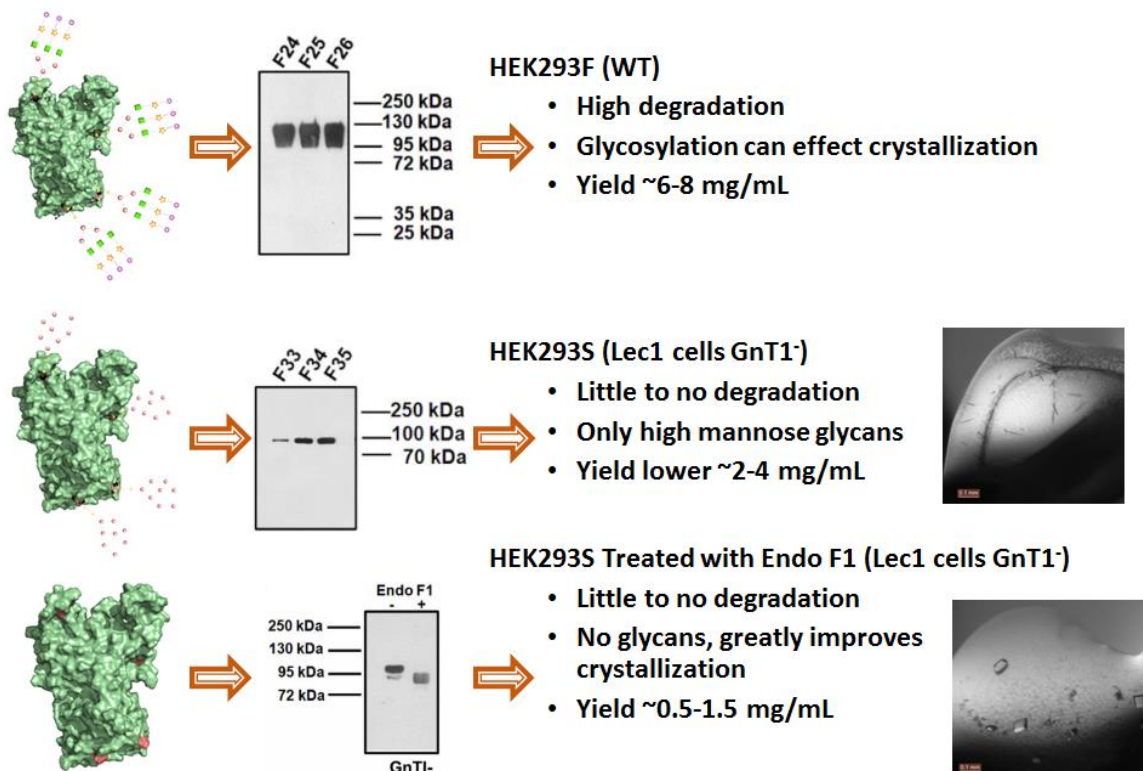


**Figure 2.3 – History of mCaSR expression optimization.**  
**Initial expression was done in WT HEK293 cells but showed high degradation.**

The expression procedure for Lec1 cells with CaSR-ECD transfected has already been optimized by Dr. Moremen's lab. After suspension cell growth to optimal confluency the cells are transfected with CaSR-ECD DNA previously amplified by our lab. 24 hr post-transfection, day 1, the culture is diluted 2-fold with fresh media and the culture is continued for five additional days of batch-mode protein production. This method has been successful for expression of mCaSR but was further modified for successful crystallization of the samples.

We saw high aggregates in previous expression batches though, so in order to optimize protein expression we attempted a new procedure. Same as the old method up to 24 hr post-transfection, day 1, but at this point the culture was centrifuged and resuspended in fresh media for the production phase. The media change removed excess DNA and PEI and result in protein production into clean media. Protein expression generally remains high on days 2-6 and the benefit, in this case, is that the potential for the DNA or PEI in contributing to aggregation in the final protein preparation will potentially be eliminated by the media change (Figure 2.4). Additionally, we removed the CRD and flag tag from the mCaSR ECD in order to potentially get a protein expression that could form better crystals for X-ray diffraction and not form aggregates.

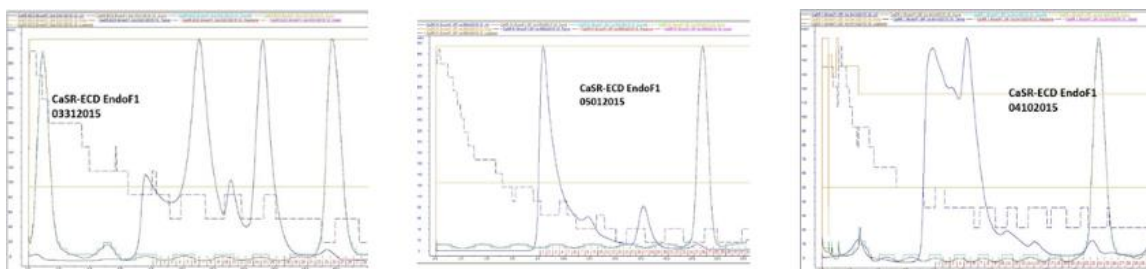


**Figure 2.4 – Three separate mCaSR expression batches under GF purification. (Left) Small third left peak is aggregation and large fourth peak in mCaSR. (Middle) All aggregated. (Right) Aggregation peak and mCaSR peak are too close together and are overlapping. (ADD ABC)**

### 2.2.2 *CaSR Determined Structures*

We were able to crystallize the CaSR ECD at 2.1 Å and showed many loops not previously seen in any other cGPCR and a unique one to CaSR. Additionally, we did a Gd<sup>3+</sup> soaking of another crystal from the same expression batch to visualize the Gd<sup>3+</sup> binding site, this crystal was 2.7 Å and the partial dimerization loop was not visible in this less resolved crystal (Figure 2.5). The Venus flytrap domain of human CaSR-ECD (hCaSR-ECD; residues 20 to 541) expressed in human embryonic kidney HEK293S (GnTI-) Lec1 cells was crystallized in the presence of 200 mM Mg<sup>2+</sup> and 10 mM Ca<sup>2+</sup>. The structure was solved by molecular replacement using the structure of

mGluR2 [Protein Data Bank (PDB) ID: 4XAQ] as the search template. hCaSR-ECD contains two globular lobes with an overall structure similar to other cGPCR family members, despite a low sequence similarity between these cGPCR family members of 20 to 30%<sup>[270]</sup>. Both the large lobe (subdomain 1) and the small lobe (subdomain 2) are typical  $\alpha/\beta$  folds where the central parallel  $\beta$  strands are sandwiched by  $\alpha$  helices. hCaSR-ECD forms a homodimer in solution and the crystal structure, with both protomers in a closed conformation similar to the equivalent closed conformation of mGluR1 bound with glutamate. Besides, the direct and extensive homodimeric subdomain 2 interactions in hCaSR-ECD are analogous to those observed in the mGluR2 dimer with a bound agonist (PDB ID: 4XAQ), strongly suggesting that hCaSR-ECD crystal structure represents an active conformation<sup>[271]</sup>. In the crystal structure, two  $Mg^{2+}$  binding sites were identified at positions designated as the new top site 3 and the dimerization site 2, and an unpublished hinge binding site 1 (Figure 2.7).

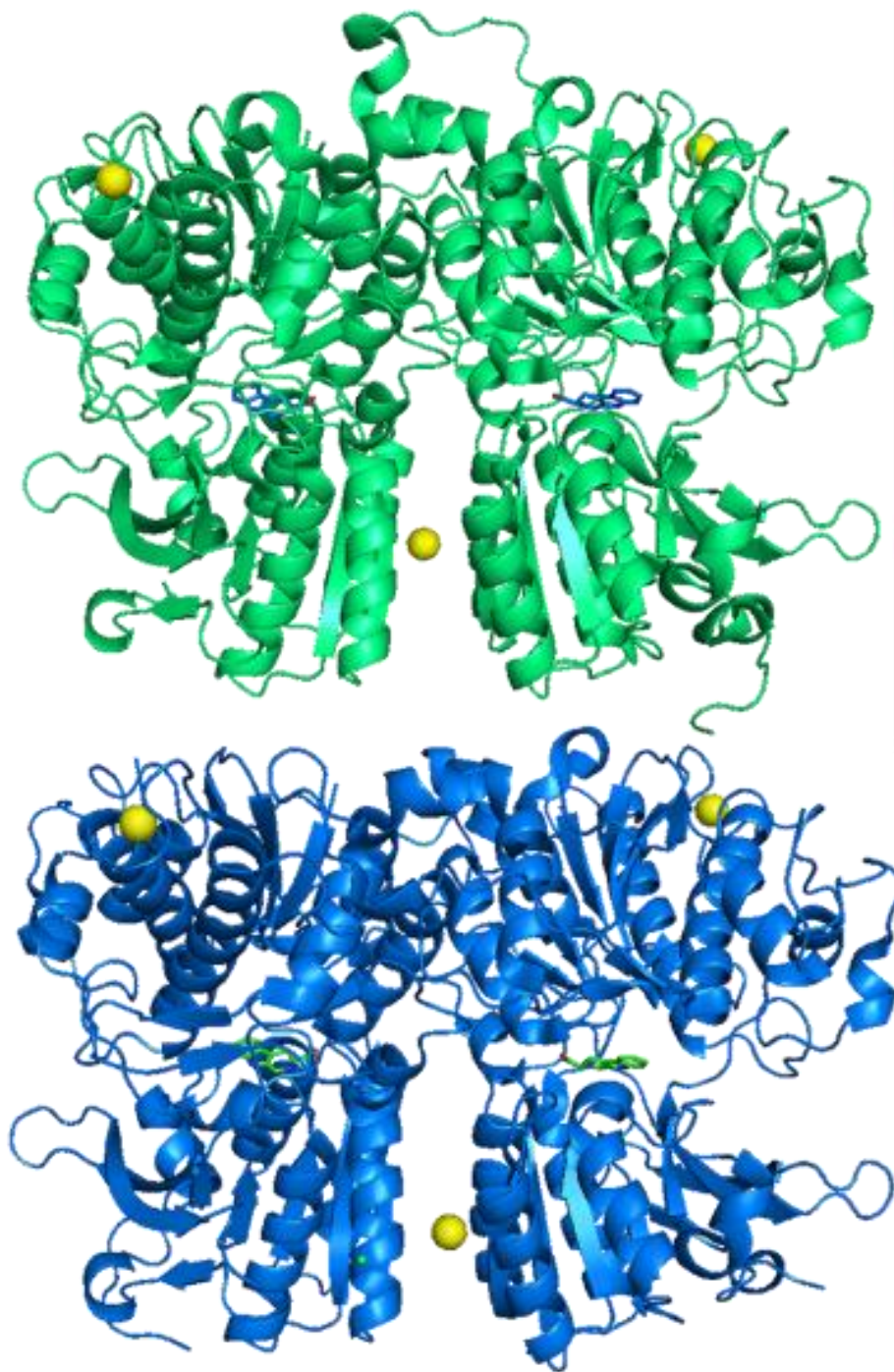


**Figure 2.5 – Science Advances CaSR structures**

**PDB 5FBK is a holo 2.1 Å form (green) with Mg<sup>2+</sup> yellow spheres and TNCA blue sticks by element. PDB 5FBH is also a holo 2.7 Å (blue) structure with Mg<sup>2+</sup> yellow spheres, TNCA green sticks by element, Gd<sup>3+</sup> green spheres, and the same conditions as 5FBK plus 0.5 mM GdCl<sub>3</sub>. These structures are of hCaSR (20-621) in pXLG vector expressed in Lec1 cells with high mannose only and cleaved with Endo F1. Under the conditions of 10% polyethylene glycol 8000, 200 mM MgCl<sub>2</sub>, 10 mM CaCl<sub>2</sub>, and 100 mM Tris-HCl, pH 7.0.**



Site 2 is located at the dimerization interface of subdomain 2 and the bound  $\text{Mg}^{2+}$  coordinates with S240 and four water molecules with an ideal geometry for a  $\text{Mg}^{2+}$  ion. Notably, site 2 is surrounded by highly conserved residues (E228, E231, and E241\*) (\* means from the other protomer) within 5 Å from an “acidic patch” composed of negatively charged residues on subdomain 2 (Figure 2.6). Site 3 is found on the periphery of subdomain 1, coordinated by S84 and backbone interactions with I81, L87, and L88, as well as two water molecules. An equivalent cation binding site has been observed in mGluR<sup>[270]</sup> and likely plays a structural role.

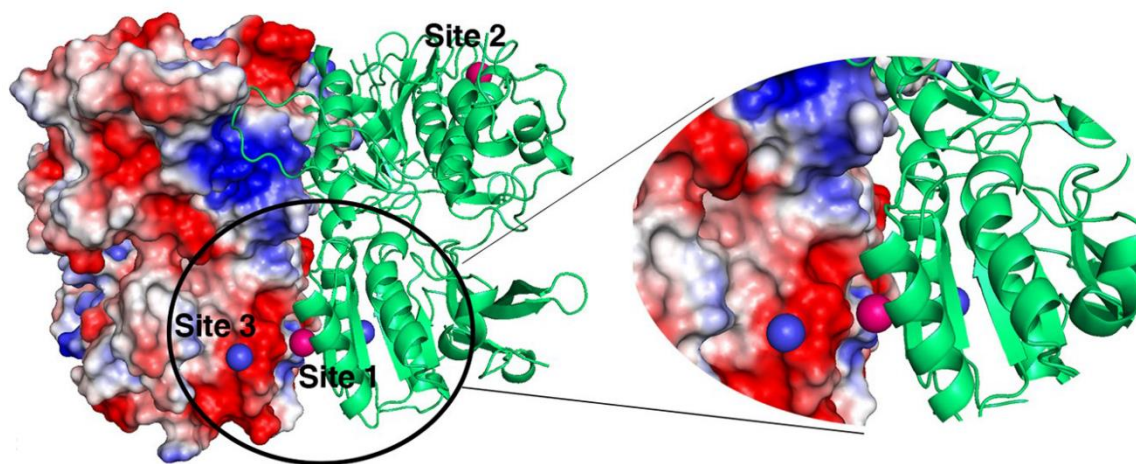


**Figure 2.6 – Metal binding at the acidic patch.**

The electrostatic potential map of hCaSR-ECD is colored in accordance with electrostatic potential; red indicates negative potential and blue indicates positive potential.  $\text{Mg}^{2+}$  is represented by hot pink spheres, while  $\text{Gd}^{3+}$  is shown as blue spheres. The large surface with negative potential at the dimerization interface of subdomain 2 is referred to the “acidic patch”, where both  $\text{Mg}^{2+}$  and  $\text{Gd}^{3+}$  bind.

To locate additional high off-rate metal binding sites, we generated  $\text{Gd}^{3+}$ -derived crystals and identified another metal binding site on the acidic patch in proximity to the subdomain 2 dimerization interface and adjacent to  $\text{Mg}^{2+}$  binding site 2 (Figure 2.6). The  $\text{Gd}^{3+}$  binding site largely overlaps with a previously predicted  $\text{Ca}^{2+}$  binding site in the dimerization region<sup>[269]</sup>. These

sites are more clearly outlined by their residues of binding and areas in the CaSR ECD in Figure 2.7.

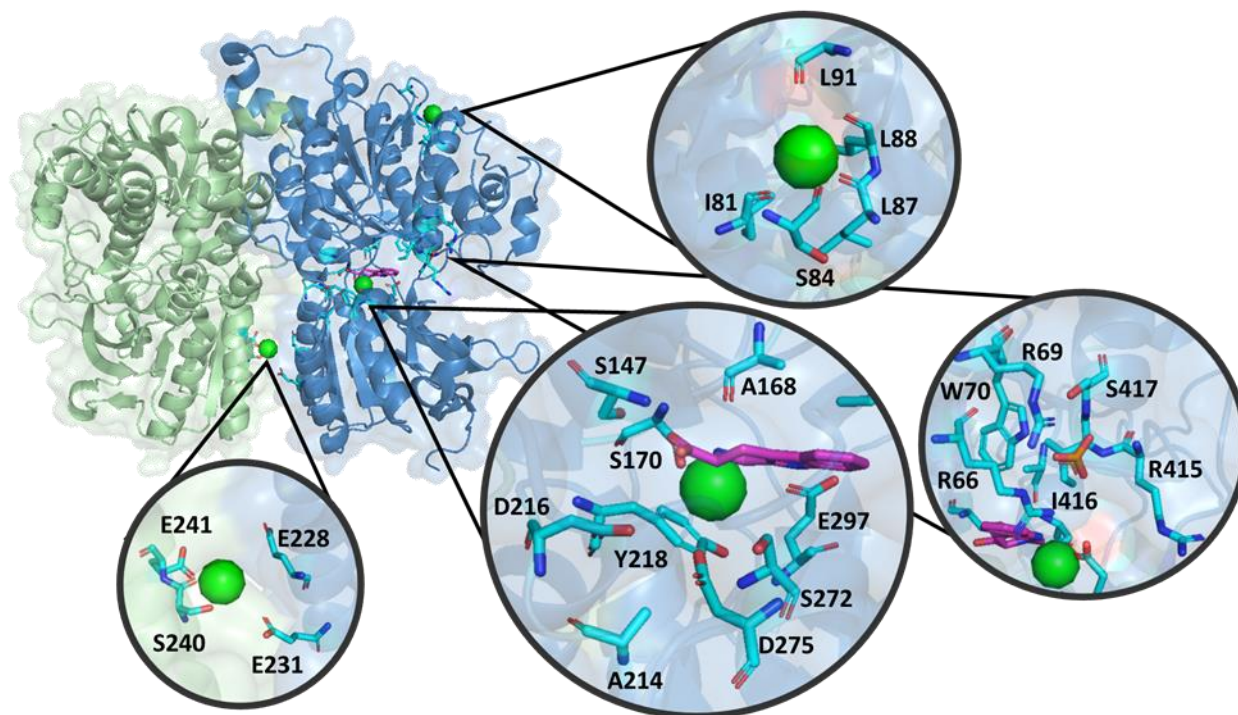


**Figure 2.7 – Binding sites of  $Mg^{2+}/Ca^{2+}/TNCA/Bicarbonate$  in CaSR ECD**  
 Binding sites on the CaSR ECD with a dimer  $Mg^{2+}/Ca^{2+}$  binding site 2 (E228, E231, S240, and E241), a hinge region TNCA/ $Mg^{2+}/Ca^{2+}$  binding site 1 (S147, A168, S170, A214, D216, Y218, S272, D275, and E297), a new top  $Mg^{2+}/Ca^{2+}$  binding site 3 (I81, S84, L87, L88, L91), and a bicarbonate binding site (R66, R69, W70, R415, I416, and S417).

Unexpectedly, an elongated planar electron density was observed in the hinge region between the two subdomains where orthosteric ligand binding is thought to occur. High-resolution liquid chromatography–electrospray ionization–mass spectrometry (LC-ESI-MS) of the purified protein preparation identified a species that was eluted at ~4.65min with a mass/charge ratio ( $m/z$ ) of 215.0824 in negative-ion mode. The predicted elemental formula based on the observed mass corresponds to  $C_{12}H_{11}N_2O_2$  (calculated mass, 215.0821; mass accuracy, 1.4 ppm). A search of PubChem identified a tryptophan derivative, L- 1,2,3,4-tetrahydronorharman-3-carboxylic acid

(TNCA) with the predicted molecular weight (MW) and shape of the observed density. When compared to tryptophan, TNCA contains one extra carbon atom linking the amine nitrogen atom and the C2 atom of the indole ring. TNCA can be detected in various food and biological systems and is likely produced by tryptophan reacting with formaldehyde or ketones in humans<sup>[272]</sup>, and is perhaps generated during production of the recombinant protein in Lec1 cells. CaSR strongly prefers aromatic amino acid ligands, such as Phe and Trp, over negatively charged Glu, which is the ligand for mGluRs. Structural comparison of the ligand binding pocket in the hinge region between subdomains 1 and 2 of hCaSR-ECD with that of mGluR1 reveals the structural basis of ligand selectivity. Although the amino acid backbone of TNCA adopts a similar conformation as Glu in mGluR1 through extensive interactions with S147, A168, S170, and Y218 (S156, S186, T188, and Y236 in mGluR1)<sup>[270]</sup>, hCaSR and mGluR1 recognize the side chains of their preferred ligands differently. Two positively charged residues in mGluR1 (R78 and K409) that associate with the carboxylate group of the Glu ligand are replaced in hCaSR by W70 and I416, which interact with the indole ring of TNCA. Bulky residues (Y74, W110, and R323) that limit the mobility of the Glu side chain are replaced by smaller residues in hCaSR (G67, N102, and S302). As a result, the size of the ligand binding pocket of hCaSR is significantly larger than that of mGluR1, consistent with the preference of CaSR for larger ligands. Unlike Trp, TNCA is in a fixed and presumably preferred conformation, accounting for the higher binding affinity compared to Trp. Mapping of disease-associated mutations on the structure of hCaSR-ECD shows that the mutations are clustered in two regions: the hinge region between subdomains 1 and 2 and the dimerization interface<sup>[273, 274]</sup>. Indeed, our structural and functional data strongly support the pivotal roles of these two regions in CaSR function.



The hinge region between subdomains 1 and 2 harbors the binding site of TNCA, supporting its role as a co-agonist of CaSR. A close inspection of the structure reveals that the side chain of E297, a critical residue predicted for Ca<sup>2+</sup> binding in site 1, swings away from the other residues in site 1 (S170, D190, Q193, and Y218), probably due to the extra carbon atom and the rigid structure of TNCA, ultimately resulting in its failure to capture the Ca<sup>2+</sup> ion in combination with other site 1 residues. A bicarbonate anion was also identified in the hinge region in proximity with TNCA, coordinated by the side chains of R66, R69, W70, and S417 and the backbone amide nitrogen atoms of I416 and S417), potentially contributing to the known pH sensitivity of the CaSR<sup>[275]</sup>. Additionally, we found two Mg<sup>2+</sup> binding sites on each crystal, as well as a TNCA compound bound in each of the hinge domains in each monomer.

### ***2.2.3 Structure Analysis***

The modeled structure's proposed Ca<sup>2+</sup> binding site 1 shares 4/5 binding residues similar to the TNCA and Trp binding sites of the determined structures (Figure 2.8). While our dimer site 2 for Mg<sup>2+</sup> overlaps 2 residues with binding site 3 dimer site for Ca<sup>2+</sup> in the modeled structure. These similarities in binding sites show that these residues are most likely conserved and crucial to the function and structure of CaSR.

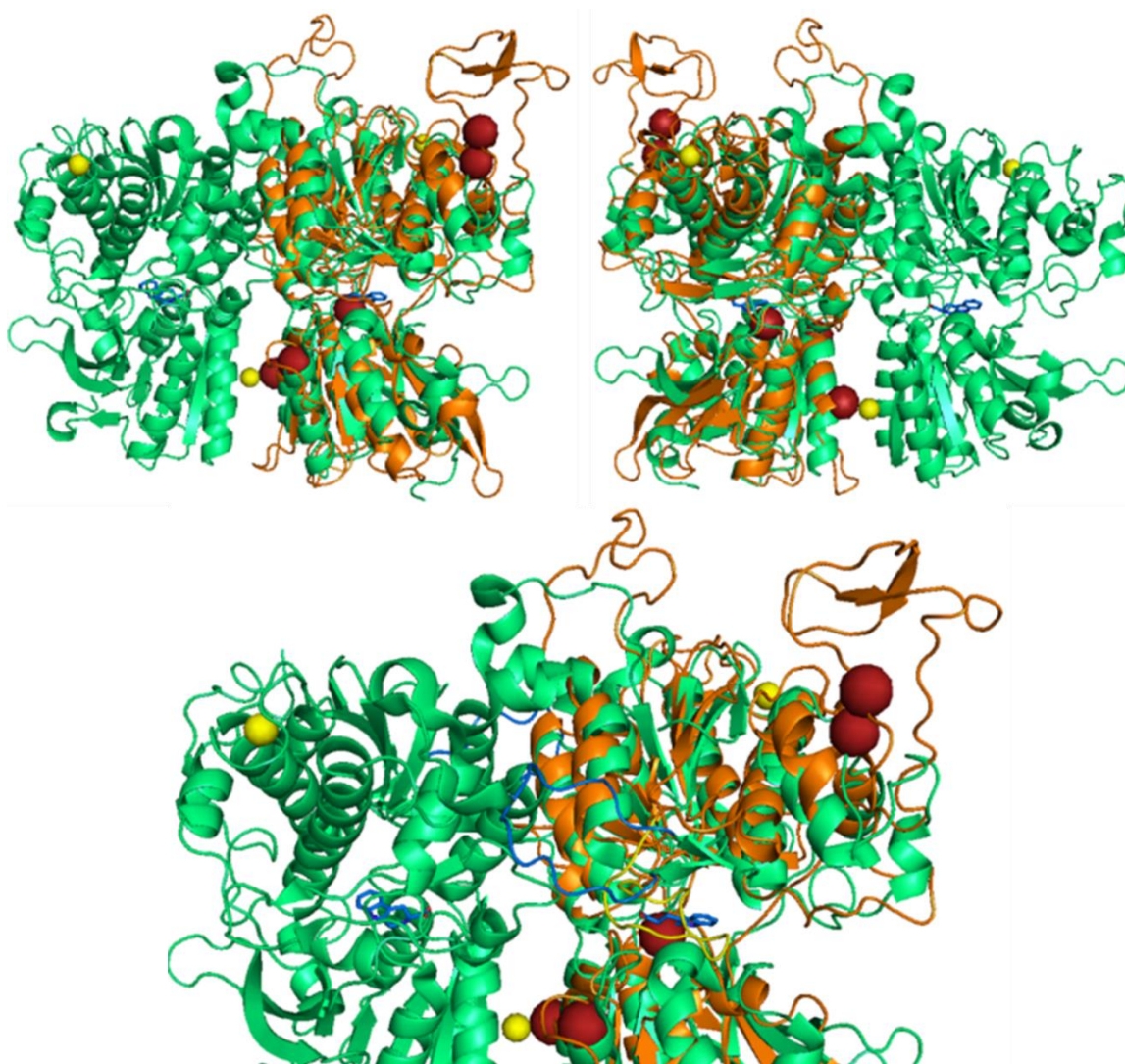


**Figure 2.8 – Comparison of our CaSR 5FBK (green) and the modeled CaSR (orange) 5FBK has  $Mg^{2+}$  yellow spheres, TNCA blue sticks by element, and Loop 1 in cyan. While the modeled CaSR has potential  $Ca^{2+}$  brick red spheres and Loop 1 in yellow.**

When comparing our determined structure to our modeled structure, we can see while there are some differences, mainly in the loops which are hardest to model, but overall they are very similar (Figure 2.8). This gives us confidence that our predictions and previous work based on this modeled structure are still viable and accurate. As mentioned, one of the main differences in the loops. First, loop 1 on the bottom of Figure 2.8 in blue for the determined structure versus yellow for the modeled one. This loop is important because it is twice as long as a similar loop in mGluRs

and a unique attribute to CaSR. It is present on both monomers stretching out to the other monomer in the dimer to form a hug-type structure and further stabilizing them. The modeled loop 1 is distorted upon itself and does not stretch out as the determined one does. Secondly, loop 2, the dimerization loop on the top, has a partial helix structure in it whereas the modeled structure shows only a loop form. This is not surprising since the mGluR structures used to model CaSR did not have this loop determined.

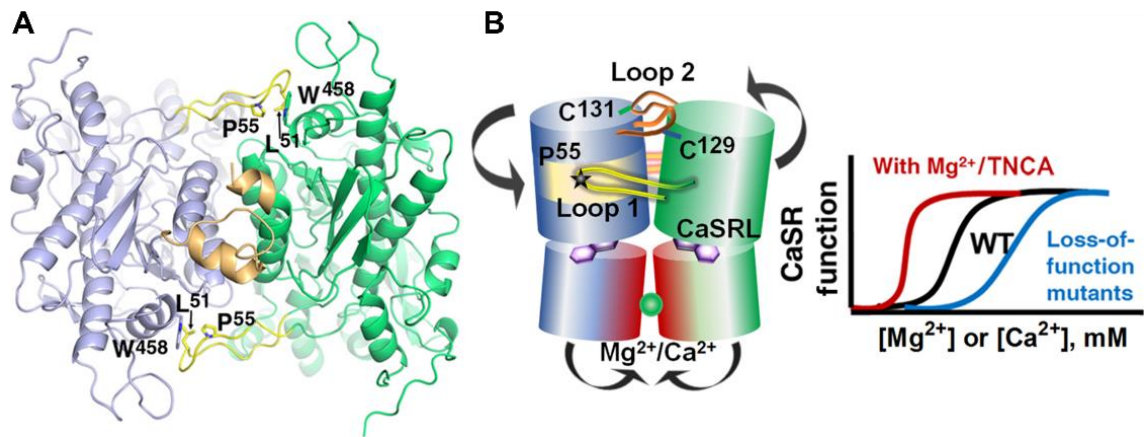


**Figure 2.9 – Key determinants for the molecular basis of disease-associated mutations and regulation.**

**(A) Involvement of loop 1 (yellow) and loop 2 (gold) in dimerization. (B) Working model for activation occurs through a conformational change induced by ligand binding at the hinge region between subdomains 1 and 2, as well as bridging interactions provided by metal ion binding at the acidic patch at the interface between the two subdomain 2 regions of their respective protomers. Mutations at these key determinants in the ECD of CaSR cause human disorders with abnormal  $[Ca^{2+}]_o$  and  $[Mg^{2+}]_o$  homeostasis.**

The loops that mediate subdomain 1 dimerization are functionally important (Figure 2.9). Loop 2, following  $\alpha 2$ , is largely disordered in mGluR structures but is known to participate in two intermolecular disulfide bonds in CaSR through two conserved cysteine residues (C129 and C131) (Figure 2.9B)<sup>[276, 277]</sup>. The N-terminal part of loop 2 forms a short  $\alpha$  helix extended from  $\alpha 2$  with a kink at N118. The  $\alpha 2a$  segments from each protomer embrace each other, likely stabilizing dimerization (Figure 2.9). Because several activating ADH mutations (L125P/F, E127G/A/K,

C129Y/F/S/R, and N118K) and one inactivating FHH mutation are present on loop 2, subdomain1 dimerization that is facilitated by loop 2 appears to be crucial in regulating the function of CaSR. Moreover, the highly conserved loop 1, which is significantly longer than the corresponding loop in mGluRs (Figure 2.9 and Figure 2.10), reaches across the dimerization interface to a hydrophobic surface on  $\alpha 13^*$ . The hydrophobic interaction, primarily mediated by P55, L51, and W458\*, stabilizes an extended conformation of loop 1, and a conserved positively charged patch also appears to contribute to dimerization of subdomain 1 (Figure 2.9). Notably, mutation of P55 causes FHH, indicative of a critical role of loop 1. Figure 2.9B summarizes our present model for receptor activation. The presumed conformational change induced by ligand/metal binding in the hinge region between subdomains 1 and 2, with homodimerization of protomer subdomains 1 through loops 1 and 2, facilitates the approach of subdomain 2 from their respective protomers. By neutralizing the repulsive effects of the conserved and negatively charged acidic patch, metal binding would stabilize subdomain 2 interactions (Figure 2.10).

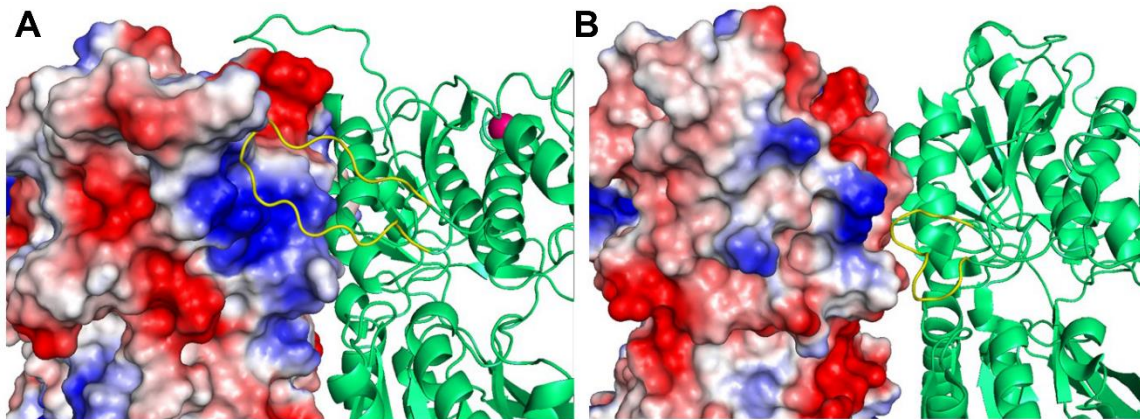


**Figure 2.10 – A positively charged pocket for loop 1 association. Loop 1 for CaSR (A) and the corresponding loop in mGluR1 (B, PDB code 1EWK) are highlighted in yellow. The electrostatic potential map is colored in accordance to charge, with red representing negative potential and blue positive potential. Loop 1 in CaSR is significantly longer than the counterpart in mGluR1, reaching across the dimer interface to nestle into a positively charged pocket which is absent in mGluR1.**

Dimerization of subdomain 2 is also critical for the activation of mGluRs and GABAB (gamma-aminobutyric acid B) receptors<sup>[278, 279]</sup> and therefore appears to be a common activation mechanism among cGPCRs that presumably leads to conformational changes of the transmembrane domain, through which the intracellular signal cascades are initiated. Thus, the proposed model, which is based on structural and associated biochemical and cellular studies on WT and mutant proteins, reveals the structural basis of agonist/co-agonist binding to CaSR and provides a framework for further studies on the mechanism of receptor activation.

#### ***2.2.4 Trp Compound Analysis and Uncovering TNCA***

Unexpectedly, an elongated planar electron density was observed in the hinge region between the two subdomains where orthosteric ligand binding is thought to occur (Figure 2.11A). No naturally occurring CaSR ligands (CaSRLs) or reagents that were used in sample preparation and crystallization or any currently known CaSRLs fit the density well, suggesting a novel CaSRL. High-resolution liquid chromatography–electrospray ionization–mass spectrometry (LC-ESI-MS) of the purified protein preparation (Figure 2.11B) identified a species that was eluted at ~4.65min with a mass/charge ratio ( $m/z$ ) of 215.0824 in negative-ion mode. The predicted elemental formula based on the observed mass corresponds to  $C_{12}H_{11}N_2O_2$  (calculated mass, 215.0821; mass accuracy, 1.4 ppm) (Figure 2.11B). A search of PubChem identified a tryptophan derivative, L-1,2,3,4-tetrahydronorharman-3-carboxylic acid (TNCA) with the predicted molecular weight and shape of the observed density. When compared to tryptophan, TNCA contains one extra carbon atom linking the amine nitrogen atom and the C2 atom of the indole ring. TNCA can be detected in various food and biological systems and is likely produced by tryptophan reacting with formaldehyde in humans<sup>[272]</sup>, and is perhaps generated during production of the recombinant



protein in HEK cells. Elution time, molecular weight, and MS fragmentation of synthetic TNCA matched those of the CaSRL, confirming the identity of the compound as TNCA (Figure 2.11B).

The ligand will be referred to hereafter as TNCA.

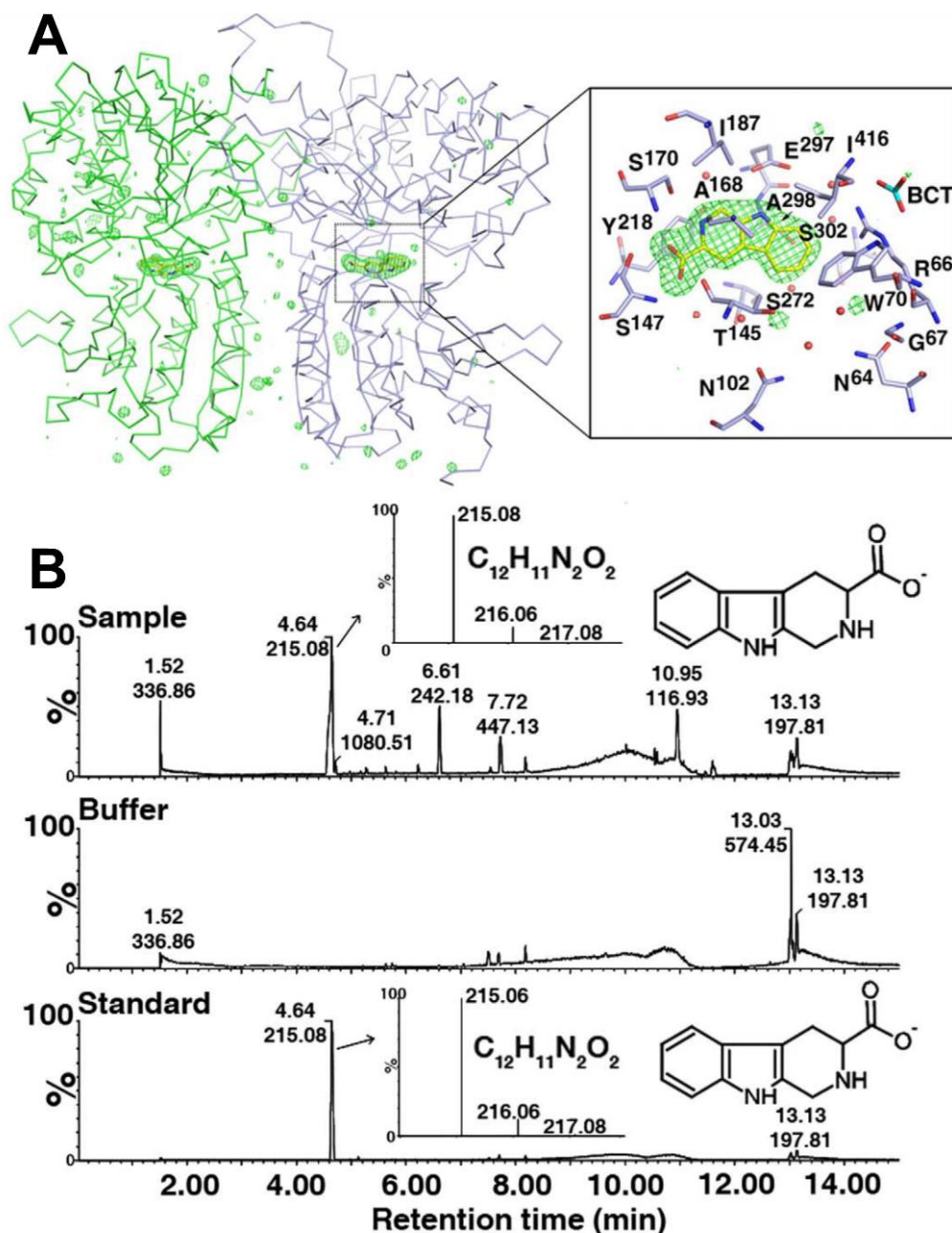


**Figure 2.11 – Identification and characterization of a tryptophan derivative bound to hCaSR-ECD as a novel high-affinity co-agonist of CaSR.**

(A) Fo-Fc omit map (Fo and Fc are the observed and the calculated structure factor amplitudes, respectively) of TNCA at  $s = 4.5$ . The protein is shown in ribbon mode,

**and the ligand is shown in stick mode. The residues around TNCA are labeled in the zoomed-in figure. (B) LC-ESI-MS of protein sample (top), buffer (middle), and the standard compound (bottom) in negative-ion mode. The high-resolution isotopic MS spectra of the indicated peaks are shown in the inserted figures.**

The discovery of an unexpected tryptophan derivative ligand (TNCA) with unusually high affinity, which potentiates the activation of CaSR by  $[Ca^{2+}]_o$  and  $[Mg^{2+}]_o$ , also opens new avenues for the development of agonists and antagonists as therapeutics for CaSR related diseases<sup>[280]</sup>.

### ***2.2.5 Molecular Regulation of CaSR by Co-activators $Mg^{2+}$ , $Ca^{2+}$ , and TNCA***

While being able to successfully crystalize the structure of the CaSR ECD is groundbreaking in our research to better understand the way CaSR functions and therefore can be targeted for disease treatment, the structure is still only of the ECD and not the full 1078 amino acid CaSR. Thus, we can turn to hCaSR studies, which refers to the full-length human CaSR transfected into HEK293 cells, so that we can test the effects on the structure of CaSR ECD has on the signaling inside the cell with WT hCaSR and mutations of the ion/drug binding sites as well as disease mutations to see the response differences with  $Ca^{2+}$  and possible drug targets.

Our data indicate that  $Mg^{2+}$  binds to hCaSR-ECD and elicits CaSR-mediated  $[Ca^{2+}]_i$  signaling and ERK1/2 phosphorylation in CaSR expressing cells with a lower potency than  $Ca^{2+}$  (Figure 2.12)<sup>[254]</sup>. Similar to  $[Ca^{2+}]_o$  activation,  $[Mg^{2+}]_o$  activation is further potentiated by the known CaSR co-agonist, L-Phe (Figure 2.13A)<sup>[23, 281]</sup>.  $[Ca^{2+}]_o$  potentiates  $[Mg^{2+}]_o$ -stimulated intracellular response mediated by CaSR because an increase of  $[Ca^{2+}]_o$  from 0.5 to 1.5 mM results in a reduction of the median effective concentration at 50% ( $EC_{50}$ ) of  $[Mg^{2+}]_o$  from  $7.2 \pm 0.4$  to  $4.5 \pm 0.3$  mM for stimulation of  $[Ca^{2+}]_i$  signaling. These results suggest that there is an additive effect of both  $Ca^{2+}$  and  $Mg^{2+}$  and that they share a similar activation mechanisms (Table 2.1)<sup>[254, 282]</sup>. The

binding of  $Mg^{2+}$  can be visualized by the reduction of intrinsic Trp fluorescence upon addition of  $Mg^{2+}$  to the purified ECD and the reduction of  $Tb^{3+}$ -sensitized energy transfer by  $Mg^{2+}$  competition. In the crystal structure, two  $Mg^{2+}$  binding sites were identified at positions designated as site 1-3. Mutation of site 2 coordinating residues (E228I or an E228I/E229I double mutant) reduced  $Ca^{2+}/Mg^{2+}$  sensing as well as  $Mg^{2+}$ -evoked intracellular  $Ca^{2+}$  mobilization. These results suggest the critical role of these metal binding sites on the acidic patch in both metal sensing<sup>[269]</sup> and regulation of CaSR function (Figure 2.6, Figure 2.16, and Table 2.2).

TNCA is a strong co-agonist with  $[Mg^{2+}]_o$  in activating  $[Ca^{2+}]_i$  oscillations and ERK1/2 phosphorylation (Figure 2.12, Figure 2.13 and Figure 2.16). Similar to Trp and other amino acids, the addition of exogenous TNCA alone cannot activate the receptor. However, TNCA is ~1000-fold more potent than Phe in reducing the  $EC_{50}$  for  $[Mg^{2+}]_o$  or  $[Ca^{2+}]_o$  activation of  $[Ca^{2+}]_i$  signaling in both WT and mutant CaSRs (Figure 2.13), with an apparent  $EC_{50}$  of  $\leq 2$  mM (Figure 2.13). The apparent  $EC_{50}$  of TNCA was indirectly determined through the  $EC_{50}$  change of  $[Mg^{2+}]_o$  when incubated with different concentrations of TNCA (Figure 2.13). Because the bound TNCA can be partially replaced by incubation with 150 mM Phe as assessed by MS, TNCA and Phe likely share the similar binding site in CaSR-ECD. Together, TNCA is a novel, high-affinity co-agonist of CaSR in the activation of both  $[Ca^{2+}]_i$  signaling and ERK activity. CaSR strongly prefers aromatic amino acid ligands, such as Phe and Trp, over negatively charged Glu, which is the ligand for mGluRs.



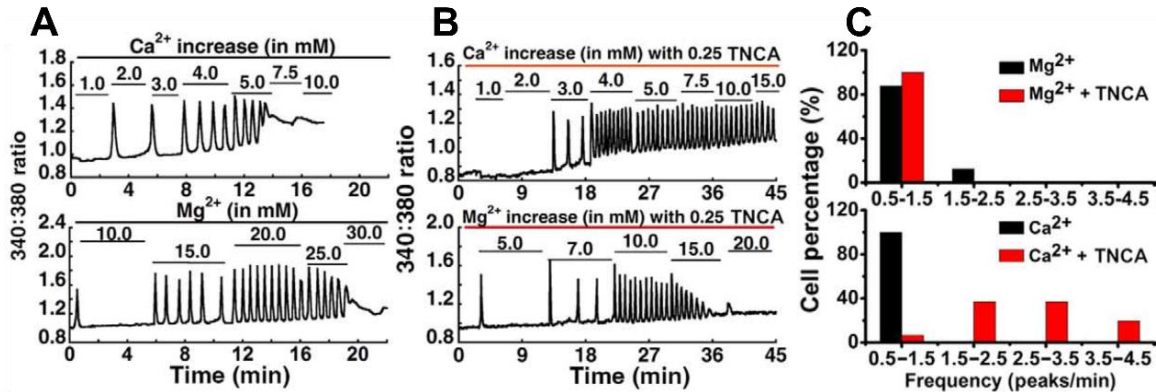


**Figure 2.12 – Cell imaging using the novel hCaSR agonist TNCA.** (A and B) A representative oscillation pattern from a single HEK293 cell stimulated with various concentrations of extracellular Ca<sup>2+</sup> or Mg<sup>2+</sup> in the absence (A) and presence (B) of 0.25 mM TNCA. (C) Frequency distribution of the [Ca<sup>2+</sup>]<sub>i</sub> oscillation frequency (peak/min) in HEK293 cells transfected with WT CaSR stimulated with metals in the presence (red bar) and absence (black bar) of TNCA. The frequency was recorded at the point when more than 50% of single cells started to oscillate. Around 40 cells were analyzed and further plotted as a bar chart.

Structural comparison of the ligand binding pocket in the hinge region between subdomains 1 and 2 of hCaSR-ECD with that of mGluR1 reveals the structural basis of ligand selectivity. Although the amino acid backbone of TNCA adopts a similar conformation as Glu in mGluR1 through extensive interactions with S147, A168, S170, and Y218 (S156, S186, T188, and Y236 in mGluR1)<sup>[270]</sup>, hCaSR and mGluR1 recognize the side chains of their preferred ligands differently.

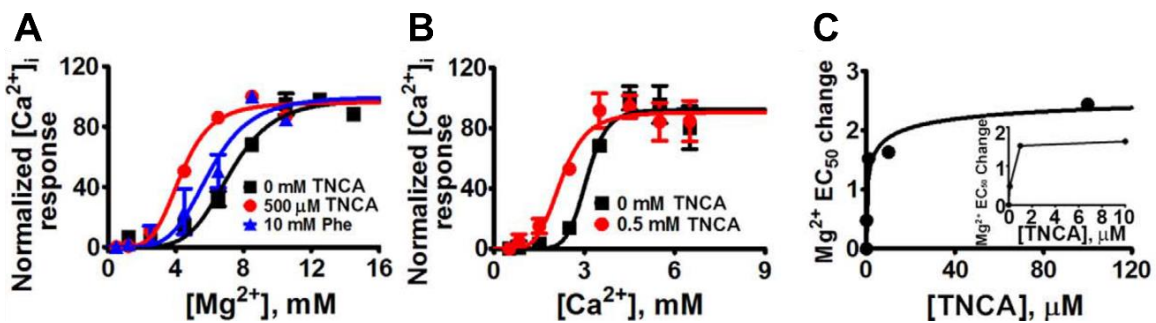


**Figure 2.13 – Cell population using the novel hCaSR agonist TNCA.** (A and B) TNCA potentiates [Mg<sup>2+</sup>]<sub>o</sub>- or [Ca<sup>2+</sup>]<sub>o</sub>-evoked [Ca<sup>2+</sup>]<sub>i</sub> responses in a population assay in HEK5001 cells measured by Fura-2 acetoxymethyl (AM) in the absence (black square) or presence of Phe (blue triangular) or TNCA (red closed circle). (C) A maximally active concentration of 0.1 to 0.5 mM TNCA markedly reduces the EC<sub>50</sub> for activation of [Ca<sup>2+</sup>]<sub>i</sub> signaling by [Mg<sup>2+</sup>]<sub>o</sub> in the presence of 0.5

**mM  $[Ca^{2+}]_o$ . Inset: The  $EC_{50}$  changes of  $[Mg^{2+}]_o$  is shown over a narrow concentration range of TNCA.**

Two positively charged residues in mGluR1 (R78 and K409) that associate with the carboxylate group of the Glu ligand are replaced in hCaSR by W70 and I416, which interact with the indole ring of TNCA. Bulky residues (Y74, W110, and R323) that limit the mobility of the Glu side chain are replaced by smaller residues in hCaSR (G67, N102, and S302). As a result, the size of the ligand binding pocket of hCaSR is significantly larger than that of mGluR1, consistent with the preference of CaSR for larger ligands. Unlike Trp, TNCA is in a fixed and presumably preferred conformation, accounting for the higher binding affinity compared to Trp.

**Table 2.1 –  $EC_{50}$  of  $[Mg^{2+}]_o$  for stimulation of  $[Ca^{2+}]_i$  signaling in the presence of different co-activators and TNCA.**

Co-activator (mM)	Population Assay		Single Cell assay	
	$EC_{50}$	Hill Number	$EC_{50}$	Hill Number
0.0 $Ca^{2+}$	ND	ND	$12.9 \pm 0.3$	$2.9 \pm 0.2$
0.5 $Ca^{2+}$	$7.2 \pm 0.4$	$5.5 \pm 0.5$	$7.5 \pm 0.3$	$4.7 \pm 0.8$
1.5 $Ca^{2+}$	$4.5 \pm 0.3$	$2.9 \pm 0.6$	$5.9 \pm 0.4$	$4.1 \pm 0.8$
0.5 $Ca^{2+}$ + 0.5 TNCA	$3.3 \pm 0.7$	$3.5 \pm 1.0$	ND	ND
0.0 $Ca^{2+}$ + 0.25 TNCA	ND	ND	$5.6 \pm 0.3$	$5.2 \pm 1.3$
0.5 $Ca^{2+}$ + 0.25 TNCA	ND	ND	$4.8 \pm 0.2$	$4.7 \pm 0.6$
1.5 $Ca^{2+}$ + 0.25 TNCA	ND	ND	$4.4 \pm 0.1$	$3.5 \pm 0.2$
0.5 $Ca^{2+}$ + 10.0 Phe	$6.0 \pm 0.7$	$4.9 \pm 2.3$	ND	ND

ND = not determined

Mapping of disease-associated mutations on the structure of hCaSR-ECD shows that the mutations are clustered in two regions: the hinge region between subdomains 1 and 2 and the dimerization interface (Figure 2.14)<sup>[273, 274]</sup>. Indeed, our structural and functional data strongly support the pivotal roles of these two regions in CaSR function.

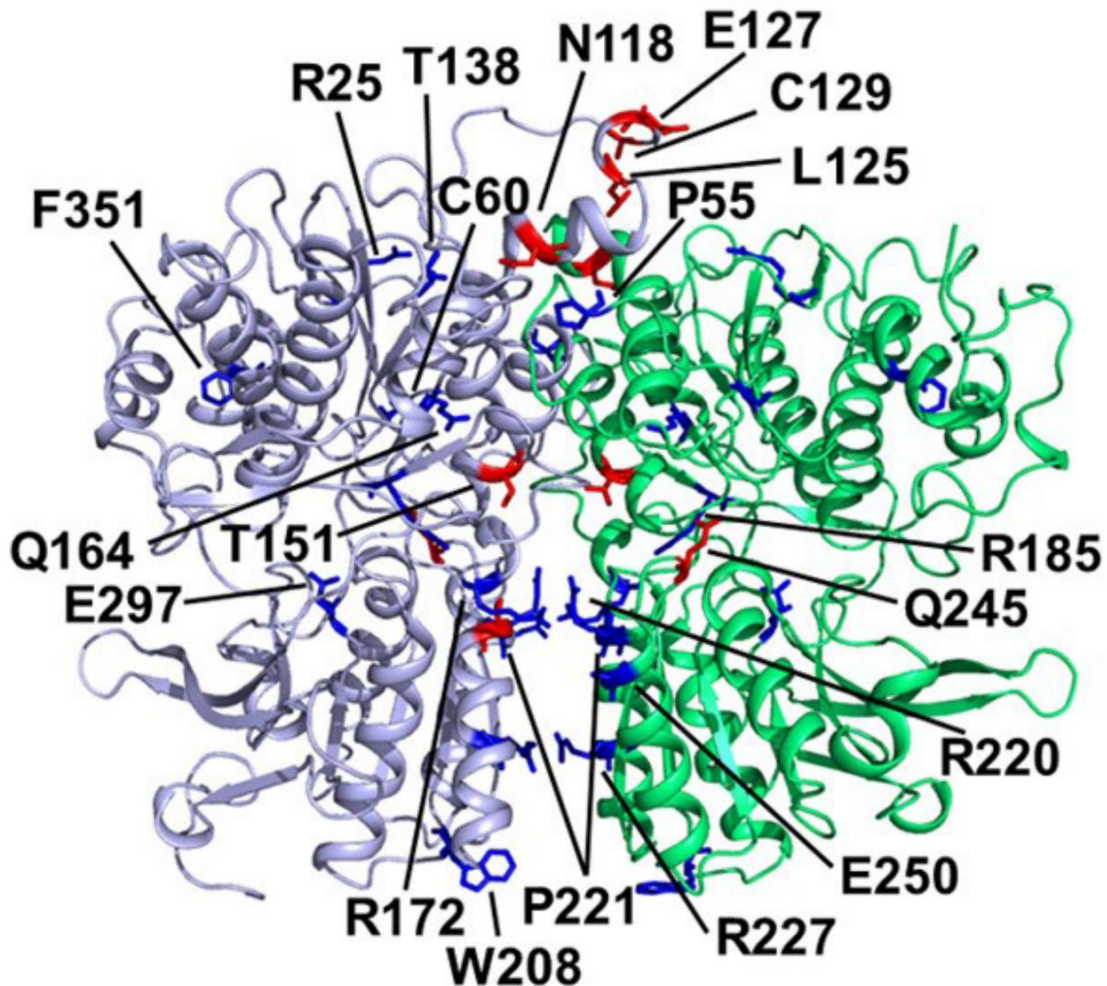


**Figure 2.14 – Disease-related mutations on CaSR ECD.**

**Blue: Loss-of-function mutations associated with familial hypocalciuric hypercalcemia (FHH), Red: Gain-of-function mutations associated with autosomal dominant hypocalcemia (ADH).**

The hinge region between subdomains 1 and 2 harbors the binding site of TNCA, supporting its role as a co-agonist of CaSR. Two other co-agonists of CaSR, Phe and Trp, likely bind in the same

position. We did not observe metal binding at the previously proposed site 1 for  $\text{Ca}^{2+}$  [259, 269, 283]. A close inspection of the structure reveals that the side chain of E297, a critical residue predicted for  $\text{Ca}^{2+}$  binding in this proposed site 1, swings away from the other residues in site 1 (S170, D190, Q193, and Y218), probably due to the extra carbon atom and the rigid structure of TNCA, ultimately resulting in its failure to capture the  $\text{Ca}^{2+}$  ion in combination with other site 1 residues. We were able to make several mutations on the ECD of hCaSR in order to test the functionality of these binding sites for TNCA and  $\text{Mg}^{2+}$ . These mutations were E297I, Y218K, S272I, D275I, and E228I.

Mutations of E297I, Y218K, S272I, and D275I saw a complete loss of cell response to  $\text{Ca}^{2+}$  (Figure 2.15). Upon testing the cell surface expression of these CaSR mutants using confocal staining of non-permeabilized cells we saw that they were expressed on the cell (Figure 2.15). The fact that these mutations are expressed on the cell but have no cellular response tells us that the mutations are critical for function and/or correct structural conformation of CaSR.

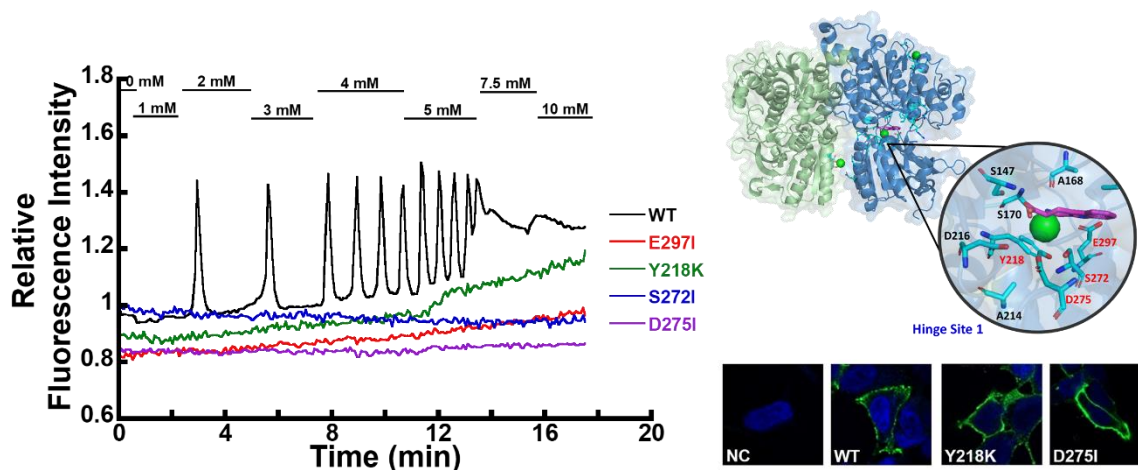


**Figure 2.15 – Complete loss of function hinge CaSR mutations.** Representative plots for WT hCaSR (black), E297I (red), Y218K (green), S272I (blue), and D275I (purple) CaSR mutants of the loss of oscillation function in response to increasing  $[\text{Ca}^{2+}]_o$ . CaSR structure (right) with zoom in on hinge binding site with mutations in red. Representative membrane expression (right lower) of CaSR on the cell surface of WT and the E297I, Y218K, S272I, and D275I CaSR mutants as shown



here with Y218K and D275I as examples. NC = no CaSR transfected, blue center = DAPI, and green outline = CaSR expression.

As for the E228I CaSR mutation was not only successfully expressed on the cell membrane but also had functionality in response to  $[Ca^{2+}]_o$  and  $[Mg^{2+}]_o$  (Figure 2.16). Although the E228I mutation does have cell expression and functionality the  $EC_{50}$  for  $[Mg^{2+}]_o$  activation is partially lost from 12.9 mM for WT CaSR to 15.6 mM for E228I mutation as well as a loss in functional cooperativity (Figure 2.16).

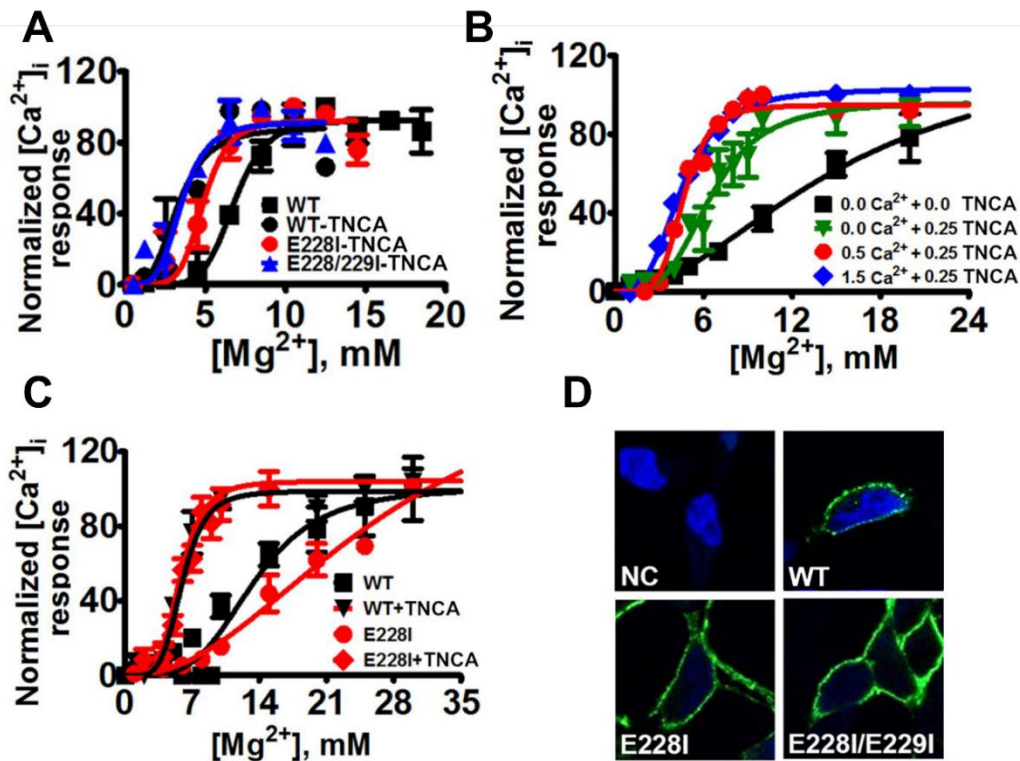


**Figure 2.16 – Determining TNCA binding capability to hCaSR-ECD.**

(A) TNCA potentiates  $[Mg^{2+}]_o$ -evoked  $[Ca^{2+}]_i$  responses in CaSR mutant E228I and the double mutant E228I/E229I analyzed using fluorimetry in cell population assay in 0.5 mM basal  $[Ca^{2+}]_o$ . (B) Calcium and (or) TNCA potentiate the  $[Mg^{2+}]_o$ -stimulated intracellular calcium responses in the single-cell imaging assay. Black squares are without  $[Ca^{2+}]_o$  or TNCA, green triangles are with 0.25 mM TNCA, red circles are with 0.5 mM  $[Ca^{2+}]_o$  and 0.25 mM TNCA, and blue diamonds are with 1.5 mM  $[Ca^{2+}]_o$  and 0.25 mM TNCA. Single-cell intracellular calcium responses were recorded using a fluorescence microscope and normalized  $[Ca^{2+}]_i$  was plotted against  $[Mg^{2+}]_o$  then further fitted using the Hill equation. (C) TNCA potentiates  $[Ca^{2+}]_i$  responses of both WT CaSR or mutant E228I to  $[Mg^{2+}]_o$  stimulation in the single-cell

imaging assay in the absence of basal  $[Ca^{2+}]_o$ . Black squares are the WT without TNCA, black triangles are the WT with 0.25 mM TNCA, red circles are the E228I mutant without TNCA, and red diamonds are the E228I mutant with 0.25 mM TNCA. (D) Membrane expression of CaSR, mutant E228I and double mutant E228I/E229I. Blue: DAPI staining cell nuclei. Green: hCaSR immunoreactivity.

We then added 0.25 mM of the Trp-derivative TNCA to the mutation which still had function E228I and found that not only does TNCA recover the loss of function of the E228I from 15.6 mM in comparison to the WT CaSR of 12.9 mM, but actually recovered the function all the way to 6.3 mM which is similar to the activated WT CaSR with TNCA itself at 5.6 mM as well as recovering the loss of functional cooperativity (Figure 2.16-Figure 2.17 and Table 2.2). This shows that TNCA is a strong calcimimetic able to recover disease related mutations affecting molecular biological functionality.

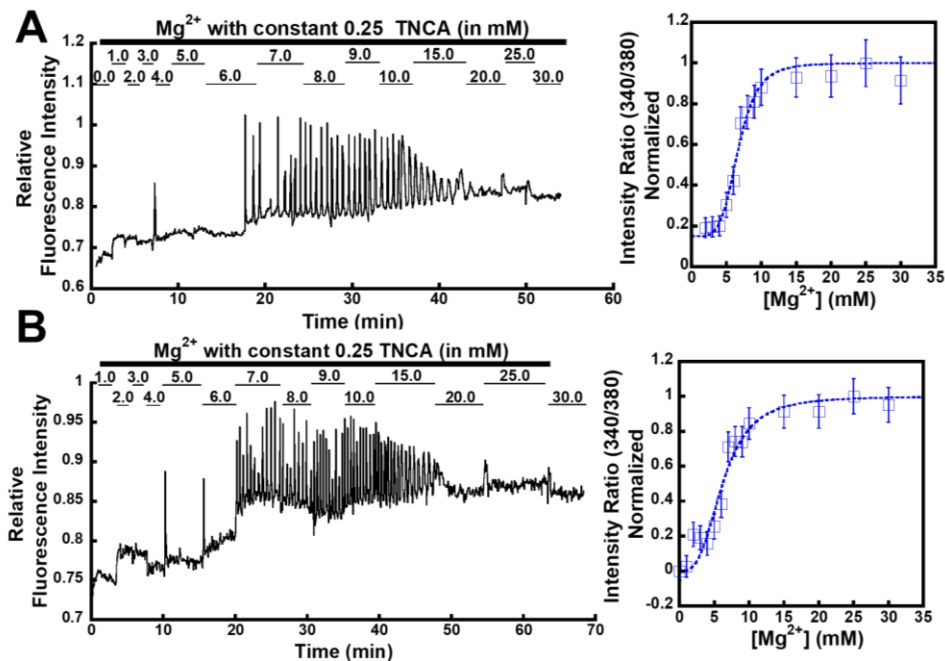


**Figure 2.17 – CaSR mutation E228I representative oscillations.**

**A&B – Representative plots for E228I CaSR mutant oscillation function in response to increasing  $[Mg^{2+}]_o$ .  $EC_{50}$  plots for the respective trials are shown on the far right.**

Nevertheless, the essential role of E297 in  $\text{Ca}^{2+}$  sensing has been supported by previous mutational studies<sup>[23, 269]</sup> and in the abrogated  $\text{Mg}^{2+}$  sensing of the E297I mutant (Table 2.2). A bicarbonate anion was also identified in the hinge region in proximity with TNCA, coordinated by the side chains of R66, R69, W70, and S417 and the backbone amide nitrogen atoms of I416 and S417, potentially contributing to the known pH sensitivity of the CaSR<sup>[275]</sup>.

**Table 2.2 – EC<sub>50</sub> of  $[\text{Mg}^{2+}]_o$  for stimulation of  $[\text{Ca}^{2+}]_i$  signaling with or without TNCA.**

<b>Co-activator (cell population)</b>	<b>0 mM TNCA</b>		<b>0.5 mM TNCA</b>	
<b>(0.5 mM <math>\text{Ca}^{2+}</math>)</b>	<b>EC<sub>50</sub></b>	<b>Hill Number</b>	<b>EC<sub>50</sub></b>	<b>Hill Number</b>
WT	7.2 ± 0.4	4.0 ± 1.0	3.3 ± 0.7	3.5 ± 1.0
E228I	10.8 ± 0.3	3.9 ± 0.4	4.9 ± 0.3	6.2 ± 2.6
E228/E229I	10.0 ± 0.5	4.6 ± 0.5	3.5 ± 0.5	4.3 ± 1.7
Y218K	No Response		No Response	
S272I	No Response		No Response	
D275I	No Response		No Response	
E297I	No Response		No Response	
<b>Co-activator (single cell imaging)</b>	<b>0 mM TNCA</b>		<b>0.25 mM TNCA</b>	
<b>(0.0 mM <math>\text{Ca}^{2+}</math>)</b>	<b>EC<sub>50</sub></b>	<b>Hill Number</b>	<b>EC<sub>50</sub></b>	<b>Hill Number</b>
WT	12.9 ± 0.3	2.9 ± 0.2	5.6 ± 0.3	5.2 ± 1.3
E228I	15.6 ± 0.9	3.5 ± 0.6	6.3 ± 0.2	4.6 ± 0.6
Y218K	No Response		No Response	
S272I	No Response		No Response	
D275I	No Response		No Response	
E297I	No Response		No Response	

No Response mutants were tested for expression and showed cell surface expression but without CaSR activity

### 2.3 Discussion

We report here the first crystal structure of the ECD of human CaSR bound with  $Mg^{2+}$  and a tryptophan derivative ligand at 2.1 Å. The structure reveals important determinants for cooperative activation of the CaSR by metal ions and aromatic amino acids, including key residues in the ECD participating in  $Mg^{2+}$  and amino acid binding. We have found two confirmed  $Mg^{2+}/Ca^{2+}$  binding sites, a drug TNCA binding site, and a bicarbonate binding site.

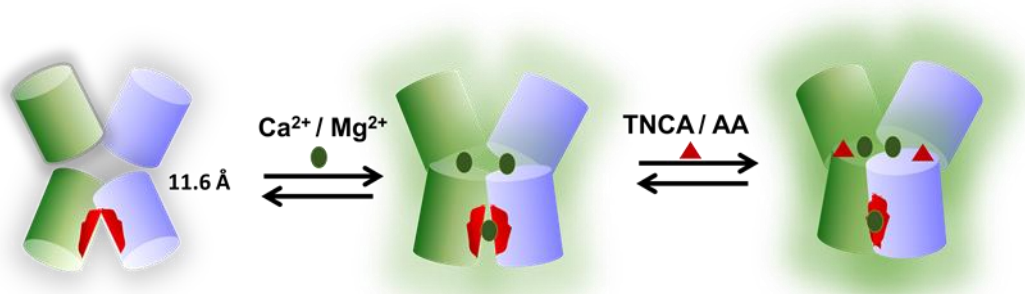


**Figure 2.18 – Working model of CaSR binding and activity. Unbound inactive CaSR is activated by  $Ca^{2+}/Mg^{2+}$  binding cooperatively upon multiple binding sites. Then CaSR is further activated and stabilized by TNCA or amino acids (AA).**

The hinge TNCA binding site consists of residues S147, A168, S170, Y218, and E297. Four of these residues overlap exactly with our predicted  $Ca^{2+}$  binding site. The dimerization binding site of  $Mg^{2+}$ , which is possible to also be  $Ca^{2+}$  since with weak binding  $Ca^{2+}$  did not show on the crystal structure, are residues E228, E231, S240 and E341 from the other monomer. Two of these residues overlap a binding site on the modeled structure. Lastly, a new  $Mg^{2+}$  site was found that was not



predicted using our modeled structure and also found in the Geng et al. paper, these residues are I81, S84, L87, and L88<sup>[284]</sup>.

Several lines of evidence indicate a critical role of CaSR-ECD dimerization in CaSR function (Figure 2.5 and Figure 2.9). First, two metal binding sites are identified within the acidic patch at the dimerization interface of subdomain 2 (Figure 2.6). A double mutant of CaSR (E228I/E229I) in site 2 showed a significantly decreased responsiveness to  $[Ca^{2+}]_o$ , and the E228I mutation also reduced activation of  $[Ca^{2+}]_i$  oscillations induced by  $[Mg^{2+}]_o$  as well as reduced  $Mg^{2+}$  binding, despite a similar level of membrane expression as WT CaSR (Figure 2.16 and Table 2.2)<sup>[259]</sup>. These data strongly suggest a role of metal binding at the acidic patch in metal sensing and signal transduction which supports our working model that  $Ca^{2+}$  and  $Mg^{2+}$  activate CaSR and that TNCA further activates and stabilizes disease mutations (Figure 2.18).

**Table 2.3 – Comparison of the binding sites between CaSR structures.**

Potential Binding Sites Modeled					CaSR Determined Structure			Elife CaSR				
Ca2+ BS 1	BS2	BS3	BS4	BS5	TNCA	Mg2+ BS1	BS2	Trp	Ca2+ BS1	BS2	BS3	BS4
S147	D215	E224	E350	T396	S147	E228	I81	S147	I81	T100	S302	E231
S170	L242	E228	E353	D398	A168	E231	S84	A168	N82	N102	S303	D234
D190	S244	E229	E354	E399	S170	E341*	L87	S170	S84	T145		G567
Y218	D248	E231	N386	E378	Y218	S240	L88	Y218	L87	G146		
E297	E253	E232	S388	E379	E297			E297	L91			

Several months after our crystal was published another group was able to crystallize the CaSR ECD with the cys-rich domain as well but lacking the dimerization loop on top. They also observed several  $Ca^{2+}$  binding sites in the holo form, as well as one in the apo form too. They also observed Trp bound in the hinge site of each monomer in the holo form, which perfectly corresponds to our TNCA binding site. The dimer site 2 for  $Mg^{2+}$  overlaps 2 residues with binding site 3 dimer site for  $Ca^{2+}$  in the modeled structure as well as 1 residue in  $Ca^{2+}$  site 4 in the Geng et al. paper<sup>[284]</sup>.

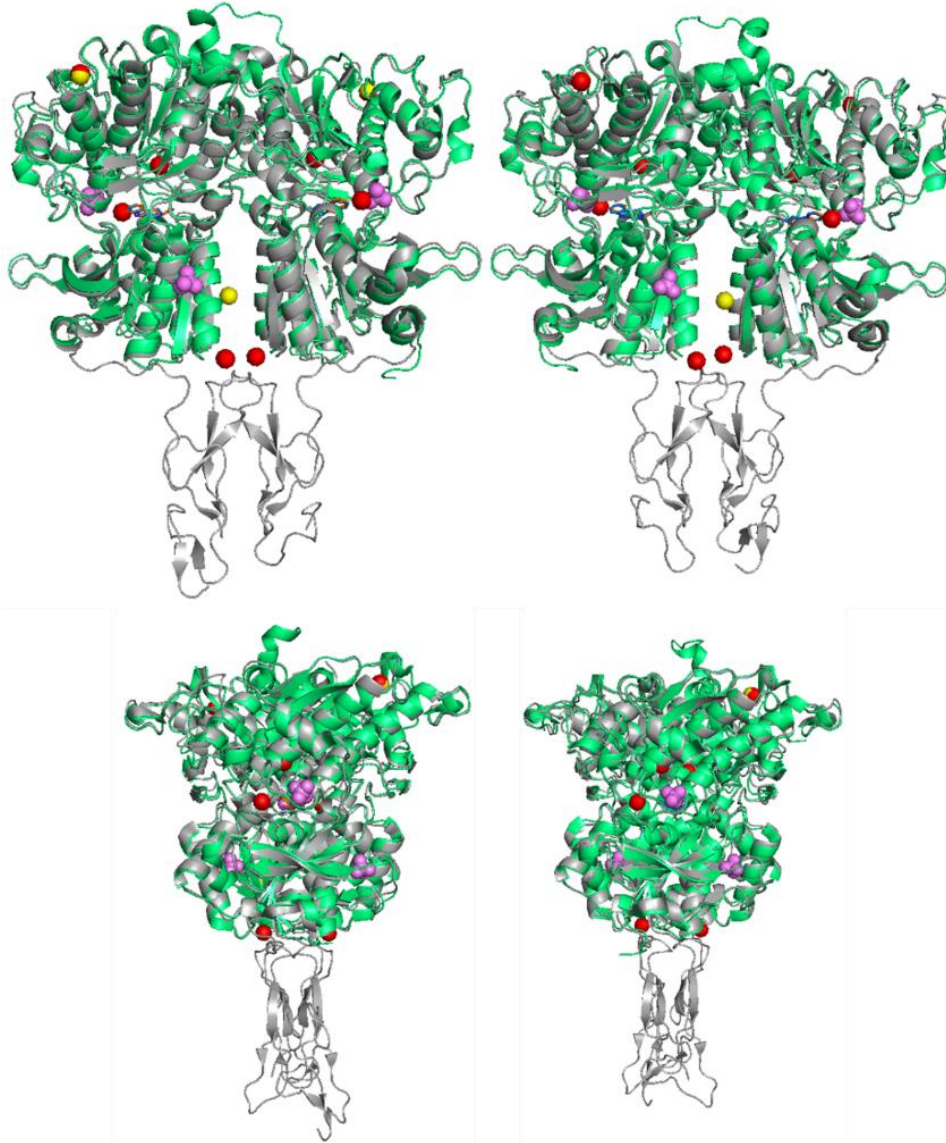


**Figure 2.19 – Comparison of our CaSR 5FBK and the Geng et al. CaSR 5K5S<sup>[284]</sup>. CaSR 5FBK (green) and the Geng et al. CaSR 5K5S (Active Form) (gray). 5FBK has Mg<sup>2+</sup> yellow spheres, and TNCA blue sticks by element, while 5K5S has Ca<sup>2+</sup> red spheres, Trp orange sticks by element, and PO<sub>4</sub> pink spheres.**

Lastly, our Mg<sup>2+</sup> binding site 3 overlaps three residues with the Geng et al. Ca<sup>2+</sup> binding site 1<sup>[284]</sup>.

These similarities in binding sites show that these residues are most likely conserved and highly important to the function and structure of CaSR. Since our structure was treated with Mg<sup>2+</sup> we had Mg<sup>2+</sup> binding sites resolved while the Geng et al. paper showed Ca<sup>2+</sup> binding sites<sup>[284]</sup>. We

also compared the TNCA and Trp binding sites as well as the modeled binding sites in table form (Table 2.3).

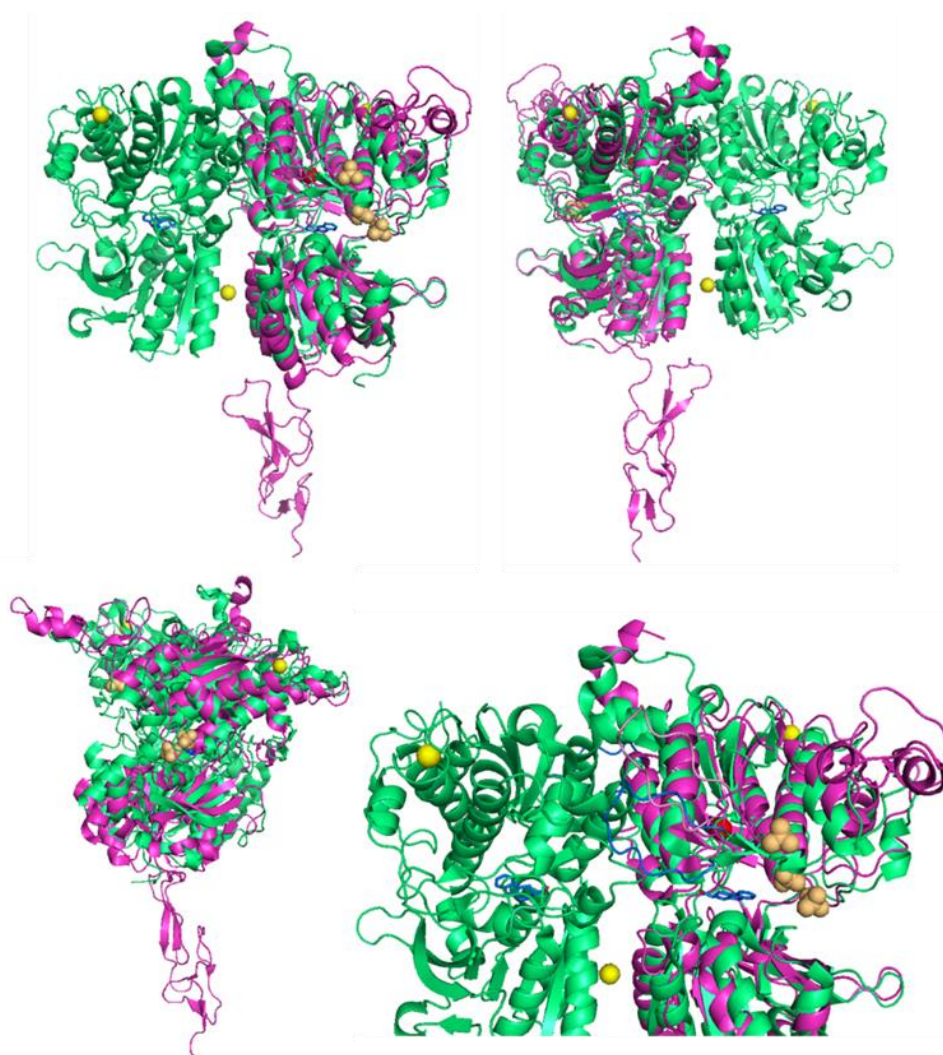


**Figure 2.20 – Comparison of our CaSR 5FBK and the Geng et al. CaSR 5K5T<sup>[284]</sup>. CaSR 5FBK (green) and the Geng et al. CaSR 5K5T (apo) (magenta). 5FBK has Mg<sup>2+</sup> yellow spheres, and TNCA blue sticks by element, while 5K5T has Ca<sup>2+</sup> red spheres, Trp orange sticks by element, and SO<sub>4</sub> yellow-orange spheres with Loop 1 in light pink.**

The structures of our holo form structure versus the Geng et al. holo form are nearly perfectly identical in their overlap regions (Figure 2.20)<sup>[284]</sup>. The main differences are that our structure has the dimer loop 2 and theirs has the cys-rich domain determined. Additionally, the metals binding is different, as described previously.

Whereas the holo forms 5FBK and 5K5S perfectly overlap, there are some structural difference between our holo form 5FBK and the Geng et al. apo form 5K5T (Figure 2.20)<sup>[284]</sup>. The most substantial differences are in the space available in the hinge region for binding and loop 1. The apo form has the hinge region more open and the helices and sheets around the region moving away from it, opening the space for binding of metal ions or TNCA. Loop 1 of the apo form also has moved up, this could be because the structure is less stable when in apo form or because it is represented only as a monomer.

Besides, extensive interactions between the disulfide linked dimeric ECDs and their respective subdomains that produce a closed and likely active conformation of the Venus flytrap motifs of the two ECDs are present. The unexpected tryptophan derivative that was bound in the hinge region between two ECD subdomains represents a novel high-affinity co-agonist of CaSR that potentiates activation of the full-length CaSR expressed in HEK293 cells by  $\text{Ca}^{2+}$  and  $\text{Mg}^{2+}$ . We showed that TNCA is able to alter the  $[\text{Ca}^{2+}]_i$  oscillation frequency when co-activated with  $[\text{Ca}^{2+}]_o$  showing alteration in cellular signaling function since we know that a change in  $[\text{Ca}^{2+}]_i$  frequency is related to a change in cellular functions where faster oscillations are necessary for quick processes such as dendritic growth and insulin production while slower frequency oscillations are related to slow processes such as fertilization or cell growth<sup>[25-28]</sup>. Furthermore, TNCA modulates  $\text{Mg}^{2+}$  activity as an agonist shifting the  $\text{EC}_{50}$  for  $\text{Mg}^{2+}$  down and having stronger  $\text{Mg}^{2+}$  functional activity as well as functional cooperativity which supports our working model that  $\text{Ca}^{2+}$  and  $\text{Mg}^{2+}$  activate CaSR and that TNCA further activates and stabilizes CaSR (Figure 2.18). In addition,  $\text{Mg}^{2+}$  with TNCA and sub activating  $\text{Ca}^{2+}$  concentrations brings the binding efficacy of  $\text{Mg}^{2+}$  down to similar to WT CaSR with  $\text{Ca}^{2+}$  alone. Mutations of the primary hinge binding pocket which binds  $\text{Ca}^{2+}$  and TNCA leads to a complete loss of functional activity and functional cooperativity.

Mutation of residues E297, S272, and D275 to hydrophobic residue Ile led to the annihilation of CaSR signaling in response to either loss of receptor binding or structural integrity disruption. Additionally, changing the Y218 residues also in this critical hinge binding pocket to a positively charged Lys residue also led to a complete loss of CaSR functional activity and functional cooperativity most likely due to the repulsion of positively charged cations  $\text{Ca}^{2+}$  and  $\text{Mg}^{2+}$ . TNCA can also act as an agonist and stabilize mutations of E228I and E228/229I which supports our working model that  $\text{Ca}^{2+}$  and  $\text{Mg}^{2+}$  activate CaSR and that TNCA further activates and stabilizes disease mutations (Figure 2.18). These mutations led to a loss of function in CaSR and TNCA was not only able to stabilize the CaSR structure of the mutants back to WT CaSR function but further to a gain-of-function activity, which TNCA was able to produce on the WT CaSR itself. Therefore, TNCA is a potent agonist able to completely remove the effects of loss of function CaSR mutations.

We would like to further engineer more mutations but rather than binding site disruption we would like to also investigate known disease mutations of the hinge, dimer, new top, and bicarbonate binding sites to examine the effects these disease mutations have on CaSR functional activity as well as cooperativity. Since these disease mutations do not often lead to fetal death, we would expect a still partially functional CaSR unlike the disruption mutations in the hinge site which led to a loss of signal. Additionally, expressing and purifying full length CaSR for crystallization would be the next step so that we could visualize the 7TM domain along with the ECD to see if drugs added to the protein bind to ECD or 7TM as confirmed by crystal structure since currently CaSR drug targets have not confirmed the region of binding using a crystal structure.

## 2.4 Materials and Methods

### 2.4.6 Computational prediction

The structure of the extracellular domain of CaSR (residues 25-530) was modeled based on the crystal structure of the metabotropic glutamate receptor 1 (mGluR1) (1EWT, 1EWK and 1ISR), and the potential Ca<sup>2+</sup>-binding sites in the CaSR ECD were predicted using MetalFinder<sup>[264]</sup> or MUG (MULTiple Geometries)<sup>[265-268]</sup>.

### 2.4.7 mCaSR ECD expression

One liter of Life Technologies Freestyle™ 293 Expression Medium was used for HEK293F or Lec1 mutant HEK293F cell culture. Cells were transfected with pXLG-hCaSR-ECD plasmid using the polyethyleneimine method when the cell density achieved 8x10<sup>5</sup>. The hCaSR-ECD was secreted into the culture media. When the cell density reached 5 x 10<sup>6</sup> cell/mL, the media was collected by centrifugation 3 times at 1500xg for 10 min. The supernatant was diluted with dilution buffer (Tris NaCl pH=8.0) at a ratio of 1:3 and further filtered through a Millipore 0.45 µm filter. The filtered medium was applied to a 16/10 GE Healthcare HisTag HP column pre-equilibrated with Buffer A (Tris 50 mM, NaCl, 150 mM, Imidazole 20 mM) and a linear segmented gradient of 0–100% Buffer B (50 mM Tris, 500 mM NaCl, and 500 mM imidazole, pH 7.4) was run using FPLC to elute the protein. The hCaSR-ECD concentrations were determined using Bio-Rad protein assay.

### 2.4.8 mCaSR ECD purification

Purification of hCaSR-ECD secreted from HEK293S GnTI- cells hCaSR-ECD (from residues Tyr20 to Phe612) was expressed in suspension culture of HEK293S GnTI- cells and purified from the culture medium by Ni<sup>2+</sup>-nitrilotriacetic acid chromatography, as previously described<sup>[285]</sup>. To deglycosylate the purified protein, hCaSR-ECD was incubated with recombinant endoglycosidase

F1 (Endo F1) at a 1:100 mass ratio of Endo F1 to hCaSR-ECD<sup>[286]</sup> overnight at 4°C in 10 mM tris buffer (pH 7.4). Further separation of hCaSR-ECD from Endo F1 was achieved by size exclusion chromatography in 10 mM HEPES buffer (pH 7.3)<sup>[287]</sup>.

#### ***2.4.9 Crystallization, data collection, and structure determination***

The dimeric hCaSR-ECD was concentrated to 10 mg/mL and crystallized in 10% polyethylene glycol (PEG)-8000, 200 mM MgCl<sub>2</sub>, 10 mM CaCl<sub>2</sub>, and 100 mM Tris-HCl (pH 7.0), using the sitting drop approach at 21°C. No crystals were formed in the absence of Ca<sup>2+</sup> or Mg<sup>2+</sup>. The plate-shaped crystals were cryoprotected using 25% glycerol and were flash-frozen in liquid nitrogen. Dehydration by soaking the crystal in 12% PEG-8000 overnight improved the resolution from 3.5–4 to 2–3 Å. The diffraction data of the crystals were collected on the beamline of 21-ID-D at LS-CAT (Life Sciences Collaborative Access Team) in APS (Argonne Photon Source) and indexed, integrated, and scaled in HKL2000<sup>[288]</sup>. The structure was solved at 2.1 Å by molecular replacement using Auto-MR (automated molecular replacement) in PHENIX<sup>[289]</sup>. The structure of chain A of mGluR2 with a bound agonist (PDB ID: 4XAQ) was used as the search template<sup>[271]</sup>. The electron density map after molecular replacement was clear enough to identify the unique features of hCaSR-ECD, and iterative model building and refinement were performed using COOT<sup>[290]</sup> and Refmac5 in the CCP4<sup>[291]</sup> suite, respectively. The restraints of 1,2,3,4-tetrahydronorharman-3-carboxylic acid (TNCA) were generated by JLigand in COOT. To generate the Gd<sup>3+</sup> derivative, the native crystals were soaked with a solution containing 12% PEG-8000, 200 mM MgCl<sub>2</sub>, 10 mM CaCl<sub>2</sub>, 100 mM Tris-HCl (pH 7.0), and 0.5 mM GdCl<sub>3</sub> overnight at 21°C. The anomalous signals of a data set at 2.7 Å collected at the wavelength of 1.6985 Å were used to locate Gd<sup>3+</sup> in the structure. The structure was solved by molecular

replacement using the previously determined structure as the search template. All the figures of protein structures were generated by PyMOL version 1.3 (Schrodinger LLC).

#### ***2.4.10 High-resolution LC-ESI-MS and identification of TNCA***

In our crystal structure, there was an unidentified ligand (CaSRL) bound at the putative orthosteric ligand binding site of CaSR-ECD. The size of the density suggested that the CaSRL contained 14 to 18 heavy atoms (C/N/O/S/P), and the absence of anomalous signal indicated that it did not contain sulfur or phosphate. To extract CaSRL, 50 mL of purified hCaSR-ECD (10 mg/mL) was mixed with 120 mL of acetonitrile and was vortexed. After highspeed centrifugation, 10 mL of the CaSRL extract was injected onto a reverse-phase ACQUITY UPLC BEH C18 column (2.1 × 100 mm, 1.7-mm particle size; Waters). The column temperature was maintained at 40°C. The flow rate was 0.3 mL/min with starting conditions at 99% solvent A (water + 0.1% formic acid) and 1% solvent B (acetonitrile). The 15-min gradient profile for elution was as follows: starting at 1% solvent B, hold for 1 min, then ramp to 98% B at 10 min, hold at 98% B to 12 min, return to 99% A/1% B at 12.01 min, and maintain until 15 min. The samples were analyzed using a Waters Xevo G2-XS QToF LC-MS interfaced to a Waters ACQUITY UPLC system. The MS settings were as follows: electrospray ionization in negative-ion mode, capillary voltage of 2.00 kV, source temperature of 100°C, desolvation temperature of 350°C, desolvation nitrogen gas flow rate of 600 L/hour, cone voltage of 35 V, and mass range of m/z 50 to 1500 with spectra accumulated at 0.1 s per function. Three separate acquisition functions were performed to generate spectra at different collision energies (5, 25, and 60 eV) providing both non-fragmenting and fragmenting conditions. Analyses of samples by electrospray ionization in the positive-ion mode were performed under the same conditions as negative-ion mode except for the collision energies



(5, 20, and 40 eV). Fragmentation, formula, and abundances were analyzed with Waters MassLynx Software.

Using the above approach, we identified a species eluting at ~4.65 min, detected by MS in both positive-ion mode ( $m/z$  of 217.0990) and negative-ion mode ( $m/z$  of 215.0824), exclusively present in protein samples from several different batches but not in the sample buffer. The predicted elemental compositions based on mass are  $C_{12}H_{13}N_2O_2$  (calculated mass = 217.0977 Daltons) for positive ion mode and  $C_{12}H_{11}N_2O_2$  (calculated mass = 215.0824 Daltons) for negative-ion mode. A thorough search in the PubChem database led to a list of candidates containing up to 200 compounds with the same MW and formula. By manually fitting the density map with these compounds, only TNCA fit the density perfectly. Synthetic TNCA dissolved in the SEC buffer was treated in the same way as the protein samples in the LC-ESI-MS experiment, and resulted in a peak detected at the same retention time and having the same mass spectrum. In the LC-ESI-MS experiment, we also noticed a minor species that eluted at ~4.57 min which was detectable only in the positive-ion mode ( $m/z$  of 215.0836) and having a predicted elemental formula of  $C_{12}H_{11}N_2O_2$ . The 2-dalton smaller MW for this related compound suggested that it was a derivative of TNCA, likely due to a double bond formation between the backbone N and a neighboring C. Because it is also likely to be a tryptophan derivative, we cannot exclude the possibility that it binds hCaSR-ECD with high affinity. This compound may also form during the extraction of TNCA from the protein sample. Nevertheless, TNCA perfectly fits the electron density at 2.1 Å, and any extra double bonds in the CaSRL structure would likely be detrimental to fitting the density.

A phenylalanine replacement experiment was carried out by mixing purified hCaSR-ECD protein (0.26 mg/mL) with phenylalanine (final concentrations are 0, 50, and 150 mM, respectively). After

overnight incubation at room temperature, hCaSR-ECD in each sample was re-purified with Ni<sup>2+</sup>-NTA beads. The protein samples were adjusted to the same concentration using SEC buffer and analyzed by LC-ESI-MS.

#### ***2.4.11 Immunohistochemistry antibody staining***

Cells transfected with hCaSR-pcDNA3.1(+) were used in the immunostaining experiments, and this construct contained a FLAG tag between Asp371 and Thr372. After 48 hours post-transfection, cells were fixed with 3.7% formaldehyde for 15 min at room temperature, followed by washing with phosphate-buffered saline (PBS) three times. Mouse anti-FLAG monoclonal antibody was diluted 500 times and incubated with cells overnight at 4°C to stain the cell-surface CaSR. The cells were subsequently washed with PBS and stained with goat anti-mouse Alexa 488-conjugated secondary antibody for 1 hour at room temperature. Nuclei were stained with 4',6-diamidino-2-phenylindole (DAPI). Fluorescence was visualized using a Zeiss LSM780 confocal microscope.

#### ***2.4.12 SDS-PAGE gels and western blot***

Cells were harvested and then suspended in 200 µL of Western blot lysis RIPA buffer on ice for 15 min. After centrifugation at 15000 × g for 15 min at 4°C, the supernatants were collected. The proteins were separated on 8.5% SDS-PAGE. After electrophoresis, equal amounts of protein from each sample were transferred to a nitrocellulose membrane. The membrane was blocked with 5% nonfat milk in TBS and then incubated with first mouse anti-flag antibody (1:3000) separately overnight at 4°C. After being washed three times with TBST, the membrane was incubated at room temperature for 1 hr with goat anti-mouse secondary antibody diluted with TBST (1:3,000). The detected protein signals were visualized by an enhanced chemiluminescence reaction system (Bio rad).

#### ***2.4.13 Cell culture and transfection***

Monolayer cultures of HEK293 cells were purchased from American Type Culture Collection (ATCC CRL-1573) and maintained in Dulbecco's modified Eagle's medium (DMEM) supplemented with 10% fetal bovine serum (FBS) and high glucose (4.5 g/L) at 37°C. WT CaSR or its mutants were transfected into HEK293 cells using Lipofectamine 2000 or 3000 (Life Technologies) by following the manufacturer's instructions. Prepare transfection solution: 1 mL/cover slip in dish of 1X Opti-medium, 1 µL of pcDNA The CaSR (1 µg/mL), 2.5 µL of transfection reagent (Lipofectamine 2000). Incubate transfection solution for 15-20 mins at room temperature in a dark area. After incubation wash each dish (with coverslip of cells ~70% confluence) with 1-1.5 mL of HBSS. Add 3 mL of 1X Opti-medium to each dish. Take 1 mL of transfection solution and add dropwise to coverslip stirring immediately after several drops. Incubate coverslips within petri dishes for 4-6 hrs. Remove transfection solution and add 2 mL of fresh, normal medium for cell type. Incubate for 24-48 hr for cell imaging.

#### ***2.4.14 Cell imaging***

The CaSR WT was transiently transfected into HEK293 cells grown on coverslips and cultured for 48 hr at 37°C. Fura 2-AM stock solution is diluted from 1 mM to 1 µM (1000-fold) by adding 2 µL Fura 2-AM stock solution into 2 mL of physiological Ringer buffer (10 mM HEPES, 121 mM NaCl, 2.4 mM K<sub>2</sub>HPO<sub>4</sub>, 0.4 mM KH<sub>2</sub>PO<sub>4</sub>, 1.2 mM MgCl<sub>2</sub>, 1.2 mM CaCl<sub>2</sub> and pH 7.4). The addition of 2 µL of the non-ionic detergent Pluronic ® F-127 can assist in the dispersion of the nonpolar AM ester in aqueous media. The cells are incubated in the 2 mL of AM ester solution for 15–20 minutes at 37°C. After incubation, the cells are washed twice with Ringer buffer, without calcium. The coverslips are mounted on a bath chamber and placed on the stage of a fluorescence microscope. The cells were alternately illuminated with 340 or 380 nm light, and the

fluorescence at an emission wavelength 510 nm was recorded in real-time as the concentration of extracellular  $\text{Ca}^{2+}$  was increased in a stepwise manner. The ratio of emission fluorescence intensity from both excitation wavelengths was further calculated as a function of  $[\text{Ca}^{2+}]_o$ . All experiments were performed at room temperature. Oscillations were identified as three successive fluctuations in the  $[\text{Ca}^{2+}]_i$  after the first main cellular peak.

#### ***2.4.15 Measurement of $[\text{Ca}^{2+}]_i$ changes by $[\text{Mg}^{2+}]_o$ in single CaSR-transfected cells***

Measurement of intracellular free  $\text{Ca}^{2+}$  was assessed as described by Huang et al.<sup>[259]</sup>. Briefly, WT CaSR or its mutants were transiently transfected into HEK293 cells grown on coverslips and cultured for 48 hours. The cells were subsequently loaded for 15 min using 2 mM Fura-2 AM in 2 mL of physiological saline buffer (10 mM HEPES, 140 mM NaCl, 5 mM KCl, and 1.0 mM  $\text{MgCl}_2$ ) (pH 7.4). The coverslips were mounted on a bath chamber on the stage of a Leica DM6000 fluorescence microscope. The cells were alternately illuminated with 340- or 380-nm light and the fluorescence at an emission wavelength of 510 nm was recorded in real-time as the  $[\text{Ca}^{2+}]_o$  and/or  $[\text{Mg}^{2+}]_o$  was increased in a stepwise manner in the presence or absence of 0.25 mM TNCA in buffer (10 mM HEPES, 155 mM NaCl, 5 mM KCl, 2 mM  $\text{NaH}_2\text{PO}_4$ , and 0.5 mM  $\text{MgCl}_2$ ) (pH 7.4). The ratio of the emitted fluorescence intensities resulting<sup>[23]</sup> from excitation at both wavelengths was utilized as a surrogate for changes in  $[\text{Ca}^{2+}]_i$  and was further plotted and analyzed as a function of  $[\text{Ca}^{2+}]_o$ . All experiments were performed at room temperature. The signals from 2 to 100 single cells were recorded for each measurement. Oscillations were identified as three continuous fluctuations in  $[\text{Ca}^{2+}]_i$  after the initial peak.

#### ***2.4.16 Intracellular calcium concentration in cell population by fluorimetry***

The  $[\text{Ca}^{2+}]_i$  responses of wild type (WT) CaSR and its mutants were measured as described by Huang et al.<sup>[259]</sup>. Briefly, CaSR-transfected HEK293, or stably transfected HEK5001, cells were

grown on  $13.5 \times 20$  mm coverslips. After the cells reached 90% or higher confluency, they were loaded by incubation with  $2 \mu\text{M}$  Fura-2 AM in 20 mM HEPES, containing 125 mM NaCl, 5 mM KCl, 0 mM  $\text{CaCl}_2$ , 0.5 mM  $\text{MgCl}_2$ , 1 mM  $\text{NaH}_2\text{PO}_4$  (pH 7.4) for 15 mins at  $37^\circ\text{C}$  and then washed twice with  $\text{Ca}^{2+}$ -free Ringer's buffer. The coverslips with transfected, Fura-2-loaded HEK cells were placed diagonally in 3-mL quartz cuvettes containing  $\text{Ca}^{2+}$ -free Ringer's buffer. The fluorescence spectra at 510 nm were measured during stepwise increases in  $[\text{Ca}^{2+}]_o$  with alternating excitation at 340 or 380 nm. The ratio of the intensities of the emitted light at 510 nm, when excited at 340 or 380 nm, was used to monitor changes in  $[\text{Ca}^{2+}]_i$ . The  $\text{EC}_{50}$  and Hill constants were fitted using the Hill equation,  $\Delta S = \frac{[M]^n}{K_d^n + [M]^n}$ , where  $\Delta S$  is the total signal change in the equation,  $K_d$  is the apparent binding affinity,  $n$  is the Hill coefficient, and  $[M]$  is the free metal concentration. Measurements of Fura-2 fluorescence at 510 nm, when excited at 340 or 380 nm, were performed on a QM1 fluorescence spectrophotometer (Photon Technology International). The emission ratio of 340/380 was calculated and used to reflect the changes in  $[\text{Ca}^{2+}]_i$  when different concentrations of  $[\text{Mg}^{2+}]_o$  were applied to the cells. To examine the coactivation of CaSR by TNCA and  $[\text{Mg}^{2+}]_o$  or  $[\text{Ca}^{2+}]_o$ , different concentrations of TNCA were placed in the experimental buffer with a fixed concentration of  $[\text{Ca}^{2+}]_o$  and varying concentrations of  $[\text{Mg}^{2+}]_o$ , or vice versa, as described in the Results section. The effects of other ligands were analyzed by comparing the changes in  $[\text{Ca}^{2+}]_i$  produced by  $[\text{Mg}^{2+}]_o$  alone or by co-application of  $\text{Mg}^{2+}$  with other ligands. The  $\text{EC}_{50}$  of  $[\text{Mg}^{2+}]_o$  obtained during incubation with various concentrations of TNCA is compared with that observed in the presence of  $[\text{Mg}^{2+}]_o$  alone. The  $\text{EC}_{50}$  changes were plotted as a function of TNCA concentration, and the curve was fit to the Hill equation,

$$\Delta S = \frac{[M]^n}{K_d^n + [M]^n}, \text{ where } \Delta S \text{ is the total signal change in the equation, } K_d \text{ is the apparent binding}$$

affinity,  $n$  is the Hill coefficient, and  $[M]$  is the free metal concentration. The activation of CaSR by the TNCA, functioning as a co-agonist with  $[Mg^{2+}]_o$ , was indicated by the increasingly left-shifted  $EC_{50}$  for  $[Mg^{2+}]_o$  as the concentration of TNCA increases.

#### ***2.4.17 BSA standard and protein analysis***

Create the samples (total volume of 1 mL) making 2 blanks (800  $\mu$ L of ddH<sub>2</sub>O and 200  $\mu$ L of Bio-Rad) and samples, one for each plate in experiment (800  $\mu$ L of ddH<sub>2</sub>O, Usually we use 1  $\mu$ L of protein so we would add 800  $\mu$ L of ddH<sub>2</sub>O and then remove 1  $\mu$ L of ddH<sub>2</sub>O to get 799  $\mu$ L of ddH<sub>2</sub>O, 1  $\mu$ L of protein, 200  $\mu$ L of Bio-Rad). Run the samples using UV-Vis quantitative method. Use the blanks to auto-zero and then run each sample by pressing Start/Run/Record depending on the instrument. (NOTE: Have the cuvettes all facing the same direction in the machine for each sample recording). Transfer data into an excel spreadsheet, either one with the already done standard curve or a new one to make the standard curve and data. After the equation  $y=mx+b$  from the standard curve is known we may use this to solve for each sample's x-value, the UV-Vis values being their respective y-values. This will be their protein concentration value.

### 3 Understanding Molecular Basis of CaSR Related Diseases

#### 3.1 Introduction

CaSR is a part of the family C of GPCR superfamily with a large ECD, a cys rich domain (CRD), a 7TM domain, and an ICD<sup>[21]</sup>. CaSR plays critical functional roles in biological and pathological regulation and is extensively expressed throughout the body in the skin, gastrointestinal, the central nervous system (CNS), cardiovascular, in bone, kidney, breast, and the parathyroid tissues<sup>[249-252]</sup>. The CaSR primary function is to regulate Ca<sup>2+</sup> homeostasis and disease related mutations can cause loss of function familial hypocalciuric hypercalcemia (FHH) and neonatal severe hyperparathyroidism (NSHPT) which reduce CaSR's sensitivity to [Ca<sup>2+</sup>]<sub>o</sub>, whereas over activating mutations for a gain of function lead to autosomal dominant hypocalcemia (ADH). Additionally, CaSR mutation and dysfunction has also been linked to carcinomas, osteoporosis, hyperparathyroidism, hypoparathyroidism, renal failure, and cardiac disease. The primary agonist for CaSR is Ca<sup>2+</sup> for the regulation of Ca<sup>2+</sup> homeostasis but has been shown to respond to various other cations such as Mg<sup>2+</sup>, Gd<sup>3+</sup>, and Tb<sup>3+</sup> <sup>[22, 253, 254]</sup>. We are interested in if we can correlate the changes between the WT CaSR and disease related mutations using bacterially expressed CaSR for structural, binding, and expression information in comparison to functional and signaling information gained from cellular CaSR studies in order to expand our understanding in disease-mediated function differences<sup>[287]</sup>.

Since CaSR is a transmembrane protein it has the issues associated with transmembrane protein expression for binding, function, and structure studies in that transmembrane proteins are notoriously difficult to stably express and crystallize. As such, we initially analyze the functional domain alone, in lieu of the full protein omitting the transmembrane domain, in the case of CaSR the main functionality is within the ECD. We looked at bacterially expressed CaSR since

mammalian expressed CaSR has the issues of glycosylation can hinder binding studies using fluorescence spectroscopy, expression and purification is more time extensive, and we found that TNCA was bound to mammalian expressed CaSR thus being a holo ECD form. Bacterial expressed CaSR has the benefit of no post-translational modifications, is quick and cost-effective, and as such does not have the time for TNCA formation through the Pictet-Spengler reaction, but does have the issue of potential incorrect protein structure formation from the foreign bacterial expression system for the human CaSR ECD.

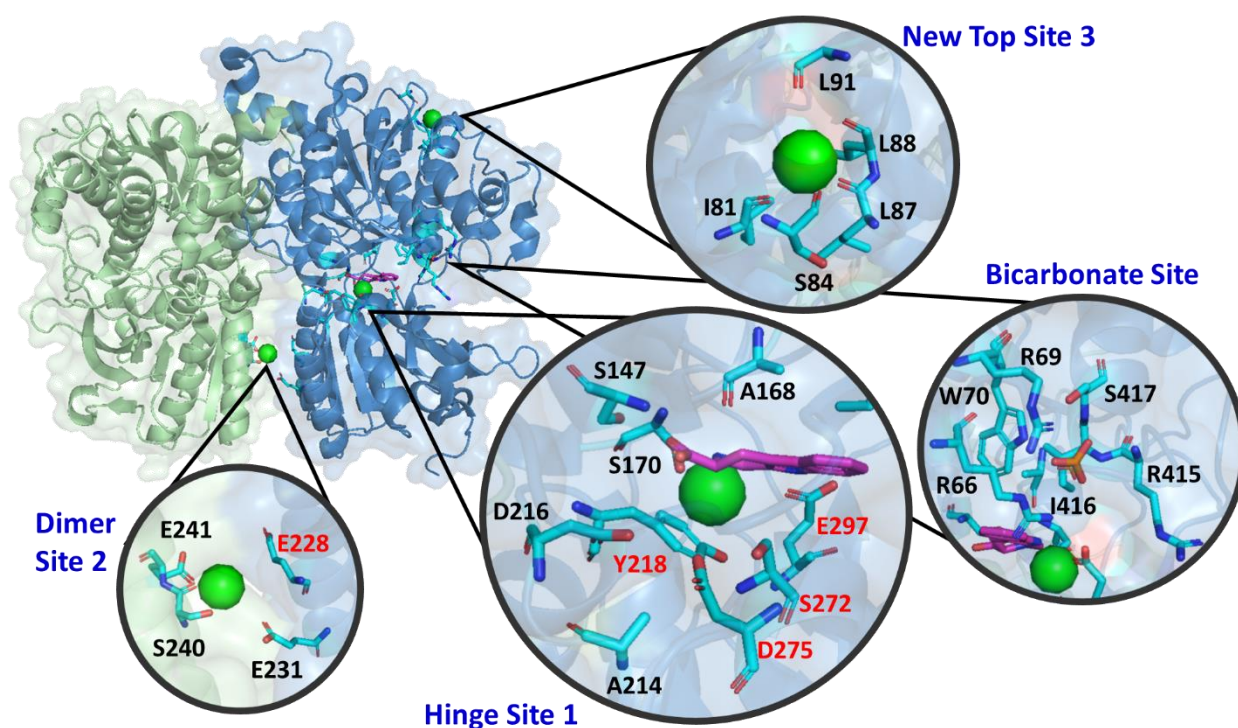


**Figure 3.1 – CaSR mutations made for functional studies in cells.**

Five binding sites on the CaSR ECD with a dimer  $Mg^{2+}/Ca^{2+}$  binding site (E228, E231, S240, and E241), a hinge region TNCA/ $Mg^{2+}/Ca^{2+}$  binding site (S147, A168, S170, A214, D216, Y218, S272, D275, and E297), a new top  $Mg^{2+}/Ca^{2+}$  binding site (I81, S84, L87, L88, L91), and a bicarbonate binding site (R66, R69, W70, R415, I416, and S417). Mutations made for functional studies are in red Y218K, E297I, S272I, D275I, and E228I.

We also wanted to correlate the functional effects the disruption mutations have on expression, structure, and binding of the CaSR ECD by utilizing a bacterial expression system. This way we



can visualize the effects of not only functional signaling and functional cooperativity in cell studies<sup>[287]</sup> but also the effects on the ECD alone without taking into effect the full-length CaSR as a dimer for binding and binding cooperativity. For our functional studies, we examined the mutations affecting the binding of the hinge domain by creating either hydrophobic or charged residues in the binding pocket to disrupt binding with mutations Y218K, E297I, S272I, and D275I (Figure 3.1)<sup>[287]</sup>. We saw that these four critical hinge region binding mutations expressed on the cell surface but led to a complete loss of functional response even up to 30 mM  $[Ca^{2+}]_i$  (Figure 2.15)<sup>[287]</sup>. The other mutation we made was to dimerization region of CaSR at E228 to disrupt the binding with a hydrophobic residue E228I (Figure 3.1)<sup>[287]</sup>. This mutation led to a loss of function effect reducing the binding of  $Mg^{2+}$  which was able to be recovered by TNCA (Figure 2.16)<sup>[287]</sup>.

## 3.2 Results

### 3.2.1 *bCaSR Expression Development*

To optimize correct CaSR ECD structure and disulfide bonds we looked at removing cys residue regions which could hinder correct CaSR ECD structure expression in a non-native bacterial expression system. We removed the mammalian shuttle region, called the signal peptide region (sp), as this would remove one cys residues and is unnecessary in a bacterial expression system since the CaSR will not need to be transported to the cell surface as in a mammalian expression system.

We also removed the cys-rich domain (CRD) since there are 9 cys residues in the CRD which could form incorrect disulfide bonds and potentially an incorrectly folded unstable protein prone to degradation (Figure 3.2). Thus, cys and sp were removed from bCaSR ECD together or separate (Figure 3.3).

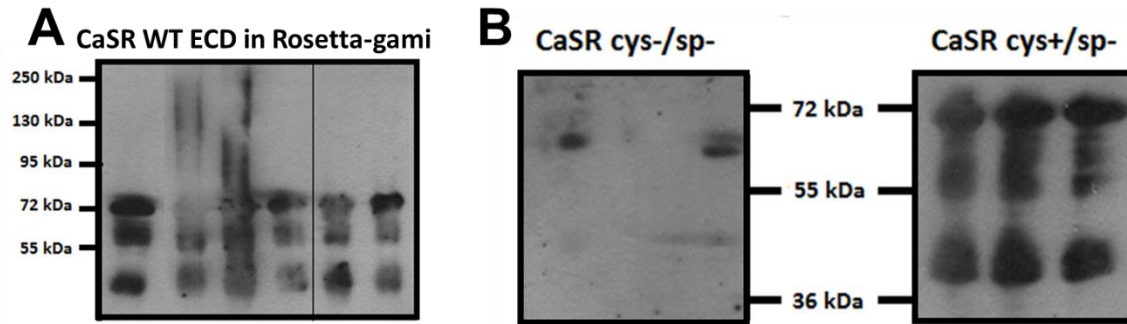


**Figure 3.2 – bCaSR WT versus bCaSR deletions using Rosetta-gami.**

**A – Western blot of WT bCaSR ECD expressed in Rosetta-gami cells and tagged with ADD CaSR antibody. B – Western blot of bCaSR ECD with signal peptide region deletion (sp-) with or without cys rich domain deleted (cys+/cys-) expressed in Rosetta-gami cells and tagged with ADD CaSR antibody. bCaSR ECD is approximately 65 kDa.**

Removal of both cys and sp (cys-/sp-) lead to the best protein expression without degradation, but also a loss of protein concentration and yield (Figure 3.2).

In order to improve the yield as well as maintain the stable expression, we further mutated four cys residues to ala residues, which would also keep the CaSR ECD in monomer form and could assist in CaSR stability. Additionally, we used an optimized *E. coli* expression system of SHuffle cells over Rosetta-gami which is optimized for correct disulfide bond formation. SHuffle and Origami, which Rosetta-gami was derived from, both have suppression of thioredoxin reductase (trxB) and glutathione reductase (gor) which break down disulfide bonds.

This allows these *E. coli* cells to form disulfide bonds, thus allowing more accurate protein folding. These also contain a mutant of alkyl hydroperoxide reductase subunit C (AhpC), which assist on the detoxification of reactive oxygen species, this mutant, AhpC\*, removes lethality of trxB and gor suppression by mimicking their roles by the ability to reduce glutaredoxin 1 (Grx1), restoring reducing power to the cells (Figure 3.4).

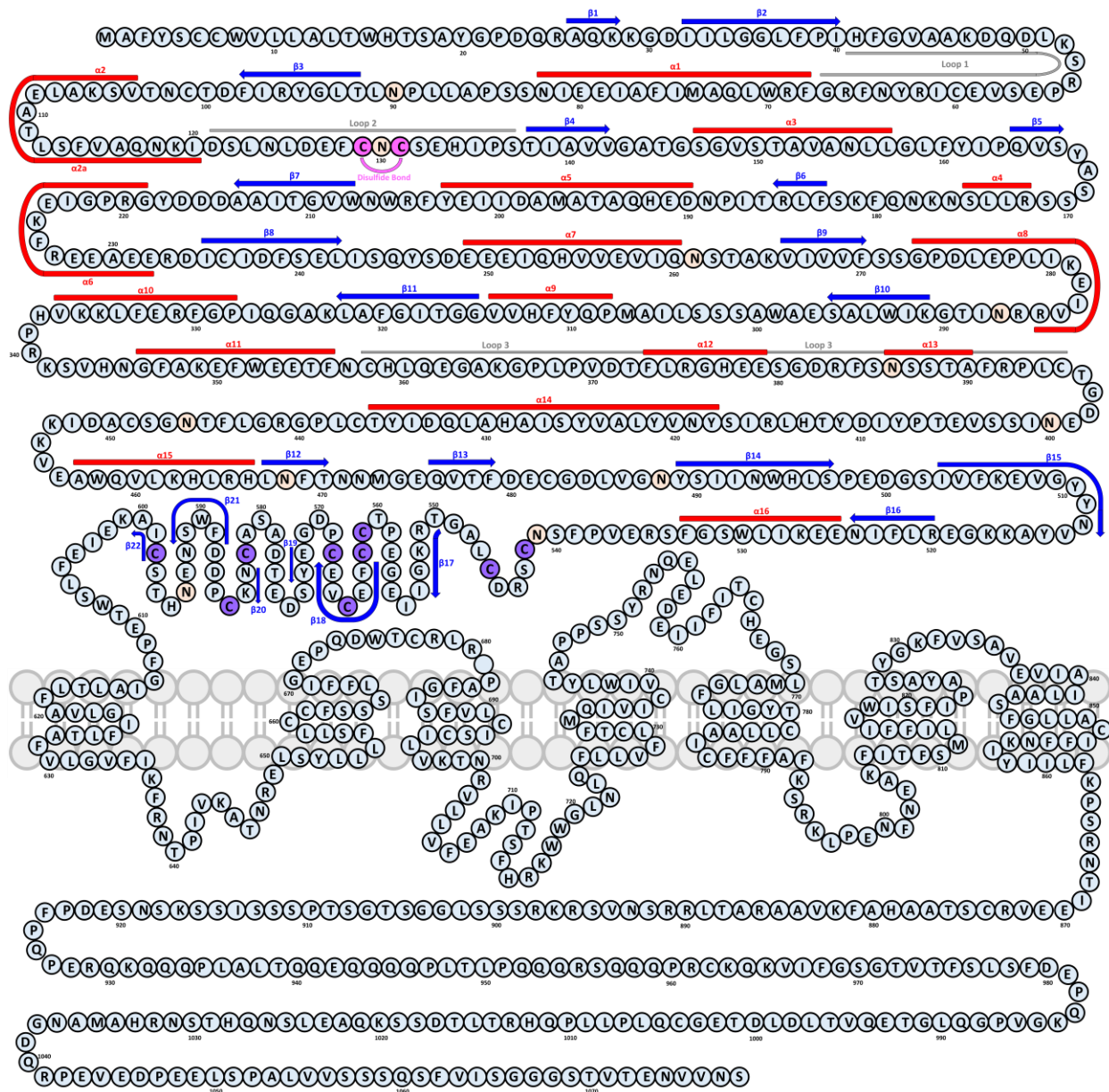


**Figure 3.3 – CaSR sequence.**

Each letter denotes an amino acid. Red bars represent  $\alpha$ -helicies, blue arrows represent  $\beta$  sheets, and gray bars represent loop regions. The ECD is shown above the gray membrane, the TMD is shown overlapping gray membrane, the amino acids with the TMD that extend above and below the membrane are the TMD loops, and the ICD is below the gray membrane. The two magenta C amino acids connected by a magenta bar represent the disulfide bond location for homodimer formation. Yellow background colored N amino acids represent potential N-linked glycosylation sites. Purple C amino acids represent the 9 cysteines in the cys-rich domain of the ECD. Amino acids are numbered every 10 amino acids.

Origami forms disulfide bonds indiscriminately since it has periplasmic DsbA (Disulfide bond isomerases family C) that leads to mis-oxidized and inactive proteins even though they present with correct molecular weight (MW) on gels.

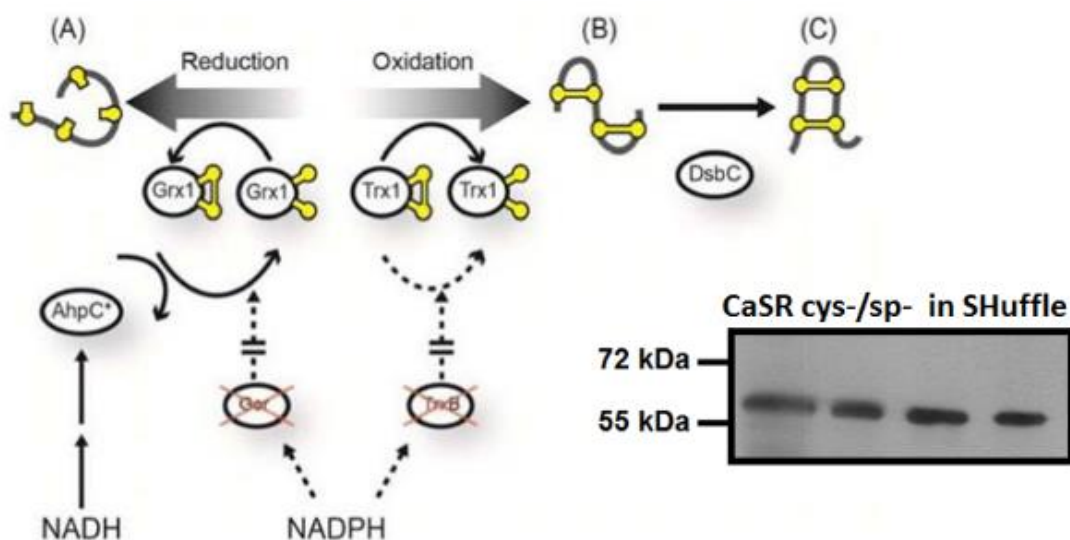


**Figure 3.4 – The difference of SHuffle compared to Rosetta-gami. The western blot performed with ADD CaSR antibody.**

While SHuffle has cytoplasmically over-expressed DsbC under the rRNA promoter *rrnB* which improves correct folding. Rosetta-Gami is an Origami derivative with enhanced expression of eukaryotic proteins containing specific codons.

### 3.2.2 Disease Related Mutations of CaSR

With the discovery of our CaSR crystal structure, we saw new avenues of mutational CaSR research to be investigated<sup>[287]</sup>. Namely, with the confirmation of the main  $\text{Ca}^{2+}/\text{Mg}^{2+}$  and agonist binding sites we could look into disease mutations on these binding regions in order to further understand how these mutations affect CaSR binding and binding cooperativity between the binding sites which could further lead us to therapeutic targets to address these loss and gain of function disorders of  $\text{Ca}^{2+}$  homeostasis. We investigated the three main cation/TNCA binding sites

(BS) as well as the bicarbonate/anion/pH BS for disruption or disease related mutations (Figure 3.5).

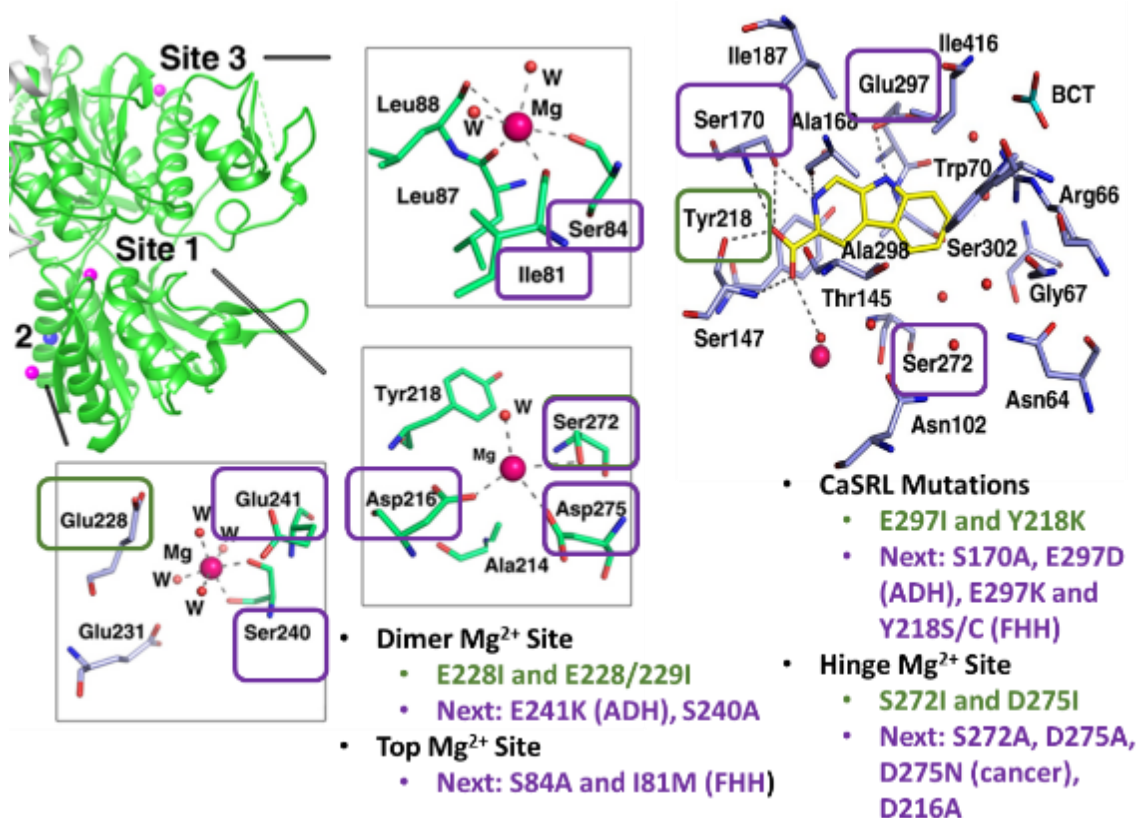


**Figure 3.5 – CaSR disease mutations for ECD.**

**Green are mutations already done previously. Purple are planned mutations and if they have disease relevance they are noted in parentheses.**

We made mutations for bCaSR so far of R66H (Anion/pH BS for FHH), D216N (Anion/pH BS for disrupt/cancer), E241K (Dimer BS for ADH), S272A (Hinge BS for disruption), E297K (Hinge BS for FHH/NSHPT), H254A (Anion/pH BS for disruption), E228Q and E228K (Dimer BS for ADH), these mutations were successfully made using the KOD DNA polymerase (Table 3.1).

**Table 3.1 – CaSR disease mutations.**

Binding Sites	Binding Residues	Disease Mutations (bCaSR-Hu/hCaSR/both)
New Site	I81, S84, L87, L88, L91	<i>FHH/NSHPT</i> : I81M <i>Disruption</i> : S84A
TNCA Site	S147, A168, S170, Y218, E297	<i>FHH/NSHPT</i> : Y218S, Y218C, E297K, L173P, P221Q <i>ADH</i> : E297D, L173F, P221L
Hinge Site	A214, D216, Y218, S272, D275	<i>Disruption</i> : S272A <i>Cancer</i> : D275N
Anion Site	R66, R69, W70, R415, I416, S417	<i>FHH/NSHPT</i> : R66C, R66H <i>Disruption</i> : R69L
Dimer Site	E228, E229, E231, E232, S240, E241	<i>ADH</i> : E228Q, E228K, E241K <i>Disruption</i> : E224I
pH/pKa Effects	N/A	<i>Disrupt pH/pKa</i> : R69L, D215I, D216N, H254A, S296A <i>Cancer</i> : D216N, S296A

Planned mutations in black, bCaSR in red, hCaSR in blue, and both in green.

### 3.2.3 Expression and Purification of bCaSR

After the successful PCR point mutations were made we did a small scale expression of 25 mL and a large scale expression of 600 mL to see if the bCaSR WT and variants were having protein expression in the SHuffle cells (Figure 3.6). We saw that bCaSR WT, D216N, E241K, H254A, S272A, and E297K had expression after IPTG treatment on small scale but that R66H, E228K, and E228Q did not have CaSR expression and that trend remained upon large scale expression (Figure 3.6).

We then purified the large scale expression of bCaSR WT and the eight mutants and showed that bCaSR WT was able to be purified using a His-tag column on FPLC (Figure 3.7A). The purification for bCaSR ECD WT eluted with one single large peak between 20-60% imidazole and was desalted using a size exclusion column (Figure 3.7A). We then attempted mutation purification for the bCaSR mutations and found that R66H, E228K, and E228Q had no protein present after purification based on the UV below 100, the lack of protein bands on the western blot and no detectable protein concentration (Figure 3.7-Figure 3.8).



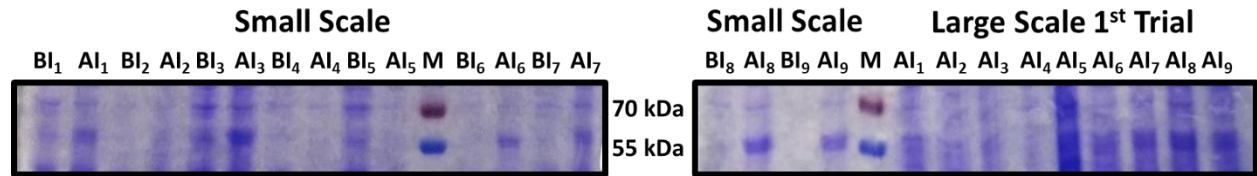


**Figure 3.6 – Coomassie blue SDS-PAGE gel of bCaSR WT and mutants expression.** A 25 mL small scale was done followed by a 600 mL large scale of bCaSR WT (1), and mutations R66H (2), D216N (3), E228K (4), E228Q (5), E241K (6), H254A (7), S272A (8), and E297K (9). BI is before induction with IPTG, AI is 16 hours after induction with IPTG, and M is the marker.

The other mutants which were able to express were also purified from the large-scale expression and all had protein purified using FPLC as well as detectable protein concentration after concentrating the purified protein.

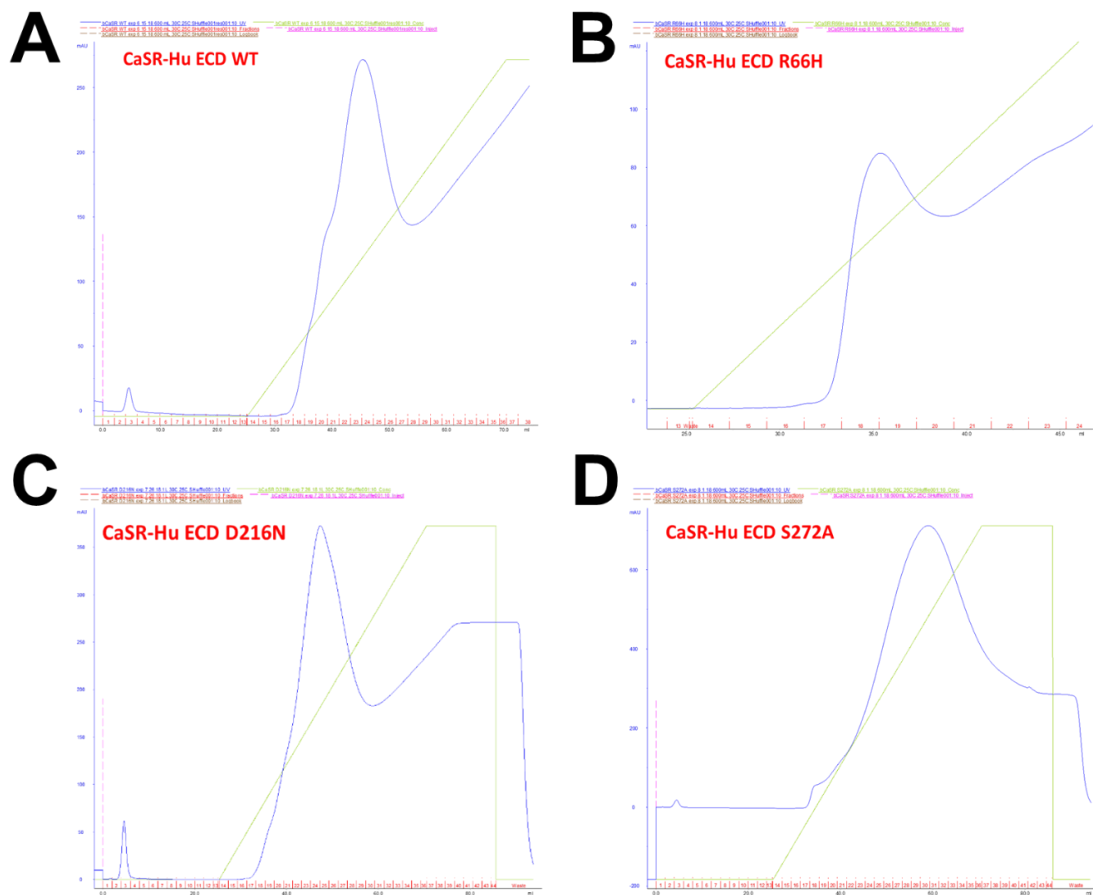


**Figure 3.7 – bCaSR WT and representative mutant purification from SHuffle cells.** His-tag FPLC purification of bCaSR WT (A), R66H (B), D216N (C) and S272A (D) from SHuffle bacterial cells.

D216N and the WT bCaSR both showed great expression and purification with good single peak elution at imidazole of 20-60% and bands at 65 kDa on coomassie blue and western blot SDS page gels (Figure 3.7-Figure 3.8). The mutant D216N does show some lower bands below the 65 kDa band whereas the WT bCaSR does not, these bands could be degradation of the D216N protein or fragmented parts of the protein (Figure 3.8).

This could also imply that this mutation is detrimental to the structure and stability of the bCaSR ECD. The elution peak for S272A is shifted to the right and seems to be a wider peak which begins eluting out around 40% imidazole gradient and completes at approximately 85% imidazole gradient whereas the WT and D216N bCaSR elution's presented around 20-60% imidazole gradient (Figure 3.7).

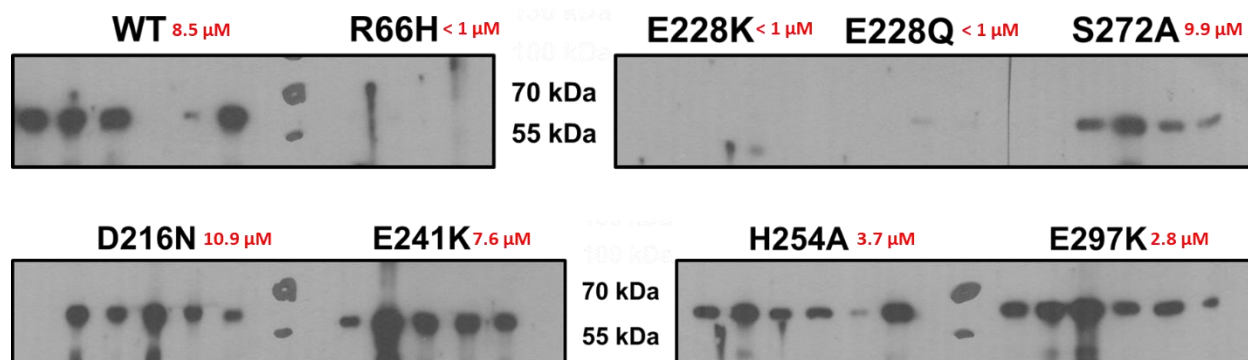


**Figure 3.8 – Western blot gel ADD antibody for bCaSR WT and mutants purification. Western blot results for histag and desalting peaks for bCaSR WT, R66H, E228K, E228Q, S272A, D216N, E241K, H254A, and E297K mutants. R66H, E228K, and E228Q had little to no protein present while H254A and E297K had not enough protein present.**

This change in elution time could indicate a structural change of the protein which allows for the polyhistidine chain of bCaSR S272A to bind more tightly or efficiently to the column thus needing more imidazole to remove from the column. Similarly, to the D216N bCaSR mutant, we see the S272A protein at 65 kDa but also see lower bands not present with the WT bCaSR gels implicating



some degradation or fragmented protein contaminants (Figure 3.8). While S272A and D216N had suitable concentrations at 9.9 and 10.9  $\mu\text{M}$ , respectively, which is more than the WT at 8.5  $\mu\text{M}$  the other mutants had lower concentration of 7.6  $\mu\text{M}$  for E241K, 3.7  $\mu\text{M}$  for H254A, and 2.8  $\mu\text{M}$  for E297K which shows these mutations lowered protein expression and overall yield (Figure 3.7- Figure 3.8). We thus performed biophysical studies with WT bCaSR, S272A, and D216N since they had the highest protein concentrations enabling triplicate studies for multiple binding experiments.

### ***3.2.4 Biophysical Studies of CaSR***

Expressing protein in a bacterial or mammalian system can allow for further binding studies using fluorescence spectroscopy, circular dichroism, NMR, SPR, etc. These instruments can be vital in not only further confirming cellular experiments but elucidating additional information about structural changes and drug affinities. We examined CaSR ECD binding, binding cooperativity, and structure utilizing ANS hydrophobicity binding, Trp fluorescence spectroscopy, Tb<sup>3+</sup>/Trp FRET with Tb<sup>3+</sup> titration and Ca<sup>2+</sup> competition, as well as circular dichroism (CD). Further potential drug targets can also be titrated to examine if the binding K<sub>d</sub>, cooperativity, and/or structure is altered.

### ***3.2.5 Circular dichroism***

Circular dichroism (CD) is an excellent technique for analyzing the secondary structure of a protein. It can show if the protein is predominately  $\alpha$ -helices,  $\beta$ -sheets, loops, turns, or a combination between them. In the case of the CaSR ECD, it is mostly  $\alpha$ -helices thus we expect to see the typical  $\alpha$ -helix spectrum of a slight W. The WT bCaSR ECD has the expected  $\alpha$ -helices

shape where the black line is with no calcium addition. As the calcium concentration increases, the shape is changed with more calcium indicating a change in the conformation of the protein with the binding of calcium (Figure 3.9). The older defrosted bCaSR ECD sample is less stable than the fresh purified bCaSR ECD sample and has a loss of structure upon calcium titration (Figure 3.9). It is also possible that the observed conformational change is originally from the dimerization or aggregation of CaSR ECD.

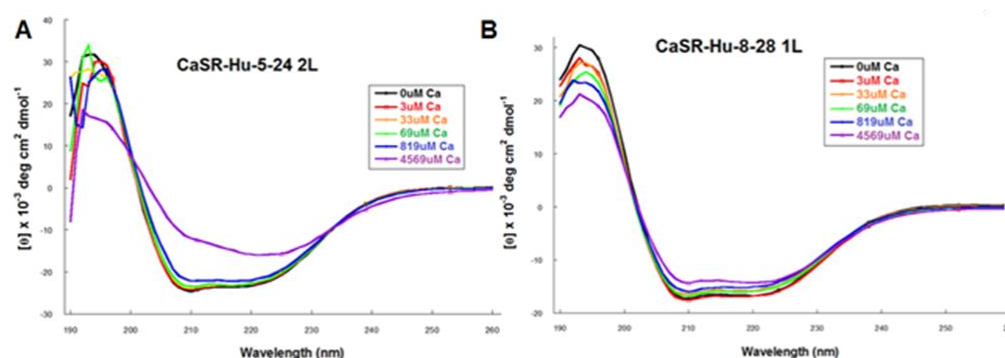


**Figure 3.9 – Circular dichroism  $\text{Ca}^{2+}$  titration on bCaSR ECD WT.**  
**A&B – 2  $\mu\text{M}$  bCaSR ECD WT expressed in SHuffle in 5/25/14 and 8/28/14, respectively, but both run on 8/28/14 and titrated with increasing  $[\text{Ca}^{2+}]$  in 10 mM Tris-HCl, pH 7.4.**

### 3.2.6 Trp fluorescence spectroscopy

Calcium titration using fluorescence spectroscopy is an excellent way to analyze conformational change and binding by titration. Trp fluorescence spectroscopy does not show the secondary structure shape but rather fluorescence peak shifts. Trp fluorescence looks at the fluorescence excitation and emission from Trp residues in the sample. Our sample is CaSR ECD protein with Trp inside we see a fluorescence peak correlating to bCaSR ECD Trp fluorescence. Thus, upon titration of  $\text{Ca}^{2+}$  or other compounds we should see a change in the fluorescence if the Trp in the protein get either closer together or further apart leading to a fluorescence intensity change which indicates the titrant bound to the protein which induced a conformational change on the protein

near Trp locations. We can see that bCaSR ECD has Trp spread throughout the structure with several near the binding sites for the CaSR ECD (Figure 3.10).

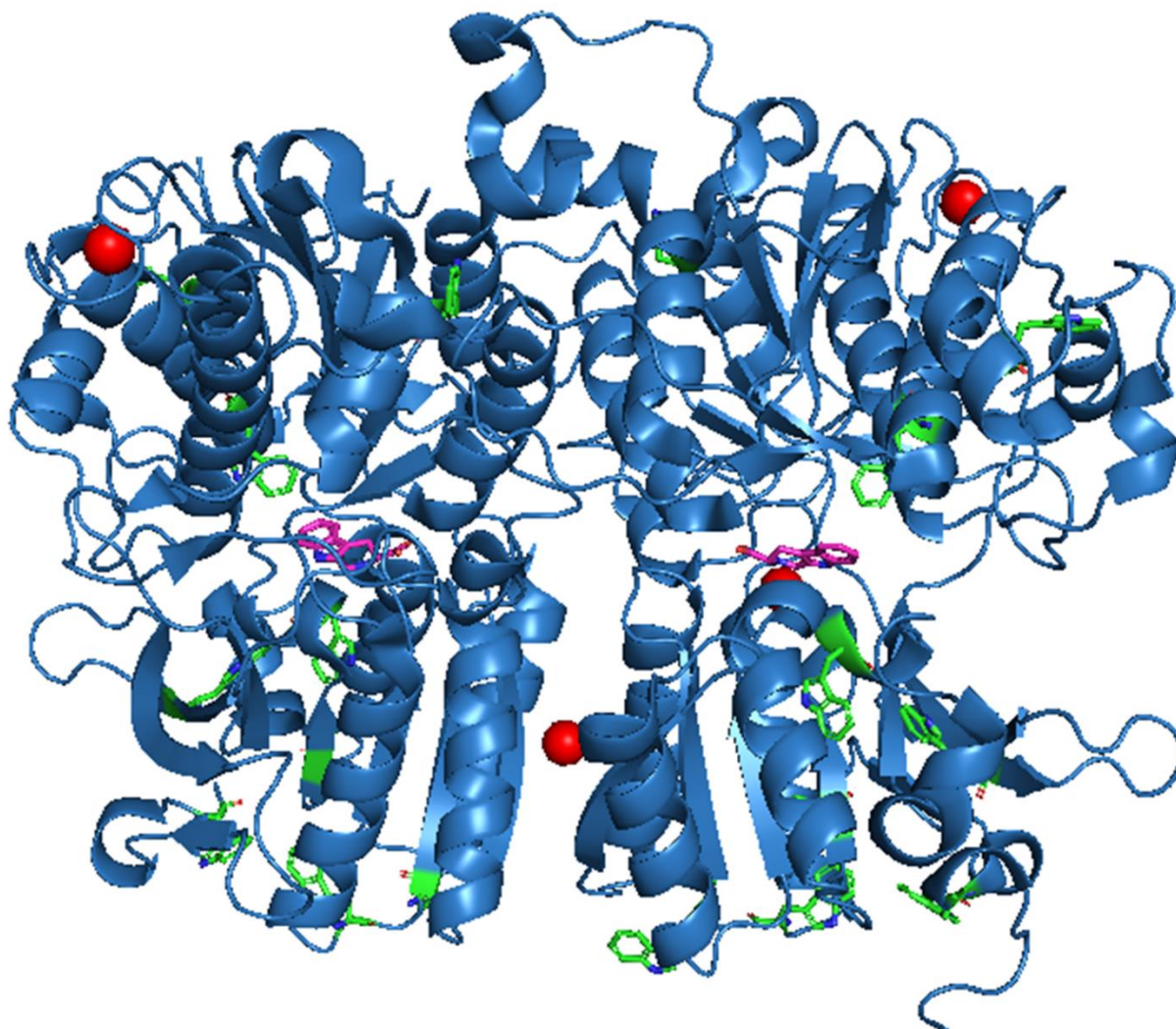


**Figure 3.10 – Trp residues in CaSR ECD.**  
Structure of CaSR ECD showing all Trp residues highlighted in green sticks, with Ca<sup>2+</sup> in red spheres, and TNCA in pink sticks.

We used our purified 2  $\mu\text{M}$  bCaSR ECD WT to do Ca<sup>2+</sup> titration Trp fluorescence spectroscopy in triplicate and saw a decrease in fluorescence signal upon Ca<sup>2+</sup> titration (Figure 3.11A). The  $K_d$  for Ca<sup>2+</sup> was  $5.3 \pm 0.2$  mM with a Hill number of  $1.6 \pm 0.1$ , implying there is cooperative binding of Ca<sup>2+</sup> to CaSR ECD (Figure 3.11D).

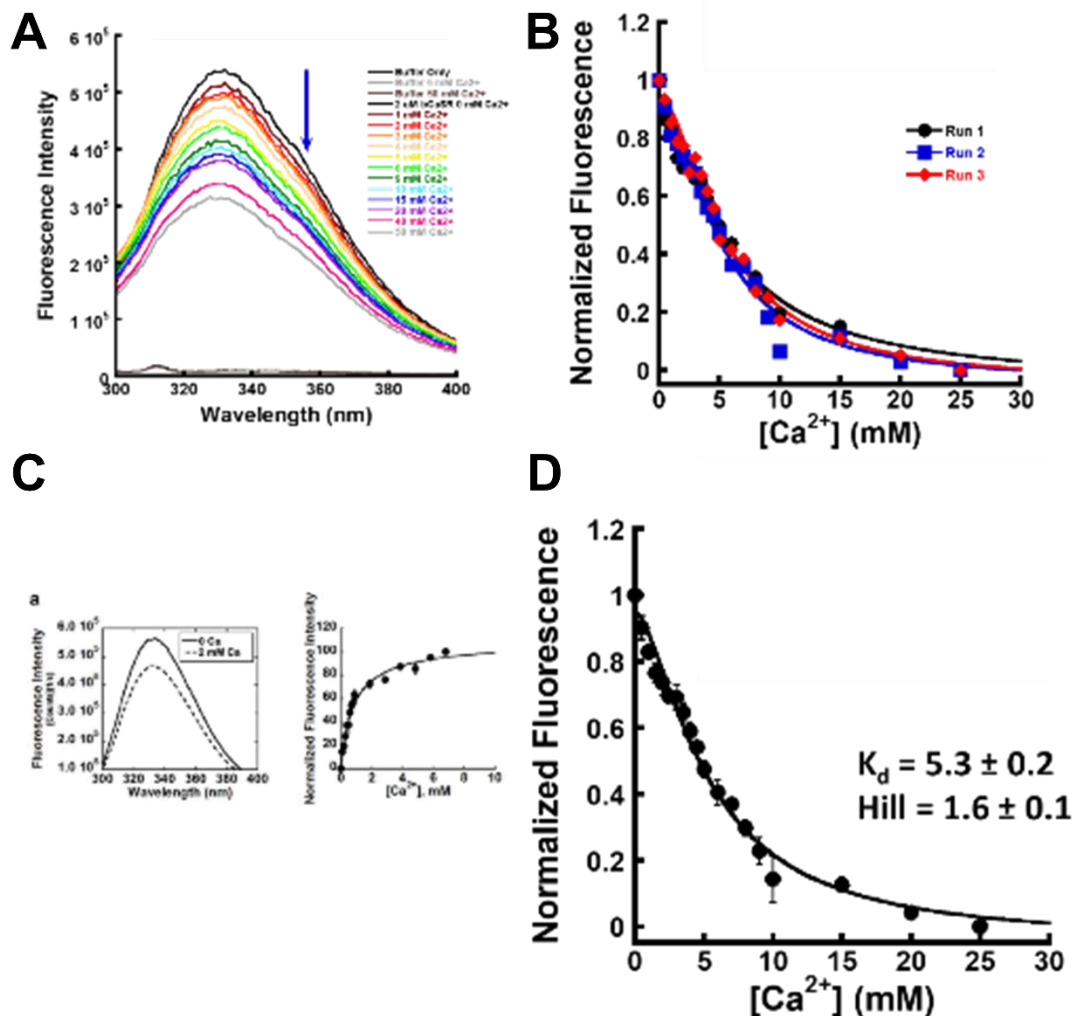


**Figure 3.11 – Trp fluorescence Ca<sup>2+</sup> titration on 2 μM bCaSR ECD WT.**  
 This experiment was done in 10 mM Tris-HCl with a pH of 7.4 and 2 μM of bCaSR in triplicate. **A** – Representative plot of Ca<sup>2+</sup> titration, buffer alone is shown near the bottom. **B** – K<sub>d</sub> of each run. **C** – Previous member’s data for comparison, which also goes down but normalized to be up. **D** – K<sub>d</sub> plot for the triplicate trials plotted.

We next examined the effect of anion binding by titrating in PO<sub>4</sub>. We wanted to investigate the effect of PO<sub>4</sub> on bCaSR since the Geng et al. paper showed a PO<sub>4</sub> binding site similar to our bicarbonate binding site<sup>[284, 287]</sup>. Since PO<sub>4</sub> is not stable at neutral pH and the binding must be done around pH 7.4 for CaSR stability, we used the stable analog K<sub>2</sub>HPO<sub>4</sub>. We saw a decrease in signal in Trp fluorescence with bCaSR in response to Ca<sup>2+</sup> titration with a K<sub>d</sub> of  $4.8 \pm 0.1$  mM and a Hill number  $1.3 \pm 0.04$ . When bCaSR ECD WT is titrated with K<sub>2</sub>HPO<sub>4</sub> there is a decrease in

Trp fluorescence in response with a  $K_d$  of  $10.6 \pm 0.4$  mM and a Hill number of  $0.9 \pm 0.04$  (Figure 3.12).

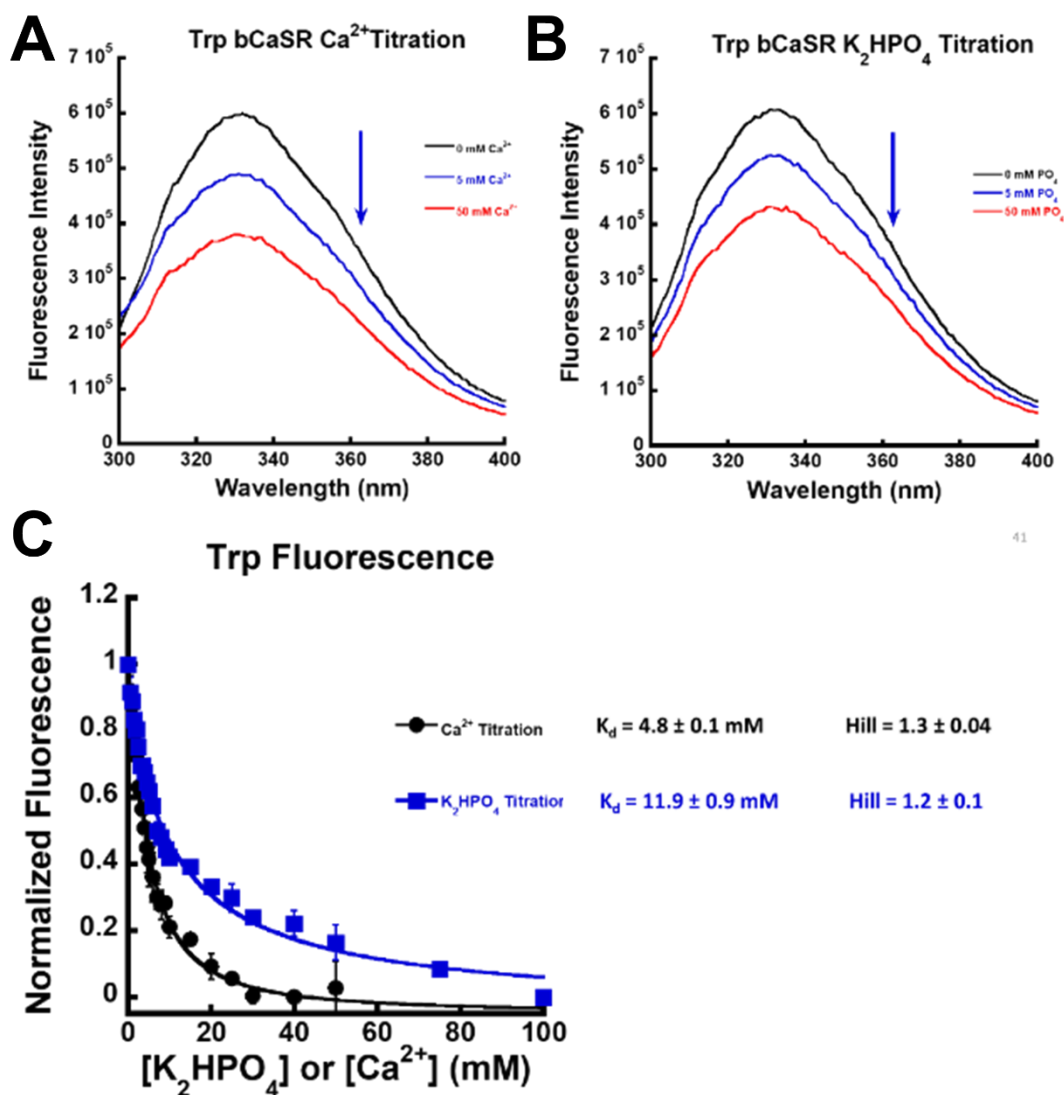


**Figure 3.12 – Trp fluorescence  $\text{Ca}^{2+}$  and  $\text{PO}_4$  titration on  $2 \mu\text{M}$  bCaSR ECD WT. This experiment was done in 10 mM Tris-HCl with a pH of 7.4 and  $2 \mu\text{M}$  of bCaSR in triplicate. Top –  $\text{Ca}^{2+}$  and  $\text{PO}_4$  titration representative plots. Bottom –  $K_a$  plot for the trials the  $K_d$  values. Red is KCl  $K_d$  value.**

Since TNCA and Trp have overlapping excitation and emission profiles, being that TNCA is a Trp derivative, the titration of TNCA under Trp fluorescence spectroscopy cannot be performed since TNCA will give an increase in fluorescence and therefore a false-positive result.

We investigated the effect of disease and disruption related mutations of D216N and S272A would have upon  $\text{Ca}^{2+}$  titration using Trp fluorescence spectroscopy (Figure 3.13).

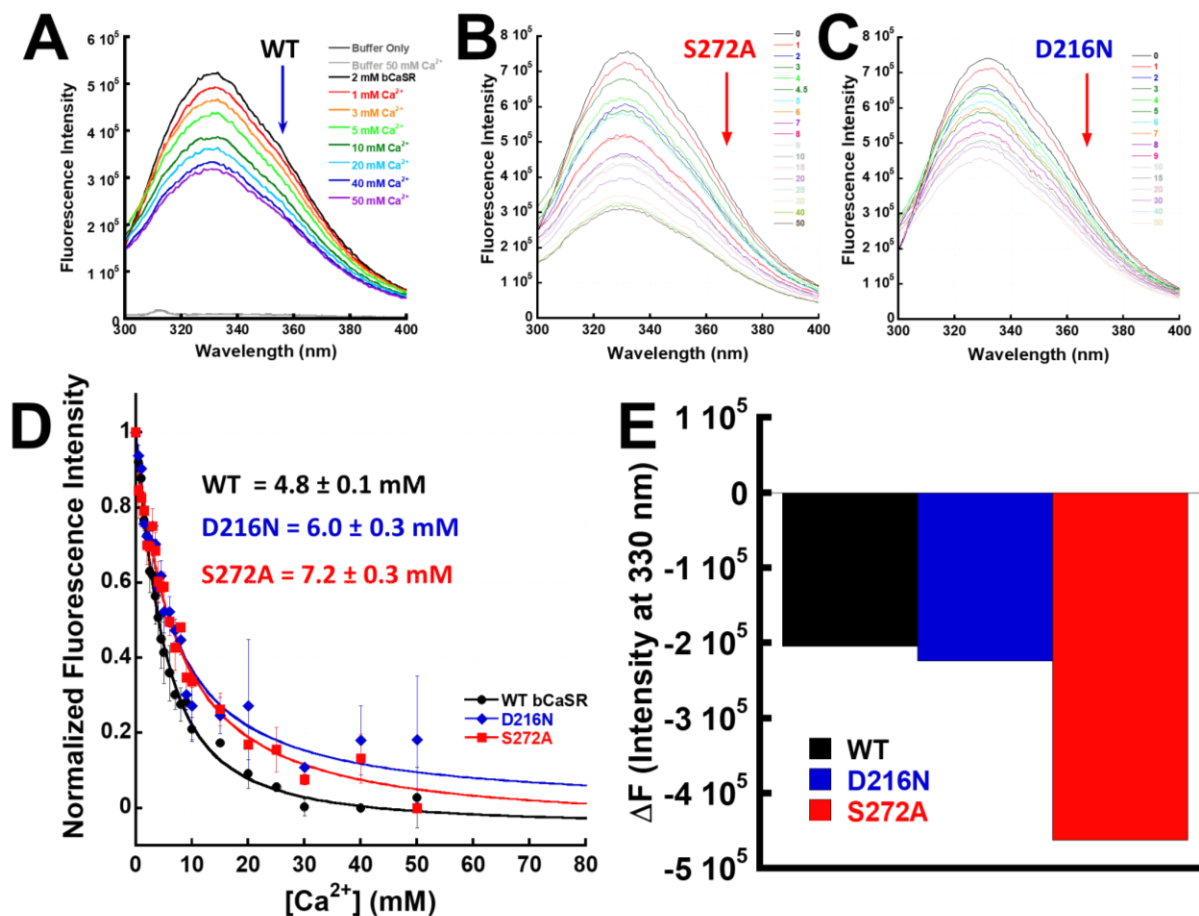


**Figure 3.13 – Trp fluorescence  $\text{Ca}^{2+}$  titration on bCaSR WT, S272A, and D216N.** This experiment was done in 10 mM Tris-HCl with a pH of 7.4 and 2  $\mu\text{M}$  of bCaSR in triplicate. A-C – WT (A), S272A (B), and D216N (C) bCaSR representative raw data titration. D – WT, S272A, and D216N normalized plot for  $K_d$  for triplicate runs with error bars and insert of  $K_d$  values are shown for each. E – Bar graph depicting the average  $\Delta F$  from 0 mM  $\text{Ca}^{2+}$  to 50 mM  $\text{Ca}^{2+}$  titrated for WT (black), D216N (blue) and S272A (red).

Both of these mutations are located in the hinge pocket where  $\text{Mg}^{2+}/\text{TNCA}/\text{Ca}^{2+}$  bind since this is a critical pocket for CaSR function we expect a substantial disruption in the signal change. In fact, when doing mutations in cells, the hinge site mutations such as Y218K and E297I led to a loss of cellular functional activity of hCaSR while the cell surface expression was maintained<sup>[287]</sup>. While

doing the  $\text{Ca}^{2+}$  titration on the bCaSR D216N mutation the 2  $\mu\text{M}$  of protein in solution was stable but after 10 mM of  $\text{Ca}^{2+}$  the protein began to precipitate leading to jumping around of the signal and high error bars (Figure 3.13D). Although we did have precipitation issues, the protein did at least still decrease in response to  $\text{Ca}^{2+}$  (Figure 3.13C-E). We saw that the S272A mutation also decreased in response to  $\text{Ca}^{2+}$  titration (Figure 3.13B). Both of these mutations did lead to a decrease in the  $K_d$  compared to the WT, where the WT was  $4.8 \pm 0.1$  mM  $\text{Ca}^{2+}$  while the mutants were higher with S272A having  $7.2 \pm 0.3$  mM  $\text{Ca}^{2+}$  and D216N having  $6.0 \pm 0.3$  mM  $\text{Ca}^{2+}$ . We also wanted to examine the mutations to  $\text{Tb}^{3+}$  titration using  $\text{Tb}^{3+}/\text{Trp}$  FRET compared to the bCaSR WT and began with the S272A mutant since it was more stable in solution than D216N and did not precipitate at low calcium concentrations in titration or aggressively (Figure 3.21).

### ***3.2.7 ANS binding fluorescence spectroscopy***

8-anilino-1-naphthalenesulfonic acid (ANS) is a commonly used fluorescent probe for the characterization of protein binding sites. A blue shift and an increase of fluorescence intensity are generally attributed to the hydrophobicity of a binding site and the restricted mobility of ANS.

The main differences from mCaSR and bCaSR is that mCaSR would have glycosylation and would have retained the signal peptide region as well as the 4 Cys residues allowing mCaSR to be fully dimer and not monomer/dimer mixture as with bCaSR. When we performed ANS binding using 2  $\mu\text{M}$  of mCaSR, though, we were surprised to see that the  $\text{Ca}^{2+}$  had little effect on mCaSR conformational changes even up to 30 mM  $\text{Ca}^{2+}$  (Figure 3.14).



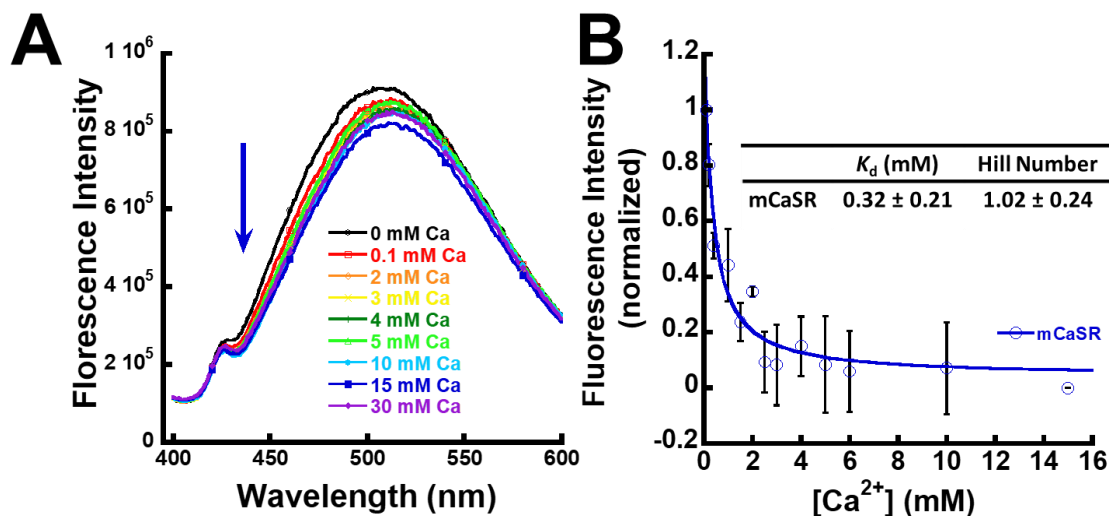


**Figure 3.14 – ANS binding Ca<sup>2+</sup> titration of mCaSR ECD WT.**

**A – Representative plot of the titration of Ca<sup>2+</sup> with 2  $\mu$ M mCaSR up to 30 mM B – Plot showing the triplicate data of mCaSR titration where little to no change is observed even up to 30 mM with fully bound already at 2-3 mM Ca<sup>2+</sup>.**

The mCaSR had very little change in response to Ca<sup>2+</sup> titration and seemed to be immediately bound to Ca<sup>2+</sup> much tighter than bCaSR and without any cooperativity, as indicated by the Hill number at  $1.02 \pm 0.24$  (Figure 3.10).

Upon bCaSR ECD WT titration of Ca<sup>2+</sup> we saw that the ANS fluorescence signal decreased (Figure 3.15). The  $K_d$  for Ca<sup>2+</sup> titration using ANS fluorescence spectroscopy was  $5.8 \pm 0.25$  mM, with a Hill number of  $2.2 \pm 0.22$  (Figure 3.15). Since we were examining the ANS fluorescence signal during titration onto bCaSR ECD, we did not have an overlap of TNCA signal and were able to do TNCA titration onto bCaSR ECD using ANS fluorescence spectroscopy. To confirm that the TNCA excitation at 370 nm for ANS would not affect the signal response of ANS we examined the emission of 0.5 mM of TNCA over 400-600 nm and found there was emission in response to TNCA with the emission peak at 450 nm whereas bCaSR WT ANS binding Ca<sup>2+</sup> titration has the peak at 470 nm (Figure 3.16A). Since TNCA can activate CaSR in cells at lower concentrations than 0.5 mM we also titrated TNCA into the buffer without ANS or bCaSR present



to see at what concentration did TNCA have emission response to 370 nm excitation and observed that the 450 nm peak began to resolve after 50  $\mu\text{M}$  of TNCA was added in, thus the TNCA titration on bCaSR ECD for ANS fluorescence spectroscopy would need to be below 50  $\mu\text{M}$  TNCA (Figure 3.16B).

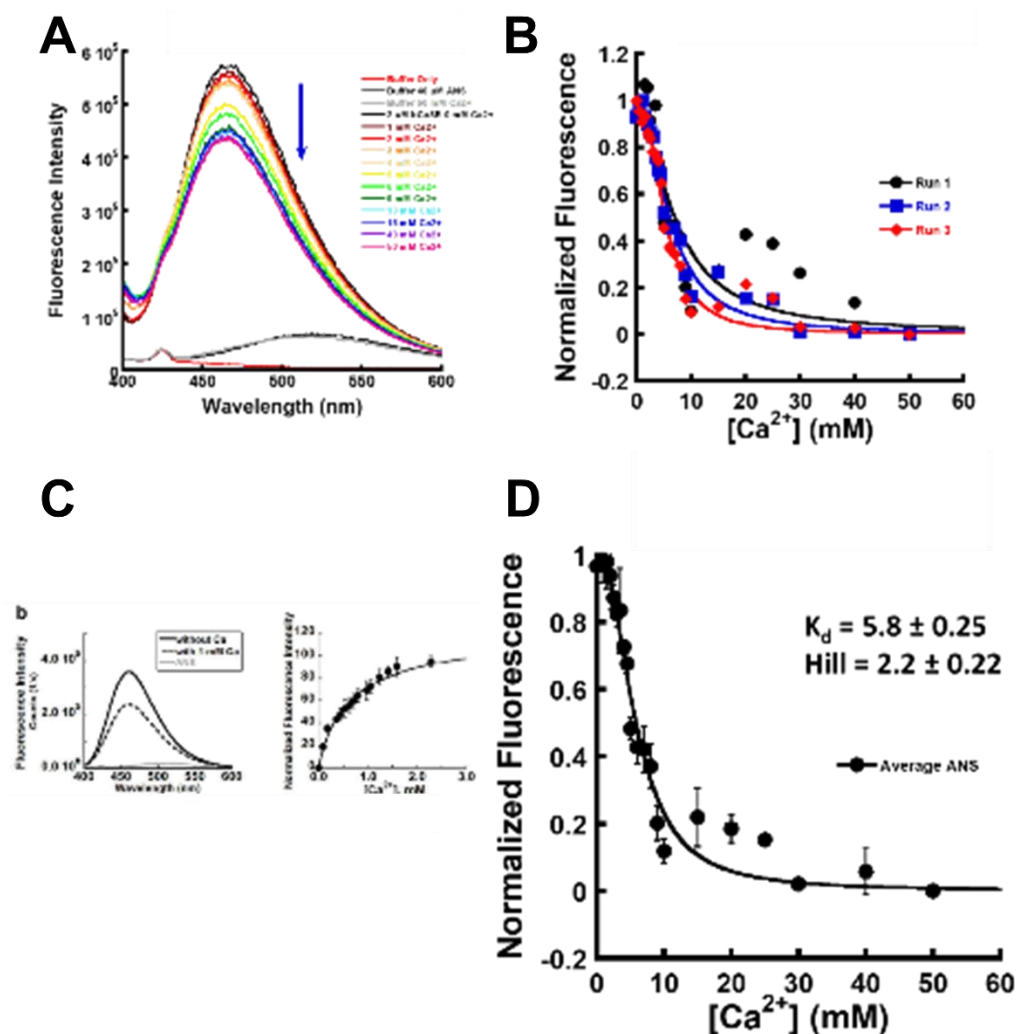


**Figure 3.15 – ANS binding  $\text{Ca}^{2+}$  titration on 2  $\mu\text{M}$  bCaSR ECD WT.**

This experiment was done with 40  $\mu\text{M}$  of ANS in 20 mM Tris-HCl and 50 mM KCl with a pH of 7.4 and 2  $\mu\text{M}$  of bCaSR in triplicate. Protein and ANS were allowed to incubate in the dark at 4°C for 1 hour prior to  $\text{Ca}^{2+}$  titration. A – Representative plot of  $\text{Ca}^{2+}$  titration, ANS alone in gray near the bottom. B – The plot of the peak for  $K_d$  of each run. C – Previous member's data for comparison of decrease. D –  $K_d$  plot for the triplicate trials.

Thus, any  $K_d$  plots from TNCA titration ANS binding can only go to 40  $\mu\text{M}$  TNCA so we examined TNCA binding upon bCaSR ECD with ANS fluorescence spectroscopy in comparison to  $\text{Ca}^{2+}$  titration upon bCaSR ECD (Figure 3.16C-F and Figure 3.15).

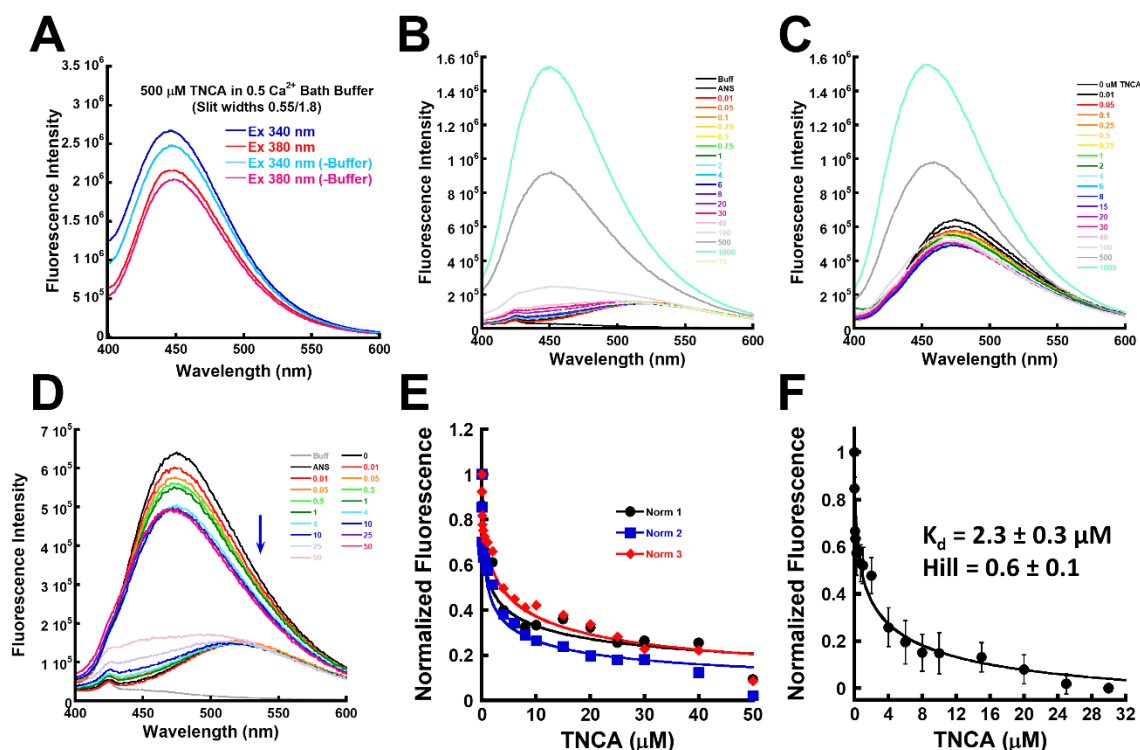


**Figure 3.16 – ANS binding TNCA titration on 2  $\mu\text{M}$  bCaSR ECD WT.**

This experiment was done with 40  $\mu\text{M}$  of ANS in 20 mM Tris-HCl and 50 mM KCl with a pH of 7.4 and 2  $\mu\text{M}$  of bCaSR in triplicate. Protein and ANS were allowed to incubate in the dark at 4°C for 1 hour prior to TNCA titration. A – TNCA excitation alone. B – TNCA titration without protein. C – TNCA titration with bCaSR up to 1 mM TNCA. D – Representative TNCA titration on bCaSR ECD up to 50  $\mu\text{M}$  with ANS titrated with TNCA without bCaSR at the bottom. E – The plot of the peak for  $K_d$  of each run. F –  $K_d$  plot for the triplicate trials.

We observed that the TNCA titration also decreased the ANS binding similar to  $\text{Ca}^{2+}$ , but the  $K_d$  was much lower for TNCA versus  $\text{Ca}^{2+}$  alone, with  $\text{Ca}^{2+}$  average of 6 trials being  $4.4 \pm 0.2$  mM and TNCA for 3 trials being  $2.3 \pm 0.3$   $\mu\text{M}$ . Additionally, the Hill numbers for  $\text{Ca}^{2+}$  and TNCA were different with  $\text{Ca}^{2+}$  Hill number at  $1.9 \pm 0.2$  showing cooperative binding and potentially multiple binding sites while TNCA Hill number was  $0.6 \pm 0.1$  which shows TNCA does not have

cooperative binding with TNCA for bCaSR WT and potentially only a single binding site as confirmed by the CaSR determined structure. This binding experiment shows that TNCA does cause a hydrophobic conformational change on bCaSR WT (Figure 3.16).

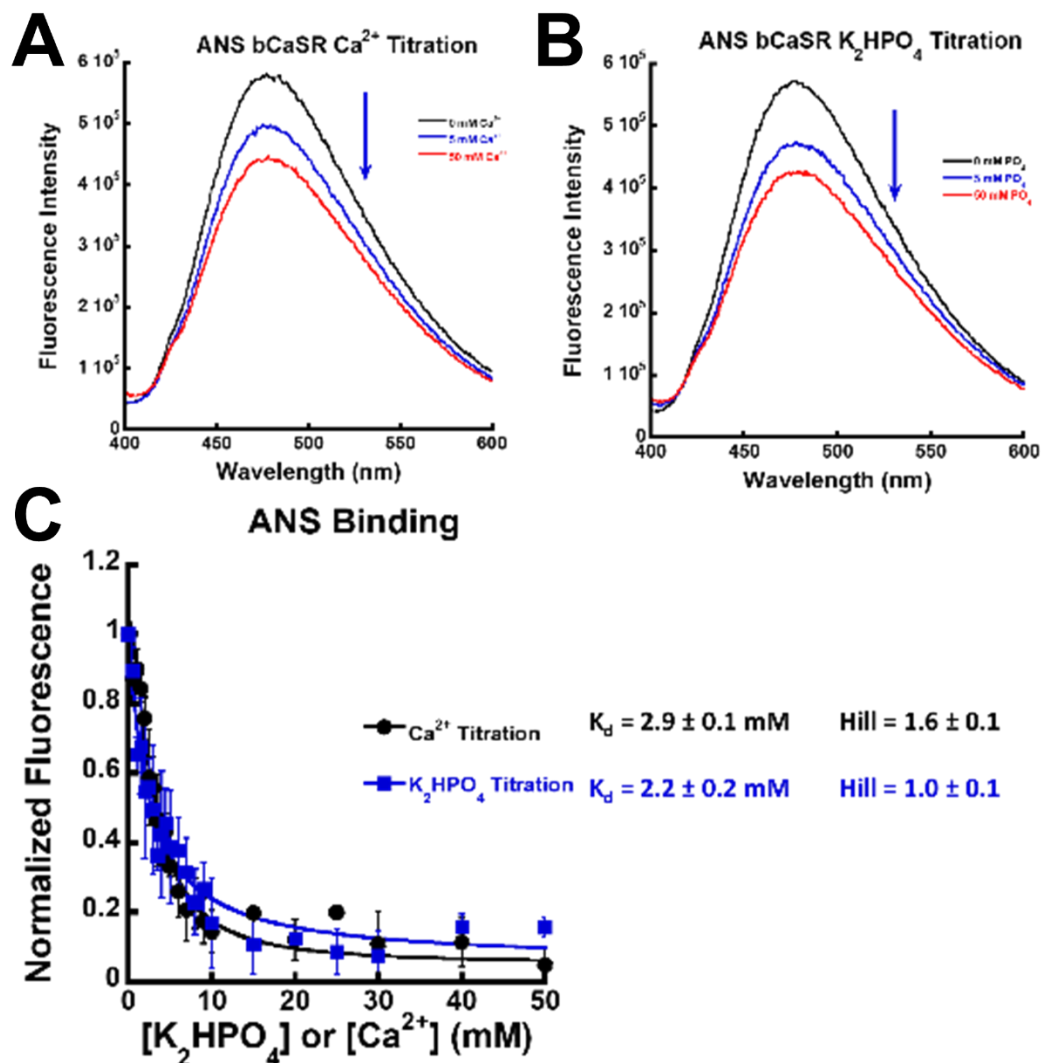


**Figure 3.17 – ANS binding  $\text{PO}_4$  and  $\text{Ca}^{2+}$  titration on  $2 \mu\text{M}$  bCaSR ECD WT.** This experiment was done with  $40 \mu\text{M}$  of ANS in  $20 \text{ mM}$  Tris-HCl and  $50 \text{ mM}$  KCl with a pH of 7.4 and  $2 \mu\text{M}$  of bCaSR in triplicate. Protein and ANS were allowed to incubate in the dark at  $4^\circ\text{C}$  for 1 hour prior to titration. Top –  $\text{Ca}^{2+}$  and  $\text{PO}_4$  titration representative plots. Bottom –  $K_d$  plot for the trials the  $K_d$  values.

We further investigated the  $\text{PO}_4$  effect on bCaSR utilizing ANS fluorescence spectroscopy to correlate the responses we observed with Trp fluorescence (Figure 3.12 and Figure 3.17).  $\text{Ca}^{2+}$

and  $\text{PO}_4$  were able to induce a conformational change on bCaSR with similar binding  $K_d$  values with  $\text{Ca}^{2+}$  being 2.9 mM and  $\text{PO}_4$  being 2.2 mM (Figure 3.17). Thus, the  $\text{PO}_4$  binding at 2.2 mM is stronger than  $\text{Ca}^{2+}$  but with drastically different Hill numbers. The  $\text{PO}_4$  Hill number was  $1.0 \pm 0.1$  which implies non-cooperative binding and a single  $\text{PO}_4$  binding site for bCaSR WT which is correlated by the single bicarbonate binding site found in the CaSR crystal structure (Figure 3.17). While Trp fluorescence and ANS binding fluorescence spectroscopy both give a multitude of bCaSR binding information they are both more indirect binding assays since we are not examining the fluorescence of the titrator but are instead looking at the change of the protein structure for Trp fluorescence or the exposure of hydrophobic regions of the protein for ANS binding. We, therefore, decided to also look at the  $\text{Tb}^{3+}$ /Trp Förster/fluorescence resonance energy transfer (FRET) and further competition with  $\text{Ca}^{2+}$  to examine more direct fluorescence changes of  $\text{Tb}^{3+}$  binding and release.

### ***3.2.8 Terbium/Trp FRET and $\text{Ca}^{2+}$ competition***

Terbium(III) itself is fluorescent with a yellow color resulting from a green emission line.  $\text{Tb}^{3+}$  has been used as a fluorescent probe for calcium binding sites in proteins since they are both positively charged cations with similar molecular radiuses, where  $\text{Ca}^{2+}$  is 187 pm and  $\text{Tb}^{3+}$  is 200 pm.  $\text{Tb}^{3+}$  behaves similarly to but is more potent (50-fold) than  $\text{Ca}^{2+}$  which combined with its +3 charge makes it better for studying metal binding properties of proteins with weak  $K_d$  values since the  $\text{Tb}^{3+}$  will bind tighter than  $\text{Ca}^{2+}$  in the same binding pockets. Terbium titration using fluorescence spectroscopy is a good way to analyze conformational changes and binding affinity on top of binding cooperativity when using the Hill number from the Hill equation.

Additionally, using  $Tb^{3+}$ /Trp FRET leads to a more accurate signal since the  $Tb^{3+}$  or Trp signals themselves cannot give a peak at emission spectra at 500-600 nm when excited at 282 nm and only has a large fluorescence change over 500-600 nm when FRET between  $Tb^{3+}$  and Trp occurs, implying that  $Tb^{3+}$  is bound to the interested protein with a Trp near enough to the binding pocket for FRET (Figure 3.18).

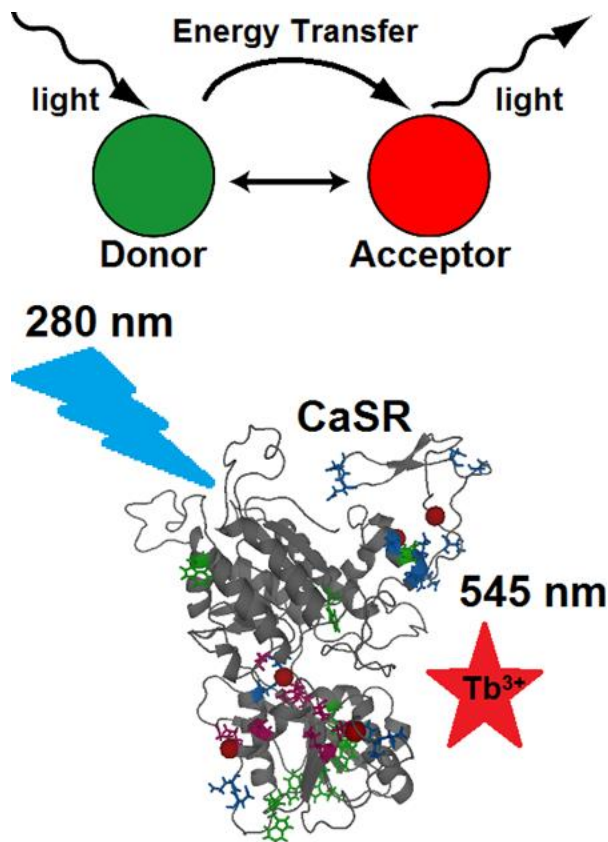


**Figure 3.18 –  $Tb^{3+}$ /Trp FRET diagram for CaSR.**

**Terbium titration into bCaSR after excitation at 282 nm for Trp excitation leads to energy exchange between  $Tb^{3+}$  and Trp to have an emission peak at 545 nm. Trp alone does not emit at 545 nm and  $Tb^{3+}$  alone has low fluorescence at 545 nm without FRET signal.**

The  $Tb^{3+}$  FRET was done on bCaSR ECD WT, which led to an increase in signal and an interesting trend of the beginning part of the titration being linear before becoming sigmoidal (Figure 3.19). This biphasic response has been seen previously<sup>[269]</sup> and could indicate multiple binding sites are

present but not as readily seen for the weaker binding of  $\text{Ca}^{2+}$ . The strong initial binding for  $\text{Tb}^{3+}$  was  $6.1 \pm 0.4 \mu\text{M}$  with slight binding cooperativity indicated by the Hill value of  $1.5 \pm 0.2$ . The  $\text{Tb}^{3+}$   $K_d$  was found to be  $50.7 \pm 0.6 \mu\text{M}$  for the weaker secondary sigmoidal binding, so the  $\text{Ca}^{2+}$  competition of  $\text{Tb}^{3+}$  was done at  $40 \mu\text{M}$  just below the  $K_d$ . The Hill number for the second binding curve was much higher at  $7.4 \pm 0.6$ .

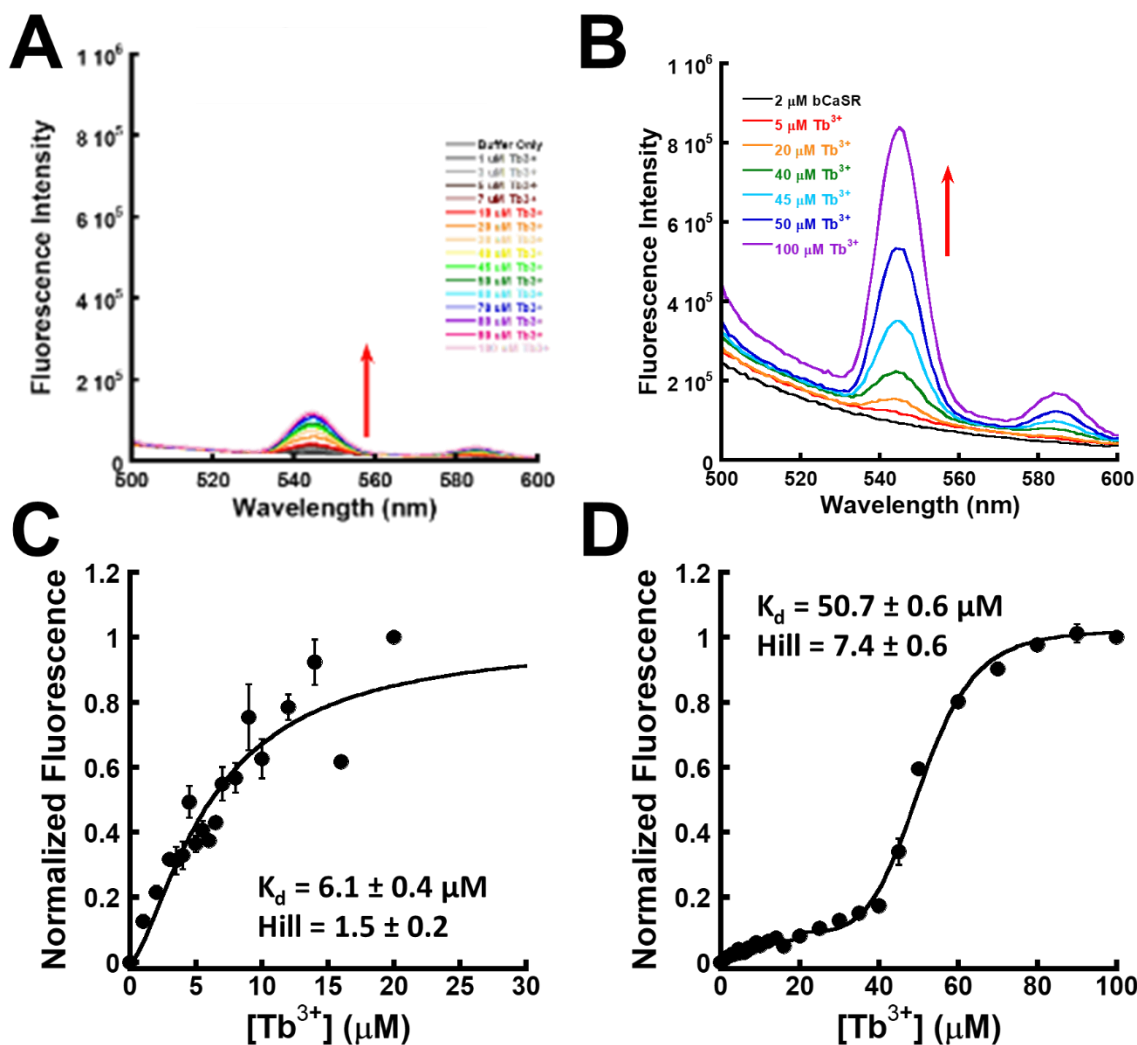


**Figure 3.19 –  $\text{Tb}^{3+}$ /Trp FRET with  $\text{Tb}^{3+}$  titration on 2  $\mu\text{M}$  bCaSR ECD WT.** This experiment was done in 20 mM PIPES and 10 mM KCl with a pH of 6.8 and 2  $\mu\text{M}$  of bCaSR in triplicate. **A** – Buffer with  $\text{Tb}^{3+}$  titrated. **B** – Representative plot of  $\text{Tb}^{3+}$  titration with background subtracted. **C** –  $K_d$  plot for the triplicate trials with strong binding up to 20  $\mu\text{M}$   $\text{Tb}^{3+}$ . **D** –  $K_d$  plot for the triplicate trials with a weaker second binding curve and the strong binding curve from C.

In order to investigate whether  $\text{Ca}^{2+}$ , the main binding partner for CaSR, was able to displace  $\text{Tb}^{3+}$  for CaSR binding we titrated  $\text{Ca}^{2+}$  onto bCaSR ECD WT which was pre-treated with  $40 \mu\text{M}$  of  $\text{Tb}^{3+}$ .  $\text{Ca}^{2+}$  was able to successfully compete out the  $\text{Tb}^{3+}$  at a  $K_d$  of  $6.1 \pm 0.2 \text{ mM}$ , which is slightly higher than the  $K_d$  of  $\text{Ca}^{2+}$  alone, as expected for a competition assay since the  $\text{Ca}^{2+}$  needs to first overcome the bound substituent before binding itself thus skewing the  $K_d$  value (Figure 3.20). These results again parallel previous lab member's results (Figure 3.20C) confirming the success of this bCaSR WT version with cys-/sp- expressed in SHuffle cells in binding and that the removal of these regions does not affect the binding sites for  $\text{Ca}^{2+}$ .

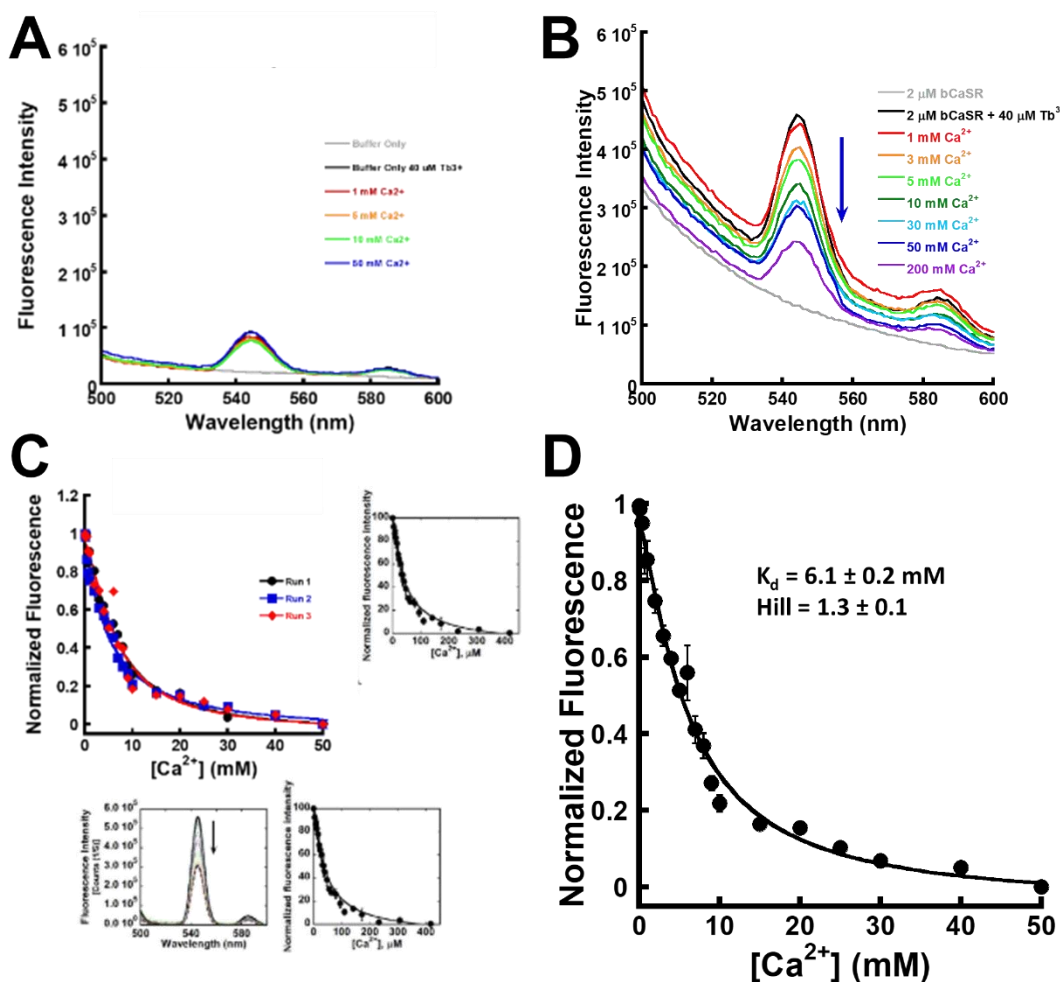


**Figure 3.20 –  $\text{Tb}^{3+}$ /Trp FRET with  $\text{Ca}^{2+}$  competition titration on bCaSR ECD WT.** This experiment was done in 20 mM PIPES and 10 mM KCl with a pH of 6.8 and 2  $\mu\text{M}$  of bCaSR in triplicate. 40  $\mu\text{M}$   $\text{Tb}^{3+}$  was added before  $\text{Ca}^{2+}$  was titrated in. A –

Buffer with 40  $\mu\text{M}$   $\text{Tb}^{3+}$ . **B** – Representative plot of  $\text{Ca}^{2+}$  titrated into bCaSR with 40  $\mu\text{M}$   $\text{Tb}^{3+}$ . **C** –  $K_d$  plot for the triplicate trials in comparison to previous member's data. **D** –  $K_d$  plot for the triplicate trials averaged.

We next examined  $\text{Tb}^{3+}$  FRET titration on the bCaSR S272A mutant which is a hydrophobic mutation of the main hinge binding site for  $\text{Ca}^{2+}$  and TNCA (Figure 3.21). These results of biphasic binding were also seen in our subdomain studies where  $\text{Tb}^{3+}$  titration upon subdomain 1 which includes the main hinge binding site also presented with biphasic binding as well as disruption mutations caused a change in this biphasic binding pattern<sup>[269]</sup>.

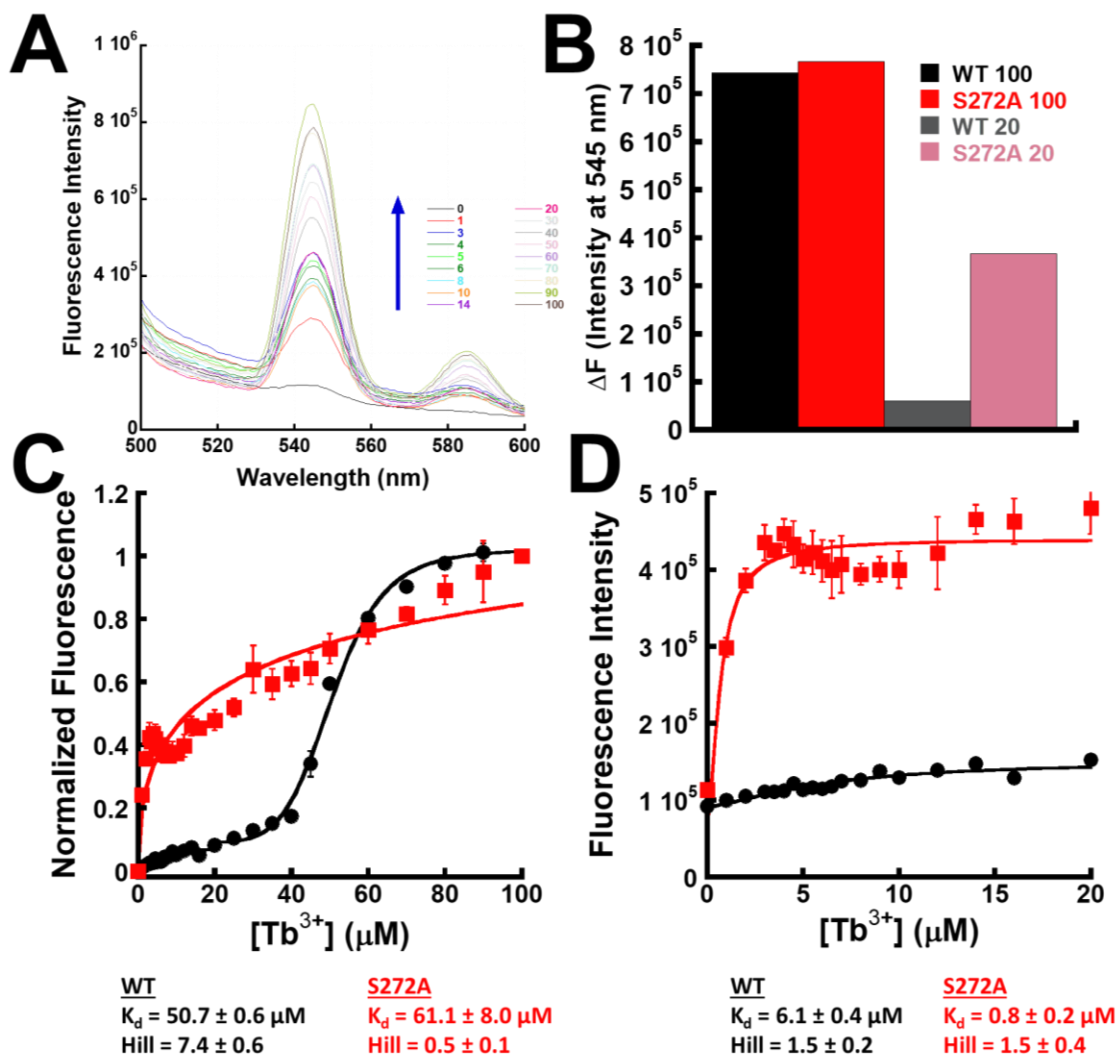
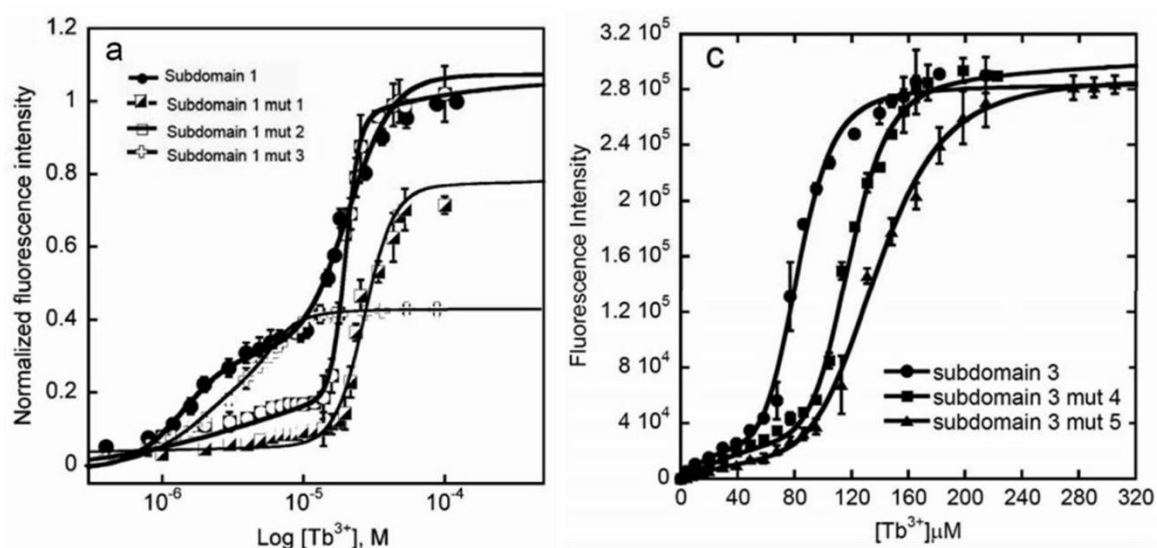


Figure 3.21 –  $\text{Tb}^{3+}$ /Trp FRET with  $\text{Tb}^{3+}$  titration on 2  $\mu\text{M}$  bCaSR WT and S272A.



This experiment was done in 20 mM PIPES and 10 mM KCl with a pH of 6.8 and 2  $\mu\text{M}$  of bCaSR WT (black) and S272A (red) in triplicate. A – Representative titration curve for S272A. B – Bar graph depicting the average  $\Delta F$  from 0  $\mu\text{M}$   $\text{Tb}^{3+}$  to 100  $\mu\text{M}$   $\text{Tb}^{3+}$  (WT black, S272A red) or to 20  $\mu\text{M}$   $\text{Tb}^{3+}$  (WT gray, S272A pink) titrated. C – The full  $\text{Tb}^{3+}$  FRET titration curve showing the second binding for WT and the lack of the sigmoidal curve for S272A. D – Show the zoomed-in first 20  $\mu\text{M}$   $\text{Tb}^{3+}$  titration for WT and S272A.

Unlike the bCaSR ECD WT response though, the S272A response was not sigmoidal but instead was 1:1 binding with a linear response after initial binding past 20  $\mu\text{M}$  (Figure 3.21).



**Figure 3.22 –  $\text{Tb}^{3+}$ /Trp FRET with  $\text{Tb}^{3+}$  titration of CaSR ECD subdomains<sup>[269]</sup>.**

A – Subdomain 1 has previous proposed binding site 1 (S147, S170, D190, Y218, E297), site 2 (D215, L242, S244, D248, Q253), and site 3 (E224, E228, E229, E231, E232) with mutation 1 (D190A/E297I), mut 2 (D215A/D248A), and mut 3 (E224I/E228I/E229I/E231I/E232I). C – Subdomain 3 has previous proposed binding site 4 (E350, E353, E354, N386, S388) and site 5 (E378, E379, T396, D398, E399) with mut 4 (E350I/E353I/E354I) and mut 5 (E378I/E379I/D398A/E399I)<sup>[269]</sup>.

The S272A mutant had drastic effects upon  $\text{Tb}^{3+}$  titration binding where the first binding process is much quicker and has greater fluorescence changes where 20  $\mu\text{M}$  of  $\text{Tb}^{3+}$  can illicit a fluorescence increase of 350000 compared to the bCaSR ECD WT increasing to only 85000 in the same amount of titrant (Figure 3.21B&D). The binding for this first curve for the bCaSR S272A

mutant was much tighter as indicated by the  $K_d$  of  $0.8 \pm 0.2 \mu\text{M Tb}^{3+}$ , but the cooperativity for the first process is similar with a Hill number of  $1.5 \pm 0.4$ .

**Table 3.2 – Summary of bCaSR WT binding titrations.**

bCaSR	Titrant	Trp Fluorescence	ANS Fluorescence	Tb <sup>3+</sup> /Trp FRET	Tb <sup>3+</sup> /Trp FRET Ca <sup>2+</sup> Competition
WT					
K <sub>d</sub>	Ca <sup>2+</sup> (mM)	$5.0 \pm 0.1$ (n = 6)	$4.4 \pm 0.2$ (n = 6)	N/A	$6.1 \pm 0.3$
	Tb <sup>3+</sup> (μM)	N/A	N/A	$50.7 \pm 0.6$	N/A
	TNCA (μM)	N/A	$2.3 \pm 0.3$	N/A	N/A
	PO <sub>4</sub> (mM)	$10.6 \pm 0.4$	$2.2 \pm 0.2$	N/A	N/A
Hill number	Ca <sup>2+</sup>	$1.5 \pm 0.1$ (n = 6)	$1.9 \pm 0.2$ (n = 6)	N/A	$1.3 \pm 0.1$
	Tb <sup>3+</sup>	N/A	N/A	$6.2 \pm 0.4$	N/A
	TNCA	N/A	$0.6 \pm 0.1$	N/A	N/A
	PO <sub>4</sub>	$0.9 \pm 0.04$	$1.0 \pm 0.1$	N/A	N/A

N/A – not applicable. n = 3 if not listed otherwise.

The S272A mutant also dramatically affects the cooperativity of the second binding process where the WT had a sigmoidal curve and a Hill number of  $7.4 \pm 0.6$ , the S272A mutant has a 1:1 binding curve with a Hill number of  $0.5 \pm 0.1$ . Additionally, S272A reduced the binding strength of the second binding process from  $50.7 \pm 0.6 \mu\text{M Tb}^{3+}$  for WT to  $61.1 \pm 8.0 \mu\text{M Tb}^{3+}$  for S272A.

### 3.3 Discussion

Previously the mutations have been unsuccessful, but with research we found the correct primer formation and PCR protocols to successfully produce bCaSR and hCaSR mutants. Using the correct DNA polymerase for the size of the plasmid and protein for site-directed mutagenesis is critical. Although the primers and protocol are optimized, this does not necessitate that the mutations will effectively work during PCR. There are many factors influencing primers and PCR, most notably temperature, run cycles, and primer design. Thus, looking at alternative reasons and going back to protocols when we were successful is vital. By doing this we have found out the KOD DNA polymerase is better for larger plasmids and that primer design can also matter for plasmid size. Using the new primers and KOD polymerase resulted in a successful mutation.

We were able to PCR three mutations for hCaSR and bCaSR of E297K (FHH), S272A, R66H (FHH). With the maintenance of our epifluorescence microscope for almost a year, we focused on bCaSR mutation binding assays. We were able to purify each mutant and the WT for bCaSR, although R66H both times had such a low concentration of protein through purification that binding studies were not possible. The WT bCaSR and E297K and S272A mutants went forward with binding studies. We first optimized our binding study protocols where we did not utilize EGTA since the  $\text{Ca}^{2+}$  present was negligible and adding EGTA can lead to saturation or pH changes. Also increasing the amount of titration added from 1-2  $\mu\text{L}$  to  $\sim 4 \mu\text{L}$  helped to

significantly reduce error, by keeping the volume closer to 4-5  $\mu\text{L}$  we can also reduce dilution effects of the bCaSR.

We looked at Trp fluorescence, ANS hydrophobicity binding fluorescence,  $\text{Tb}^{3+}/\text{Trp}$  FRET, and  $\text{Tb}^{3+}/\text{Trp}$  FRET with  $\text{Ca}^{2+}$  competition on the WT with  $\text{Ca}^{2+}$ , TNCA, and  $\text{PO}_4$  to investigate the normal response, the drug effects of TNCA in bCaSR binding and the possible bicarbonate binding site using  $\text{PO}_4$  (Table 3.2).

We saw that for WT bCaSR with  $\text{Ca}^{2+}$  Trp fluorescence decreases with a  $K_d$  of  $5.0 \pm 0.1$  mM and a Hill of  $1.5 \pm 0.1$  showing weak binding and high cooperativity. These results are further correlated by ANS binding having a  $K_d$  of  $4.4 \pm 0.2$  mM and a Hill number of  $1.9 \pm 0.2$  and the  $\text{Tb}^{3+}/\text{Ca}^{2+}$  competition having a  $K_d$  of  $6.1 \pm 0.3$  mM and Hill number of  $1.3 \pm 0.1$  (Table 3.2). We could not use TNCA in any binding assay besides ANS since Trp and TNCA overlap in fluorescence excitation and emission and would lead to false positives. Additionally, we could not use higher than 50  $\mu\text{M}$  TNCA for ANS binding since the fluorescence of TNCA also partially overlaps with ANS fluorescence, where higher than 50  $\mu\text{M}$  shows on the fluorimeter. TNCA and  $\text{Ca}^{2+}$  together with ANS binding showed that TNCA acts as an agonist for CaSR where the  $K_d$  was decreased to  $2.3 \pm 0.3$   $\mu\text{M}$ , although the binding of TNCA does disrupt the cooperativity of  $\text{Ca}^{2+}$  indicated by the Hill number of  $0.6 \pm 0.1$ . We know that mCaSR was found in crystallization to be bound to TNCA to the hinge region of CaSR and that TNCA and  $\text{Ca}^{2+}$  act as competitive co-agonists, this helped to explain this unusual results we saw with mCaSR ANS binding since the ECD was likely already occupied by TNCA as confirmed by crystal and mass spectrometry studies<sup>[287]</sup>. Therefore, studies need to be done using mCaSR as a comparison after Phe removal to ensure that the mCaSR is an unoccupied form.

While  $\text{PO}_4$  did show effects on bCaSR binding the  $\text{PO}_4$  form of  $\text{K}_2\text{HPO}_4$  show that the  $\text{K}_2\text{HPO}_4$  binding site is not as strong as the  $\text{Ca}^{2+}$  binding sites since the binding strength is lower considering the higher  $K_d$  of  $10.6 \pm 0.4$  mM. Additionally, the Hill number greater than 1.0 implies cooperative binding for  $\text{Ca}^{2+}$  and potentially multiple binding sites while the Hill number lower than 1.0 at  $0.9 \pm 0.04$  for  $\text{K}_2\text{HPO}_4$  implies there is only a single binding site, which is the bicarbonate binding site (Figure 3.12). We also tested the effect of KCl on bCaSR using Trp fluorescence to see if the  $\text{K}_2\text{HPO}_4$  effects were from the  $\text{PO}_4$  binding or the  $\text{K}_2$  binding (data not shown). The KCl was also able to cause a decrease in signal upon titration with  $2 \mu\text{M}$  bCaSR. The  $K_d$  of KCl was, problematically, almost identical to the  $\text{K}_2\text{HPO}_4$  binding at  $11.9 \pm 0.9$  mM. There was a difference between KCl and  $\text{K}_2\text{HPO}_4$  in their Hill numbers, where  $\text{K}_2\text{HPO}_4$  has a Hill number less than 1.0 indicating non-cooperative binding and a single binding site. KCl also has a Hill number of  $1.2 \pm 0.1$  which implies KCl has cooperative binding and potentially multiple binding sites. We found that the KCl and  $\text{K}_2\text{HPO}_4$  were both able to induce a conformational change of CaSR. While KCl is able to induce changes similarly to  $\text{K}_2\text{HPO}_4$  more studies need to be done to determine if these changes are related to K, Cl, or  $\text{PO}_4$ .

While our purification of the bCaSR mutants S272A, D216N, and E241K was successful this, unfortunately, did not translate to all of our mutations. R66H, E228K, and E228Q saw a complete loss of expression while H254A and E297K both had diminished expression and purification of CaSR with only 20-30% protein yield in comparison to the WT. This shows that R66 and E228 residues are critical for correct protein expression since mutation of these sites led to a loss of protein expression potentially from protein misfolding. The E297K mutation had much lower expression than the WT and was not enough protein for biophysical studies, this site is in the hinge site 1 and disruption of this site could also show a loss of correct or stable conformation which can

also be seen by the smeared degradation band for western blot. When we tried any of the binding studies on the S272A and D216N mutants, they invariably had precipitation around 1-6 mM  $\text{Ca}^{2+}$  with D216N being much more susceptible to precipitation than S272A and as such the data would broadly fluctuate from the diffraction on the precipitation. This indicates that these residues are critical for structural stability. Additionally, S272A and D216N both reduced the binding  $K_d$  for  $\text{Ca}^{2+}$  upon Trp fluorescence titrations with S272A having  $7.2 \pm 0.3$  mM  $\text{Ca}^{2+}$  and D216N having  $6.0 \pm 0.3$  mM  $\text{Ca}^{2+}$  compared to WT at  $4.8 \pm 0.1$  mM  $\text{Ca}^{2+}$ . Since D216N had precipitation issues early on in titration we decided to look at S272A for  $\text{Tb}^{3+}$ /Trp FRET titration. We saw that the WT CaSR ECD under  $\text{Tb}^{3+}$ /Trp FRET has two binding processes a quick initial tight binding at  $6.1 \pm 0.4$   $\mu\text{M}$   $\text{Tb}^{3+}$  and slight cooperativity with a Hill number of  $1.5 \pm 0.2$  and a slower extremely cooperative binding process with a  $K_d$  of  $50.7 \pm 0.6$   $\mu\text{M}$  and a Hill number  $7.4 \pm 0.6$ . The S272A mutant had drastic effects upon  $\text{Tb}^{3+}$  titration where the first binding process is much quicker and has more considerable fluorescence changes where 20  $\mu\text{M}$  of  $\text{Tb}^{3+}$  can illicit a fluorescence increase of 350000 compared to WT increasing to only 85000 in the same amount of titration. The binding for this first curve was much tighter as indicated by the  $K_d$  of  $0.8 \pm 0.2$   $\mu\text{M}$   $\text{Tb}^{3+}$  but the cooperativity for the first process is similar with a Hill number of  $1.5 \pm 0.4$ . The S272A mutant also dramatically affects the cooperativity of the second binding process where the WT had a sigmoidal curve and a Hill number of  $7.4 \pm 0.6$ , the S272A mutant has a 1:1 binding curve with a Hill number of  $0.5 \pm 0.1$ . Additionally, S272A reduced the binding strength from  $50.7 \pm 0.6$   $\mu\text{M}$   $\text{Tb}^{3+}$  for WT to  $61.1 \pm 8.0$   $\mu\text{M}$   $\text{Tb}^{3+}$  for S272A. This indicated that either FRET was not occurring with  $\text{Tb}^{3+}$  binding to the protein in the higher  $\text{Tb}^{3+}$  concentrations or that there was only one binding site in the protein. This could be because the protein is unfolded or degraded or that the binding site was disrupted so much that the  $\text{Tb}^{3+}$  was not able to interact with the Trp just floating

around outside of the protein structure thus increasing linearly or because disrupting the major hinge binding site allowed for only one or no binding site to be present in the bCaSR S272A protein (Figure 3.21). Since we have previously shown that  $Tb^{3+}$  itself cannot increase on such a large scale we hypothesize this linear increase in FRET between unbound  $Tb^{3+}$  and nearby stable, denatured, or precipitated bCaSR S272A. We did see a slight 1:1 binding curve for the beginning change of S272A  $Tb^{3+}$  titration as we have seen with the WT, but the error bars were much higher past a few  $\mu M$  of  $Tb^{3+}$  due to precipitation not seen in the WT (Figure 3.21). This tells us that the hinge region binding site is not only critical for binding of  $Ca^{2+}/Tb^{3+}$  but is also the epicenter of cooperative binding throughout the CaSR ECD and disruption of this region leads to a loss of binding, a reduction and loss in cooperative binding in other binding sites, as well as a loss of structure stability as seen by precipitation issues of D216N. This also correlates with our hCaSR functional studies since the hinge region mutations of Y218K, S272I, D275I, and E297I all led to a loss of functional response while still expressing the protein on the cell surface.

We need to perform CD on the mutants to see if this is just a loss of CaSR function issue or if the CaSR structure is greatly disturbed by the mutations. Additionally, we want to look at the binding effects of the other mutants which can be purified E297K, H254A, E241K, as well as repeating S272A and D216N for Trp fluorescence, ANS binding, and  $Tb^{3+}/Trp$  FRET. It would also be critical to investigate if TNCA is able to recover the binding effects seen between the WT and mutants since previously the E228I mutant under functional cell imaging was able to be recovered by TNCA. We would expect to see that the stabilization and cooperativity of TNCA binding in the hinge site would recover the binding loss from mutation of the hinge site as well as the dimer site. Overall the bCaSR binding studies have the advantages of no post-translational modifications such as glycosylation as found in mCaSR expression systems, and additionally does not have

TNCA already bound to the CaSR ECD in bCaSR expression from shorter expression time frames. Although there are advantages to bCaSR expression the major drawback is a non-native expression system can lead to incorrect protein structure leading to aggregation and degradation which causes a loss of protein stability in solution. Efforts previously have been done to optimize these conditions by using glycerol to stabilize the protein. Further optimization can be done to help stabilize the WT and mutants for precipitation in titration spectroscopy studies using aides such as 5-30% glycerol or sucrose and adjusting pH or salt concentrations.

### **3.4 Materials and Methods**

#### ***3.4.9 Plasmid extraction***

Ampicillin positive agarose plates were streaked with Invitrogen™ MAX Efficiency™ DH5 $\alpha$  competent cells with the CaSR and CaSR mutants. These plates were incubated overnight at 37°C. Then tubes of 10 mL Fisher BioReagents™ LB Miller broth with 1:1000 of Ampicillin were inoculated with one colony each and put into a shaker overnight at 220 rpm and 37°C. The samples were centrifuged, and DNA extracted per QIAprep spin miniprep kit protocol. The plasmid utilized for mammalian CaSR mutational studies was human CaSR-pcDNA3.1 (+) (gift from Dr. Edward Brown from Brigham and Women's Hospital, Boston) and for bacterial studies the plasmid was pET-17b.

#### ***3.4.10 Primer construction***

The base pair (bp) sequence was utilized of the CaSR to make mutation primers at possible cation, bicarbonate, and compound binding sites. The primers were a 27-35 base pairs around the targeted amino acid. The primers were a minimum of 25 bp and adhere to the equation for  $T_m > 78^\circ\text{C}$  using



the equation  $T_m = 81.5 + (0.41 * \%GC) - (675 / (\#bp \text{ total}))$ . All of the full-length CaSR mutants were generated by site-directed mutagenesis on the basis of the sequence of CaSR.

#### ***3.4.11 Polymerase chain reaction (PCR)***

PCR site directed mutagenesis was performed using either G-Biosciences Pfu DNA polymerase or Sigma-Aldrich KOD DNA polymerase according to the manufacturer's instructions. Briefly, a pair of complementary primers were designed for generating each mutant with the mutation placed at the middle of the primers. The template CaSR DNA was amplified using with these primers for 30 cycles in a polymerase chain reaction instrument (Techne). After digestion of the template DNA with New England Biolabs Dpn1, the amplified mutant DNA was transformed and amplified using Agilent XL10-Gold ultracompetent cells. All the DNA sequences were verified by Genewiz ([www.genewiz.com](http://www.genewiz.com)).

#### ***3.4.12 Agarose gel electrophoresis***

The agarose gel for visualization of the PCR product was made using 50 mL of Thermo Scientific™ TAE Buffer (Tris-acetate-EDTA) at 1x concentration with 0.8% agarose. This mixture was heated for 90 seconds until boiled and fully dissolved. The mixture was then allowed to cool until warm to the touch so 1:10,000 ratio of SYBR Safe DNA Gel Stain (10,000 x DMSO) could be added to the mixture and poured into the UV transparent gel tray and left in the dark until solidified. The samples were run on agarose gel using gel electrophoresis at 80-120 V and imaged using UV light.

#### ***3.4.13 Inoculation and expression***

Cells were streaked on an Ampicillin positive agarose plate using extracted CaSR plasmid, then incubated overnight at 37°C. 600mL of Fisher BioReagents™ LB Miller broth was prepared at a 25 g/L ratio and then autoclaved for sterility. Tubes of 10 mL Fisher BioReagents™ LB Miller

broth with 1:1000 Ampicillin were inoculated with one colony each and put into a shaker overnight at 220 rpm and 37°C. After a minimum of 12 hours, 1.5 mL was added to each 600 mL flask of Fisher BioReagents™ LB Miller broth with 1:1000 Ampicillin and shaken at 220 rpm at 30°C. Measured O.D. using UV until approximately 0.600 absorbance for expression. Added isopropyl  $\beta$ -D-1-thiogalactopyranoside (IPTG), to trigger lac operon and allow the protein to express overnight at 220 rpm at 25°C. After a minimum of 12 hours the sample was centrifuged at 15000  $\times$  g for 30 min at 4°C and the pellet was collected.

#### ***3.4.14 CaSR ECD purification***

Prepared Buffers as follows; Buffer A: 50 mM Tris-HCl, 250 mM NaCl, 20 mM Imidazole, pH 7.5. Buffer B: 50 mM Tris-HCl, 250 mM NaCl, 500 mM Imidazole, pH 7.5. The protein pellet was resuspended in Lysis buffer with cOmplete™, Mini, EDTA-free Protease Inhibitor Cocktail. The cells were broken up using a sonicator and cell disruptor. The sample was then filtered and run using a His-tag column on Fast protein liquid chromatography (FPLC). The target protein will bind to the beads while in buffer A and then dissociated by the high concentration of Imidazole in buffer B, increasing steadily from 0 to 100%. The purified protein is desalted using size exclusion column GE Healthcare HiTrap™ Chelating HP Columns in 10 mM Tris with pH 7.4.

#### ***3.4.15 SDS-PAGE and western blot***

Samples were incubated in Bio-Rad Laemmli Sample Buffer with or without Sigma-Aldrich 2-Mercaptoethanol and boiled for 10 minutes. The proteins were separated on an 8.5% SDS-PAGE gel. After electrophoresis, the gel was either stained with coomassie blue or transferred to a 0.45  $\mu$ m nitrocellulose membrane for western blot. The nitrocellulose membrane was blocked with 5% Bio-Rad Blotting-Grade Blocker non-fat milk in Tris Buffered Saline and then incubated with first mouse anti-CaSR ADD antibody (1:4000) for 1 hour at room temp or overnight at 4°C. After

being washed three times with TBS with 0.1% tween (TBST), the membrane was incubated at room temperature for 1 hr with goat anti-mouse secondary antibody diluted with TBST (1:4000). The detected protein signals were visualized by Bio-Rad enhanced chemiluminescence reaction system.

#### ***3.4.16 Circular dichroism spectroscopy***

The circular dichroism spectra were recorded from 190 to 260 nm on a Jasco-810 spectropolarimeter purged with N<sub>2</sub> and equipped with a temperature control system CTC-345. Spectral dependent measurements were performed at a bandwidth of 2 nm using a U-type quartz cell of path length 0.1 mm with protein concentrations ranging from 8 to 10  $\mu$ M in 10 mM Tris-HCl, pH 7.4. The spectra were recorded at a scan rate of 50 nm/min and response time of 1s. The cuvette was sealed with parafilm to prevent solvent evaporation. The spectra were deconvoluted using the selcon method after subtracting the spectrum of the buffer as the blank and the CD data were depicted in units of molar ellipticity per residue.

#### ***3.4.17 Intrinsic tryptophan fluorescence spectroscopy***

A PTI lifetime fluorimeter was used to record the fluorescence spectra at room temperature using a 1-cm path length cell. Intrinsic tryptophan emission spectra were recorded from 300 to 400 nm with the excitation wavelength at 282 nm. The slit widths were set at 1-4 nm for excitation and 3-8 nm for emission, respectively. The calcium titration was performed in 10 mM Tris with the protein concentration of 2.0  $\mu$ M at pH 7.4 by adding known amount of CaCl<sub>2</sub>.

#### ***3.4.18 Terbium FRET spectroscopy***

For the Trp-sensitized Tb<sup>3+</sup> Forester's resonance energy transfer (FRET) assay, protein samples (2.0  $\mu$ M) were in 20 mM PIPES-10 mM KCl at pH 6.8. The emission spectra were collected from 500-600 nm with the excitation at 282 nm. The slit widths were set at 1-4 nm for excitation and

3-8 nm for emission, respectively. Secondary Rayleigh scattering was circumvented by using a glass filter with a cutoff of 320 nm. The Tb<sup>3+</sup> titration was performed by adding various volumes of Tb<sup>3+</sup> stock solutions stepwise into the cuvettes. The Ca<sup>2+</sup>-Tb<sup>3+</sup> competition experiments were performed in solutions containing 40 μM Tb<sup>3+</sup> and 2 μM protein as the starting point. The stock solution of CaCl<sub>2</sub> was gradually added into the mixture. The background fluorescence intensity was subtracted using logarithmic fitting and the Tb<sup>3+</sup> binding affinity of the protein was calculated by fitting normalized fluorescence intensity data using the Hill equation,  $\Delta S = \frac{[M]^n}{K_d^n + [M]^n}$ ,

where  $\Delta S$  is the total signal change in the equation,  $K_d$  is the apparent binding affinity,  $n$  is the Hill coefficient, and  $[M]$  is the free metal concentration.

#### ***3.4.19 ANS-binding spectroscopy***

For the ANS (8-anilino-1-naphthalenesulfonic acid) binding assay, protein samples were incubated with 40 μM ANS in 50 mM Tris-HCl and 100 mM KCl (pH 7.4) for 1 hr prior to measurement. The excitation wavelength was set at 370 nm, and the emission spectra were acquired from 400 to 600 nm. For the Ca<sup>2+</sup> titration, the protein concentration was 2 μM and the Ca<sup>2+</sup> concentration was increased in 20 mM Tris- HCl and 50 mM KCl, pH 7.4.

## 4 Structure Based Drug Design

### 4.1 Introduction

Therapeutics targeting GPCRs account for over a third of the available Food and Drug Administration (FDA) approved drugs on the market and developing compounds targeting GPCRs is an ever-expanding niche with revenue from these FDA approved GPCR targeted drugs amassing over \$180 billion annually<sup>[292-295]</sup>. Family C GPCRs consist of eight metabotropic glutamate receptors (mGluR1-8), a calcium-sensing receptor (CaSR), two heterodimeric aminobutyric acid B (GABAB) receptors, three taste receptors (T1R), an amino acid receptor (GPCR6A), and five orphan receptors. Additionally, therapeutics targeting the family C of GPCR is low with only 2 compounds, one targeting GABAB receptors called baclofen and one which has been developed for CaSR targeting, cinacalcet, for treatment of hyperparathyroidism<sup>[296]</sup>. Furthermore, only one drug so far has been targeted to the CaSR ECD, AMG416, which is currently going through FDA approval<sup>[297-299]</sup>. Intermittent increases in parathyroid hormone (PTH) result in bone formation whereas chronically elevated levels lead to bone loss, thus finding a CaSR antagonist could lead to the treatment of osteoporosis as well as hypoparathyroidism<sup>[300]</sup>. Many antagonists for CaSR have been developed such as NPS-2143, ronacaleret, and encaleret but none of these have made it to FDA approval because of the bone formation and loss were equivalent or no marked improvement in human trials<sup>[301]</sup>.

After our discovery of the novel CaSR binding partner TNCA found bound to the CaSR structure we drove forward with structure-based drug design utilizing TNCA as our lead compound in order to find potential agonists or antagonists for CaSR<sup>[287]</sup>. Since TNCA is a naturally occurring compound formed from Trp through the Pictet-Spengler reaction it cannot be used as a patentable drug target<sup>[302]</sup>. Currently, almost all drugs which have been designed for CaSR targeting have

been thought to be bound to the loops of the transmembrane domain (TMD) or inside of the TMD channel themselves. These studies were done by mutation of proposed binding sites based on homology models of the CaSR TMD<sup>[303, 304]</sup>. Since the full length of CaSR had yet to be crystallized there is the possibility that these drugs target different regions of the CaSR structure so finding TNCA bound to the CaSR ECD structure gives us a lead compound to do drug design based off of TNCA. Since TNCA itself is naturally occurring in the body it cannot be used as a drug itself but modifications of TNCA could induce a novel therapeutic as a calcimimetic or calcilytic. Therefore, we set out to do structure-based drug design utilizing TNCA as a lead chemical compound in order to identify selective CaSR agonists and antagonists with improved binding and pharmacokinetic profiles.

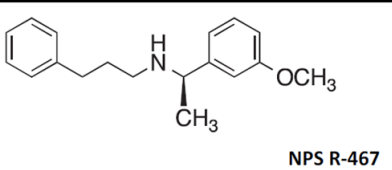
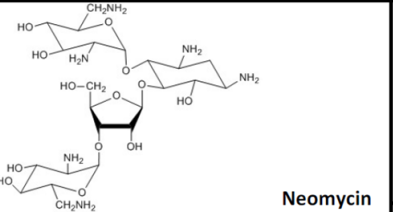
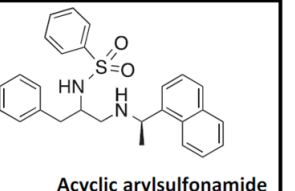
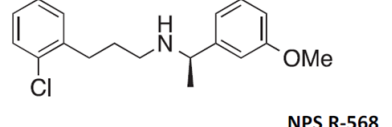
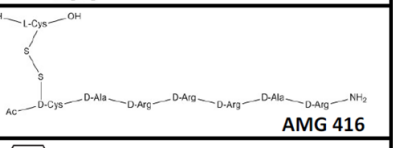
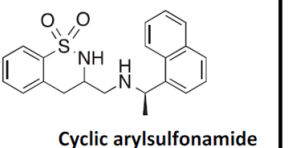
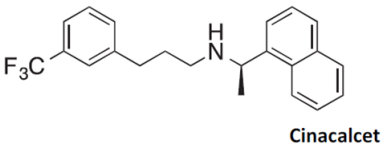
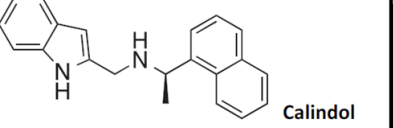
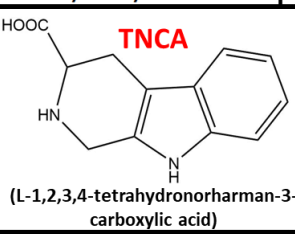
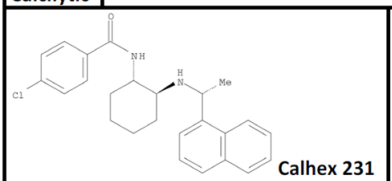
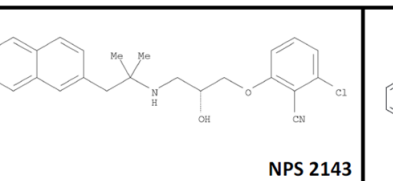
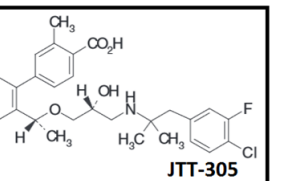
## **4.2 Results**

### ***4.2.1 Lead Drug Compound Design***

We compared TNCA to other CaSR drugs that were designed which did not make it to FDA approval and also the only CaSR drug that was successfully FDA approved, cinacalcet (Table 4.1). Many of the compounds have a commonality of multiple aromatic rings in their structure and often have an extended structure.

We tested several compounds, CSR-101 to CSR-106, from our collaborator Dr. Binghe Wang in their stock of synthesized compounds for other projects that were similar in structure to TNCA (Figure 4.1). These compounds have structural similarity to TNCA, and we were interested in the effects these modifications to the TNCA backbone would have on the CaSR functional activity and functional cooperativity in comparison to Ca<sup>2+</sup> and TNCA.

**Table 4.1 – Compounds of CaSR agonists (calcimimetics) or antagonists (calcilytics).**

Calcimimetic		
 NPS R-467	 Neomycin	 Acyclic arylsulfonamide
 NPS R-568	 AMG 416	 Cyclic arylsulfonamide
 Cinacalcet	 Calindol	 <b>TNCA</b> (L-1,2,3,4-tetrahydronorharman-3-carboxylic acid)
Calcilytic		
 Calhex 231	 NPS 2143	 JTT-305

These CSR-101 to 106 compounds did not have good docking scores to the ECD binding pocket of CaSR using Sybyl and additionally had no significant changes on the CaSR function or cooperativity in HEK293 cells using single-cell imaging and cell population (Figure 4.10). We performed lead drug design and docking studies to decide which drug synthesis route to attempt based on TNCA structure and preliminary structure binding pocket analysis we designed eight lead backbones to begin with as possible templates (Table 4.2). We investigated Lead A and replaced R2 with other charged oxygen species for the tight binding in the negatively charged binding pocket. We also examined if a smaller sized TNCA compound would bind stronger to CaSR, so we also looked at Lead A without the third aromatic ring.

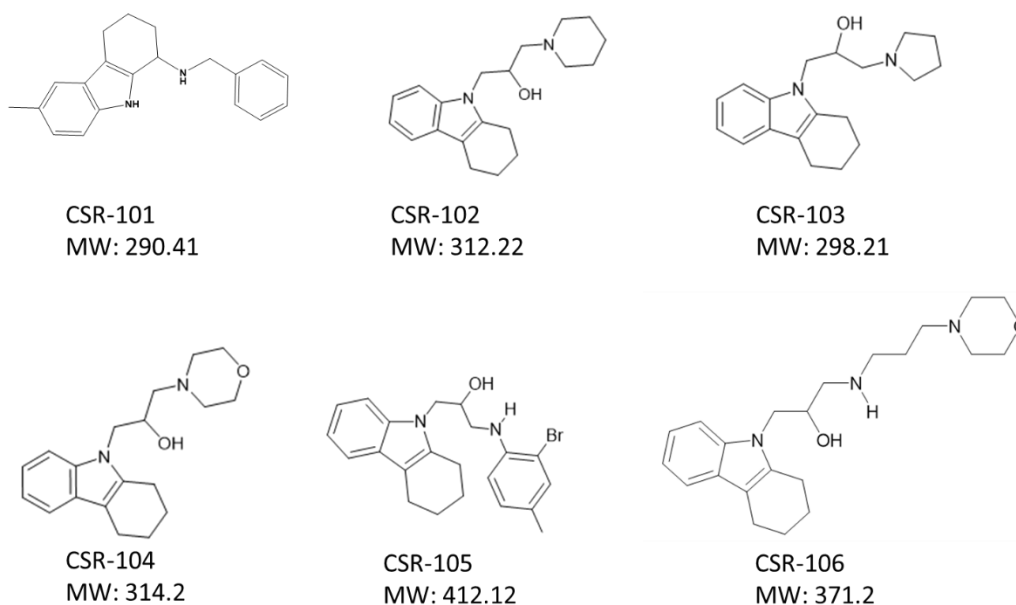
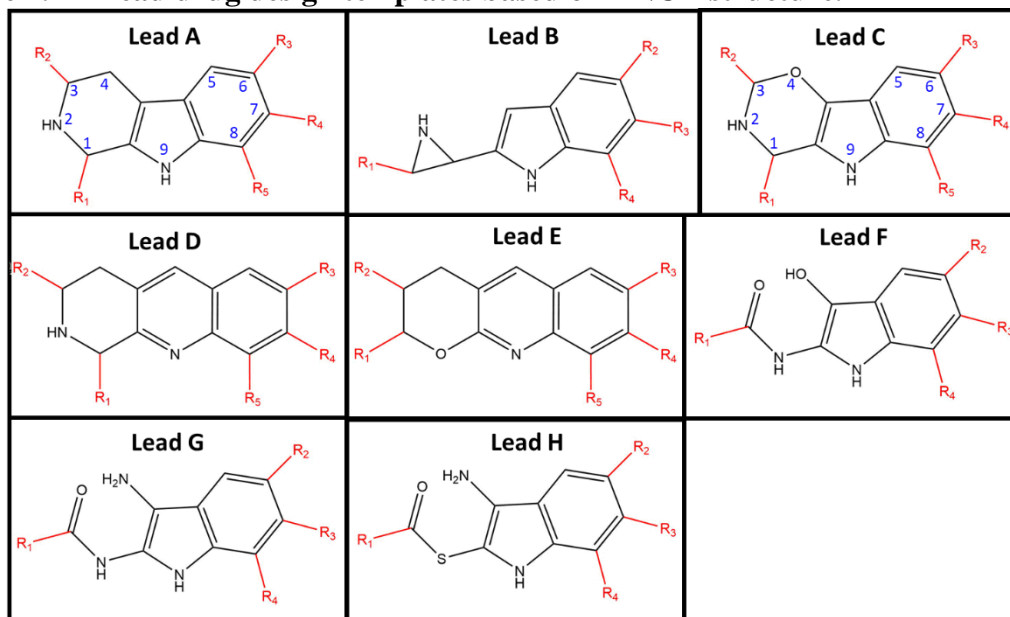


**Figure 4.1 – CSR-101 to 106 compound structures and molecular weights.**  
The first six compounds were given to us by the Wang lab from their stock of synthesized compounds since they were similar to the TNCA structure.

Utilizing a lead drug design software LADI, a library building software, designed by Mengyuan Zhu in Dr. Wang's research group (<https://github.com/MengyuanZhu/LADI>) we generated analogs/lead co-conformers based on TNCA and other leads designed (Table 4.2).

**Table 4.2 – Lead drug design templates based on TNCA structure.**

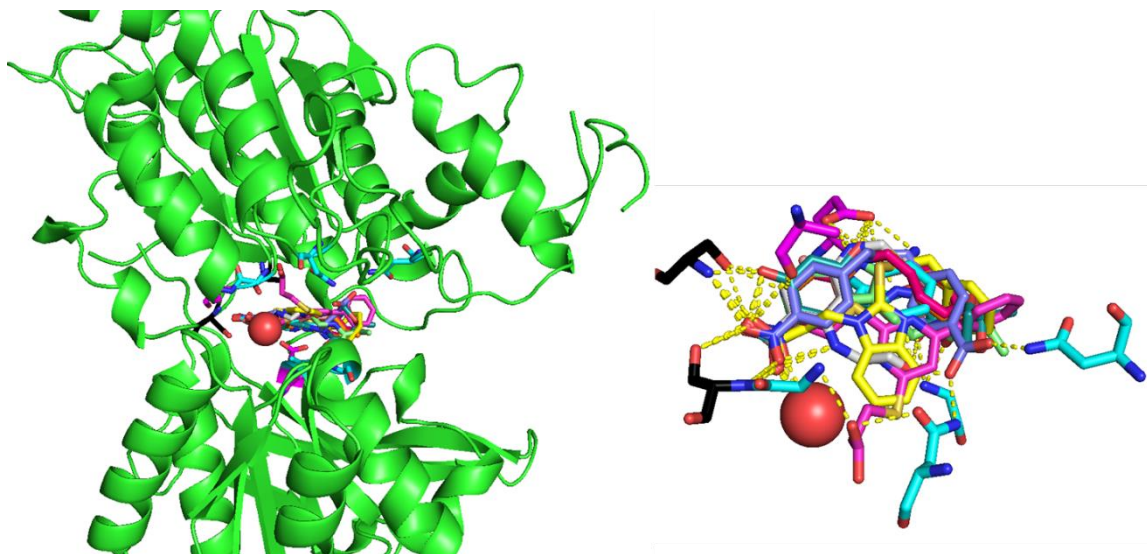


Where R<sub>1</sub>-R<sub>5</sub> can be CO<sub>2</sub>, NO<sub>2</sub>, SO<sub>2</sub>, OH, or they can be linkers (Ph, Ar, Me, EtOH, Ester, etc.)





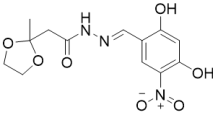
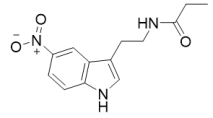
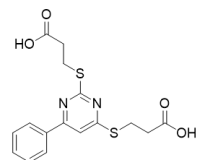
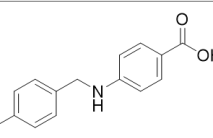
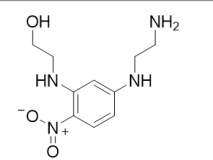
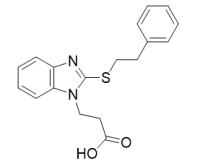
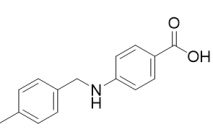
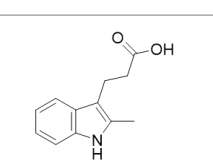
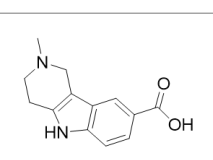
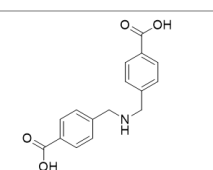
Then in conjunction with Sybyl and LADI these compounds with each R group modification is bound to CaSR using Sybyl docking software. Sybyl then gives the relative binding efficiency rate of all the R groups in percent, called the hit rate, and the relative binding score, an arbitrary value which indicates the strength of binding into the pocket where the higher the value the higher the binding strength (Figure 4.3).



**Figure 4.4 – Specs compounds bound to CaSR.**  
Using OEDocking FRED software from OpenEye the Specs potential compounds were docked into CaSR binding site to investigate their score and these 10 had the best binding as shown above.

The three ring structures were too bulky in comparison to the two ring structure which had a 100% hit rate and the highest score of approximately 15 on average (Figure 4.3D). The R groups added on to the TNCA unaltered backbone had a 54% hit rate and a score of approximately 8 on average (Figure 4.3A). The sulfonamide replacement of the carboxylic acid on the TNCA backbone had a hit rate of 16% and a score of approximately 7 on average (Figure 4.3B). The sulfur dioxide replacement of the carboxylic acid on the TNCA backbone led to no binding and a score of approximately 4 on average (Figure 4.3C).

**Table 4.3 – Specs compounds ordered for CaSR targeting after computational evaluation of Specs library.**

Structure	Lot Number	Sample ID	M.W.	Zinc Number	Score
	AG-205/36286002	BW-CSR-107	325.28	19943353	10.29
	AH-262/37116011	BW-CSR-108	261.28	00287726	10.67
	AG-690/15434541	BW-CSR-109	364.43	2980249	11.08
	AN-465/41988477	BW-CSR-110	306.16	359861	9.36
	AG-670/12382020	BW-CSR-111	240.26	4046668	10.45
	AG-690/11168001	BW-CSR-112	326.41	193448	10.37
	AN-465/41988475	BW-CSR-113	241.29	259187	9.94
	AE-641/00851021	BW-CSR-114	203.24	2565049	10.26
	AE-641/11948155	BW-CSR-115	230.27	2726205	9.27
	AN-465/43411235	BW-CSR-116	285.3	10475236	10.03

With these binding results we were able to begin the synthesis process through both the lead pathways of TNCA R-group replacement as well as the two ring backbone R-group replacement (Figure 4.3A and D). Since compound synthesis is a long process, we also simultaneously began looking at other readily available compounds with good binding scores we could test on CaSR to examine their effects and direct our lead drug design further. Therefore, we turned to the Specs compound library which offered over 200,000 compounds available for testing.

Specs compound library of over 200,000 compounds was examined for potential compounds with adequate Sybyl CaSR ECD binding similar to our examined LADI compounds. Using an OpenEye program called FRED we docked the 200K+ Specs library and then took top 2000 structures to model in Sybyl. From our Sybyl docking results, we took the best 20 compounds and then looked at each one docked into CaSR to pick the best 10 to order from Specs, CSR-107 to CSR-116 (Figure 4.4 and Table 4.3).

#### ***4.2.2 TNCA and Determined Related Compounds Optical Properties***

The TNCA absorbance, excitation and emission is similar to Trp since TNCA is a derivative of Trp (Figure 4.5). TNCA, previously referred to as CaSRL, has an excitation shift compared to Trp from 300 nm to 280 nm but only a couple nm shift for emission (Figure 4.5A&B). The absorbance plots for TNCA and Trp were almost entirely identical (Figure 4.5C). We saw that a TNCA concentration greater than 0.5 mM in water saw shards of undissolved TNCA and thus was the highest concentration possible for imaging studies (Figure 4.5D).

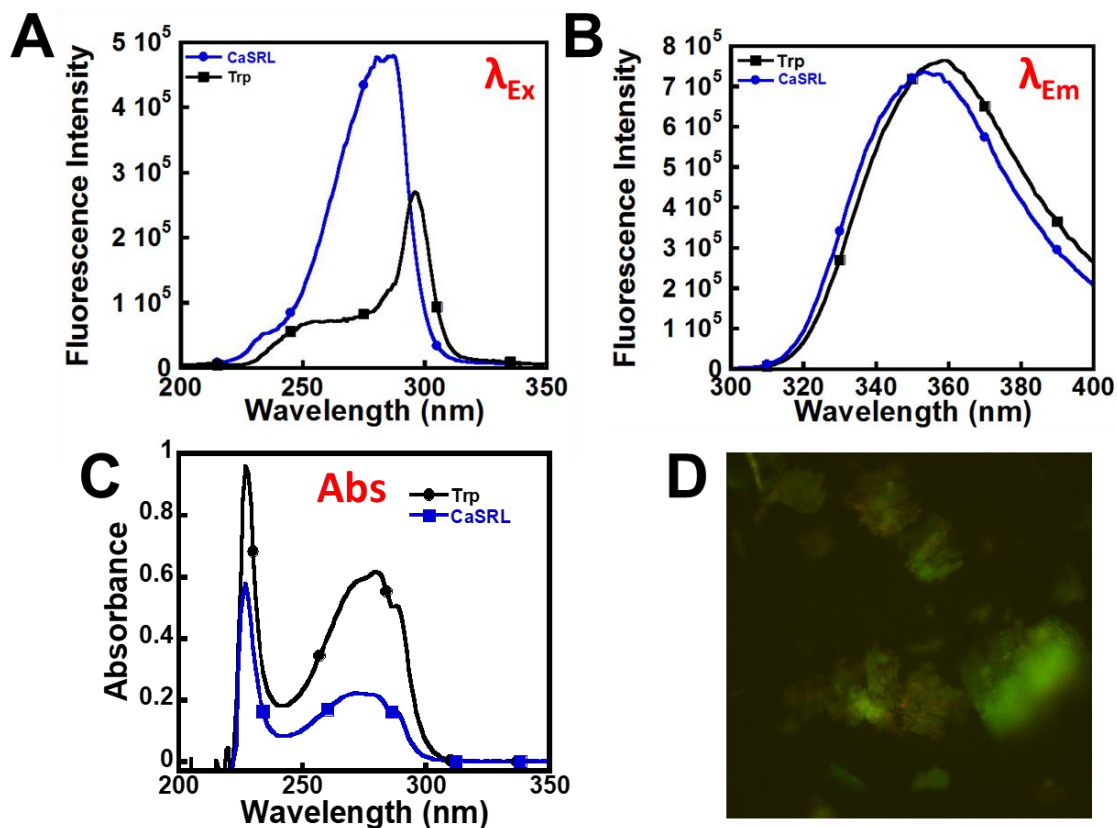


**Figure 4.5 – TNCA optical properties.**

CaSR ligand (CaSRL) was the initial term given for TNCA. A-C – Excitation scan at 360 nm emission (A) and emission scan at 280 nm excitation (B) and absorbance (C) scan of TNCA (blue) versus Trp (black). D – 0.75 mM TNCA in cell imaging showing TNCA shards and that TNCA is not dissolvable in water higher than 0.5 mM.

We investigated the optical properties of the CSR series of compounds from Specs, CSR-107 to 116. The CSR compounds had variable absorbance, excitation and emissions with none showing dissonance with Fura-2  $Ca^{2+}$  dye at 340/380 nm excitation and 510 nm emission (Figure 4.6-Figure 4.7).

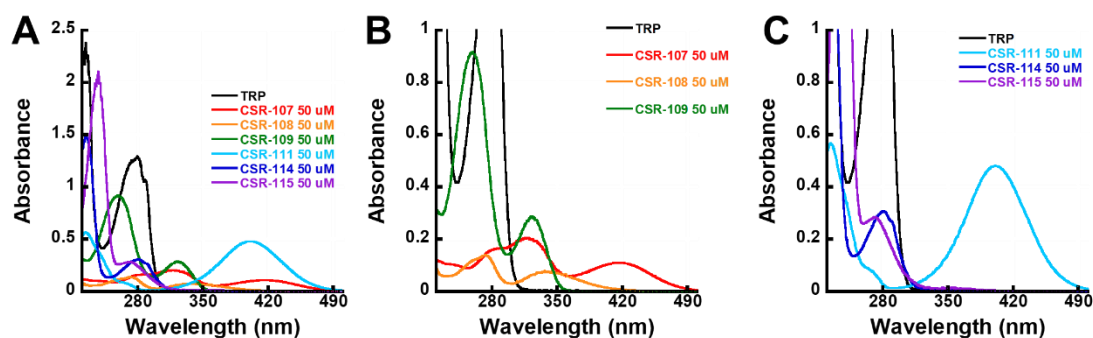


**Figure 4.6 – CSR-107 to CSR-115 absorbance properties.**

**A – Absorbance of CSR-107 to 115 over 220 to 500 nm in comparison to Trp (black) in full zoomed-out scale. B – CSR-107 to 109 and Trp zoomed in to show more clearly. C – CSR-111 to 115 and Trp zoomed in to show more clearly.**

For CSR-107 we excited with 280, 318, and 416 nm and saw an emission peak at 310 and 356 nm, although these peaks were all under 500,000 fluorescence making their overlap peak higher than emission/excitation peaks indicating no true fluorescence present for those wavelengths (Figure 4.7A). CSR-108, CSR-109, and CSR-111 also did not have any peaks above 500,000 fluorescence making their overlap peak higher than emission/excitation peaks indicating no actual fluorescence present for those wavelengths either (Figure 4.7B-D). CSR-114 and CSR-115 did have a response to excitation with CSR-114 being similar to Trp with an excitation at 280 nm producing a peak  $\approx 2,800,000$  fluorescence intensity with an emission peak at 370 nm, which then produces an excitation peak back at 280 nm with the same fluorescence intensity (Figure 4.7E). CSR-115 had emissions to two excitations of 237 and 271 nm with an overlapping emission peak at 382 nm with a fluorescence intensity  $\approx 3,400,000$  and when the excitation scan was done at 382 nm there was an excitation peak also at the same intensity at 271 nm with a smaller side peak on the curve at 245 nm (Figure 4.7F).

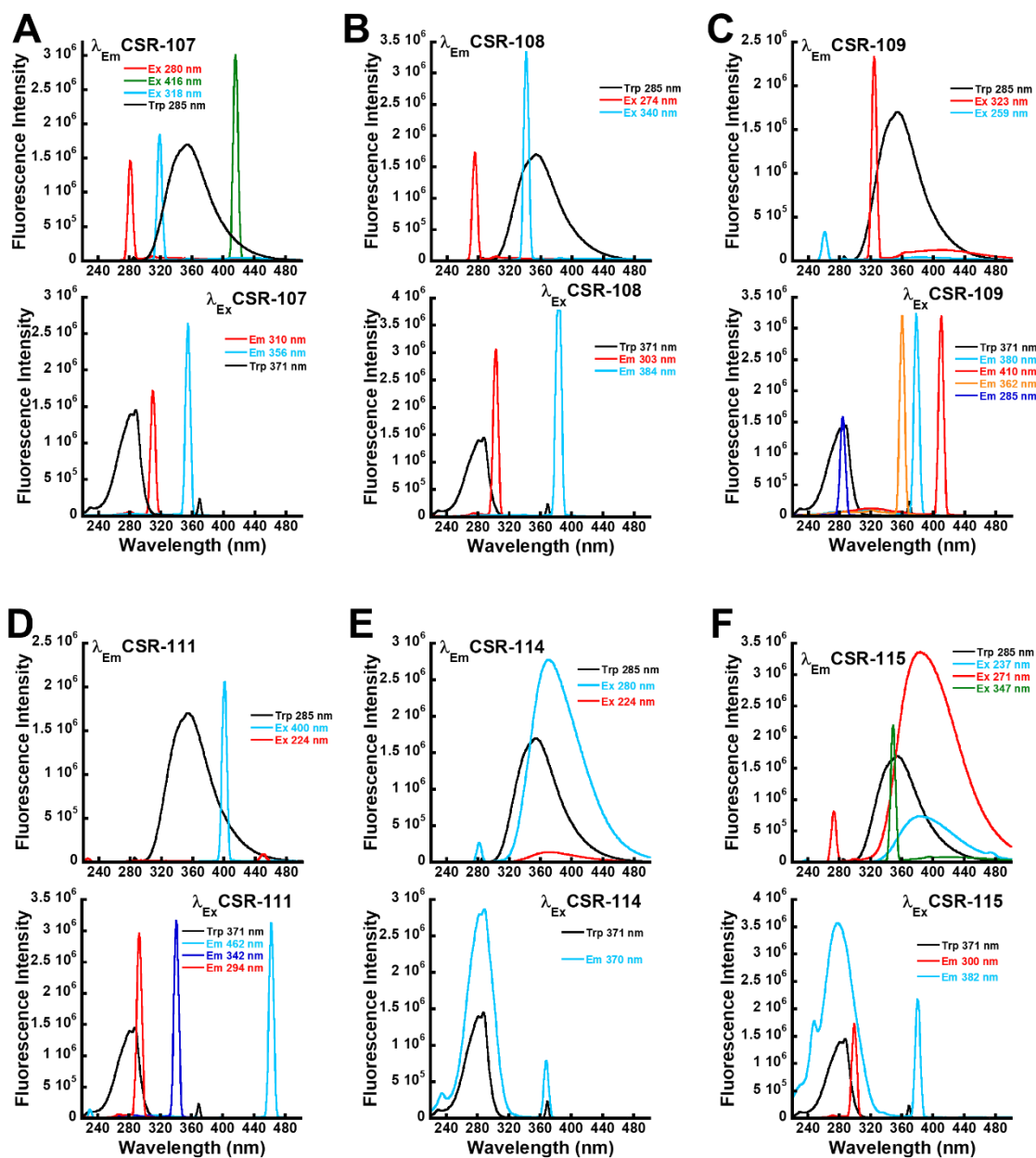


**Figure 4.7 – CSR-107 to CSR-115 excitation and emission properties.**  
**Emission and excitation scans from 220 to 500 nm for each CSR compound based on the absorbance plots with Trp (black) as comparison. CSR-107 (A), CSR-108 (B), CSR-109 (C), CSR-111 (D), CSR-114 (E), CSR-115 (F).**

We did not see any overlap with the CSR compounds or Fura-2 for excitation and emission spectra meaning any signal changes seen on hCaSR with Fura-2 and compound additions will be real changes and not fluorescence intersection.



### 4.2.3 Determining Drug Effectiveness Using Single Cell Imaging

We performed CSR drug testing using single-cell imaging and cell population. TNCA is unable to activate CaSR alone without first activating CaSR with  $\text{Ca}^{2+}$  first (Figure 4.8A).

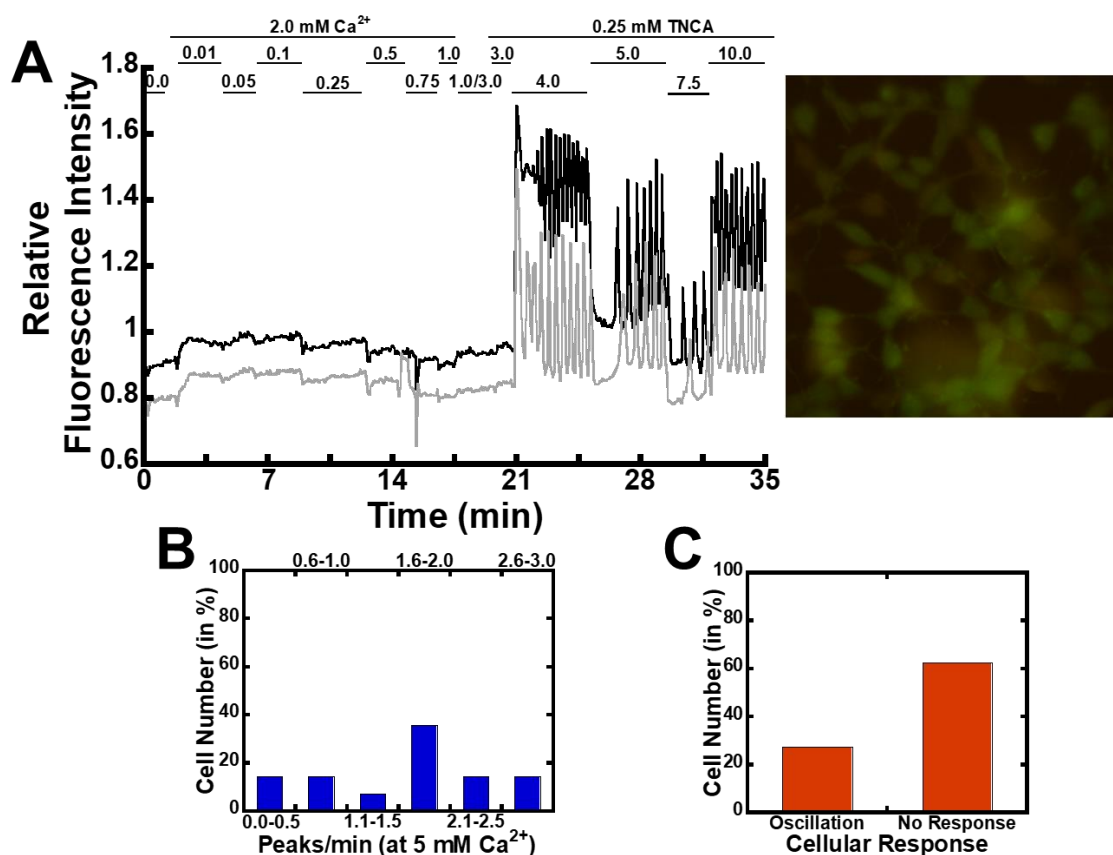


**Figure 4.8 – TNCA live-cell imaging with hCaSR in HEK293 cells.**

**A** – Fura-2 cell imaging of hCaSR with increasing TNCA at sub-activating  $\text{Ca}^{2+}$  levels the CaSR does not react, but with  $\text{Ca}^{2+}$  levels higher than 3 mM the cell is able to respond. **B** – The oscillation frequency bar graph in peaks/min for these cells. **C** – The number of cells which responded and did not respond in percent.

The oscillations with TNCA and  $\text{Ca}^{2+}$  were at a much higher frequency for hCaSR as compared to the WT frequency (Figure 4.8-Figure 4.9). Although there was an increase in oscillation frequency for TNCA treated hCaSR cells over the  $\text{Ca}^{2+}$  only cells, the  $\text{EC}_{50}$  of CaSR remained the same with 2.6 and 2.7 mM, respectively (Figure 4.9 & Figure 4.8B). While the oscillations of hCaSR with



$\text{Ca}^{2+}$  only and TNCA do have an overlap for their frequency of peaks per minute the TNCA oscillations range to high-frequency oscillations (Figure 4.9& Figure 4.8C).

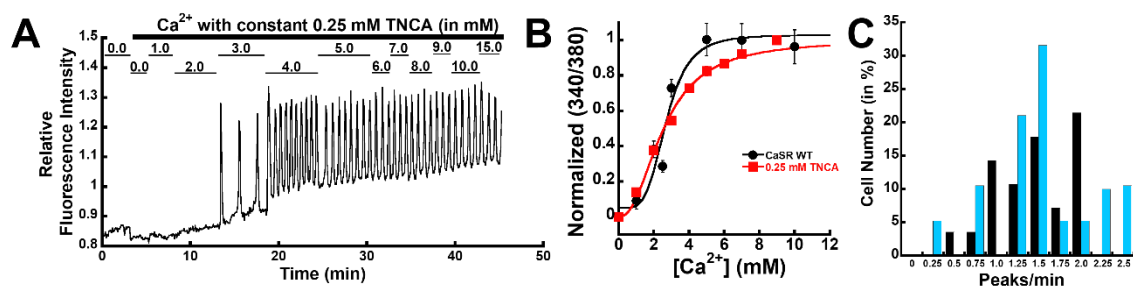


**Figure 4.9 –  $\text{Ca}^{2+}$  and TNCA live-cell imaging with hCaSR in HEK293 cells.**  
**A – Fura-2 cell imaging of hCaSR with 0.25 mM TNCA at increasing  $[\text{Ca}^{2+}]_o$ . B – The  $\text{EC}_{50}$  of WT hCaSR without (black) and with 0.25 mM TNCA (red). C – The oscillation frequency bar graph in peaks/min for WT hCaSR (black) versus with 0.25 mM TNCA (blue).**

While TNCA does not have an effect on the  $\text{EC}_{50}$  of  $\text{Ca}^{2+}$  induced hCaSR response, TNCA does affect  $\text{Mg}^{2+}$  induced hCaSR response as well as recovery of inactivating disease mutations<sup>[287]</sup>.

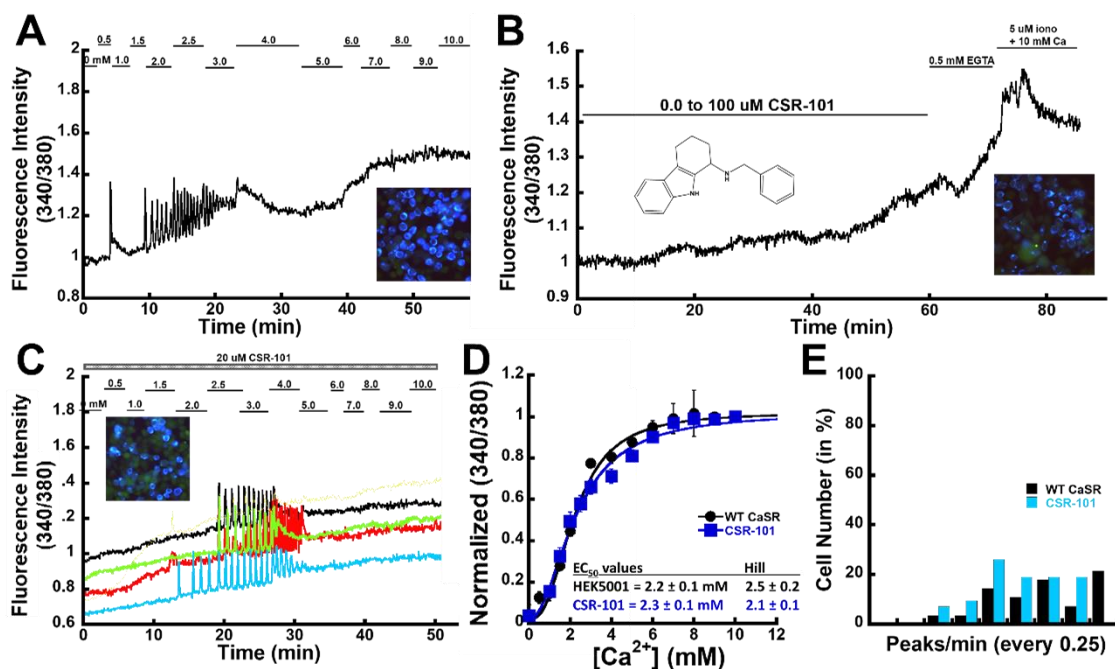


**Figure 4.10 –  $\text{Ca}^{2+}$  and CSR-101 live-cell imaging with hCaSR in HEK293 cells.**  
**A – Fura-2 WT hCaSR imaging with increasing  $[\text{Ca}^{2+}]_o$  elicits an oscillation response. B – CSR-101 is unable to elicit a response on WT hCaSR alone. C – 20  $\mu\text{M}$  CSR-101 with increasing  $[\text{Ca}^{2+}]_o$  on WT hCaSR using Fura-2. D&E – CSR -101 (blue) shows no difference from WT hCaSR (black) in  $\text{EC}_{50}$  or oscillation responses, respectively.**

The CSR-101 solubility in water was 100  $\mu\text{M}$  with toxicity present at 20-40  $\mu\text{M}$ , so we tested 20  $\mu\text{M}$  on hCaSR with  $\text{Ca}^{2+}$  increasing to avoid cell toxicity (Figure 4.10). CSR-101 to 106 did not show any effects on hCaSR cell imaging alone or with  $\text{Ca}^{2+}$  increasing and had no additional effects on oscillation frequency such as TNCA had, data shown is just CSR-101 for a representative plot (Figure 4.10D&E).

#### ***4.2.4 Screening Potential Drugs Using Cell Population Assay***

Single-cell imaging can give a plethora of information such as oscillation frequency, oscillation start and end times,  $\text{EC}_{50}$ , and cellular response rates. The tradeoff being that only a few cells are imaged at a time and several trials need to be done to get a high enough n number to confirm the reliability of the results. Cell population, on the other hand, images an area on the slide which can contain thousands if not hundreds of thousands of cells per experiment, leading to much more reliable, consistent, and quicker results. Cell population analyzes the  $\text{IP}_3$  oscillation signal on a much larger scale utilizing  $n=1,000$  to 1,000,000 as opposed to single-cell imaging where  $n=20-200$ . For cell population we do not see oscillations since with the thousands of cells present we can see the initial  $\text{Ca}^{2+}$  release from the ER as a sharp increase but as all the cells begin to oscillate as slightly varying frequencies, as shown in the single-cell imaging, these varied frequency peaks lead to cancellation of signal to get an average signal line which is called destructive wave interference.

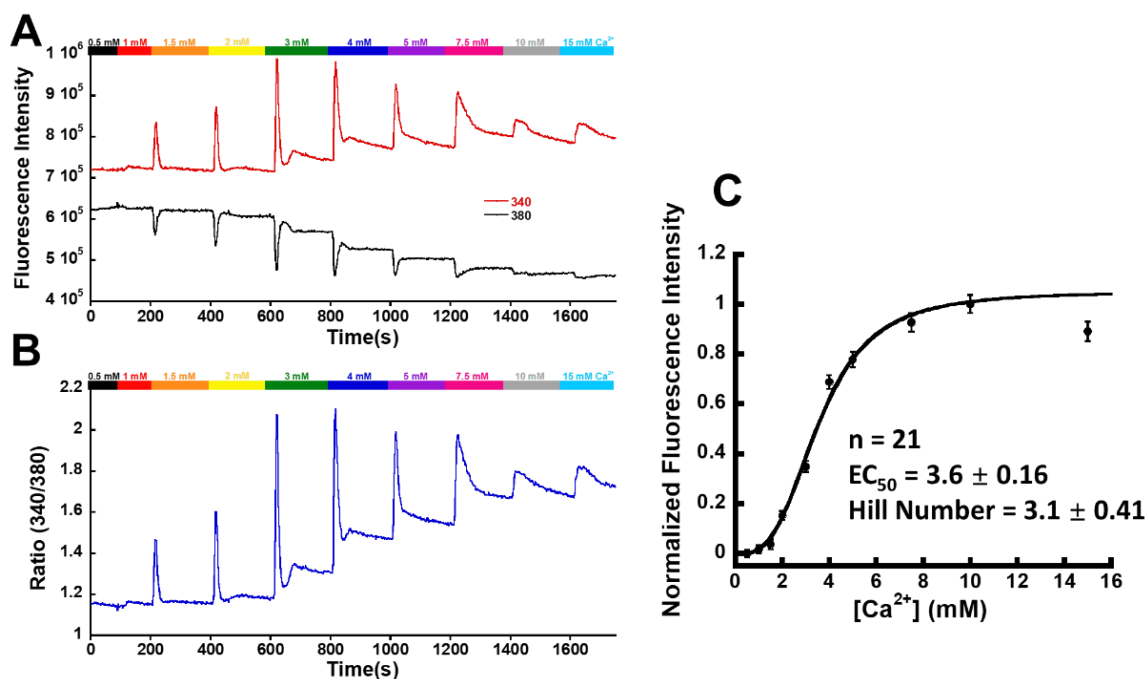


**Figure 4.11 – Representative cell population data for WT hCaSR.**  
**A – Raw data of Ca<sup>2+</sup> additions to WT hCaSR using Fura-2 with Ca<sup>2+</sup> binding to Fura-2 intracellularly leading to an increase in signal at 340 nm and a decrease in the signal at 380 nm simultaneously. B – The ratio of 340/380 nm of A. C – the EC<sub>50</sub> plot of normalized fluorescence intensity ratio versus the increase in Ca<sup>2+</sup> to WT hCaSR where the values are calculated from the plateau of the Fura-2 signal.**

hCaSR treated with increasing levels of Ca<sup>2+</sup> leads to a sharp increase and a just as rapid decrease to a plateau with each increasing Ca<sup>2+</sup> addition leading to less recovery for the plateau back to baseline as more and more Ca<sup>2+</sup> saturates the cytosol and Fura-2 signal (Figure 4.11). The functional EC<sub>50</sub> for Ca<sup>2+</sup> is 3.6 ± 0.16 mM with high functional cooperativity with a Hill number of 3.1 ± 0.41.

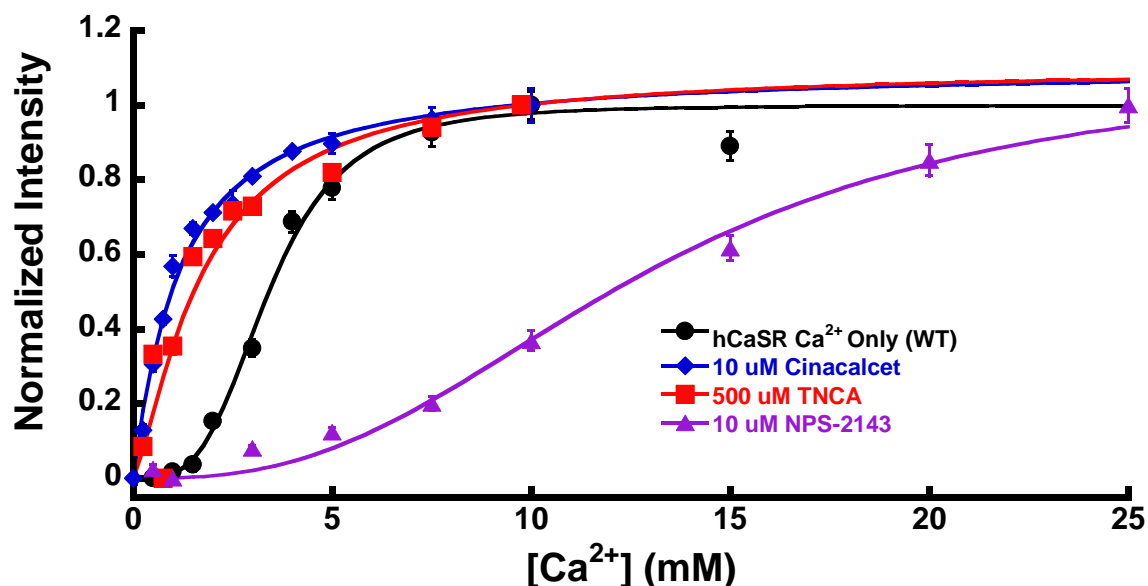


**Figure 4.12 – EC<sub>50</sub> cell population data for WT hCaSR with control compounds.** Cell population EC<sub>50</sub> response plots calculated from the cell population data with the WT hCaSR alone (black), 10 μM cinacalcet (blue), 500 μM TNCA (red), or 10 μM NPS-2143 (purple) in either raw or log scale in HEK5001 cells at n ≥ 3. Cinacalcet is an agonist calcimimetic and NPS-2143 is an antagonist calcilytic.

We tested the WT (Ca<sup>2+</sup> only), TNCA, known agonist cinacalcet, and known antagonist NPS-2143 as controls for what an antagonistic and agonistic result would present as to determine the potential CSR efficacy (Figure 4.12). 500 μM TNCA and 10 μM cinacalcet are agonists with an EC<sub>50</sub> of  $1.74 \pm 0.22$  mM and  $1.14 \pm 0.04$  mM and reduced functional cooperativity with Hill numbers of  $1.3 \pm 0.24$  and  $1.1 \pm 0.05$ , respectively which would be helpful for disease mutations which shift the CaSR activity to the right, such inactivating diseases as FHH and NSHPT (Figure 4.12). Additionally, 10 μM NPS-2143 is an antagonist with an EC<sub>50</sub> of  $12.85 \pm 0.41$  mM and reduced functional cooperativity with a Hill number of  $2.7 \pm 0.22$  for CaSR (Figure 4.12).

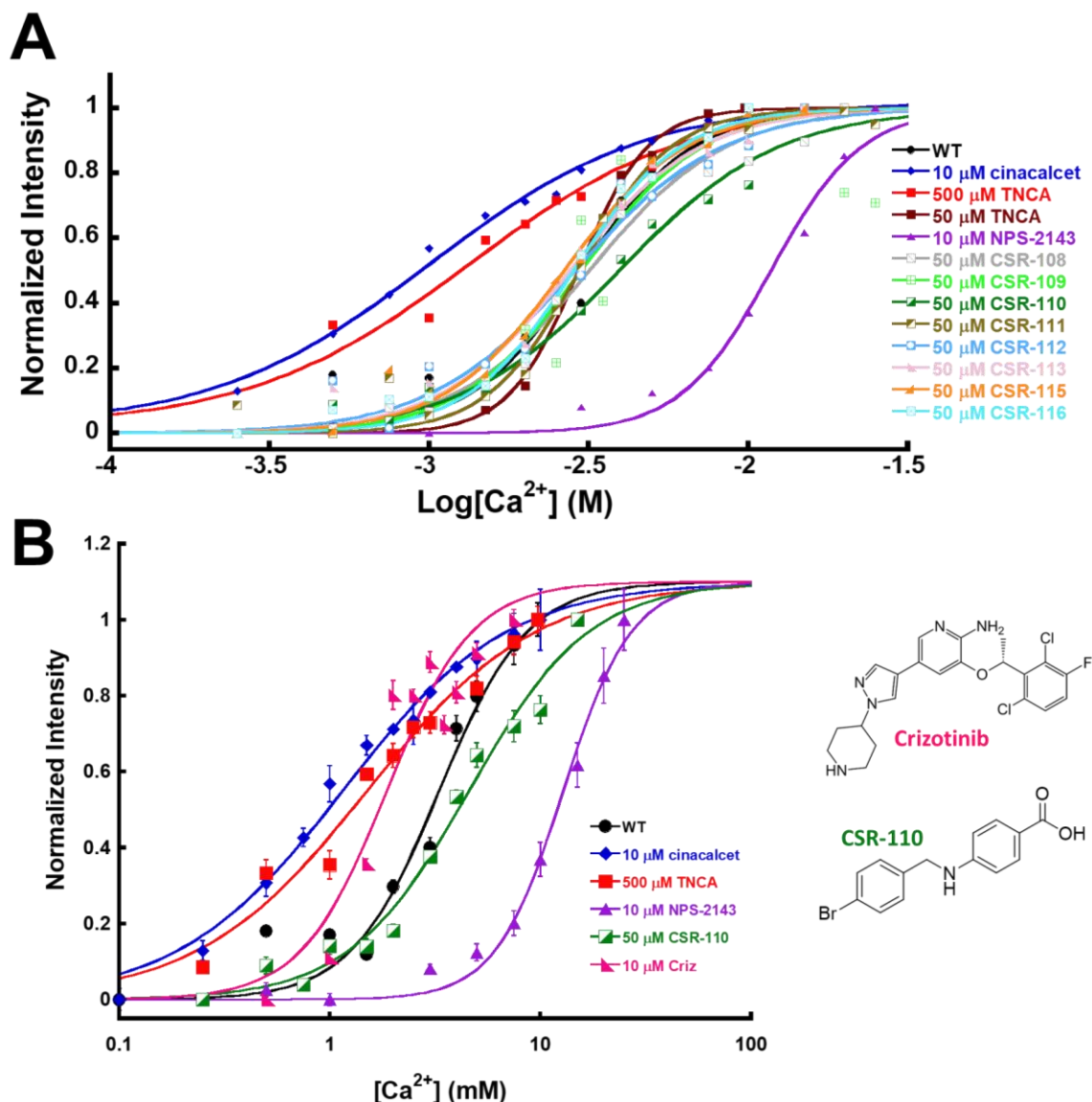


**Figure 4.13 – EC<sub>50</sub> for WT hCaSR with possible lead compounds.**  
 Cell population EC<sub>50</sub> response plots calculated from the cell population data with the WT hCaSR alone (black) and 50 μM of Specs compounds (CSR series), 10 μM cinacalcet (blue), 500 μM TNCA (red), 50 μM TNCA (brick red), or 10 μM NPS-2143 (purple) in log scale in HEK5001 cells at n ≥ 3. Cinacalcet is an agonist calcimimetic and NPS-2143 is an antagonist calcilytic. The best three potential targets are shown in raw scale with controls, 50 μM CSR-110 (green), and 10 μM Crizotinib (magenta).

Cinacalcet and NPS-2143 show us the standard of drug activity for agonists we would expect at least an EC<sub>50</sub> ≤ 2.5 mM and for antagonists we would expect at least an EC<sub>50</sub> ≥ 5 mM Ca<sup>2+</sup> for our potential lead compounds. Additionally, cinacalcet and NPS-2143 are effective at 10 μM and we

expect the CSR compounds to be at least effective at 50  $\mu\text{M}$  to be considered agonists or antagonists. CSR-107 to CSR-116 at 50  $\mu\text{M}$  each are mostly similar to the hCaSR  $\text{Ca}^{2+}$  only response (Figure 4.13). 50  $\mu\text{M}$  CSR-110 has an  $\text{EC}_{50}$  at  $4.6 \pm 0.24$  mM and a Hill number of  $1.5 \pm 0.13$ . While chemotherapy agent Crizotinib at 10  $\mu\text{M}$  has an  $\text{EC}_{50}$  at  $1.9 \pm 0.2$  mM and a Hill number of  $2.1 \pm 0.5$  (Figure 4.13). The rest of the CSR series did not have statistically significant differences in comparison to hCaSR  $\text{Ca}^{2+}$  alone and can be considered nonreactive.

### 4.3 Discussion

We were able to find 16 compounds similar to TNCA for initial drug studies. These compounds CSR-101 to 116 were acquired from Dr. Wang lab and the Specs compound library. We tested these compounds using single-cell imaging or cell population assay in HEK5001 cells stably transfected with hCaSR. We did increasing levels of  $[\text{Ca}^{2+}]_o$  alone or with 10  $\mu\text{M}$  cinacalcet, 500  $\mu\text{M}$  TNCA agonist, 10  $\mu\text{M}$  NPS-2143, 50  $\mu\text{M}$  of each of the CSR series of compounds, and 10  $\mu\text{M}$  of a chemotherapy agent Crizotinib. Agonists TNCA and cinacalcet, as well as antagonist NPS-2143, showed drastic responses compared to  $\text{Ca}^{2+}$  alone. TNCA and cinacalcet both decreased the  $\text{EC}_{50}$  of  $\text{Ca}^{2+}$  alone from  $3.6 \pm 0.16$  mM to  $1.74 \pm 0.22$  mM and  $1.14 \pm 0.04$  mM, respectively, with cinacalcet being a stronger agonist than TNCA (Figure 4.12). Both TNCA and cinacalcet also reduce the functional cooperativity of  $\text{Ca}^{2+}$  alone based on the Hill number reduction of  $3.1 \pm 0.41$  to  $1.3 \pm 0.24$  and  $1.1 \pm 0.05$ , respectively, showing that both of these agonists lead to an over-activated form of CaSR upon binding where cooperativity is reduced since the  $\text{Ca}^{2+}$  are able to bind more readily and cooperativity is no longer as critical (Figure 4.12). NPS-2143, on the other hand, reduced the functional activity and functional cooperativity of hCaSR compared to  $\text{Ca}^{2+}$  alone with an  $\text{EC}_{50}$  of  $12.85 \pm 0.41$  mM and a Hill number of  $2.7 \pm 0.22$  (Figure 4.12). This

reduction of cooperativity is not as extreme as seen with the agonists since instead of no longer needing as much functional cooperativity in the case of over-activated agonist bound hCaSR the antagonist is actually disrupting the potential functional cooperativity which further potentiates the loss of function of hCaSR as seen by the decrease in functional activity by the lower  $EC_{50}$  value. The CSR compounds did show some effects on hCaSR using cell population studies which showed CSR-1110 as an antagonist with a decrease in functional activity as seen by the weaker  $EC_{50}$  of  $4.6 \pm 0.24$  mM as well as having a reduction in functional cooperativity similar to NPS-2143 but even more disruptive to functional cooperative binding with a Hill number of  $1.5 \pm 0.13$  (Figure 4.13). Additionally, Crizotinib an agonist, but still weaker than TNCA or cinacalcet with an  $EC_{50}$  of  $1.9 \pm 0.2$  mM and since this over activated form is intermediate between cinacalcet and  $Ca^{2+}$  alone the functional cooperativity is still necessary for this bound hCaSR version as seen by a Hill number of  $2.1 \pm 0.5$  (Figure 4.13). Both of these compounds are good potential calcimimetic and calcilytic drug lead potential to further potentiate their activity and effect on hCaSR with further compound modification.

Future research can be done to follow these routes of lead optimization. We did use the LADI library program to design potential lead drugs and found that modification of the R group on TNCA and a reduction of TNCA from three rings to two rings had the best Sybyl docking scores (Figure 4.3). Future collaborative efforts will be targeted to synthesizing these compounds to test new potential CaSR therapeutic targets.

## 4.4 Materials and Methods

### 4.4.5 Cell culture and transfection

Monolayer cultures of HEK293 cells were purchased from American Type Culture Collection (ATCC CRL-1573) and maintained in Dulbecco's modified Eagle's medium (DMEM) supplemented with 10% fetal bovine serum (FBS) and high glucose (4.5 g/L) at 37°C. WT CaSR or its mutants were transfected into HEK293 cells using Lipofectamine 2000 or 3000 (Life Technologies) by following the manufacturer's instructions. Coverslips are incubated in transfection solution 4-6 hr. Transfection solution is aspirated and fresh DMEM is added and imaging is performed 24-48 hr later.

### 4.4.6 Measurement of $[Ca^{2+}]_i$ changes in single CaSR-transfected cells

The CaSR WT was transiently transfected into HEK293 cells grown on coverslips and cultured for 48 hr at 37°C. 1  $\mu$ M Fura 2-AM is added into physiological Ringer buffer (10 mM HEPES, 121 mM NaCl, 2.4 mM  $K_2HPO_4$ , 0.4 mM  $KH_2PO_4$ , 1.2 mM  $MgCl_2$ , 1.2 mM  $CaCl_2$  and pH 7.4). The addition of the non-ionic detergent Pluronic ® F-127 can assist in the dispersion of the nonpolar AM ester in aqueous media. The cells are incubated in the Fura-2 AM and F-217 solution for 15–20 minutes at 37°C. The cells were washed twice with Ringer buffer, without calcium. The coverslips were mounted on a bath chamber and placed on the stage of a Leica DM6100B inverted microscope with a cooled EM-CCD camera. The cells were alternately illuminated with 340 or 380 nm light using a Till Polychrome V monochromator and xenon lamp, and the fluorescence at emission wavelength 510 nm was recorded in real-time as the  $[Ca^{2+}]_o$  and/or  $[Mg^{2+}]_o$  was increased in a stepwise manner in the presence or absence of 0.25 mM TNCA in buffer (10 mM HEPES, 155 mM NaCl, 5 mM KCl, 2 mM  $NaH_2PO_4$ , and 0.5 mM  $MgCl_2$ ) (pH 7.4). The ratio of the emitted fluorescence intensities resulting<sup>[23]</sup> from excitation at both



wavelengths was utilized as a surrogate for changes in  $[Ca^{2+}]_i$  and was further plotted and analyzed as a function of  $[Ca^{2+}]_o$ . All experiments were performed at room temperature. The signals from 2 to 100 single cells were recorded for each measurement. Oscillations were identified as three successive fluctuations in  $[Ca^{2+}]_i$  after the initial peak.

#### ***4.4.7 Intracellular calcium concentration in cell population by fluorimetry***

The  $[Ca^{2+}]_i$  responses of wild type (WT) CaSR and its mutants were measured as described by Huang et al.<sup>[259]</sup>. Briefly, CaSR-transfected HEK293, or stably transfected HEK5001, cells were grown on  $13.5 \times 20$  mm coverslips. After the cells reached 90% or higher confluency, they were loaded by incubation with 2  $\mu$ M Fura-2 AM in 20 mM HEPES, containing 125 mM NaCl, 5 mM KCl, 0 mM  $CaCl_2$ , 0.5 mM  $MgCl_2$ , 1 mM  $NaH_2PO_4$  (pH 7.4) for 15 mins at 37°C and then washed twice with  $Ca^{2+}$ -free Ringer's buffer. The coverslips with transfected, Fura-2-loaded HEK cells were placed diagonally in 3-mL quartz cuvettes containing  $Ca^{2+}$ -free Ringer's buffer. The fluorescence spectra at 510 nm were measured during stepwise increases in  $[Ca^{2+}]_o$  with alternating excitation at 340 or 380 nm on a QM1 fluorescence spectrophotometer (Photon Technology International). The ratio of the intensities of the emitted light at 510 nm when excited at 340 or 380 nm was used to monitor changes in  $[Ca^{2+}]_i$ . The  $EC_{50}$  and Hill constants were fitted using the

Hill equation,  $\Delta S = \frac{[M]^n}{K_d^n + [M]^n}$ , where  $\Delta S$  is the total signal change in the equation,  $K_d$  is the

apparent binding affinity,  $n$  is the Hill coefficient, and  $[M]$  is the free metal concentration. The emission ratio of 340/380 was calculated and used to reflect the changes in  $[Ca^{2+}]_i$  when different concentrations of  $[Mg^{2+}]_o$  were applied to the cells. To examine the coactivation of CaSR by TNCA and  $[Mg^{2+}]_o$  or  $[Ca^{2+}]_o$ , different concentrations of TNCA were placed in the experimental buffer with a fixed concentration of  $[Ca^{2+}]_o$  and varying concentrations of  $[Mg^{2+}]_o$ , or vice versa,

as described in the Results section. The effects of other ligands were analyzed by comparing the changes in  $[Ca^{2+}]_i$  produced by  $[Mg^{2+}]_o$  alone or by co-application of  $Mg^{2+}$  with other ligands. The  $EC_{50}$  of  $[Mg^{2+}]_o$  obtained during incubation with various concentrations of TNCA is compared with that observed in the presence of  $[Mg^{2+}]_o$  alone. The  $EC_{50}$  changes were plotted as a function of TNCA concentration, and the curve was fit to the Hill equation,  $\Delta S = \frac{[M]^n}{K_d^n + [M]^n}$ , where  $\Delta S$

is the total signal change in the equation,  $K_d$  is the apparent binding affinity,  $n$  is the Hill coefficient, and  $[M]$  is the free metal concentration. The activation of CaSR by the TNCA, functioning as a co-agonist with  $[Mg^{2+}]_o$ , was indicated by the increasingly left-shifted  $EC_{50}$  for  $[Mg^{2+}]_o$  as the concentration of TNCA increases.

## 5 Visualizing Subcellular Ca<sup>2+</sup> Dynamics Using Designed Ca<sup>2+</sup> Sensors

### 5.1 Introduction

The endoplasmic/sarcoplasmic reticulum (ER/SR) are the primary internal calcium storage for cells with concentrations in the mM range and regulates cellular calcium dynamics. In addition to regulating Ca<sup>2+</sup> dynamics, the ER also is responsible for protein synthesis, modification, trafficking, lipid synthesis, and drug metabolism. Protein synthesis imbalance from the demand of synthesis and the capacity for protein storage in the ER can lead to ER stress, from the accrual of misfolded or unfolded proteins, which then causes cellular apoptosis<sup>[305-307]</sup>. There are three key players for ER Ca<sup>2+</sup> dynamic regulation the ryanodine receptor (RyR) for Ca<sup>2+</sup> release down to the ms range, the inositol (1,4,5)-trisphosphate receptor (IP<sub>3</sub>R) for Ca<sup>2+</sup> release to the second range, and the sarco/endoplasmic reticulum calcium-ATPase (SERCA) pump for Ca<sup>2+</sup> refilling in the ER in the sub-second range (Figure 5.1). Being able to examine the distinct Ca<sup>2+</sup> dynamics through all three of these major players and at the kinetic rates they each present with as well as cell-specific kinetic rates such as heart and skeletal muscles in the 1-100 ms range is critical for further understanding of the ER/SR Ca<sup>2+</sup> dynamics. These receptors and pump which regulate Ca<sup>2+</sup> dynamics have been found to have heterogeneous expression and differential Ca<sup>2+</sup> dynamics depending on expression in ER/SR as well as the varying cell types. The morphology of the ER/SR was initially considered to be a uniform system which could communicate and send Ca<sup>2+</sup> throughout but has recently been found to be more heterogeneous not only in protein distribution but also in pockets of Ca<sup>2+</sup> signaling either due to binding of CaBPs or having Ca<sup>2+</sup> microdomains<sup>[308-310]</sup>.

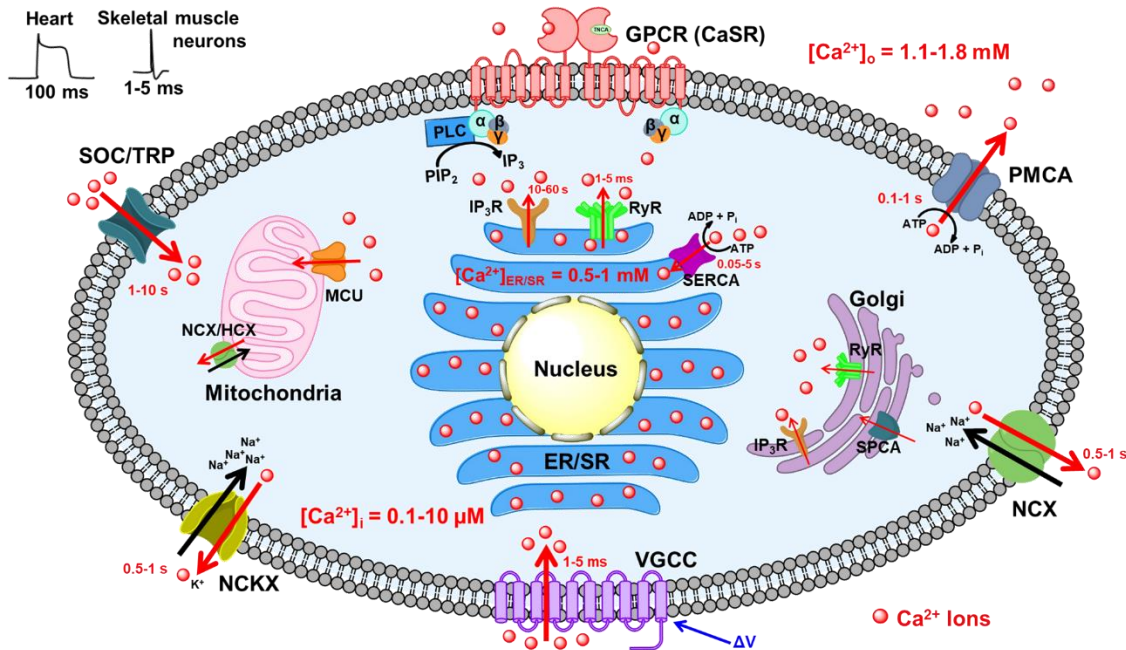


**Figure 5.1 – ER/SR calcium signaling inside the cell.**

$\text{Ca}^{2+}$  signaling dynamics in the cell to communicate the  $\text{Ca}^{2+}$  homeostasis between the high  $[\text{Ca}^{2+}]_o$  extracellularly in the mM range and the low  $[\text{Ca}^{2+}]_i$  intracellularly in the  $\mu\text{M}$  range is regulated by a multitude of proteins as well as by the internal organelle  $\text{Ca}^{2+}$  storage in the ER/SR in the mM range. These proteins operate in a variety of differing rates of  $\text{Ca}^{2+}$  transport from the millisecond (ms) to seconds (s) range. On the plasma membrane are channels that either remove  $\text{Ca}^{2+}$  from the cytosol to maintain the  $\mu\text{M}$   $[\text{Ca}^{2+}]_i$  or that bring  $\text{Ca}^{2+}$  back into the cytosol from the  $[\text{Ca}^{2+}]_o$ . The plasma membrane  $\text{Ca}^{2+}$  ATPase (PMCA), the sodium-calcium exchanger (NCX), and the potassium-dependent sodium-calcium exchanger (NCKX) are just a few proteins which pump  $\text{Ca}^{2+}$  out of the cell in exchange for energy adenosine triphosphate (ATP) or gradient transfer ( $\text{Na}^+/\text{K}^+$ ). On the other hand, proteins such as store-operated channels (SOCs), transient receptor potential (TRP) channels, and voltage-gated calcium channels (VGCCs) deliver  $\text{Ca}^{2+}$  from the extracellular into the cytosol.  $[\text{Ca}^{2+}]_i$  concentration is also further regulated by ER proteins such as the  $\text{IP}_3\text{R}$ , RyR, and SERCA pump with either release  $\text{Ca}^{2+}$  from the ER/SR into the cytosol or pump  $\text{Ca}^{2+}$  back into the ER/SR, respectively. Additionally, GPCRs such as CaSR can sense  $[\text{Ca}^{2+}]_o$  and lead to a production of  $\text{IP}_3$  which then binds the  $\text{IP}_3\text{R}$  and release ER/SR  $[\text{Ca}^{2+}]_i$  into the cytosol. The  $[\text{Ca}^{2+}]_i$  is also regulated by the mitochondria by the mitochondrial calcium uniporter (MCU) and the NCX/hydrogen-calcium exchanger (HCX) whereas the Golgi is regulated by  $\text{IP}_3\text{R}$ , RyR and secretory pathway  $\text{Ca}^{2+}$ -ATPase (SPCA).

The RyR,  $\text{IP}_3\text{R}$ , and SERCA pump, as well as ER  $\text{Ca}^{2+}$  signaling, are critical for cellular function and stability where dysfunction leads to a multitude of disease states and cell death. ER  $\text{Ca}^{2+}$

dysregulation has been linked to multiple neurodegenerative diseases such as Alzheimer's disease, Parkinson's disease, schizophrenia, etc. Mutations on the RyR, IP<sub>3</sub>R, and SERCA pump are associated with malignant hyperthermia, arrhythmias, skin disease, central core disease, deafness, and diabetes<sup>[153, 311-318]</sup>. The complex and not fully understood ER/SR morphology, Ca<sup>2+</sup> microdomains, and protein subcellular distribution differences provide challenges in further understanding the Ca<sup>2+</sup> dynamics of the ER/SR as well as the relation to disease states.

**Table 5.1 – Expression of ER/SR proteins in different cell lines.**

Cells	IP <sub>3</sub> R	RyR	SERCA pump
C2C12	Type 1 and 3	Type 1 and 3	Type 1, 2a, 2b
Cos-7	Type 1-3	TBD	TBD
HEK293	Type 1-3	Type 1 and 2	Type 2b, 3d, and 3e
HeLa	Type 1-3	Type 2	Type 2b, 3d, and 3e

TBD = To be determined

Examining multiple common cell types utilizing antibody staining, western blot, or DNA/mRNA level analysis shows RyR, IP<sub>3</sub>R, and the SERCA pump are expressed in each cell type with varying isoforms (Table 5.1)<sup>[44, 319-329]</sup>. Many cell lines have yet to be investigated for these protein expressions, isoform type, and expression patterns. Research is continually evolving and showing new discoveries in isoforms of these ER/SR proteins as well as illuminating their expression levels in a multitude of cell types. Thus this is an ongoing field of study for a better understanding of cellular protein expression. In order to investigate these crucial gaps in ER Ca<sup>2+</sup> dynamics, we designed a Ca<sup>2+</sup> sensor targeted to the ER/SR with fast kinetics capable of capturing fast ms range responses as well as slower seconds to minutes range as well as having a K<sub>d</sub> in the mM range for cellular imaging studies.

Although FRET pairs are the more commonly used type of  $\text{Ca}^{2+}$  sensor, their distance dependence allows room for intrusion from other molecules in physiological conditions. Due to the electrostatic nature of  $\text{Ca}^{2+}$  ions,  $\text{Ca}^{2+}$  binding sites are formed by residues with oxygen atoms, especially charged residues such as Asp and Glu<sup>[330]</sup>. Using our established expertise for designing novel  $\text{Ca}^{2+}$  sensors, by utilizing a diverse number of charged ligand residues (2-5) in the intended metal binding site in EGFP, our group engineered several novel EGFP-based sensors, Ca-G1 and CatchER (Calcium sensor for detecting high concentration in the ER), as well as a modified improved version of CatchER called CatchER<sup>+</sup> (Figure 5.2)<sup>[331-334]</sup>. Ca-G1 was created by the addition of a single EF-hand motif and is valuable as a ratiometric sensor, but has a small dynamic range and slow kinetics<sup>[335]</sup>. CatchER and CatchER<sup>+</sup> exhibit the largest  $\text{Ca}^{2+}$  induced fluorescence changes over other available sensors, a comparable  $K_d$  for ER/SR measurements, and fast kinetics<sup>[331-334]</sup>. The electrostatics of the binding site, the area around it, and the subsequent effect on the chromophore influence the fluorescent and kinetic properties of CatchER and CatchER<sup>+</sup><sup>[331-334]</sup>. CatchER has a large dynamic range at 510 nm when excited at both 395 and 488 nm (Figure 5.2)<sup>[331-334]</sup>. CatchER exhibits an unparalleled  $\text{Ca}^{2+}$  off rate of  $700 \text{ s}^{-1}$  allowing CatchER and CatchER<sup>+</sup> to measure  $\text{Ca}^{2+}$  release from the ER/SR in various cell types<sup>[331-334, 336]</sup>. CatchER<sup>+</sup> had three mutations, S175G, Y39N, and S30R, to improve thermostability and brightness at  $37^\circ\text{C}$  for enhanced use *in situ* experiments (Figure 5.2). All of our designed sensors are advantageous for several reasons, because they are able to be readily targeted to cellular compartments containing  $\text{Ca}^{2+}$ , they have fast kinetics and affinities to cover the broad range of  $[\text{Ca}^{2+}]$  in different organelles, and a direct  $\text{Ca}^{2+}$  binding site not using a CaBP binding motif which improves the kinetic rate of binding and releasing  $\text{Ca}^{2+}$ .

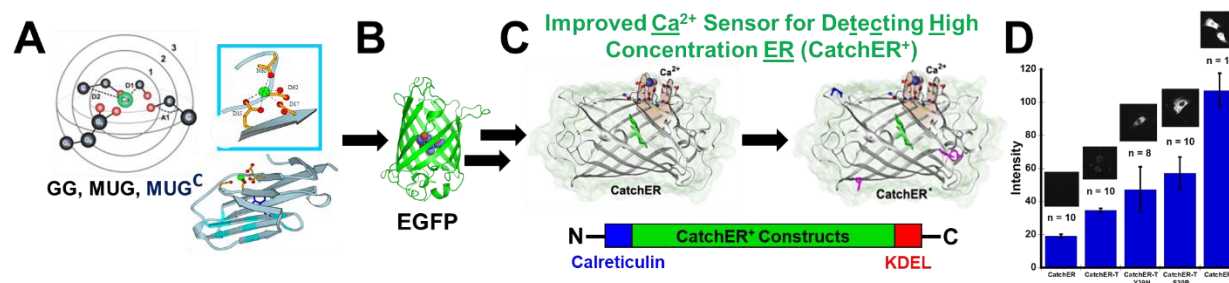


**Figure 5.2 – CatchER<sup>+</sup> sensor design and improvement process.** Shows that the design process for CatchER and CatchER<sup>+</sup>. **A** – We identified common Ca<sup>2+</sup> binding motifs based on natural Ca<sup>2+</sup> binding proteins, then designed algorithms to calculate potential Ca<sup>2+</sup> binding sites (GG, MUG, and MUG<sup>C</sup>). **B&C** – We applied the Ca<sup>2+</sup> binding site prediction onto EGFP to create CatchER, with retention sequences KDEL and calreticulin for ER/SR retention. **C** – Mutations S175G, Y39N, and S30R to CatchER to generate the improved CatchER<sup>+</sup>. **D** – Improvement mutations made between CatchER and CatchER<sup>+</sup> at 37°C.

We confirmed that the CatchER<sup>+</sup> sensor can be successfully transfected into a cell and is uniformly expressed throughout the ER using confocal imaging in comparison to our CatchER<sup>+</sup> sensor and ER Tracker Red (Figure 5.3).

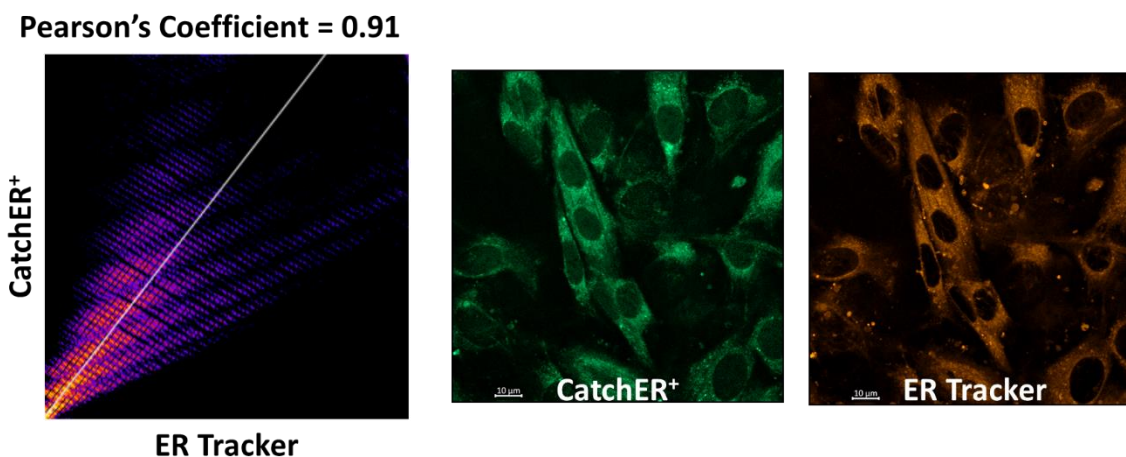


**Figure 5.3 – CatchER<sup>+</sup> confocal imaging in C2C12 with ER Tracker.** Pearson's coefficient for colocalization of ER Tracker red 555 dye (orange) and CatchER<sup>+</sup> (green) 488 nm.

The Pearson's correlation coefficient (PCC) shows the relationship between two variables where a value of 1 is a perfect positive correlation, and a value of 0 is no linear correlation. Here we see

with a PCC value of 0.91 that CatchER<sup>+</sup> and ER Tracker Red have a high correlation showing that CatchER<sup>+</sup> is successfully targeted to the ER and is uniformly expressed throughout (Figure 5.3). With the successful design, targeting, and imaging of our CatchER<sup>+</sup> sensor we could then begin testing it in live-cell imaging.

## 5.2 Results

### 5.2.1 Using Epifluorescence Imaging to Analyze CatchER<sup>+</sup> Function

We examined CatchER<sup>+</sup> in C2C12 mouse myoblast muscle cells, HEK293 human embryonic kidney cells, Cos-7 fibroblast-like monkey kidney cells, and HeLa human epithelial adenocarcinoma cells. We looked at 4-cmc to initiate a release of Ca<sup>2+</sup> through the RyR from the ER leading to a signal decrease of CatchER<sup>+</sup> (Figure 5.4A). We also treated with CPA to reversibly inhibit the SERCA pump which refills the ER and while inhibited leads to a decrease in Ca<sup>2+</sup> from the ER without able to refill the ER until washed away (Figure 5.4B). Lastly, we looked at activating the IP<sub>3</sub>R indirectly since IP<sub>3</sub> is not cell permeable we instead had to activate a GPCR to produce IP<sub>3</sub> by either ATP for the purinergic receptor (P2YR) or with HeLa cells histamine for the histamine receptor (H1R) (Figure 5.4C). Since this method of Ca<sup>2+</sup> release is an indirect release of Ca<sup>2+</sup> from the ER then the signal is lower than direct compounds which illicit direct release from the ER. Since ATP must go through a GPCR to illicit IP<sub>3</sub> production, then the amount of IP<sub>3</sub>R activation is less than just adding IP<sub>3</sub> itself would be. Since IP<sub>3</sub> does not pass the plasma membrane, then this indirect method must be utilized. With this method, we can only see a 5-15% release of Ca<sup>2+</sup> from the ER. This is much lower than the 20-50% release we see with 4-cmc and CPA, which leads to a higher signal to noise (S/N) ratio.



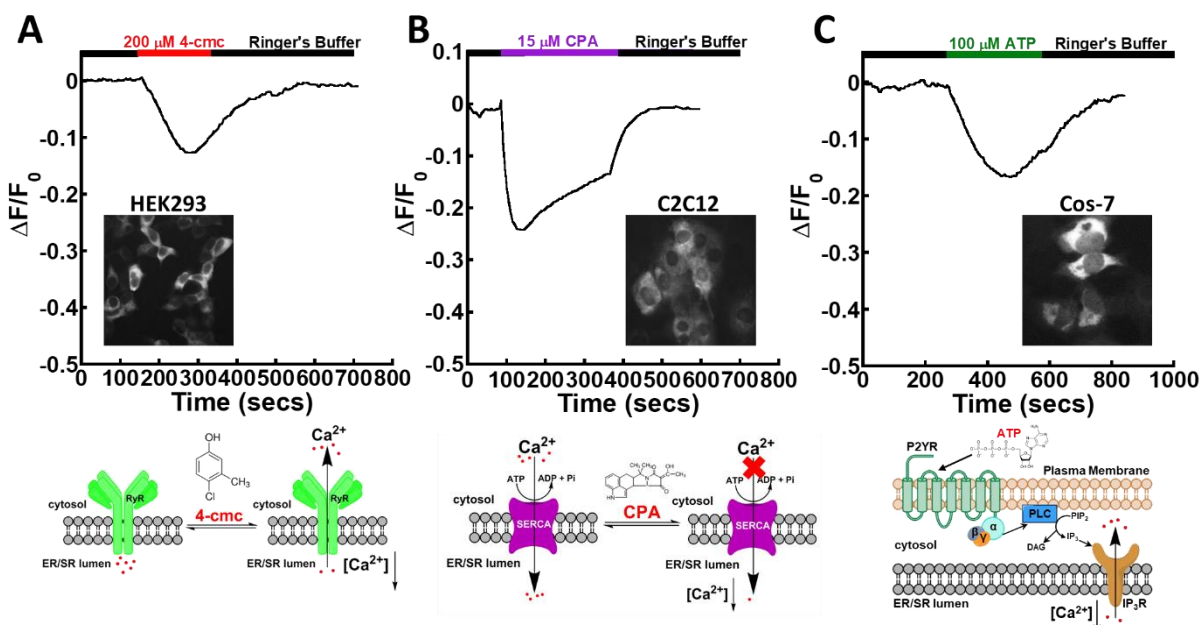


**Figure 5.4 – CatchER<sup>+</sup> epifluorescence in response to 4-cmc, CPA, and ATP.**

**A – Small volume 200 μM of 4-cmc was added to initiate a release of Ca<sup>2+</sup> from the ER in HEK293 cells with a representative plot. Below is the schematic of 4-cmc activation on the RyR, which releases Ca<sup>2+</sup> from the ER. B – Small volume 15 μM of CPA was added to initiate a release of Ca<sup>2+</sup> from the ER in C2C12 cells with a representative plot. Below is the schematic of CPA inhibition of the SERCA pump, which reduces ER Ca<sup>2+</sup> since the ER [Ca<sup>2+</sup>] cannot refill. C – Small volume 100 μM of ATP was added to initiate a release of Ca<sup>2+</sup> from the ER in Cos-7 cells with a representative plot. Below is the schematic of ATP indirect activation on the IP<sub>3</sub>R, which releases Ca<sup>2+</sup> from the ER after production of IP<sub>3</sub> from P2YR activation.**

These representative plots are not only for the overall responses seen in HEK293, C2C12, and Cos-7 cells in response to each drug but also for the overall responses seen for each drug over each cell line. All of these cell lines responded similarly to each compound under epifluorescence conditions (Table 5.2).

**Table 5.2 – Epifluorescence  $\Delta F/F_0$  responses in each cell type to 4-cmc, CPA, and ATP.**

Cell Type	Drug Type	Epifluorescence Imaging		
		[Drug] ( $\mu\text{M}$ )	$\Delta F/F_0$ (%)	# of cells
C2C12	4-cmc	200	$18.6 \pm 1.1$	43
Cos-7	4-cmc	200	$7.3 \pm 0.6$	19
HEK293	4-cmc	200	$12.0 \pm 0.8$	8
HeLa	4-cmc	ND	ND	ND
C2C12	CPA	15	$24.2 \pm 1.6$	35
Cos-7	CPA	15	$26.0 \pm 1.9$	10
HEK293	CPA	15	$21.0 \pm 0.8$	14
C2C12	ATP	100	$10.3 \pm 1.0$	14
Cos-7	ATP	100	$13.0 \pm 1.0$	9
HEK293	ATP	100	$6.0 \pm 1.5$	4

Data represents mean  $\pm$  SEM error. ND – No data. Data collected at room temperature.

$\Delta F/F_0$  – change in fluorescence intensity over initial intensity.

There were some differences such as RyR response to 4-cmc being the highest at  $18.6 \pm 1.1\%$  for C2C12 since, as a mouse muscle cell line, there is a higher expression of RyR in order for muscle contraction to occur (Table 5.2). All three cell lines were very similar and within error of each other for CPA responses while the ATP responses were similar for C2C12 and Cos-7 but almost half the response for HEK293 cells which may be due to less P2YR expression (Table 5.2).

### 5.2.2 *Highly Inclined and Laminated Optical Sheet (HILO) Microscopy*

Analyzing the  $\text{Ca}^{2+}$  dynamic changes of CatchER using epifluorescence we noticed consistent changes in  $\text{Ca}^{2+}$  release between cells and trials, but we were not able to resolve subcellular changes throughout the structure of the ER due to the low imaging quality in epifluorescence as well as the contamination in light from the other layers of the cell. There is an array of imaging available to analyze processes on the cellular level. Getting high-resolution images to examine subcellular ER/SR morphology as well as potential microdomains on live cells is not simplistic. Often to achieve high resolution with confocal microscopy fixatives are required, which can damage or alter the organelles wanting to be investigated. Additionally, when wanting to examine a very narrow area of the cells more advanced microscopy is needed than simple light or fluorescence microscopy can provide, both which often give the overall signal of the cell and not in specific organelles. Total Internal Reflection Fluorescence (TIRF) microscopy excites only a narrow slice of tissue (~100 nm) which can reduce background and enhance visibility to organelle and membrane-localized processes. A significant drawback of confocal and TIRF microscopy is the cost of the system. Since TIRF has the restriction of only penetrating 20-100 nm into the surface of the cell because of the angle of reflection, there is a lack of distinguishing the full features of the ER/SR within the cell which would encompass the entirety of the cell from top to bottom, and that a cell diameter can average 25  $\mu\text{m}$ . Thus, we switched gears to another microscopy technique called highly inclined and laminated optical sheet (HILO) microscopy<sup>[337]</sup> (Figure 5.5). Both confocal microscopy and TIRF microscopy can provide high imaging capability to resolve ER structure details. Nonetheless, none of them are appropriate for imaging calcium dynamics probed by the CatchER<sup>+</sup> expressed in organelles and the microdomains in the subcellular regions of the ER<sup>[338-340]</sup>.

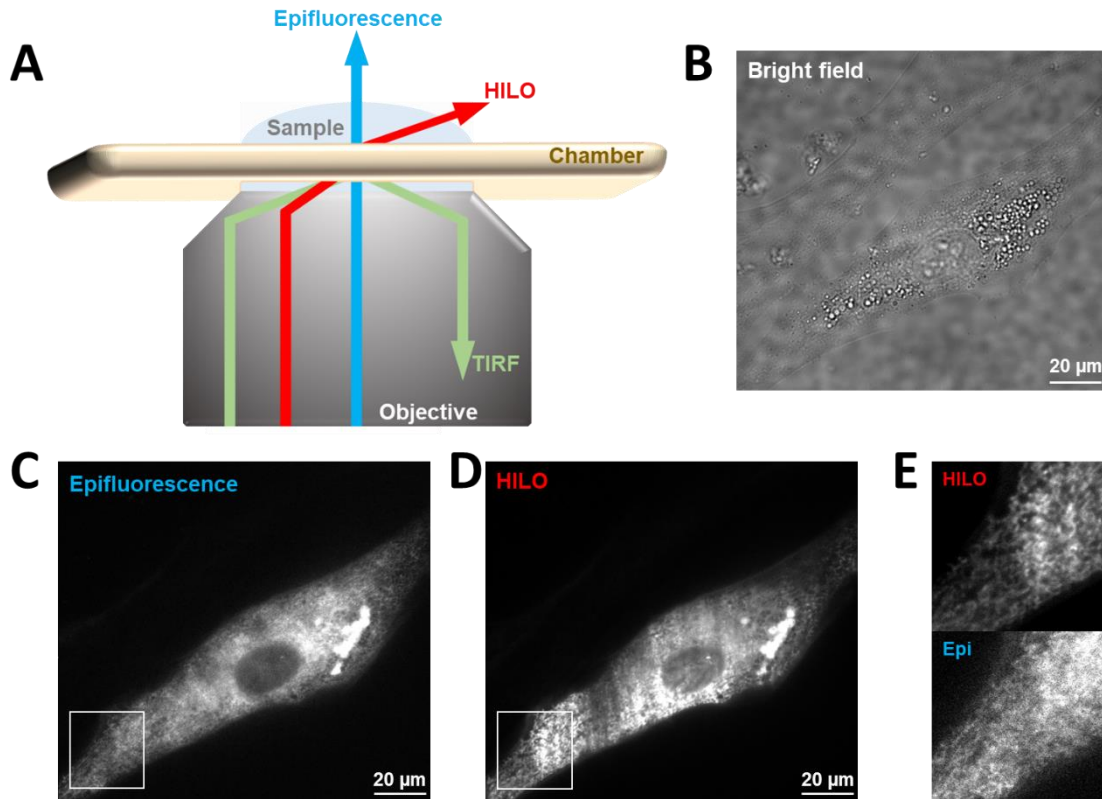


**Figure 5.5 – CatchER<sup>+</sup> captures a highly defined ER-network pattern using HILO. A – Model of differences in light angles between epifluorescence, TIRF, and HILO imaging. B-D – Bright field (B), epifluorescence 488 nm (C), and HILO 488 nm (D) images of C2C12 cell transfected with CatchER<sup>+</sup>, respectively. E) Enlargement of white box area from C-D of the ER network under epifluorescence (bottom) and HILO (top) conditions.**

The former lacks the required temporal resolution for imaging fast calcium dynamic responses, and the latter is only useful for imaging biological events within a few hundreds of nanometers from the coverslip. The ER is best expressed throughout the whole cell that includes the center of the cell around the nucleus, which would be several  $\mu\text{m}$  into the cell. It is critical to see the ER structure details for any future microdomain studies where there might be an uneven distribution of CaBPs throughout the lumen of the ER. For the limitations mentioned on confocal, epifluorescence, and TIRF microscopy, we turned to HILO microscopy<sup>[337]</sup> to best accomplish

visualization of ER details at a depth of 10  $\mu\text{m}$  while retaining the high spatial resolution and temporal resolution.

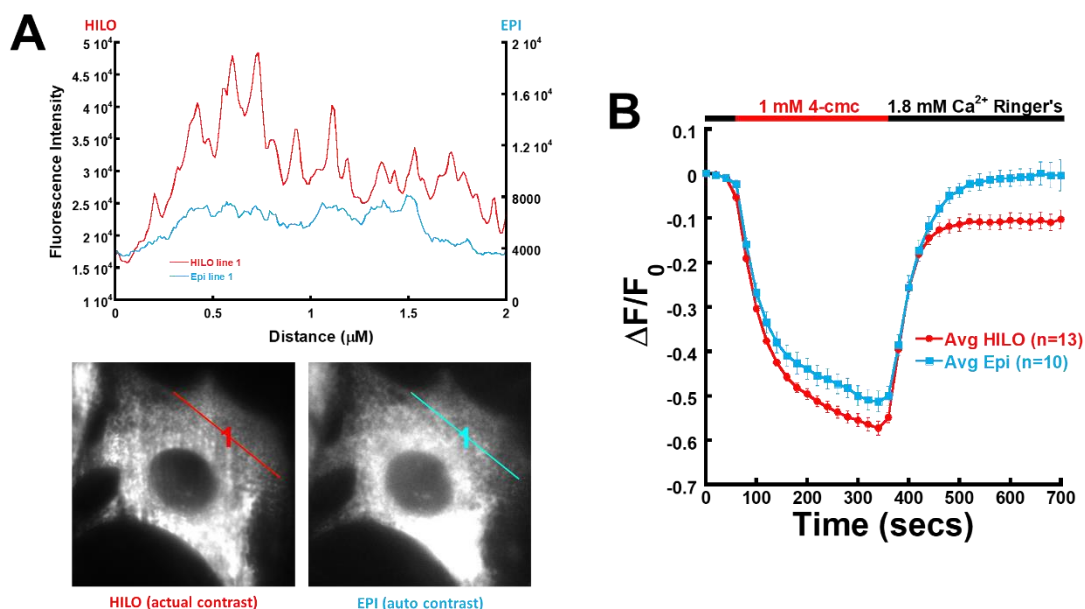


**Figure 5.6 – Epifluorescence and HILO imaging comparison.**

**A – Cross-section along the same region and same cell under epifluorescence imaging (blue) or HILO imaging (red). B – The average signaling response to 1 mM 4-cmc over the same time points using HILO (red) and epifluorescence (blue).**

This technique also reduces the fluorescence background and images at high S/N by selectively exciting the sample within submicron thickness allowing the capability to examine microdomains of the ER without Z-axis signal perturbation<sup>[341, 342]</sup>. Epifluorescence, TIRF, and HILO microscopy all rely on the same optical settings with the difference being in their respective incidence angles of the laser where epifluorescence is ideal for full cell analysis, TIRF is better for near cell surface analysis, and HILO is preferable for central cellular analysis without other regions overlap such as with epifluorescence (Figure 5.5).

Immediately, we could observe clearly defined ER network patterns when imaging CatchER<sup>+</sup> in C2C12 cells under HILO conditions as compared to the epifluorescence conditions with the same

gain, exposure and instrument settings, with the only variance being the angle of incidence of the laser (Figure 5.5).

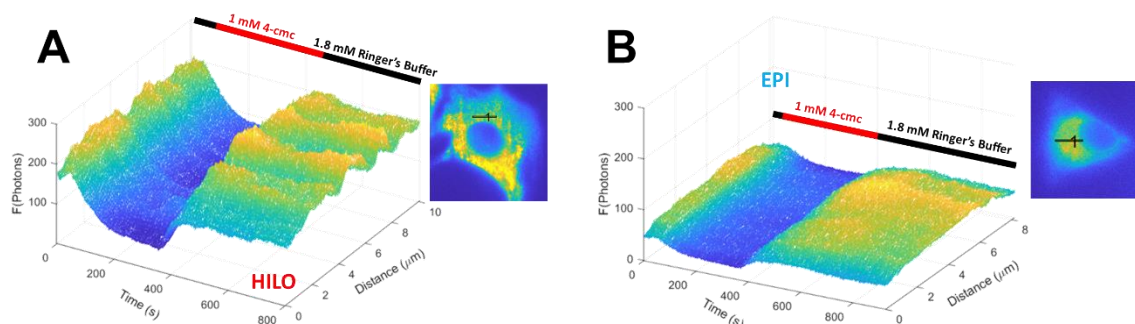


**Figure 5.7 – Epifluorescence and HILO cross-sectional 3D response comparison. Cross-sections of the signaling response to 1 mM 4-cmc in HILO (A) and epifluorescence (B) in C2C12 cells.**

To quantitatively compare the imaging quality from the epifluorescence and HILO conditions, we further used cross-section analysis of the ER network in the same region of a C2C12 cell. Clearly, we can see that the epifluorescence cross-sectional intensity profile of ER network is less defined and has a loss of peak differentiation from the overlapping of all the regions of the ER throughout the cell (Figure 5.6A). On the other hand, the cross-sectional CatchER<sup>+</sup> intensity profile in the HILO configuration had sharper defined peaks since due to the single section of CatchER<sup>+</sup> being examined elucidating the Ca<sup>2+</sup> microdomains throughout the ER as well as the S/N ratio using HILO imaging being much higher (Figure 5.6A). Under the same conditions, epifluorescence had an overall lower ER Ca<sup>2+</sup> release compared to HILO and lower fluorescence intensity distribution in addition to the loss of defined ER-network regions (Figure 5.6B). When we further look at these cross-sectional subcellular differences in CatchER<sup>+</sup> signaling on a time scale in response to treatment with 1 mM 4-cmc we can drastically see more differences between epifluorescence and HILO imaging techniques (Figure 5.7).

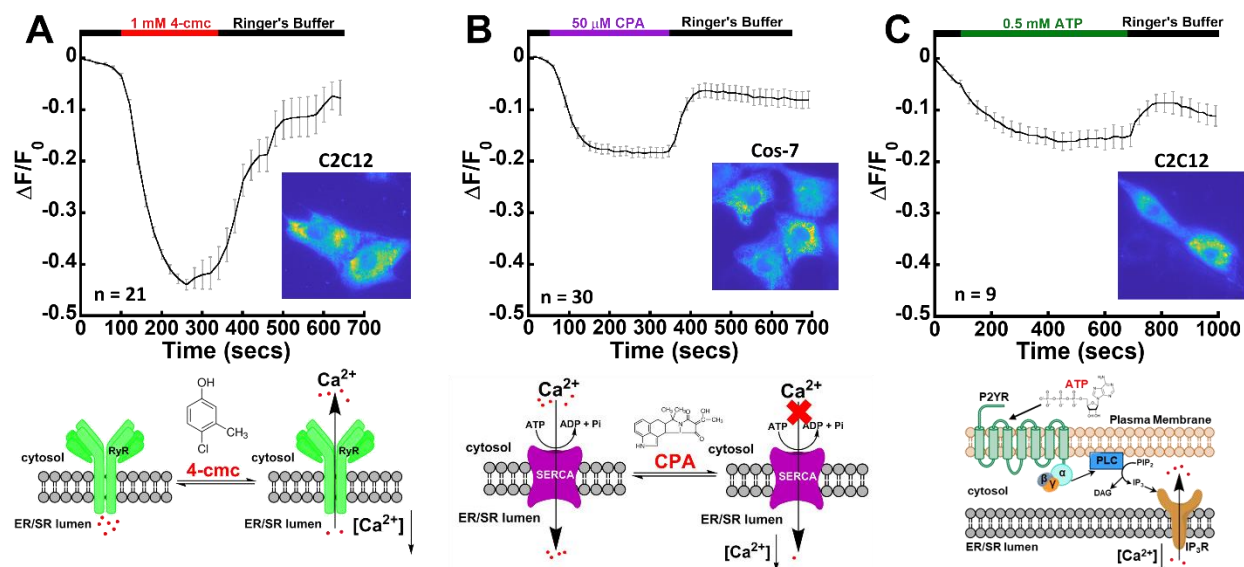


**Figure 5.8 – CatchER<sup>+</sup> HILO in response to 4-cmc, CPA, and ATP.**

**A** – Perfusion of 1 mM of 4-cmc was added to initiate a release of Ca<sup>2+</sup> from the ER in C2C12 cells with an average of 21 cells. Below is the schematic of 4-cmc activation on the RyR, which releases Ca<sup>2+</sup> from the ER. **B** – Perfusion of 50 μM of CPA was added to initiate a release of Ca<sup>2+</sup> from the ER in Cos-7 cells with an average of 30 cells. Below is the schematic of CPA inhibition of the SERCA pump, which reduces ER Ca<sup>2+</sup> since the ER [Ca<sup>2+</sup>] cannot refill. **C** – Perfusion 500 μM of ATP was added to initiate a release of Ca<sup>2+</sup> from the ER in C2C12 cells with an average of 9 cells. Below is the schematic of ATP indirect activation on the IP<sub>3</sub>R, which releases Ca<sup>2+</sup> from the ER after production of IP<sub>3</sub> from P2YR activation.

Once again we can not only see the initial subcellular Ca<sup>2+</sup> differences of CatchER<sup>+</sup> fluorescence in HILO which is lost in epifluorescence but can further see that while the release of Ca<sup>2+</sup> from the ER for the cross-section is similar to the Ca<sup>2+</sup> recovery subcellular distribution visualized using CatchER<sup>+</sup> fluorescence signal is a different pattern of distribution than the starting Ca<sup>2+</sup> distribution pattern (Figure 5.7). This shows us that there is indeed microdomains of Ca<sup>2+</sup> through this cross-section of the ER and that the differences in initial Ca<sup>2+</sup> and Ca<sup>2+</sup> recovery could be from distribution differences of RyR and SERCA pumps as well as pockets of Ca<sup>2+</sup> microdomains.

We initially examined the CatchER<sup>+</sup> to monitor changes in ER [Ca<sup>2+</sup>] in C2C12 myoblasts, Cos-7 cells, HEK293 cells, and HeLa cells under HILO microscope settings examining the global whole-

cell signal in response to 4-cmc, CPA, ATP, and histamine. We show the representative responses of CatchER<sup>+</sup> using HILO imaging with the perfusion of 1 mM 4-cmc in C2C12 myoblast cells (Figure 5.8A), 50  $\mu$ M CPA in Cos-7 cells (Figure 5.8B), and 500  $\mu$ M ATP in C2C12 myoblast cells (Figure 5.8C). Additional imaging was conducted in C2C12, Cos-7, and HEK293 cells with 4-cmc, CPA, and ATP as well as in HeLa cells with 4-cmc and histamine, as represented in Table 5.3. Since the C2C12 have a higher expression of RyR, they show the most potent response to 1 mM 4-cmc treatment which produced a  $45.5 \pm 1.3\%$  change in the fluorescence intensity of CatchER<sup>+</sup> which correlates with a 45.5% decrease in ER/SR [Ca<sup>2+</sup>] (Table 5.3).

Cos-7 and HEK293 cells were more sensitive to 1 mM 4-cmc and led to cell stress, so we treated them with 0.5 mM 4-cmc which had a release of  $12.3 \pm 0.8$  and  $22.0 \pm 1.6\%$ , respectively. HeLa cells had a release of  $23.5 \pm 0.8\%$  in response to 1 mM 4-cmc (Table 5.3). In Cos-7 cells, the addition of 50  $\mu$ M CPA led to a  $17.0 \pm 0.9\%$  release upon inhibition of the SERCA pump (Table 5.3). C2C12 and HEK293 cells had a release of  $25.7 \pm 1.5$  and  $23.3 \pm 1.2\%$ , respectively, in response to the addition of 50  $\mu$ M CPA (Table 5.3). C2C12 cells treated with 500  $\mu$ M ATP caused a  $14.0 \pm 1.1\%$  release upon indirect activation of the IP<sub>3</sub>R (Table 5.3). Cos-7 and HEK293 cells had a release of  $12.3 \pm 1.7$  and  $15.6 \pm 1.1\%$ , respectively, in response to the addition of 500  $\mu$ M ATP (Table 5.3).



**Table 5.3 – Epifluorescence and HILO CatchER<sup>+</sup>  $\Delta F/F_0$  for each cell and drug type using.**

Cell Type	Drug Type	Epifluorescence			HILO		
		[Drug] ( $\mu\text{M}$ )	$\Delta F/F_0$ (%)	# of cells	[Drug] ( $\mu\text{M}$ )	$\Delta F/F_0$ (%)	# of cells
C2C12	4-cmc	200	$18.6 \pm 1.1$	43	1000	$45.5 \pm 1.3$	32
Cos-7	4-cmc	200	$7.3 \pm 0.6$	19	500	$12.3 \pm 0.8$	36
HEK293	4-cmc	200	$12.0 \pm 0.8$	8	500	$22.0 \pm 1.6$	40
HeLa	4-cmc	ND	ND	ND	1000	$23.5 \pm 0.8$	10
C2C12	CPA	15	$24.2 \pm 1.6$	35	50	$25.7 \pm 1.5$	18
Cos-7	CPA	15	$26.0 \pm 1.9$	10	50	$17.0 \pm 0.9$	31
HEK293	CPA	15	$21.0 \pm 0.8$	14	50	$23.3 \pm 1.2$	18
C2C12	ATP	100	$10.3 \pm 1.0$	14	500	$14.0 \pm 1.1$	12
Cos-7	ATP	100	$13.0 \pm 1.0$	9	500	$12.3 \pm 1.7$	13
HEK293	ATP	100	$6.0 \pm 1.5$	4	500	$15.6 \pm 1.1$	24
HeLa	Histamine	ND	ND	ND	100	$12.6 \pm 0.8$	33

Data represents mean  $\pm$  SEM error. ND – No Data,  $\Delta F/F_0$  – change in fluorescence signal over initial fluorescence in response to drugs. Data collected at room temperature.

Lastly, HeLa cells were treated with 100  $\mu\text{M}$  histamine to activate the histamine receptor (H1R) a GPCR which also produces  $\text{IP}_3$  upon activation similarly to ATP with P2YR<sup>[343]</sup>. HeLa cells had a release of  $12.6 \pm 0.8\%$  in response to treatment with 100  $\mu\text{M}$  histamine, a result that was similar to the release observed for the activation of  $\text{IP}_3\text{R}$  in the other cell types with ATP (Table 5.3).

### 5.2.3 *Examining Microdomains using CatchER<sup>+</sup> and HILO Imaging*

Another major reason to utilize HILO imaging is the ability to measure the fluorescence in a small slice of the cell as opposed to all the layers of the cell in epifluorescence. In order to examine subcellular microdomains of Ca<sup>2+</sup> signaling in the cell throughout the ER/SR network we needed a high-resolution imaging capability and using epifluorescence is inadequate since the signal in a microdomain would be canceled out by the signal in overall ER/SR signaling on the other layers around the microdomain.

Using HILO microscopy, we can see if different regions of the ER/SR on the slice we are recording have differential Ca<sup>2+</sup> expression implying microdomains of Ca<sup>2+</sup> signaling and also of differential protein expression. Overall the global ER Ca<sup>2+</sup> dynamics in the whole cell is pretty consistent in response to 4-cmc in C2C12 cells with 45.5% release and a deviation of  $\pm 7.35\%$  in 32 whole cells (Figure 5.8A, Figure 5.9D and Table 5.3). Analyzing the raw data plots for every 50 by 50 pixel region (Figure 5.9A) over the field of view for the cells transfected with CatchER<sup>+</sup> (Figure 5.9B) we can see that there is variance in the initial Ca<sup>2+</sup> levels by fluorescence intensity as well as the ending levels (Figure 5.9A). Interestingly, there is little variance in the actual release percentage over the cells disregarding the background response and examining the plateau of release around 45.5% with  $\pm 7.35\%$  deviation (Figure 5.9C&D).

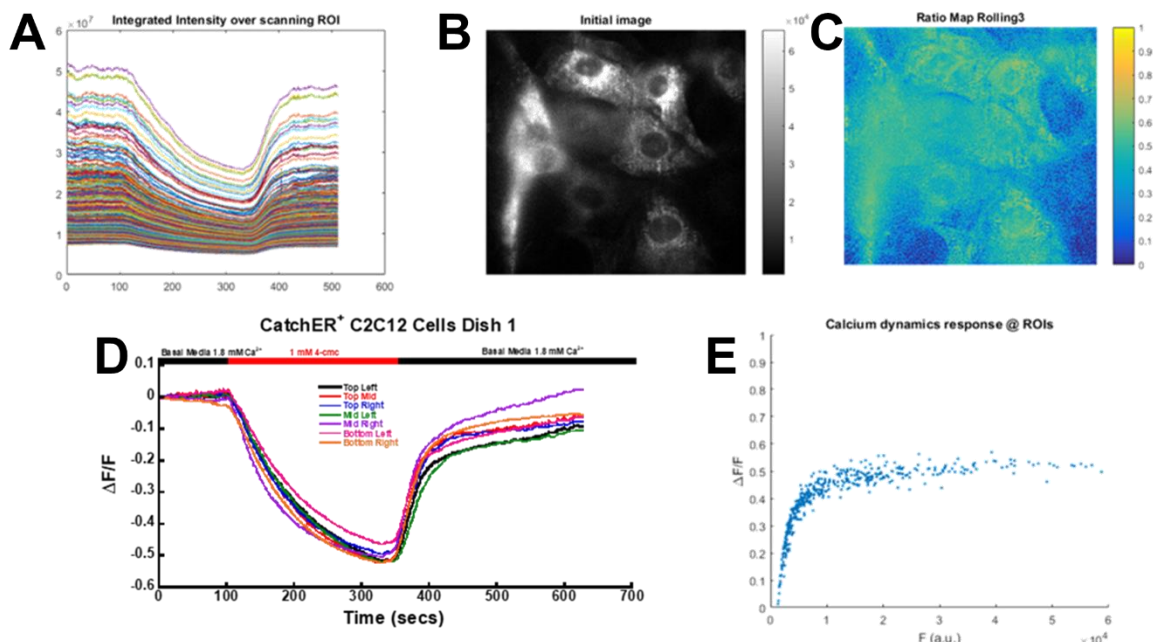


**Figure 5.9 – CatchER<sup>+</sup> HILO imaging in C2C12 in response to 1 mM 4-cmc.**  
**A – Raw plotted data for each 50x50 pixel region. B – CatchER<sup>+</sup> 488 nm was excited in C2C12 cells. C – The  $\Delta F/F$  intensity map. D – The normalized plot for each whole cell labeled accordingly. E –  $\Delta F/F$  intensity release values plot of each plot in A.**

Since C2C12 cells are mouse skeletal muscle cells they will present with ER as well as an SR and the SR is known to have regions of microdomains of expression of proteins in addition to  $\text{Ca}^{2+}$  concentration differences along the junctional SR in communication with the plasma membrane for E-C coupling. Examining the whole cell, regions of interest (ROIs) 1 and 2, in comparison to smaller potential subcellular microdomains throughout the cell, ROIs 3-27 the raw fluorescence data once again shows different starting fluorescence intensities, valley release intensities, and recovery intensities (Figure 5.10A&D). If we assume the starting  $\text{Ca}^{2+}$  was similar and normalize to  $T_0$  secs we see that the  $\Delta F/F_0$  at 300 secs was  $53.5 \pm 11.4\%$  release which is similar to the global signal for 32 cells at  $45.5 \pm 7.35\%$  release although with slightly more variance in the standard deviation which implies microdomains of RyR distribution and/or  $\text{Ca}^{2+}$  levels. Furthermore, the recovery region at  $T_{500}$  secs the signal recovered to 18% with a deviation of 66.8% showing a dramatic difference in areas of  $\text{Ca}^{2+}$  uptake and/or SERCA pump distribution (Figure 5.10C&F).

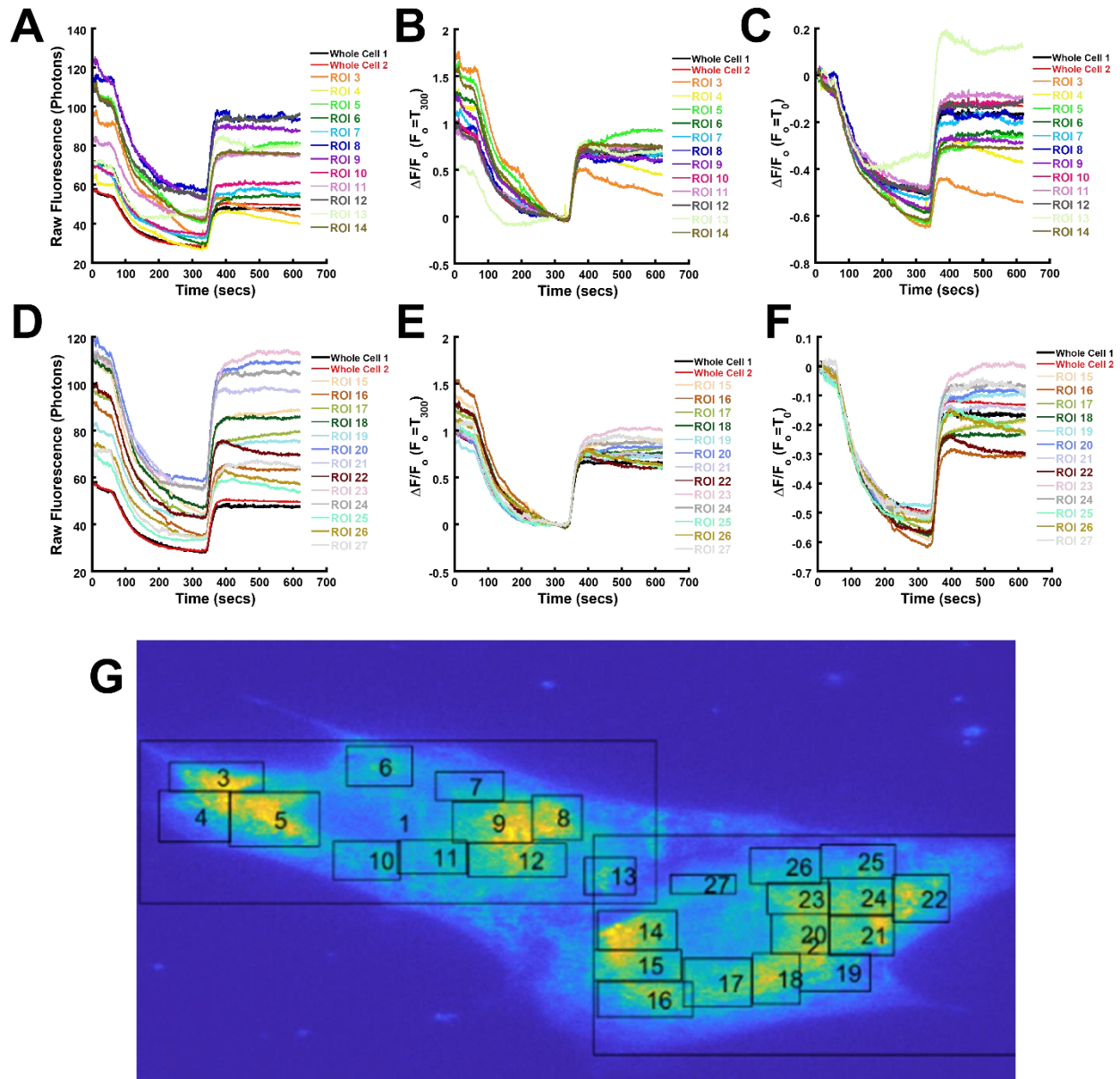


**Figure 5.10 – Analyzing subcellular microdomains using CatchER<sup>+</sup> and HILO imaging.**

**A&D – Raw plots of the ROIs in G. B&E – ROIs in G normalized to the valley intensity at 300 secs. C&F – ROIs in G normalized to the initial intensity at 0 secs. G – Cells being analyzed and the ROIs, whole-cell ROI #1-2.**

If we instead assume that the release fluorescence is generally consistent as shown by lower deviation from global cell analysis and by the  $\Delta F/F_o$  heat map and plot (Figure 5.9C&E) and

normalize the data at  $T_{300}$  secs we see that the recovery at 500 secs fluctuates 18% between each ROI while the initial intensities at 0 secs fluctuates 22.8% (Figure 5.10B&E).

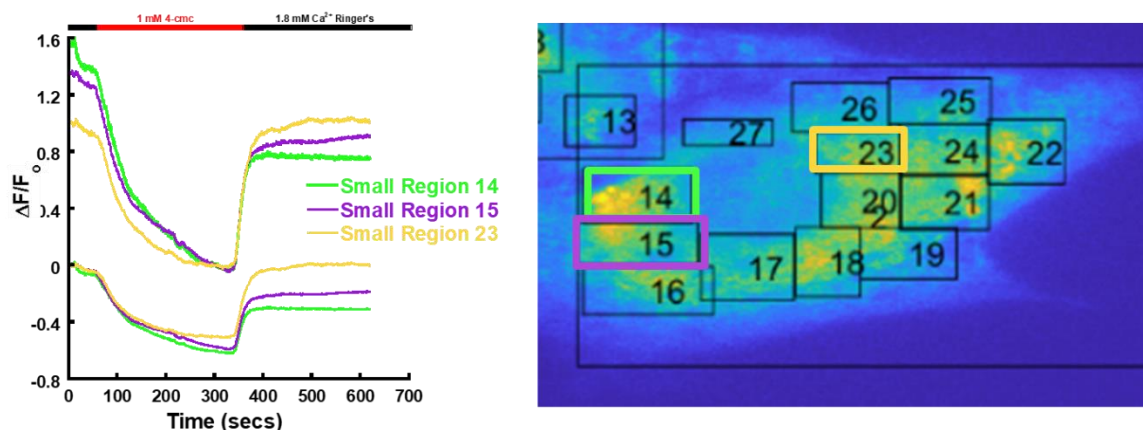


**Figure 5.11 – CatchER<sup>+</sup> HILO imaging in C2C12 with different normalization. Representative plots of the ROIs normalized to the valley intensity at 300 secs (top 3 plots) or to the initial intensity at 0 secs (bottom three plots) and the ROIs being analyzed.**

Even by analyzing 3 ROIs in one cell, we can see each ROI has different release and recovery responses, implying  $\text{Ca}^{2+}$  and/or protein distribution subcellular microdomains (Figure 5.11). In order to confirm if these differences are due to  $\text{Ca}^{2+}$  microdomains or protein distribution differences, we analyzed protein distribution utilizing confocal microscopy.

#### ***5.2.4 Confocal Imaging of Global CatchER<sup>+</sup>, RyR, and SERCA Distribution***

There is an array of imaging available to analyze processes on the cellular level. Getting high-resolution images to examine intracellular morphology and ER/SR protein distributions on cells are not as simplistic and need fluorescence labeling of proteins through immunohistochemistry techniques and then high-resolution imaging utilizing confocal microscopy. We transfected the cell with CatchER<sup>+</sup>, which is uniformly expressed throughout the cell in comparison to ER Tracker Red and a PCC of 0.91 (Figure 5.12). Additionally, we stained the nucleus with DAPI, and the

cellular actin structures were stained with phalloidin 633 dye in order to see the overall cellular assembly which is critical for multinuclear cells (Figure 5.12-Figure 5.13).

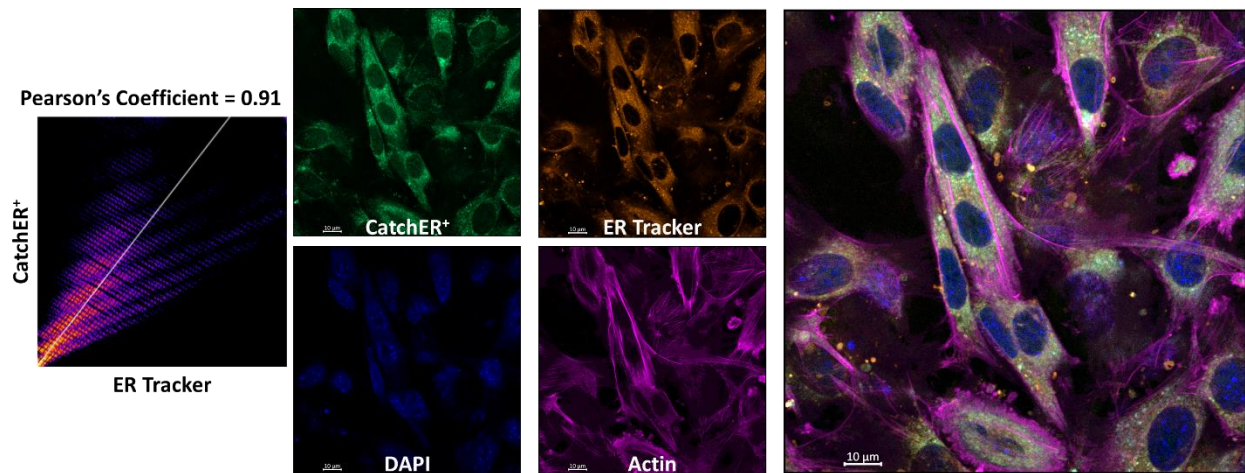


**Figure 5.12 – CatchER<sup>+</sup> confocal imaging in C2C12 with ER Tracker.** Pearson's correlation coefficient (PCC) plot of ER Tracker red 555 dye (orange) and CatchER<sup>+</sup> (green) 488 nm. Also stained Phalloidin 633 dye for actin (magenta) and DAPI nucleus stain (blue) 405 nm. The large panel is the merge of all four wavelengths merged. Figure 5.3 shows a zoomed-in version of CatchER<sup>+</sup> with ER Tracker.

In order to examine the subcellular distribution of RyR, we labeled C2C12 cells transfected with CatchER<sup>+</sup> with primary RyR and secondary 555 nm antibodies (Figure 5.13A&B). Interestingly, and most pronounced on the tubule, we can see that the RyR antibody was more distributed on the edges of the ER where we would expect RyR1 to congregate along the junctional SR for E-C coupling with dihydropyridine receptor (DHPR) on the plasma membrane, as can be seen by the orange outlines on the ER/SR structures (Figure 5.13B). There are still some RyR throughout the ER/SR though since RyR is still necessary throughout but based on the poor PCC value of 0.40 the RyR is not expressed uniformly throughout the ER/SR (Figure 5.13D).



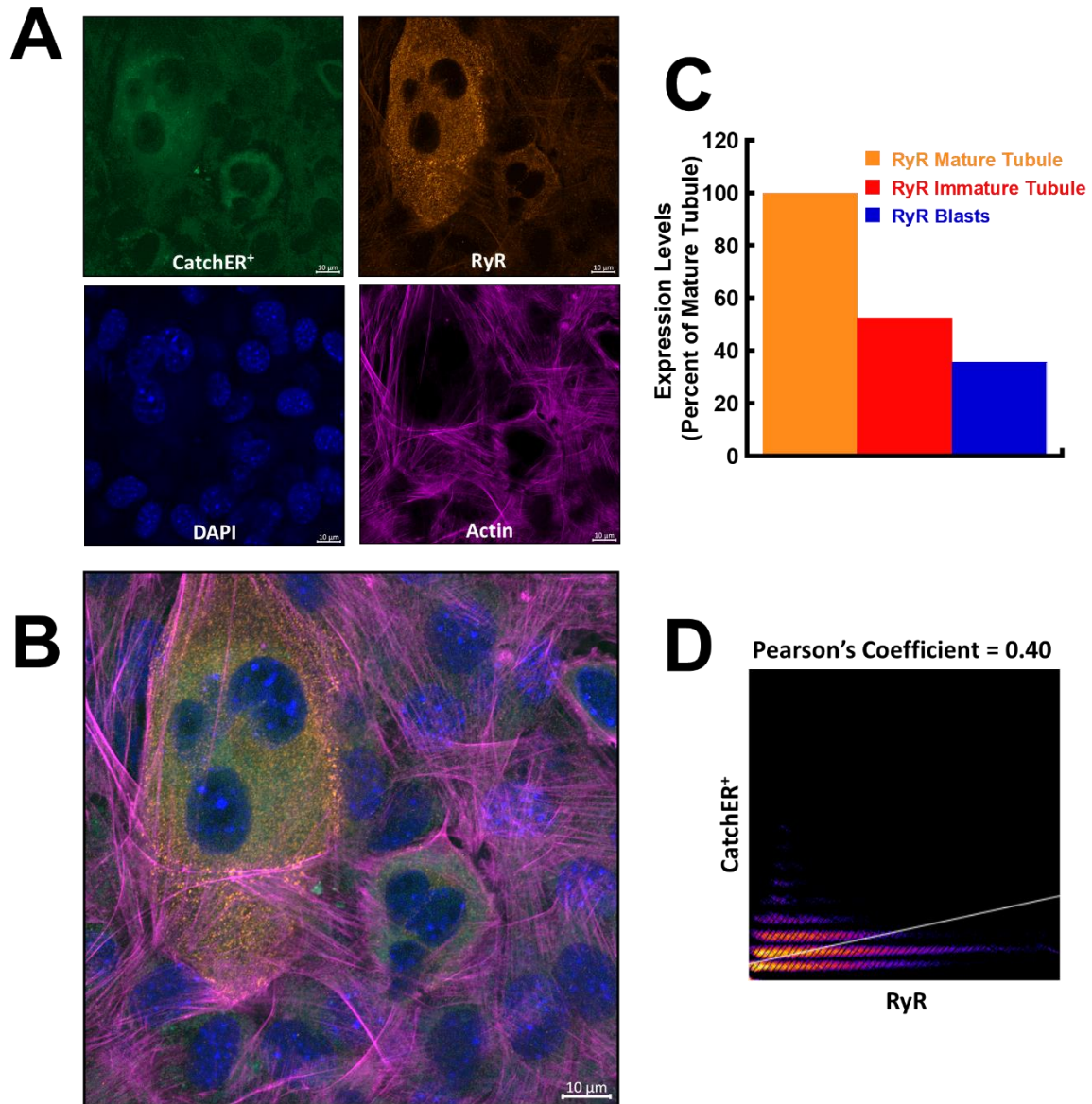


**Figure 5.13 – CatchER<sup>+</sup> confocal imaging in C2C12 with RyR antibody.**  
**A&B** – RyR 555 antibody (orange), CatchER<sup>+</sup> (green) 488 nm, stained Phalloidin 633 dye for actin (magenta) and DAPI nucleus stain (blue) 405 nm. **B** – Merge of all four wavelengths. **C** – RyR expression for blasts (single nuclei), immature tubule (2-3 indistinct nuclei), and mature tubule ( $\geq 3$  distinct nuclei). **D** – Pearson's correlation coefficient (PCC) plot of RyR and CatchER<sup>+</sup>.

Since the tubules have a higher expression of RyR from the localization of RyR to the junctional SR in communication with DHPR at the PM we also noticed that the tubule antibody staining for

RyR was significantly higher than the single nuclei blasts by 2.8 fold and that the mature tubule was still 1.9 fold higher than the forming tubule with 3 indistinct nuclei (Figure 5.13C).

With the low RyR expression we looked again at RyR expression but on lower confluency cells for C2C12 cells to confirm that the antibody was adequately binding to the cells and that the overlap of cells and high cell number were not altering the data (Figure 5.14).

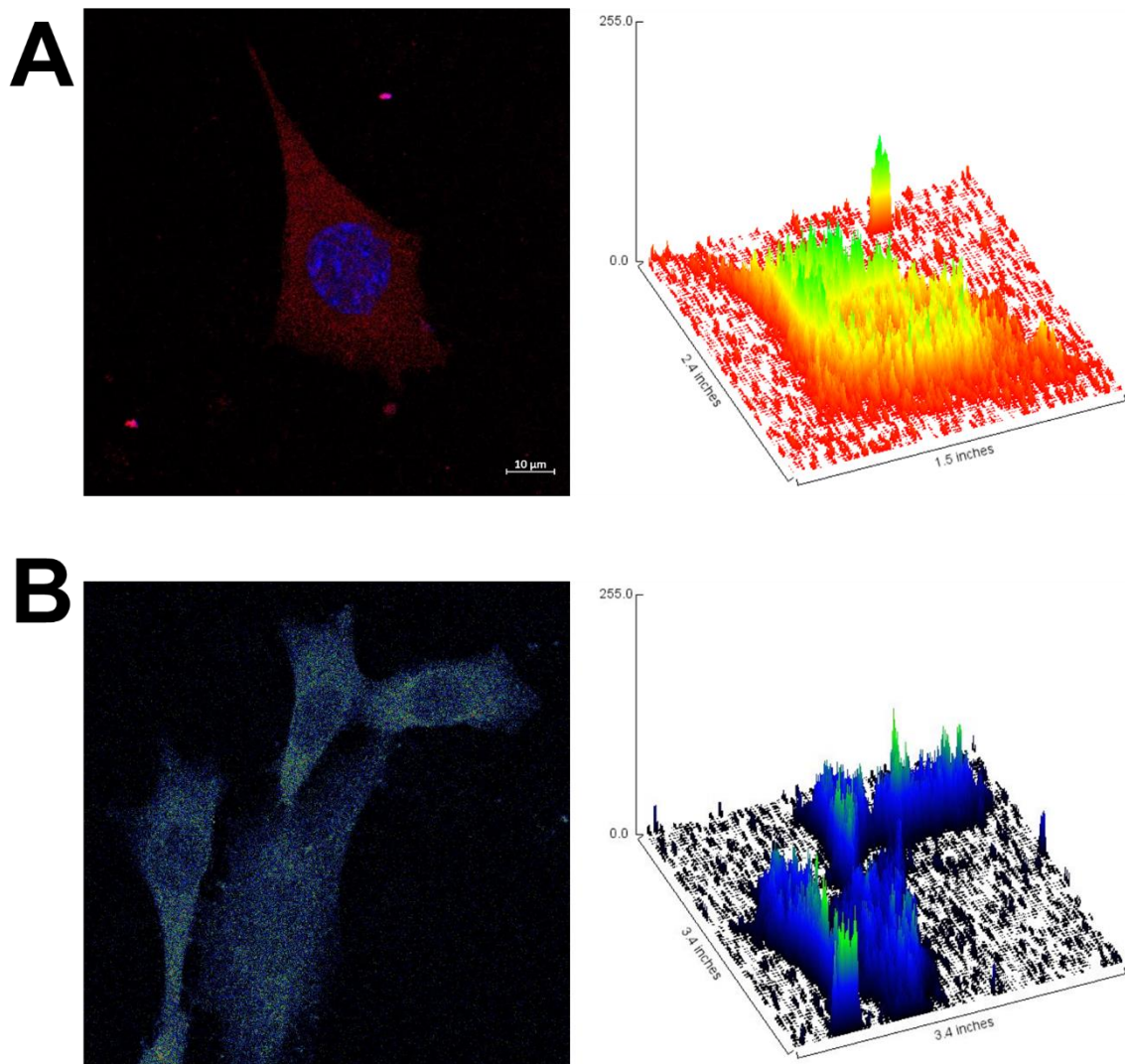


**Figure 5.14 – RyR confocal imaging in C2C12.**

**A – Confocal image of RyR 633 antibody (red) and DAPI nucleus stain (blue) and surface plot under color spectrum where green is high signal and red is the low signal.**

**A – Confocal image of RyR 633 antibody and surface plot under rainbow RGB colors where green is high signal and blue is the low signal.**



The RyR does seem to be expressed throughout the ER in the cell but that the distribution throughout the ER was not uniform and that there are microdomains of higher expression throughout the cell (Figure 5.14). There does not seem to be a pattern of microdomain distribution as seen by the varying peak heights on the surface plots, and some cells have fewer microdomains than others (Figure 5.14).

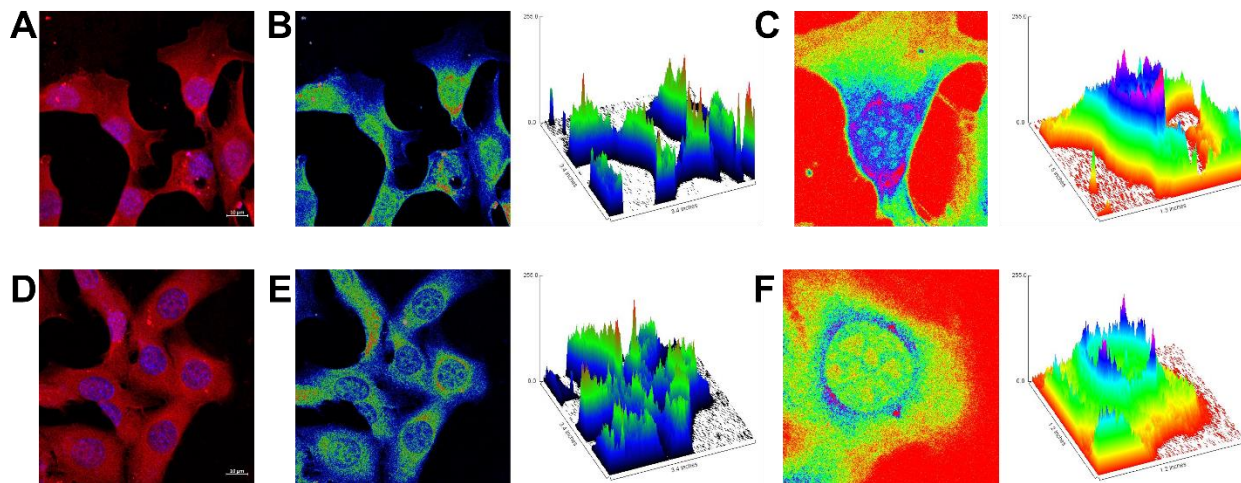


**Figure 5.15 – SERCA1 and SERCA2 confocal imaging in C2C12.**

**A – Confocal image of SERCA1 and SERCA2 633 antibody (red) and DAPI nucleus stain (blue). B – Confocal image of SERCA 633 antibody and surface plot under rainbow RGB colors where red is high signal and blue is the low signal. C – A single cell from B under spectrum colors where purple is high signal and red is the low signal. D – Confocal image of SERCA1 and SERCA2 633 antibody (red) and DAPI nucleus stain (blue). E – Confocal image of SERCA 633 antibody and surface plot under rainbow RGB colors where red is high signal and blue is the low signal. F – A single cell from D under spectrum colors where purple is high signal and red is the low signal.**

Since ER  $\text{Ca}^{2+}$  recovery is regulated by the SERCA pump, we also examined the SERCA pump distribution through antibodies targeting both SERCA1 and SERCA2 together (Figure 5.15). The SERCA pump expression was much stronger than RyR even though the same secondary antibody was utilized, which could indicate higher overall expression of SERCA pumps than RyR (Figure 5.15). Additionally, the expression distribution of SERCA pumps was much more highly

concentrated in and around the nucleus (Figure 5.15). Not only was there differential expression distributions between RyR and SERCA pumps there was also microdomains of SERCA pump expression in the nucleus region as well as distal regions as seen by the varying peaks in the surface plots (Figure 5.15). While these discoveries corroborate our results using live-cell imaging, we need to develop ways to image with CatchER<sup>+</sup> and examine these target proteins simultaneously or sequentially so we can compare the release kinetics to local protein microdomains. This can be done with advanced dual imaging methodologies as well as with localized targeted CatchER<sup>+</sup> variants.

### *5.2.5 Comparison of Localized CatchER<sup>+</sup>-JP45 vs. Global CatchER<sup>+</sup> Sensors*

In order to confirm the subcellular changes and protein distribution we were able to examine using CatchER<sup>+</sup> we collaborated with Dr. Zorzato in Italy in order to design a membrane-bound localized skeletal muscle sensor CatchER<sup>+</sup>-JP45 which we could investigate the localized versus the global ER/SR Ca<sup>2+</sup> dynamics. We constructed a targeted CatchER<sup>+</sup> protein attached to the ER membrane internally by attaching junctional protein 45 (JP45) to the N-terminus of CatchER<sup>+</sup>. This newly designed targeted sensor was named CatchER<sup>+</sup>-JP45 (Figure 5.16). CatchER<sup>+</sup>-JP45 has the JP45 protein, attached to CatchER<sup>+</sup> sensor, which co-localizes to the RyR1 in the SR of cells. The CatchER<sup>+</sup>-JP45 protein faces inside of the SR next to the RyR1 luminal opening. In SR the RyR co-localizes with JP45 when communicating with the DHPR protein on the plasma membrane of the cell in order to shuttle Ca<sup>2+</sup> quickly between the SR to the cytosol and also from extracellularly to the cytosol for voltage-gated action potentials necessary for muscle contraction and release (Figure 5.16) <sup>[344-346]</sup>.

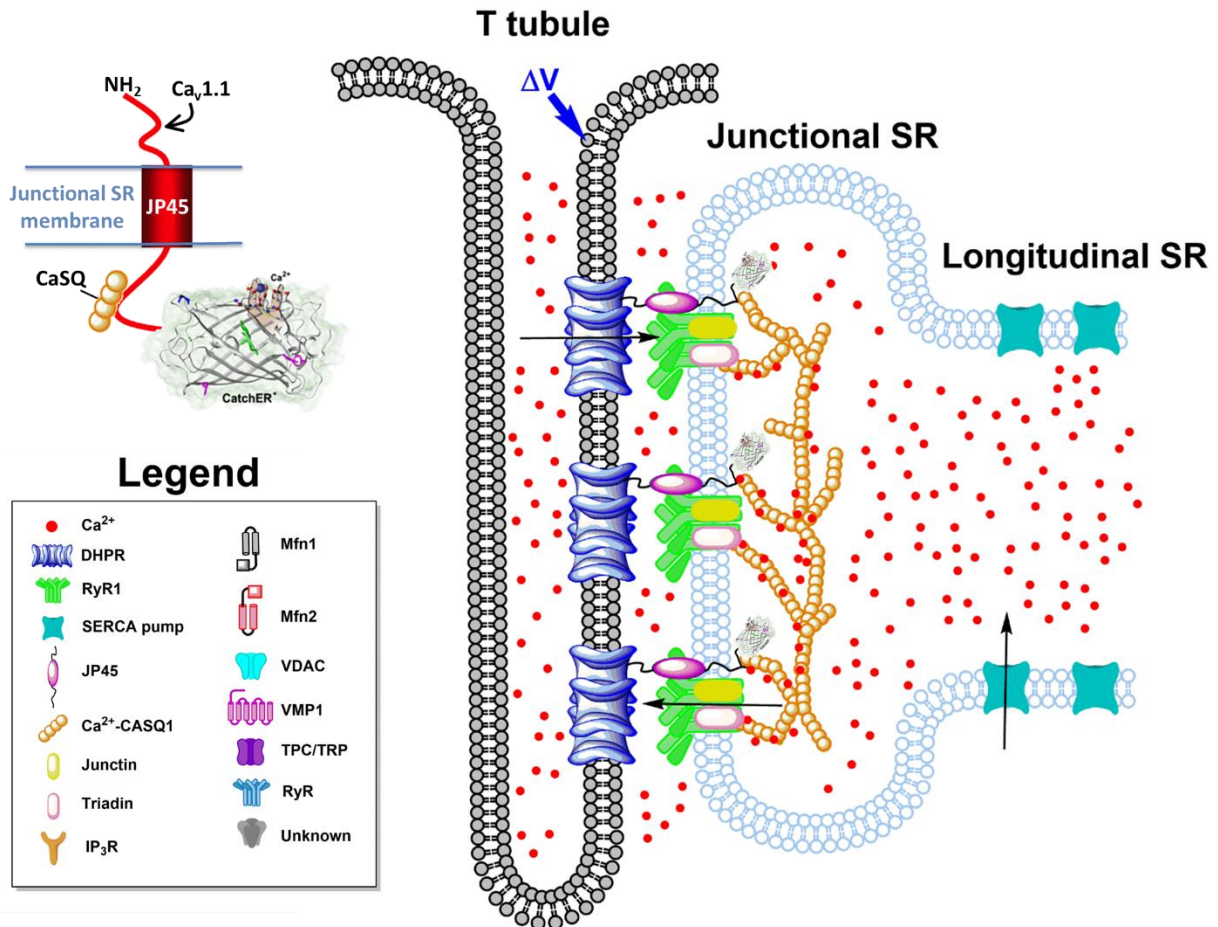


**Figure 5.16 – CatchER<sup>+</sup>-JP45 sensor design and SR expression.**

**Diagram showing communication of DHPR and RyR1 in muscle cells for the simultaneous release of Ca<sup>2+</sup> from the SR through RyR1 and CaSQ Ca<sup>2+</sup> release and through DHPR from the extracellular both into the cytosol upon voltage on the plasma membrane for muscle contraction. Insert upper left shows the design of CatchER<sup>+</sup>-JP45 sensor.**

In order for the SR Ca<sup>2+</sup> concentration to not be unnaturally large a CaBP calsequestrin (CaSQ) binds Ca<sup>2+</sup> and then binds JP45 colocalized to the RyR1 in this junctional zone to keep a higher [Ca<sup>2+</sup>] in this region for muscle contraction (Figure 5.16). Currently, the exact function and disease relevance of JP45 and CaSQ have not been fully elucidated and the CatchER<sup>+</sup>-JP45 sensor can help us with these discoveries.

We were interested in comparing the global  $\text{CatchER}^+$  signal and response in C2C12 myoblast and myotubules with targeted local  $\text{CatchER}^+$ -JP45 to further elucidate the subcellular microdomains seen with HILO imaging. We first did this by transfecting both into myoblast C2C12 cells to examine the response differences in regards to ER  $\text{Ca}^{2+}$  dynamics using epifluorescence (Figure 5.17). While we do see the response, the intensity is dimmer for  $\text{CatchER}^+$ -JP45 which is to be expected since this sensor is only colocalized with RyR instead of being uniformly expressed throughout the whole ER/SR as for  $\text{CatchER}^+$ . The release of  $\text{Ca}^{2+}$  from the ER for  $\text{CatchER}^+$  in response to 4-cmc is  $18.6 \pm 7.4\%$  while the  $\text{CatchER}^+$ -JP45 is around  $8.8 \pm 6.5\%$  where the localized  $\text{CatchER}^+$ -JP45 releases and recovers similar to  $\text{CatchER}^+$  (Figure 5.17).

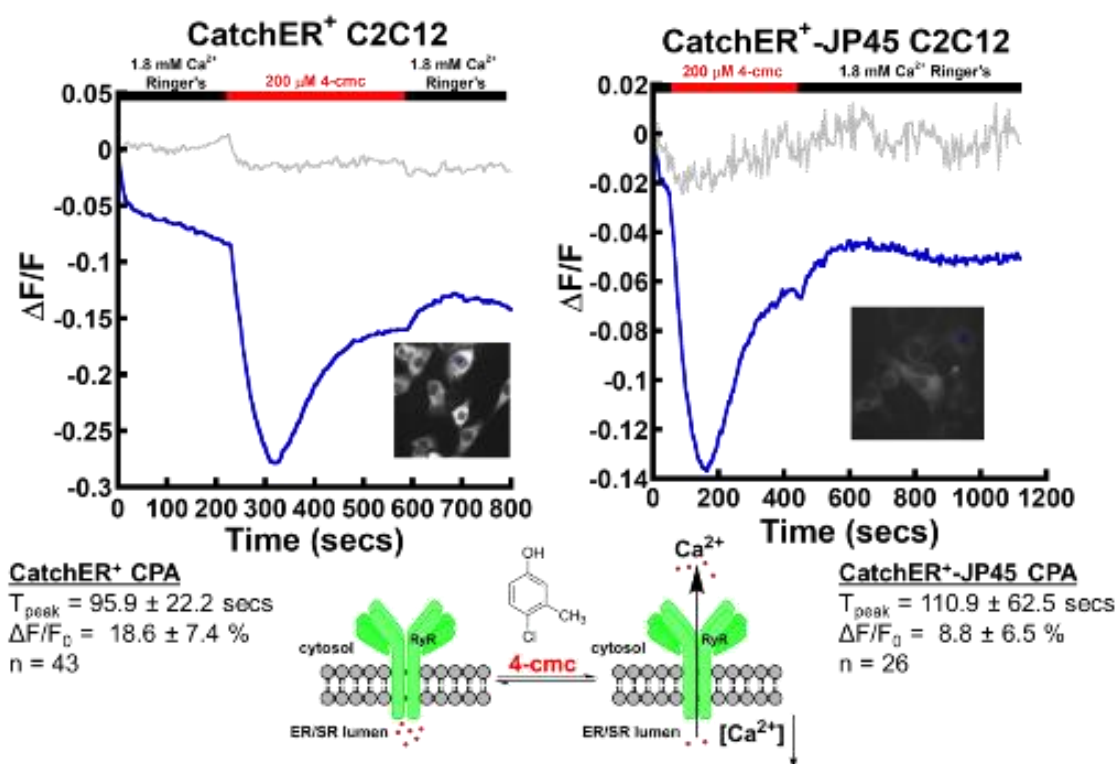


**Figure 5.17 –  $\text{CatchER}^+$  and  $\text{CatchER}^+$ -JP45 in myoblasts of C2C12 cells with 4-cmc.  $\text{CatchER}^+$  (left) and  $\text{CatchER}^+$ -JP45 (right) with 200 μM of 4-cmc added to initiate a release of  $\text{Ca}^{2+}$  from the ER from the RyR. The peak time and  $\Delta F$  for each experiment and a diagram illustrating the pathway of release from ER through RyR after addition of 4-cmc.**

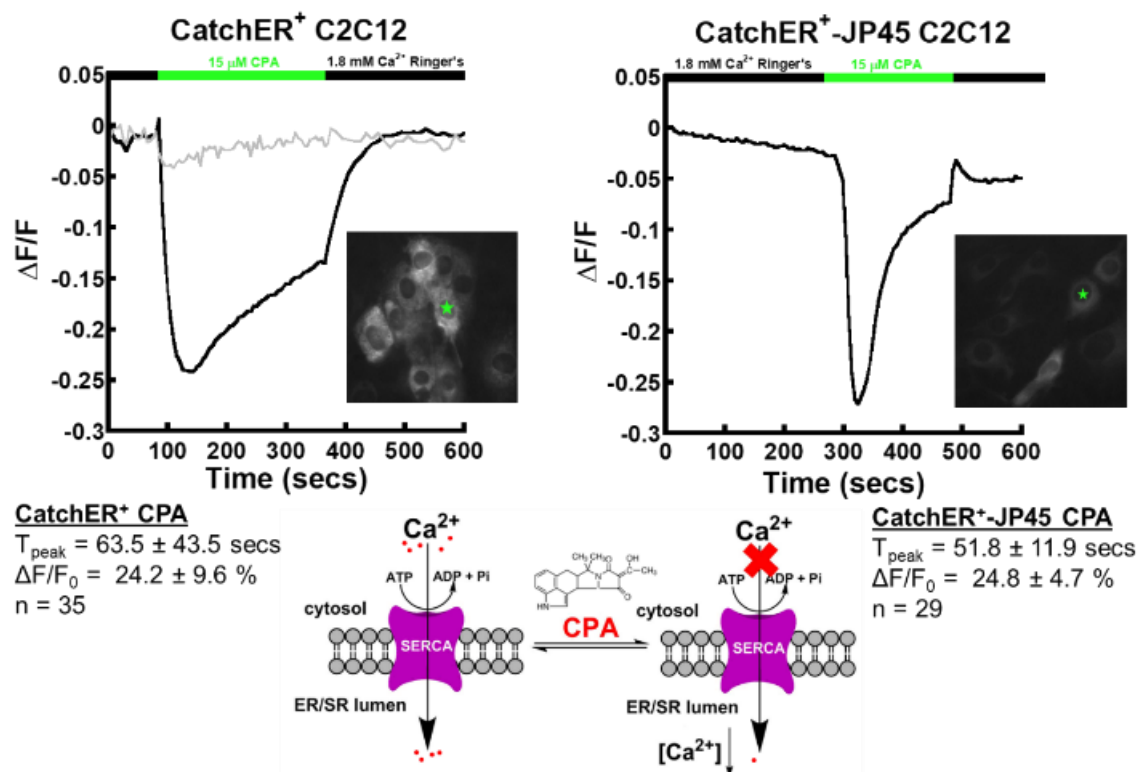


**Figure 5.18 – CatchER<sup>+</sup> and CatchER<sup>+</sup>-JP45 in myoblasts of C2C12 cells with CPA. Top – CatchER<sup>+</sup> (left) and CatchER<sup>+</sup>-JP45 (right) with 200  $\mu$ M of 4-cmc added to initiate a release of Ca<sup>2+</sup> from the ER from the inhibition of the SERCA pump. Bottom – The peak time and  $\Delta F$  for each experiment and a diagram illustrating the pathway of release from ER through SERCA pump blocking not allowing the refilling of the ER after addition of CPA.**

CatchER<sup>+</sup>-JP45 shows quicker ER/SR emptying upon SERCA pump inhibition by CPA and interestingly can recover much more rapidly and efficiently the Ca<sup>2+</sup> concentration in this localized microdomain much more readily than the global Ca<sup>2+</sup> refills while CPA is inhibiting the SERCA pump (Figure 5.18). This could be due to CaSQ binding to high levels of Ca<sup>2+</sup> in the junctional SR which is then released from CaSQ for junctional SR refilling of Ca<sup>2+</sup> circumventing the slower SERCA pump refilling of the ER/SR.

We allowed C2C12 cells to differentiate from myoblasts into myotubules, which is the early stage of muscle fiber formation marked by having 3 or more distinct nuclei in one cell. When the myotubules and muscle fibers form there is more SR present and thus a higher number of RyR1

for JP45 to co-localize with for our localized CatchER<sup>+</sup>-JP45 studies. Since myotubules are resistant to transfection we transfected the C2C12 three times over one week in order to ensure expression of the CatchER<sup>+</sup> and CatchER<sup>+</sup>-JP45 sensors in the myotubules.

We investigated the effect of 500  $\mu$ M 4-cmc treatment on myotubules between global CatchER<sup>+</sup> and localized CatchER<sup>+</sup>-JP45 (Figure 5.19).

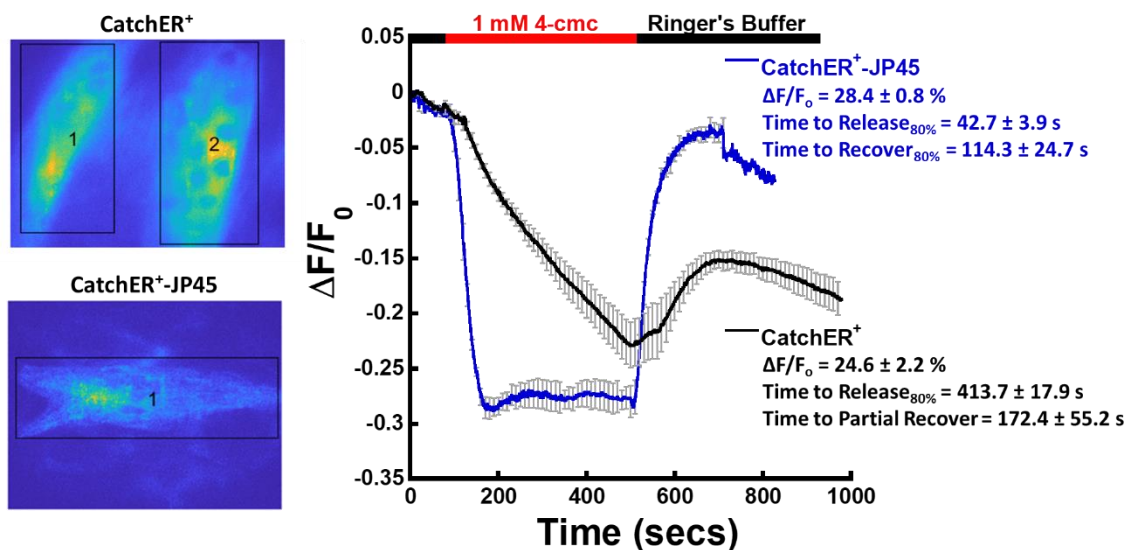


**Figure 5.19 – CatchER<sup>+</sup> and CatchER<sup>+</sup>-JP45 HILO imaging in C2C12 tubule cells. The normalized plot for CatchER<sup>+</sup> (black) for n = 6 cells and CatchER<sup>+</sup>-JP45 (blue) for n = 3 cells is shown on the right after exposure to 500  $\mu$ M 4-cmc.**

Additionally, since there is such a high expression of RyR1 in myotubules over myoblasts we decreased the 4-cmc concentration to 0.5 mM as to not fully saturate the release of Ca<sup>2+</sup> from the ER/SR allowing for the comparison of release by the global and localized sensors. The release slope for global CatchER<sup>+</sup> in tubules in response to 500  $\mu$ M 4-cmc treatment is much more linear with slower kinetics as opposed to the myoblasts with the myotubules not reaching a plateau even at ~400 seconds (Figure 5.8 & Figure 5.19). On the other hand the localized CatchER<sup>+</sup>-JP45 sensor had a markedly different response to 4-cmc treatment in the localized junctional SR microdomain where the Ca<sup>2+</sup> fully releases and plateaus at  $28.4 \pm 0.8\%$  and 80% of this change occurs in  $42.7 \pm$



3.9 secs whereas CatchER<sup>+</sup> does not plateau and reaches  $24.6 \pm 2.2\%$  global Ca<sup>2+</sup> release and 80% of this change takes  $413.7 \pm 17.9$  secs (Figure 5.19). Additionally, when the 4-cmc is washed away localized CatchER<sup>+</sup>-JP45 can immediately recover back to baseline and 80% of this recovery happens in  $114.3 \pm 24.7$  secs whereas global CatchER<sup>+</sup> cannot fully recover the ER/SR Ca<sup>2+</sup> back to baseline (Figure 5.19).

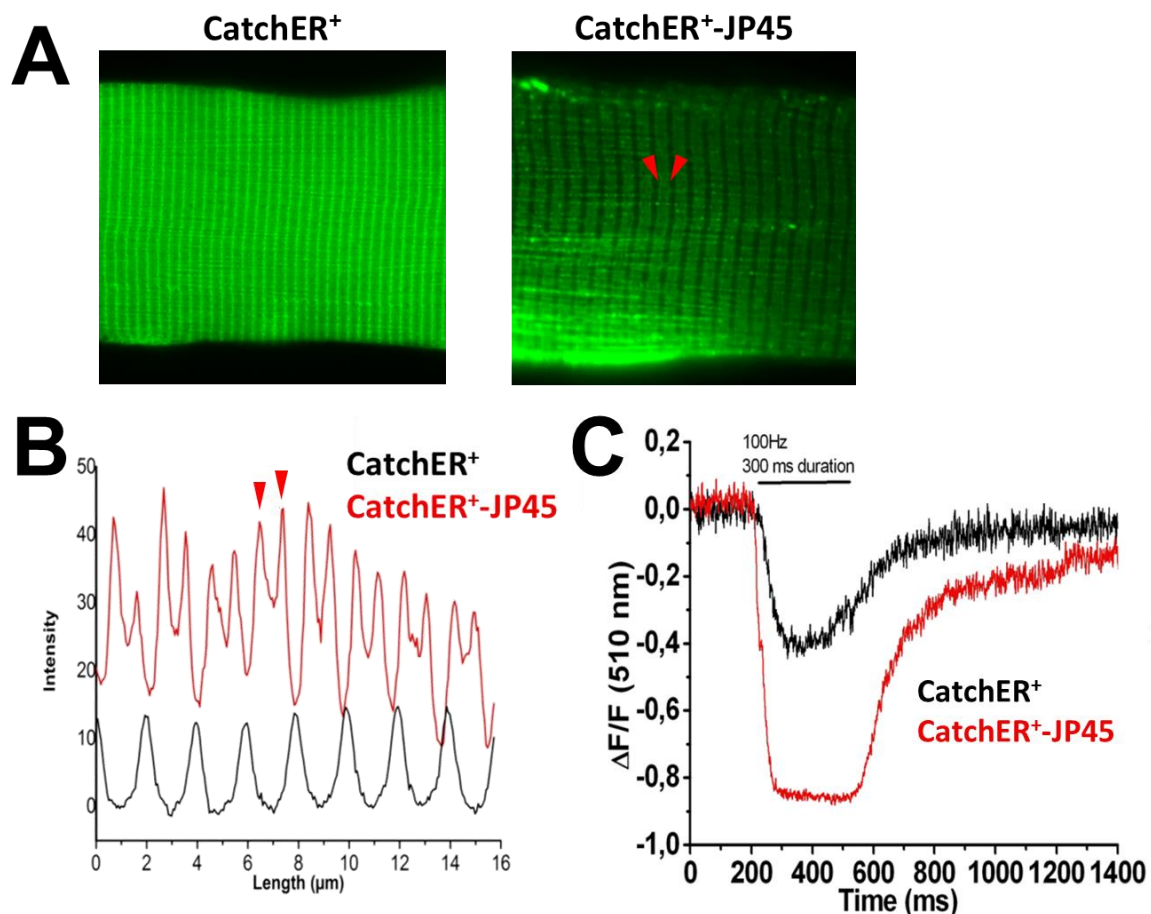


**Figure 5.20 – CatchER<sup>+</sup> and CatchER<sup>+</sup>-JP45 FDB fiber analysis.**  
**A** – Expression of CatchER<sup>+</sup> and CatchER<sup>+</sup>-JP45 in mouse flexor digitorum brevis foot muscle. **B** – Cross-section distribution pattern of fluorescence intensity for CatchER<sup>+</sup> (black) and CatchER<sup>+</sup>-JP45 (red) from A with the doublet peak red arrows corresponding to red arrows in A. **C** – 100 Hz electrical stimulation of transfected FDB mouse fibers for CatchER<sup>+</sup> (black) and CatchER<sup>+</sup>-JP45 (red).

We wanted to further see the application of our localized CatchER<sup>+</sup>-JP45 sensor in comparison to our global CatchER<sup>+</sup> sensor for analyzing subcellular microdomains on a tissue scale as opposed to single-cell studies, so we transfected both sensors into mouse flexor digitorum brevis (FDB) muscle fibers (Figure 5.20A). We saw that the global CatchER<sup>+</sup> sensor was uniformly expressed throughout the ER/SR of the FDB skeletal muscle and when examining a cross-section of the muscle we can see the uniform single peaks of CatchER<sup>+</sup> expression in each fiber of the FDB muscle (Figure 5.20A-B). Interestingly, we see that the localized CatchER<sup>+</sup>-JP45 sensor had a differential expression pattern and can be seen on the cross-section by a doublet peak as the sensor is expressed co-localized to RyR1 at the plasma membrane contacts with the junctional SR as indicated by the red arrows (Figure 5.20A-B).

Furthermore, these FDB muscles were exposed to 100 Hz of electrical stimulation for 300 ms to activate skeletal muscle E-C coupling through the activation of voltage-gated DHPR on the plasma membrane which have the allosteric interaction with RyR1 on the junctional SR colocalized with JP45 leading to a release of Ca<sup>2+</sup> from the SR to the cytoplasm<sup>[344-346]</sup>. For the global CatchER<sup>+</sup> sensor there was a 40% release of Ca<sup>2+</sup> in 100 ms whereas the localized CatchER<sup>+</sup>-JP45 sensor had over 85% release of Ca<sup>2+</sup>, two-fold greater than the global signal, in less than 50 ms (Figure 5.20C).

For imaging the complex and dynamic structure of the ER a microscopy technique was needed that would overcome the resolution limit from the diffraction of light. Since light diffraction limits the resolution and the distance at which two items can be distinguished to approximately half of the wavelength of light<sup>[347]</sup>. Thus we not only utilized epifluorescence, confocal, and HILO imaging but also did photon switch imaging using the stochastic optical reconstruction microscopy (STORM)<sup>[348]</sup> technique. STORM can image in the 20-40 nm range by utilizing photo switchable



fluorescent molecules which can be switched on and off thousands of times before being photobleached.

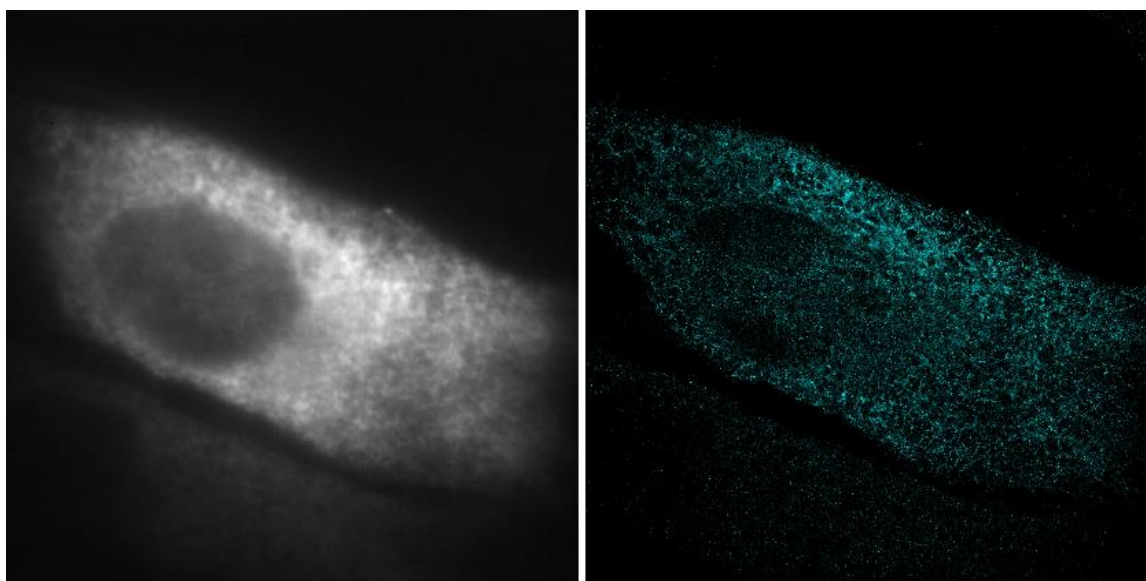


**Figure 5.21 – CatchER<sup>+</sup> STORM imaging in C2C12 mouse muscle cells. GFP/EGFP antibody that is Rabbit polyclonal to GFP (ab6556) with a secondary Donkey Anti-Rabbit IgG H&L (ab6701). CatchER<sup>+</sup> at 488 nm (white) and 647 nm (cyan).**

Most commonly utilized is the cyanine dye (Cy5) switched between a fluorescent and dark state by alternating red (638 nm) and green (532 nm) laser pulses, this switching between fluorescent and non-fluorescent is readily reversible and easily controlled through laser pulsing<sup>[348, 349]</sup>. This reconstruction technique makes sub-diffraction imaging of the ER structure possible by avoiding the limitation of the wavelength of light and instead utilizing the photons emitted.

We can more clearly visualize the ER network pattern by utilizing STORM imaging (Figure 5.21). We can see in comparison to the epifluorescence image at 488 nm for CatchER<sup>+</sup> that the 647 nm STORM image is much clearer and background fluorescence from other layers of the cell are removed (Figure 5.21).

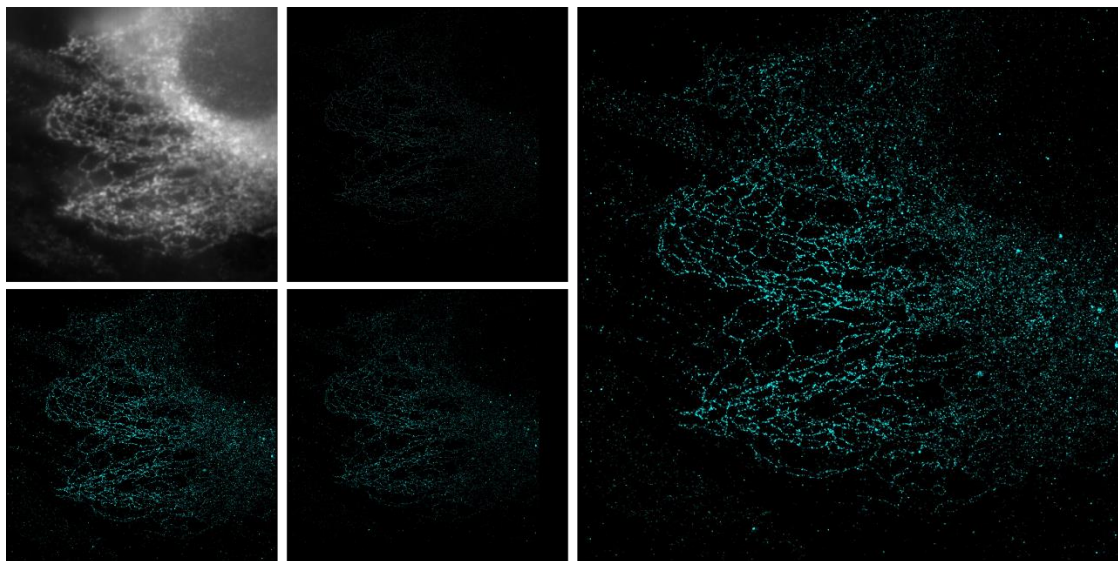


**Figure 5.22 – CatchER<sup>+</sup>-JP45 STORM imaging in C2C12 mouse muscle cells. GFP/EGFP antibody that is Rabbit polyclonal to GFP (ab6556) with a secondary Donkey Anti-Rabbit IgG H&L (ab6701). CatchER<sup>+</sup>-JP45 at 488 nm (white) and 647 nm (cyan).**

We also simultaneously looked at the CatchER<sup>+</sup>-JP45 in C2C12 cells at 488 nm epifluorescence in comparison to 647 nm GFP tagged photo-switchable antibody for STORM imaging (Figure 5.22-Figure 5.23).

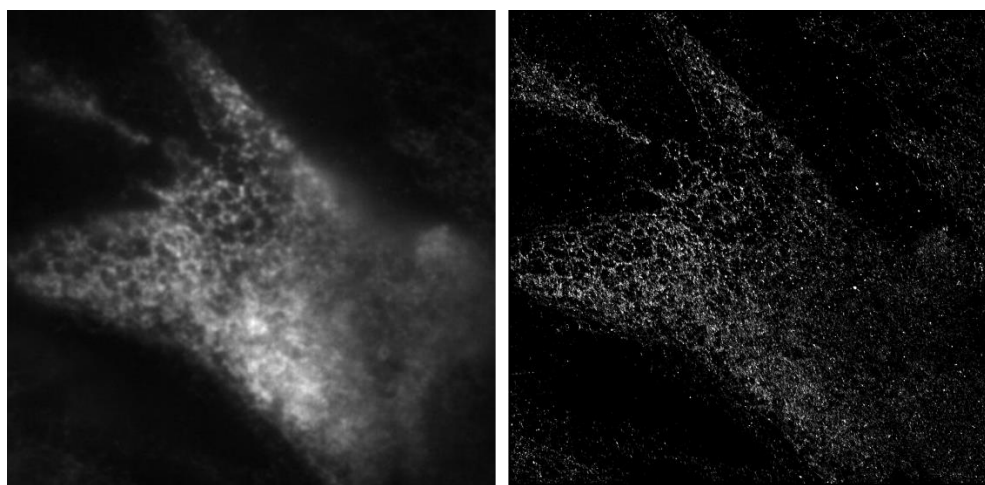


**Figure 5.23 – CatchER<sup>+</sup>-JP45 STORM imaging in C2C12 mouse muscle cells. GFP/EGFP antibody that is Rabbit polyclonal to GFP (ab6556) with a secondary Donkey Anti-Rabbit IgG H&L (ab6701). CatchER<sup>+</sup>-JP45 at 488 nm (white) and 647 nm (cyan).**

The signal for CatchER<sup>+</sup>-JP45 in epifluorescence seems to have higher intensity around the nucleus from all of the cell layers but that upon examining the 647 nm STORM signal we can see that the signal is actually most highly concentrated for localized CatchER<sup>+</sup>-JP45 near the edges of the cell structure where the ER/SR would have plasma membrane contacts (Figure 5.22-Figure 5.23).

### 5.3 Discussion

The HILO imaging technique is an improvement over epifluorescence imaging in that there is an excellent separation of signal from the background as well as an overall higher dynamic range. We found for C2C12 cells that 1 mM of 4-cmc had a release of  $45.5 \pm 1.3\%$  for 32 cells, 50  $\mu\text{M}$  of CPA had a release of  $25.7 \pm 1.5\%$  in 18 cells, and 500 ATP had a release of  $14.0 \pm 1.1\%$  in 12 cells (Table 5.3). HEK293 cells were more sensitive to higher drug concentrations, so we did 500  $\mu\text{M}$  of 4-cmc that had a release of  $22.2 \pm 1.6\%$  for 40 cells, 50  $\mu\text{M}$  of CPA had a release of  $23.3 \pm 1.2\%$  in 18 cells, and 500 ATP had a release of  $15.6 \pm 1.1\%$  in 24 cells. HEK293 was comparable in response to C2C12 for CPA and ATP while only lower for 4-cmc because of the lower concentration. Cos-7 cells were also more sensitive to drug concentrations and also had did 500  $\mu\text{M}$  of 4-cmc that had a release of only  $12.3 \pm 0.8\%$  for 36 cells, 50  $\mu\text{M}$  of CPA had a release of  $17.0 \pm 0.9\%$  in 31 cells, and 500 ATP had a release of  $12.3 \pm 1.7\%$  in 13 cells. Cos-7 was significantly lower in the response of all three drugs in comparison to the other cell lines, with ATP being only remotely close to the other two. Overall it seems that the Cos-7 cells have lower ER responses. Lastly, we tested 4-cmc and histamine on HeLa cells. HeLa cells, unlike the other cell lines we investigated, do not have a P2YR activated by ATP but instead has the histamine receptor (H1R) which is activated by histamine. Many other sensors test the IP<sub>3</sub>R activity through

the H1R activation by histamine since the activation of H1R in HeLa cells leads to oscillations of  $\text{Ca}^{2+}$  from the ER. Thus, we were interested in seeing if we were able to see these oscillations with CatchER<sup>+</sup>. Similarly, to the Cos-7 cells the  $\Delta F/F$  for 1 mM 4-cmc was lower than in C2C12, at ~25% as opposed to ~45%. This is most likely due to the much higher RyR expression in C2C12 cells since they are skeletal muscle cells versus HeLa cells which are cervical cancer tumor cells. We also did a photobleaching test on CatchER<sup>+</sup> to we could see if the downward slope of some of our responses was indeed real signal change or if the sensor was photobleaching over time with the two fps collection by the HILO laser with a constant laser exposure at 0.7 mW power and 0.5 exposure. The cells did not show any significant change in fluorescence over 2500 seconds, which is much longer than any experiments we currently perform. Thus, any downward sloping of the sensor in our imaging is due to the real constant release of  $\text{Ca}^{2+}$  from the ER and not photobleaching of the sensor.

We saw that the overall whole-cell signal for 4-cmc response in C2C12 cells was consistent but when analyzing the individual regions of interest in the cell for potential subcellular microdomains we saw significant variance on the starting  $\text{Ca}^{2+}$  fluorescence, the release and recovery fluorescence as well. When we normalized the results to the initial time point at 0 secs and the release plateau time point of 300 secs, we saw additional significant variances in the recovery, release, and initial fluorescence signals for  $\text{Ca}^{2+}$  bound to CatchER<sup>+</sup>. This indicates that the variance between each ROI in release and recovery is not merely due to an increase in errors in normalization but that there are actual microdomains present. Variance in RyR distribution, as well as  $\text{Ca}^{2+}$  concentrations in those ROIs, account for the variability in the release valley differences at 300 secs. While the distribution of SERCA pump and the  $\text{Ca}^{2+}$  nearby for SERCA pump to uptake in the cytosol account for the variable recovery rates at 500 secs. We confirmed

that there is differential expression of RyR between a blast C2C12 cell and myotubule using confocal microscopy. Additionally, we confirmed that the RyR expression was distributed throughout the ER but examining the surface plots of the cells we saw peaks of differential expression microdomains throughout the cell (Figure 5.14). We also examined SERCA pump distribution and expression using confocal imaging to correlate the kinetic recovery differences (Figure 5.15). Interestingly we see that the SERCA pump not only has microdomains of expression indicated by the peak height differences on the surface plot but that the SERCA pumps are overall mainly expressed in the ER around and in the nucleus of the cell (Figure 5.15). Overall the SERCA pump antibody signal was brighter than the RyR signal for the same ratio and secondary antibody which could be because the SERCA pump uptake of  $\text{Ca}^{2+}$  to the ER is a much slower process requiring an ATP for each  $\text{Ca}^{2+}$  shuttled so having higher expression of SERCA pumps could overcome the slower kinetics of SERCA pumps for ER  $\text{Ca}^{2+}$  dynamics by having more in place to function. We can then further perform confocal or STORM imaging on the same cells to see if the ROIs have differential receptor expression or if these variances are solely from  $\text{Ca}^{2+}$  concentration microdomains.

We further analyzed potential localized subcellular microdomains by designing a targeted CatchER<sup>+</sup> variant which is attached to JP45 and col-localizes with RyR1 at the PM for E-C coupling with DHPR called CatchER<sup>+</sup>-JP45. We saw that the whole-cell signaling in C2C12 blast cells for 4-cmc treatment was similar in release and recovery kinetics with the CatchER<sup>+</sup>-JP45 sensor being slightly dimmer due to the lower RyR expression in blast cells as seen by the confocal imaging. The whole-cell signaling in response to SERCA pump inhibition by CPA was markedly different on the recovery kinetics where CatchER<sup>+</sup> has slow recovery with a full recovery after washing away CPA whereas CatchER<sup>+</sup>-JP45 is able to recover the  $\text{Ca}^{2+}$  almost as rapidly as

released. This is most likely due to the CaSQ network at the junctional SR which binds high  $[Ca^{2+}]$  for storage for E-C coupling response and can release  $Ca^{2+}$  from CaSQ for SR release or to recover the free SR  $[Ca^{2+}]$ , this response could also be due to other methods of ER/SR refilling in the region of the junctional SR such as STIM/ORAI influx of  $Ca^{2+}$  from the extracellular space. Since JP45 and RyR1 synthesis is upregulated in myotubules we also compared the global CatchER<sup>+</sup> and localized CatchER<sup>+</sup>-JP45 signal in response to 4-cmc in C2C12 myotubules and found that the global ER/SR  $Ca^{2+}$  dynamics led to a slow release over 413.7 secs to  $24.6 \pm 2.2\%$   $Ca^{2+}$  release whereas CatchER<sup>+</sup>-JP45 rapidly releases and plateaus  $Ca^{2+}$  from the SR at  $28.4 \pm 0.8\%$  within  $42.7 \pm 3.9$  secs (Figure 5.19). CatchER<sup>+</sup>-JP45 shows that upon washing away of 4-cmc the junctional SR  $Ca^{2+}$  can immediately recover back to baseline and 80% of this recovery happens in  $114.3 \pm 24.7$  secs whereas global CatchER<sup>+</sup> shows that the whole ER/SR cannot fully recover the ER/SR  $Ca^{2+}$  back to baseline (Figure 5.19). When comparing these results to mouse FDB muscle electrical stimulation with CatchER<sup>+</sup> and CatchER<sup>+</sup>-JP45, we see the similar trend where CatchER<sup>+</sup>-JP45 shows significant  $Ca^{2+}$  release at 85% in 40 ms while CatchER<sup>+</sup> indicates the global  $Ca^{2+}$  release is only 50% and much slower at 100 ms although both are able to recover to baseline (Figure 5.20). In the future, we will further investigate the microdomain visualization, especially in comparison of CatchER<sup>+</sup> and CatchER<sup>+</sup>-JP45 within myoblasts and myotubules of C2C12 cells. Furthermore, STORM dual-color and confocal imaging of C2C12 cells and other cell lines are necessary to confirm the microdomain protein expression to correlate the HILO imaging results. Also, we should do a  $Ca^{2+}$  free trial of CatchER<sup>+</sup> imaging using  $100 \mu M La^{3+}$  in the  $0 Ca^{2+}$  Ringer's buffer to prevent any  $Ca^{2+}$  in buffer/cell media from entering the cell, therefore preventing refilling of ER/SR.  $La^{3+}$  is a  $Ca^{2+}$  chelator since it is a  $Ca^{2+}$  channel blocker. This can provide critical

information about ER/SR refilling routes. There is also a need to target CatchER<sup>+</sup> to other organelles as well as designing versions of CatchER<sup>+</sup> based on RFP, YFP, and CFP.

## 5.4 Materials and Methods

### 5.4.6 Cloning of CatchER<sup>+</sup>

Mutations were made using Pfu DNA polymerase (G-biosciences) by following the manufacturer's instructions and using primers 5'-AAGTTCAGCGTGCGCGGCGAGGGCGAG-3' and 5'-CTCGCCCTCGGCGCGCACGCTGAACTT-3' for S30R, 5'-GGCGATGCCACCAACGGCAAGCTG-3' and 5'-CAGCTTGCCGTTGGTGGCATCGCC-3' for Y39N, and 5'-GAGGACGGCGGCGTGCAGCT-3' and 5'-AGCTGCACGCCGCGTCCTC-3' for S175G.

### 5.4.7 Cell culture and transfection of CatchER<sup>+</sup>

Cultures of C2C12 (CRL-1772), Cos-7 (CRL-1651), HEK293 (CRL-1573) and HeLa (CRM-CCL-2) cells were purchased from American Type Culture Collection (ATCC) and maintained in Dulbecco's modified Eagle's medium (DMEM) supplemented with 10% fetal bovine serum (FBS) and high glucose (4.5 g/L) at 37°C. CatchER<sup>+</sup> was transfected into cells using Lipofectamine 3000 (Life Technologies) by following the manufacturer's instructions. Seed HEK293, Cos-7 or HeLa cells onto sterilized 22 mm x 40 mm glass microscope slides in 6 cm dishes, so they are ~70% confluent the day of transfection. The next day cells were transfected using 2 µg of CatchER<sup>+</sup> cDNA and a 1:3 (weight/volume) DNA: transfection reagent ratio in the reduced serum media Opti-MEM at 20-100% Opti-MEM. DNA: transfection reagent mixture was incubated for 4-6 hr at 37 °C and after cells are washed then incubated at 37 °C for 48 hr so CatchER<sup>+</sup> can be expressed. C2C12 myoblast cells were trypsinized, resuspended in DMEM, and seeded onto slides at a final

confluence of 60%. Cells were transfected during resuspension as outlined above and then incubated for 24 hr at 37 °C then washed and incubated at 37 °C for 48 hr so CatchER<sup>+</sup> can be expressed.

#### ***5.4.8 Confocal imaging of CatchER<sup>+</sup>***

We used confocal laser scanning microscopy (CLSM) Zeiss LSM 800 on fixed cells and then used Invitrogen<sup>™</sup> Molecular Probes<sup>™</sup> BODIPY<sup>™</sup> ER-Tracker<sup>™</sup> Red for staining the ER and Invitrogen<sup>™</sup> ProLong<sup>™</sup> Gold Antifade Mountant with DAPI for staining the nucleus, CatchER<sup>+</sup> was transfected into the cells two days before fixing. Cells were fixed with 3.7% Thermo Scientific<sup>™</sup> Pierce<sup>™</sup> 16% Formaldehyde (w/v), Methanol-free, permeabilized with 0.1% Triton X-100, and non-specific binding was blocked with 0.1% Bovine Serum Albumin (BSA) all in phosphate buffered saline (PBS).

#### ***5.4.9 Epifluorescence imaging of CatchER<sup>+</sup>***

CatchER<sup>+</sup> was transiently transfected into cells grown on coverslips and cultured for 48 hr at 37°C. Cells were washed twice with 2 mL of physiological Ringer buffer (10 mM HEPES, 121 mM NaCl, 2.4 mM K<sub>2</sub>HPO<sub>4</sub>, 0.4 mM KH<sub>2</sub>PO<sub>4</sub>, 1.2 mM MgCl<sub>2</sub>, 1.8 mM CaCl<sub>2</sub> at pH 7.4). The coverslips were mounted on a Warner Instruments low profile open diamond bath imaging chamber. The cells were illuminated with 488 nm, and the fluorescence at an emission wavelength 510 nm was recorded in real-time as the concentration of ER/SR Ca<sup>2+</sup> was perturbed with 4-cmc, CPA, or ATP. All experiments were performed at room temperature on a Leica DM6100B inverted microscope with a Hamamatsu cooled EM-CCD camera and illuminated with a Till Polychrome V monochromator and a xenon lamp.



#### ***5.4.10 HILO imaging of CatchER<sup>+</sup>***

HILO microscopy was accomplished based on a Nikon TiE inverted microscope. Briefly, a fiber coupled 488 nm laser (Oxxius) was collimated and introduced into the optical train of the microscope. The laser was then focused at the back focal plane of a 100X TIRF objective (N.A. 1.49, Nikon) by using an achromatic optical lens (Thorlabs) with 200 mm focal length. The laser collimation system and focusing lens were both mounted a mechanic translation stage (Thorlabs) so that its optical axis of incident laser could be laterally shifted to change the incident angle of the laser at the cell-coverslip interface. The HILO imaging condition was achieved by operating at sub-critical angles of the total internal reflection. Since the thickness of cells, as well as the depth of ER structure, varied among individual cells, the best HILO imaging conditions were achieved by carefully tuning the incident angle of the excitation laser. Moreover, the epifluorescence images used for comparison with HILO images were taken by setting the incident angle at 0 degrees. Large scale data analysis was done with a self-written MATLAB script.

#### ***5.4.11 Preparing cells for STORM imaging***

Cells were fixed in standard fixing solution: 3% paraformaldehyde (PFA) and 0.1% glutaraldehyde (GA) in PBS. Cells were reduced with 2 mL of 0.1% NaBH<sub>4</sub>, prepared immediately before use and washed with PBS. Cells were blocked in blocking buffer of 3% BSA and 0.1% Triton-X100 in PBS and then aspirated. Primary antibody 2 ug/mL was added in blocking buffer and incubated for 30 mins at RT or O/N at 4°C. Cells were aspirated and washed three times with washing buffer of 0.2% BSA and 0.05% Triton-X100 in PBS. Secondary antibody 2 ug/mL was added in blocking buffer and incubated for 30 mins at RT while shaking and covered with foil to protect fluorophore from light. Cells were aspirated and washed three times with washing buffer in the dark at room temperature.

## 6 Neuronal Application of CatchER<sup>+</sup>

### 6.1 Introduction

Neuron Ca<sup>2+</sup> dynamics are a complex system between pre and post-synaptic neurons for neurological communications. Presynaptic Ca<sup>2+</sup> influx triggers exocytosis of neurotransmitter-containing synaptic vesicles.

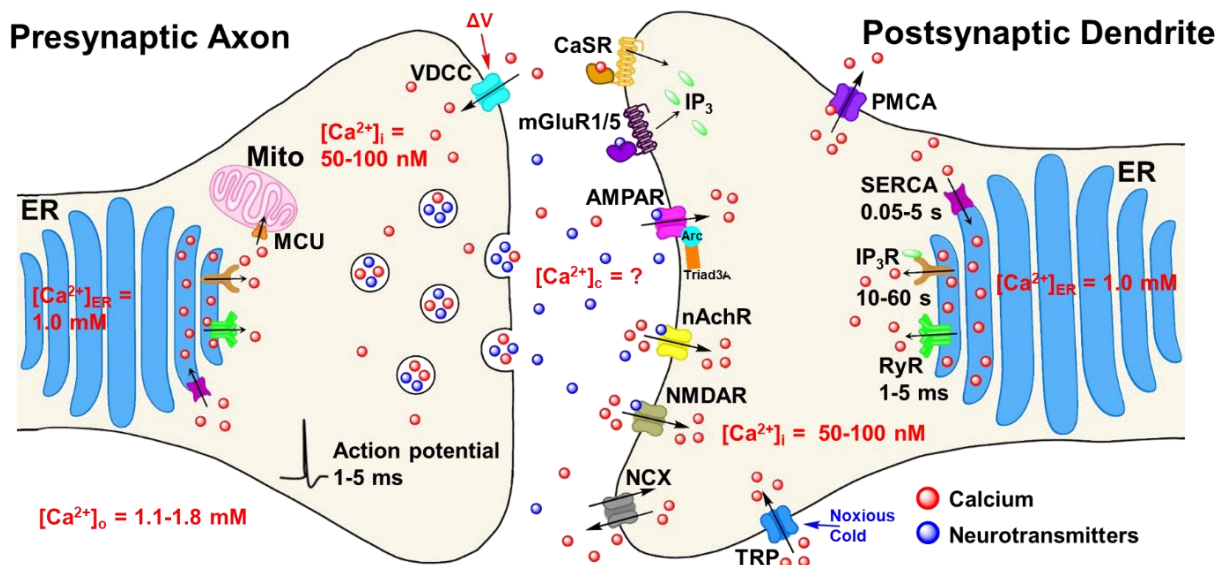


**Figure 6.1 – Calcium dynamics in neurons.**

Ca<sup>2+</sup> is a neurotransmitter secreted in the synaptic cleft through synaptic vesicles with an unknown [Ca<sup>2+</sup>] inside of the synaptic cleft. The ER is the primary store of Ca<sup>2+</sup> in neurons at ~1 mM [Ca<sup>2+</sup>] while the cytosolic [Ca<sup>2+</sup>] is in the nM range. Multiple channels and receptors shuttle Ca<sup>2+</sup> into and out of the neurons as well as activating Ca<sup>2+</sup> release from the ER through downstream regulation, for example, the IP<sub>3</sub>R being bound by IP<sub>3</sub> from mGluR activation.

Ca<sup>2+</sup> release depends on the ER Ca<sup>2+</sup> dynamics in order for neuron Ca<sup>2+</sup> signaling from the presynaptic axon to the postsynaptic dendrite<sup>[350]</sup>. A transient rise in postsynaptic calcium in dendritic spines is essential for the induction of activity-dependent synaptic plasticity. Intracellular Ca<sup>2+</sup> in neurons is 50-100 nM but can increase up to 100-fold upon generation of an action potential. Many channels, pumps, receptors, and organelles are involved in the neuronal Ca<sup>2+</sup>

dynamics. In order to regulate the  $\text{Ca}^{2+}$  homeostasis between the extracellular and intracellular spaces, as well as the internal organellar stores and the synaptic cleft a multitude of proteins are utilized to keep this intricate balance and  $\text{Ca}^{2+}$  communication functioning<sup>[351-370]</sup>.

In order to shuttle  $[\text{Ca}^{2+}]_o$  to the cytosol the neurons utilize  $\alpha$ -amino-3-hydroxy-5-methyl-4-isoxazolepropionic acid receptor (AMPA), nicotinic acetylcholine receptors (nAChR), N-methyl-D-aspartate receptor (NMDAR), voltage-gated/voltage-dependent calcium channel (VGCC/VDCC), and transient receptor potential channel (TRP) proteins. All these proteins have  $\text{Ca}^{2+}$  shuttling capabilities based on their activation cascades. AMPAR has four agonist binding sites with the conventional agonist being glutamate, upon binding of at least 2 binding sites the receptor's central pore is opened enough through conformational change to allow cations of  $\text{Ca}^{2+}$ , as well as potassium and sodium to flow intracellularly, which ions go through AMPAR, is subunit selective<sup>[351, 352]</sup>. This processes of AMPAR opening and closing occurs relatively quickly within 1 ms, which allows for the necessary CNS fast excitatory synaptic transmissions<sup>[351]</sup>. Similarly, to AMPAR the NMDAR also allows cations to flow through its pore upon binding glutamate and glycine (or D-serine), although the major cation in the case of NMDAR is sodium with lesser amounts of calcium and potassium being able to flow into the cytosol<sup>[353-362]</sup>. nAChR is a non-selective cation channel which when in its open conformation allows the passage of cations to flow in or out of the cytosol. nAChR undergoes a conformational change upon binding of its agonist acetylcholine<sup>[363, 364]</sup>. VDCCs are one of the main ways to allow  $\text{Ca}^{2+}$  to quickly pass into the cytosol, upon membrane depolarization the VDCC is activated and allows for the mM  $[\text{Ca}^{2+}]_o$  to flow into the micromolar intracellular cytosolic calcium concentration ( $[\text{Ca}^{2+}]_i$ )<sup>[365, 366]</sup>. TRP channels have many stimuli leading to the transport of  $\text{Ca}^{2+}$  into the cytosol depending on cellular

or species expression<sup>[367-370]</sup>. TRP channels have been found to be activated by cold or hot stimulus, taste, pain, and other compounds<sup>[367-370]</sup>.

In addition to proteins which directly transport  $\text{Ca}^{2+}$  into the cytosol, there are also proteins whose signaling leads to  $\text{Ca}^{2+}$  release into the cytosol from the ER. The transmembrane GPCR proteins CaSR and mGluR, upon binding to an agonist extracellularly, lead to  $\text{IP}_3$  production which in turn binds to the  $\text{IP}_3\text{R}$  in the ER membrane and releases oscillatory or transient  $\text{Ca}^{2+}$ , respectively. CaSR binds  $\text{Ca}^{2+}$  to achieve this purpose while mGluR binds glutamate or other drugs such as dihydroxyphenylglycine (DHPG).

While these proteins all lead to the increase in  $[\text{Ca}^{2+}]_i$ , there must be proteins which help maintain the cytosolic  $[\text{Ca}^{2+}]_i$  in the micromolar range. The proteins responsible for shuttling  $\text{Ca}^{2+}$  out of the cytosol in neurons are the plasma membrane  $\text{Ca}^{2+}$  ATPase (PMCA) pump, the sodium-calcium exchanger (NCX), the SERCA pump, and ion/neurotransmitter containing vesicles. PMCA pumps  $\text{Ca}^{2+}$  against the gradient from the micromolar cytosol to the millimolar extracellular space, this requires energy in the form of ATP to shuttle  $\text{Ca}^{2+}$ . PMCA is essential in maintaining this homeostasis, without which the neuron and body as a whole would be unable to continue with  $\text{Ca}^{2+}$  signaling in the cell. PMCA has a high affinity for  $\text{Ca}^{2+}$  in the nanomolar range but requires the hydrolysis of one ATP molecule per each  $\text{Ca}^{2+}$  ion moved extracellularly, making this process slow and costly but accurate<sup>[371-374]</sup>. NCX, on the other hand, has a much lower affinity for  $\text{Ca}^{2+}$  than PMCA but is able to much more quickly shuttle  $\text{Ca}^{2+}$  extracellularly, up to 5000  $\text{Ca}^{2+}$  ions per second, at a much lower energy cost<sup>[375-377]</sup>. NCX relies on the gradient of  $\text{Na}^+$  versus  $\text{Ca}^{2+}$  and can remove one  $\text{Ca}^{2+}$  per addition of 3  $\text{Na}^+$  to the cytosol<sup>[376, 377]</sup>. The speed at which NCX functions is critical for neuronal action potentials which need  $\text{Ca}^{2+}$  signaling recovery at rapid

rates<sup>[375]</sup>. PMCA and NCX are the two primary methods for any cell to regulate the removal of  $\text{Ca}^{2+}$  from the cytosol<sup>[374, 378]</sup>.

Not only is neuron  $\text{Ca}^{2+}$  dynamics critical for neurological function, but it is also related to a plethora of neuron related disease from dysregulation of  $\text{Ca}^{2+}$  dynamics as seen in Table 6.1. Thus, being able to monitor these ER  $\text{Ca}^{2+}$  dynamics in response to potential disease mutations and therapeutic targets can help us to better understand these diseases and treat them effectively. Additionally, there are many disorders that can be affected by ER  $\text{Ca}^{2+}$  dynamics that have not been understood or unearthed in their functionality, such as how ER  $\text{Ca}^{2+}$  dynamics are affected in synaptic plasticity (Table 6.1).

**Table 6.1 – ER/SR related diseases.**

Inositol trisphosphate receptor (IP <sub>3</sub> R)	Ryanodine receptor (RyR)	Sarco/endoplasmic reticulum $\text{Ca}^{2+}$ -ATPase (SERCA) pump
Alzheimer's disease (AD)	Alzheimer's disease (AD)	Epilepsy
Bipolar disorder (BPD)		Depression
Amyotrophic lateral sclerosis (ALS)		
Huntington's disease		
Schizophrenia		
Spinocerebellar ataxias		
Epilepsy		

The ER network not only surrounds the nucleus comprising the nuclear envelope but then extends all the way to distal dendrites and dendritic spines. The ER network has higher concentrations at branch points of dendrites to help produce necessary local proteins needed for function in dendrites and synaptic activity in dendritic spines<sup>[379]</sup>. Neurons have a tortuously complex and continuous ER network which is still currently being investigated<sup>[380-385]</sup>. The ER extends throughout the whole neuron and is even found in some dendritic spines where synaptic activity can occur<sup>[379, 386-390]</sup>. Similarly, to other cells, the significant players for ER  $\text{Ca}^{2+}$  release and uptake are still  $\text{IP}_3\text{R}$ , RyR, and the SERCA pump. Additionally, neurons have calcium induced calcium release (CICR) through the STIM/ORAI complex<sup>[391]</sup>. Presynaptic neurons can localize to the dendritic spines of postsynaptic neurons for neurotransmitter communication.  $\text{Ca}^{2+}$  release from the ER in presynaptic neurons triggers spontaneous neurotransmitter release. The neurotransmitters then bind to receptors on the surface of the postsynaptic neurons causing  $\text{Ca}^{2+}$  release from  $\text{IP}_3\text{R}$  and/or RyR as well as CICR, this can lead to long-term potentiation or depression (LTP or LTD)<sup>[391]</sup>. The rough ER in neurons is found primarily in the soma and proximal dendrites and has ribosomes for protein transcription<sup>[379, 391]</sup>. The smooth ER is found mainly in distal dendrites, dendritic spines, and axons with some ribosomes for local protein transcription<sup>[379, 391]</sup>. The Golgi apparatus also has satellite Golgi complexes that are in the dendrites for signaling and protein shuttling in these regions<sup>[379]</sup>.

Neuronal ER  $\text{Ca}^{2+}$  imaging is not a new field and has been investigated before. Henderson et al. examined GCaMP6s in neuroblastoma and rat cortical neurons using different drugs to stimulate ER  $\text{Ca}^{2+}$  release<sup>[392]</sup>. They used 10  $\mu\text{M}$  CPA to inhibit the refilling of the SERCA pump, thus creating a decrease of ER  $\text{Ca}^{2+}$ , and 300 nM thapsigargin to also irreversibly inhibit the SERCA pumps<sup>[392]</sup>. With 10  $\mu\text{M}$  CPA they saw a 40-60% release where we see a 30-50% release with 15

$\mu\text{M}$  CPA depending on cell types. For rat cortical neurons they used 25  $\mu\text{M}$  CPA to inhibit the SERCA pump, 50-100  $\mu\text{M}$  DHPG to bind mGluR1/5 and cause  $\text{IP}_3$  production which binds to the  $\text{IP}_3\text{R}$  and releases  $\text{Ca}^{2+}$  from the ER<sup>[392]</sup>. Additionally, they used 5 mM Caffeine on cardiomyocytes to induce  $\text{Ca}^{2+}$  release from the RyR<sup>[392]</sup>. They saw a 40-50% release with CPA, whereas we see a 30-50% release depending on cell type. Choi et al. used Fura-2 to investigate the cytosolic changes in response to ER  $\text{Ca}^{2+}$  release in mouse midbrain dopamine neurons<sup>[393]</sup>. They used 20 mM Caffeine to induce the RyR to release  $\text{Ca}^{2+}$  from the ER, they also used 20  $\mu\text{M}$  DHPG to release  $\text{Ca}^{2+}$  from the  $\text{IP}_3\text{R}$  and found that if they already emptied the ER using Caffeine and then added DHPG there was no response since the  $\text{Ca}^{2+}$  was all already released<sup>[393]</sup>. They also used MagFluo-4 dye to image the ER signal changes using 20 mM Caffeine to induce RyR  $\text{Ca}^{2+}$  release from the ER and 4  $\mu\text{M}$  thapsigargin to irreversibly block ER  $\text{Ca}^{2+}$  refilling through the SERCA pump<sup>[393]</sup>. They got a ~40-45% release with Caffeine and a ~60% release by thapsigargin. Solovyova et al. used Mag-Fura-2 to image the ER signal changes using 20 mM Caffeine to induce RyR  $\text{Ca}^{2+}$  release from the ER and 5  $\mu\text{M}$  thapsigargin to irreversibly block ER  $\text{Ca}^{2+}$  refilling through the SERCA pump in dorsal root ganglia neurons<sup>[394]</sup>.

While imaging in neurons with and without looking directly at ER  $\text{Ca}^{2+}$  has been done previously there is an unmet need for an imaging method capable of imaging specifically in the ER and within these small dendritic spines with excellent spatial resolution and strong fluorescence signal. We were also interested in the microdomains through the variable ER expression of neuronal systems, so we applied our designed sensor CatchER<sup>+</sup> in hippocampal neurons to see the differential subcellular signaling in response to DHPG activation of mGluR1/5 to potentiate LTD.

## 6.2 Results

### 6.2.1 *CatchER<sup>+</sup> HILO Imaging in Neurons*

HILO imaging has shown to be successful for CatchER<sup>+</sup> imaging studies for looking at differential signaling, and subcellular microdomains throughout the ER network, which while not uniform in a cell is less diverse than the neuron ER structure. In order to investigate the differential and extensive neuronal ER structure, we utilized CatchER<sup>+</sup> sensor and HILO high-resolution imaging in hippocampal neurons (Figure 6.3) and cortical neurons (Figure 6.4) from post-natal mice as well as GFP for negative control (Figure 6.2). GFP showed no response to DHPG as expected since it was a negative control transfected into the cytosol of the neuron without Ca<sup>2+</sup> sensing capabilities (Figure 6.2).

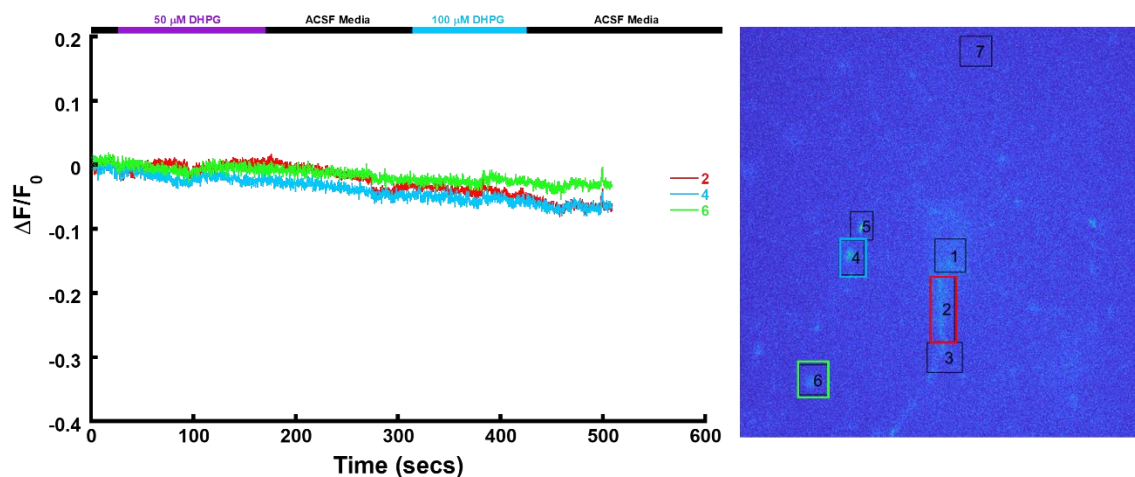


**Figure 6.2 – GFP control representative response in mouse hippocampal neuron.** The response to the perfusion of 50 and 100  $\mu\text{M}$  DHPG is shown through the  $\Delta F/F_0$  plot with a heat map of GFP transfected into the mouse hippocampal neuron cytosol. The color of the lines corresponds with the regions highlighted by boxes in the heat map.

Initially, we investigated the effect of 50  $\mu\text{M}$  DHPG and subsequently 100  $\mu\text{M}$  DHPG in the hippocampal neurons to see the differing responses to pre- and post-threshold levels of DHPG to see the differences between the long term depression effects of 50 versus 100  $\mu\text{M}$  DHPG (Figure



6.3). While we were able to see some regions of the neuron had full recovery back to baseline for 100  $\mu\text{M}$  DHPG similar to the 50  $\mu\text{M}$  treatment, we also saw that some regions had partial or no recovery for 100  $\mu\text{M}$  DHPG as opposed to the 50  $\mu\text{M}$  treatment (Figure 6.3B). The response to 50 and 100  $\mu\text{M}$  DHPG led to a significant spike in the signal, either through release or uptake, and we also see a significant spike response to the washing of the ACSF buffer to remove the DHPG which correlated to that regions DHPG response, either through release or uptake (Figure 6.3A). Remarkably, the 4-cmc, thapsigargin, or CPA compounds being washed away with ACSF does not trigger this response in the neurons and is unique to the DHPG wash step (Figure 6.3C and Figure 6.4A). Another phenomenon we were able to observe was the differential  $\text{Ca}^{2+}$  signaling throughout the ER of the neuron. In most regions of the ER in the neuron, we see the expected  $\text{Ca}^{2+}$  release from the ER through the  $\text{IP}_3\text{R}$  after addition of DHPG as well as the recovery of the ER as the ER refills after release. Some areas of the neuronal ER though actually have an uptake of  $\text{Ca}^{2+}$  in response to DHPG additions (Figure 6.3A). This is thought to either be a movement of  $\text{Ca}^{2+}$  for signaling responses to different regions of the ER for local responses, CICR, or perhaps activating pulling  $\text{Ca}^{2+}$  into the ER through the STIM/ORAI1 complex. In addition to looking at the DHPG effects on the ER  $\text{Ca}^{2+}$  signaling in hippocampal neurons, we also looked at the RyR response as a control since the 4-cmc response elicited from RyR has previously been consistent and stronger than  $\text{IP}_3\text{R}$  responses in non-neuronal cell lines.

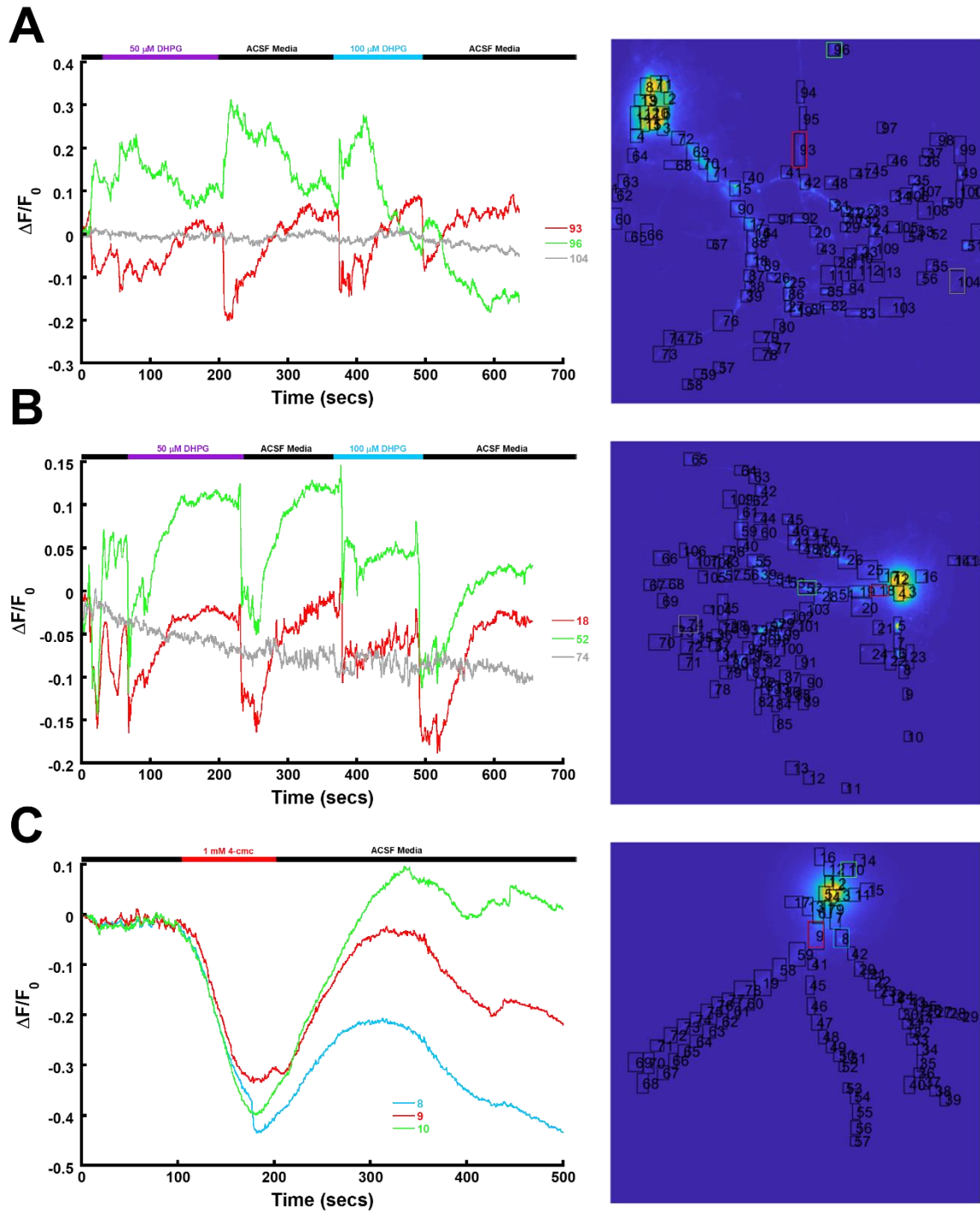


**Figure 6.3 – DHPG and 4-cmc representative response in hippocampal neurons. A&B – The response to the perfusion of 50 and 100  $\mu$ M DHPG is shown through the  $\Delta F/F_0$  plot with a heat map of CatchER<sup>+</sup> transfected into the mouse hippocampal neuron. The color of the lines corresponds with the regions highlighted by boxes in the heat map. C – The response to the perfusion of 1 mM 4-cmc is shown through the  $\Delta F/F_0$  plot with a heat map of CatchER<sup>+</sup> transfected into the mouse hippocampal**

**neuron. The color of the lines corresponds with the regions highlighted by boxes in the heat map.**

Thus we used 1 mM 4-cmc perfusion on the neurons either alone or after DHPG to see that the ER release was occurring (Figure 6.3C). All of the regions of the ER in the neurons reacted similarly in that they all had a release of  $\text{Ca}^{2+}$  upon 4-cmc treatment and some level of recovery after washing with ACSF. The release of  $\text{Ca}^{2+}$  varies between areas of the neuron of around 10-45% release. The other substantial difference throughout the neuron is the recovery rates. Some regions can recover entirely while others recover past the baseline, partially recover, barely, or not at all. While there is some variability in the 4-cmc response, it is still consistently a release of  $\text{Ca}^{2+}$  from the ER and none of the regions have an increase as seen in the DHPG treatments (Figure 6.3). In addition to imaging hippocampal neurons we also imaged cortical post-natal mouse neurons. We treated these neurons with DHPG and 4-cmc similarly to the hippocampal neurons (Figure 6.4). Similar to the hippocampal trials, we saw a decrease in signal in response to DHPG for most regions of the neuron's ER but an increase in some areas (Figure 6.4). We also added 200  $\mu\text{M}$  4-cmc instead of 1 mM 4-cmc since we did not know how the cortical neurons would respond to higher 4-cmc concentrations and did not want to lead to neuronal apoptosis (Figure 6.4A). The neurons had a release but not recovery, possibly due to the long imaging time and multiple drug treatments (Figure 6.4A).

The cortical neurons also seemed to exhibit an overall slow decrease in signal throughout the experiment that would not be photobleaching since the CatchER<sup>+</sup> sensor takes much longer to actually photobleach and that the background/non-responsive plots had minor decreases in comparison (Figure 6.4). Thus, this phenomenon of gradual decreasing in signal seems to be

indicative of true signaling dynamics in the cortical neuron ER where  $\text{Ca}^{2+}$  is slowly depleting over time.

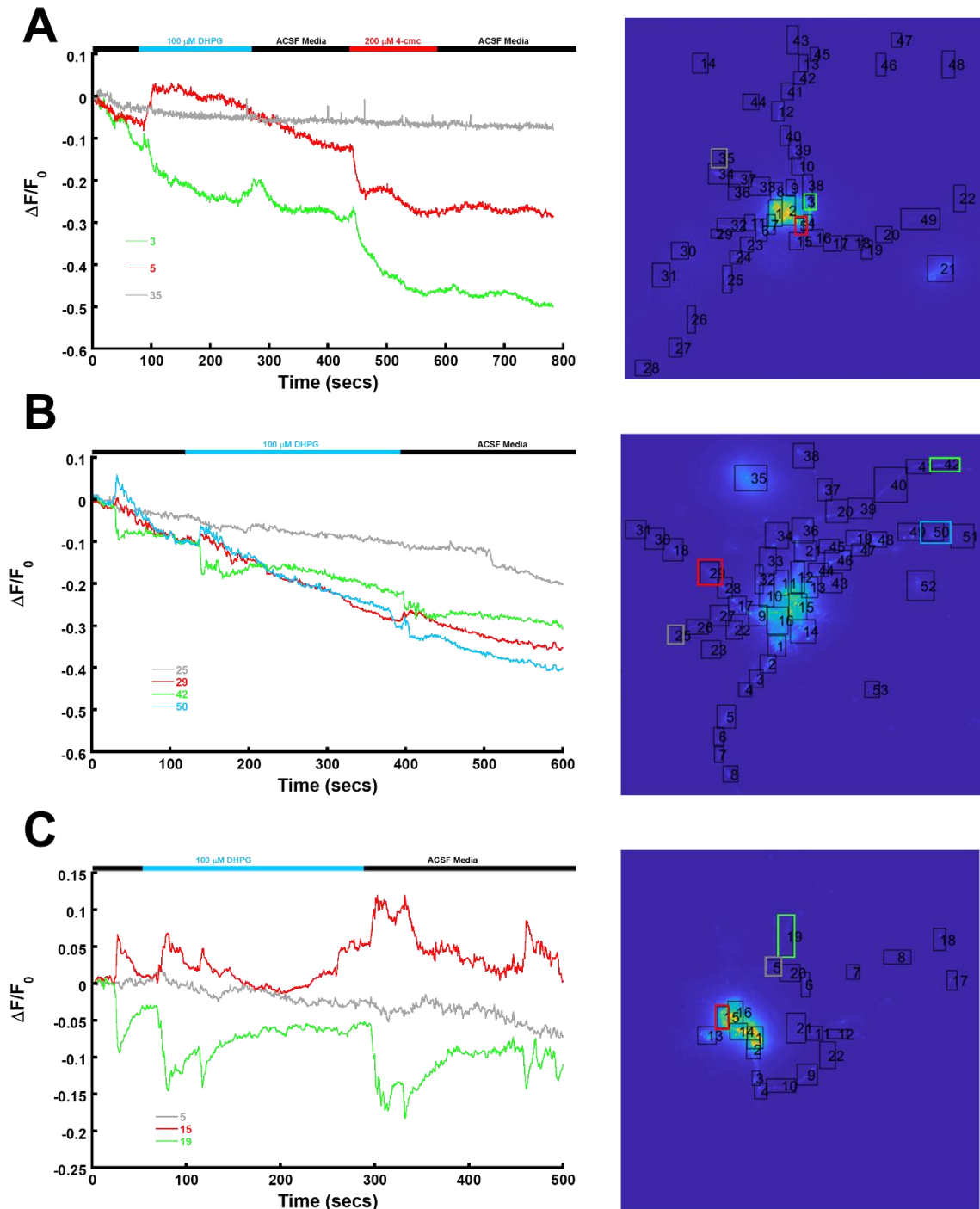


**Figure 6.4 – DHPG and 4-cmc representative response in mouse cortical neurons.**  
**A-C – The response to the perfusion of 100  $\mu\text{M}$  DHPG is shown through the  $\Delta F/F_0$  plot with a heat map of CatchER<sup>+</sup> transfected into the mouse hippocampal neuron.**

The color of the lines corresponds with the regions highlighted by boxes in the heat map. A – The response to the perfusion of 1 mM 4-cmc is shown after the DHPG response through the  $\Delta F/F_0$  plot with a heat map of CatchER<sup>+</sup> transfected into the mouse hippocampal neuron. The color of the lines corresponds with the regions highlighted by boxes in the heat map.

We then treated hippocampal neurons with 100  $\mu$ M DHPG alone to see the response were similar if the neurons were not pre-treated with 50  $\mu$ M DHPG first (Figure 6.5A-B).

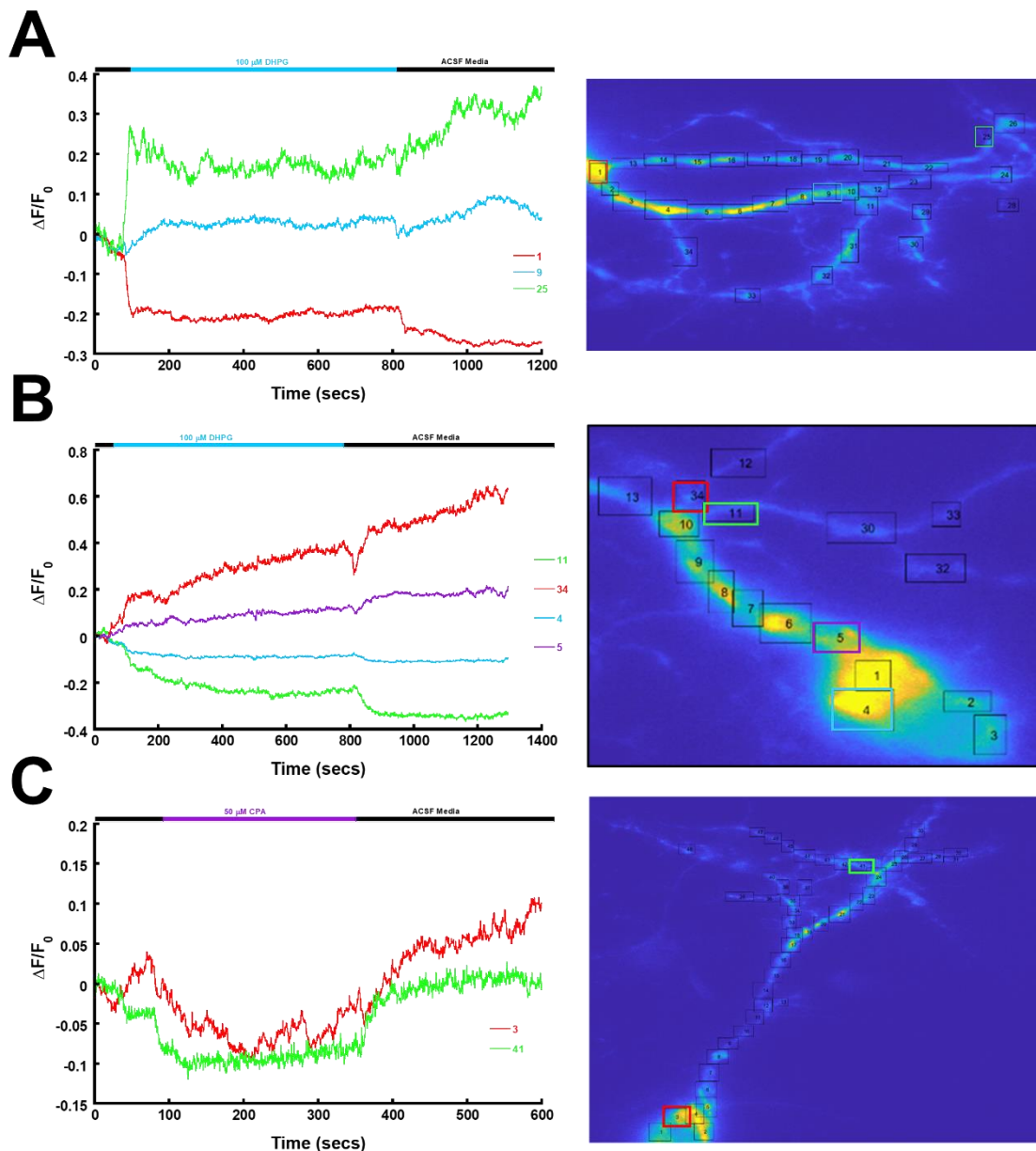


Figure 6.5 – DHPG and CPA representative response in mouse hippocampal neurons.

**A-B – The response to the perfusion of 100  $\mu\text{M}$  DHPG is shown through the  $\Delta\text{F}/\text{F}_0$  plot with a heat map of CatchER<sup>+</sup> transfected into the mouse hippocampal neuron. C – The response to the perfusion of 50  $\mu\text{M}$  CPA is shown through the  $\Delta\text{F}/\text{F}_0$  plot with a heat map of CatchER<sup>+</sup> transfected into the mouse hippocampal neuron. The color of the lines corresponds with the regions highlighted by boxes in the heat map.**

The 100  $\mu\text{M}$  DHPG treatments showed responses similar to those treated with 50 and 100  $\mu\text{M}$  DHPG with the same differential ER  $\text{Ca}^{2+}$  response where some regions increase in ER  $\text{Ca}^{2+}$  concentrations whereas most of the neuron decreases and that the 100  $\mu\text{M}$  treatment led to the ER  $\text{Ca}^{2+}$  only partially recovering or having a slight plateau where the signal does not recoup and often responds again upon washing with ACSF buffer as we have seen for all the DHPG treatments (Figure 6.5A-B).

The CPA treatment induced a response pattern similar to 4-cmc in neurons and almost identical in other CPA treated cell imaging experiments we have done using CatchER<sup>+</sup> (Figure 6.5C). The CPA in hippocampal neurons induces a 5-10% release of  $\text{Ca}^{2+}$  from the ER, which reaches a plateau until washed away with ACSF thus returning to the baseline  $\text{Ca}^{2+}$  signal (Figure 6.5C). This shows us that the SERCA pump distribution and signaling is not differential to those in other cell types especially as compared to the differential signaling we see for the IP<sub>3</sub>R release through DHPG as composed to ATP or Histamine IP<sub>3</sub>R activation in other cell types which only lead to a decrease in the ER  $\text{Ca}^{2+}$  signal, not an increase, and at a much slower rate than seen in neurons.

### 6.3 Discussion

We were able to successfully image hippocampal neurons which were obtained from post-natal mice using our fluorescence ER  $\text{Ca}^{2+}$  sensor CatchER<sup>+</sup> in epifluorescence and HILO imaging systems. We initially imaged CatchER<sup>+</sup> in neurons on an epifluorescence 40x Leica microscope in neurobasal media activating the ER response using 200  $\mu\text{M}$  4-cmc to activate the RyR  $\text{Ca}^{2+}$

release, 50  $\mu\text{M}$  DHPG or 10 mM Caffeine to activate mGluR1/5 to indirectly activate the IP<sub>3</sub>R Ca<sup>2+</sup> release, and lastly with 15  $\mu\text{M}$  CPA to inhibit SERCA pump refilling. The low resolution of our 40x objective and the overall fluorescence overlap of epifluorescence led us to change to HILO imaging technique with a 100x objective on a Nikon microscope in order to see microdomain changes throughout the neuron ER network and be able to visualize the soma, dendrites, and dendritic spines accurately.

Therefore, we examined mouse hippocampal post-natal neuron imaging (Figure 6.2-Figure 6.3 and Figure 6.5) as well as a batch of mouse cortical post-natal neuron wild type (WT) imaging (Figure 6.4), both with the HILO imaging system. We first examined that the GFP transfected neurons for control had no signal change in response to treatment with 50  $\mu\text{M}$  and 100  $\mu\text{M}$  DHPG, which they did not, confirming that any CatchER<sup>+</sup> signal changes we examine within the neurons are actual signal changes (Figure 6.2). We next looked at CatchER<sup>+</sup> responses in hippocampal neurons in response to 1 mM 4-cmc to activate the RyR Ca<sup>2+</sup> release, 50 or 100  $\mu\text{M}$  DHPG to activate mGluR1/5 to indirectly activate the IP<sub>3</sub>R Ca<sup>2+</sup> release, and lastly with 50  $\mu\text{M}$  CPA to inhibit SERCA pump refilling (Figure 6.3 and Figure 6.5). 1 mM 4-cmc is able to initiate a decrease in fluorescence signal from a release of Ca<sup>2+</sup> in the ER at  $32.5 \pm 1.7\%$ , while 50-100  $\mu\text{M}$  DHPG is able to initiate a quick release/uptake and recovery of  $\pm 14.2 \pm 2.3\%$ , and 50  $\mu\text{M}$  CPA inhibits refilling of the ER leading to a release of  $9.9 \pm 2.5\%$  (Figure 6.3 and Figure 6.5). While 4-cmc and CPA only initiate a decrease in CatchER<sup>+</sup> signal in response to treatment, DHPG can have a decrease in most neuron regions, but some regions throughout the neuron are able to have an increase in response to treatment (Figure 6.3 and Figure 6.5). Additionally, upon washing away DHPG we also see the second response in the same manner as the DHPG treatment response that is not seen with 4-cmc or CPA (Figure 6.3 and Figure 6.5). This response could be attributed to a

phantom signal response from the movement of the drug again to re-activate the receptors before being washed away or to be a depolarization effect from the change in  $\text{Ca}^{2+}$  levels extracellularly after equilibration with the  $\text{Ca}^{2+}$  release initiated from the ER leading to another wave of  $\text{Ca}^{2+}$  release from the ER from calcium-induced calcium release (CICR).

We also imaged cortical mouse neurons simultaneously in response to 200  $\mu\text{M}$  4-cmc to activate the RyR  $\text{Ca}^{2+}$  release and 100  $\mu\text{M}$  DHPG to activate mGluR1/5 to indirectly activate the  $\text{IP}_3\text{R}$   $\text{Ca}^{2+}$  release (Figure 6.4). 200  $\mu\text{M}$  4-cmc can initiate a decrease in fluorescence signal from a release of  $\text{Ca}^{2+}$  in the ER at  $21.7 \pm 2.4\%$ , while 100  $\mu\text{M}$  DHPG is able to initiate a quick release/uptake and recovery of  $\pm 12.6 \pm 2.5\%$  (Figure 6.4). Similarly, to the hippocampal neurons, we also see the bidirectional DHPG response in cortical neurons as well as the secondary ACSF response only in DHPG washing. For 100  $\mu\text{M}$  DHPG Henderson et al. saw  $\sim 40\%$  release and only  $\sim 15\%$  release with 50  $\mu\text{M}$  DHPG, where we see around 10% release using 50-100  $\mu\text{M}$  DHPG in hippocampal neurons<sup>[392]</sup>. Also, we have found that most other research looking at the ER  $\text{Ca}^{2+}$  release through DHPG activation do not see the quick response we do on the seconds scale but instead only see the slower DHPG response on the minutes scale. While we have let our experiment run for 800 seconds, we only see this quick response and recovery, which could be attributed to our sensor's superior fast kinetic on and off rate properties in the ms range.

Further research using inhibitors specifically for mGluR1, such as CPCCOEt, or for mGluR5, such as 3-((2-Methyl-4-thiazolyl)ethynyl)pyridine (MTEP), in conjunction with DHPG activation, to investigate the specific group I mGluR responsible for LTD. Furthermore, we also want to image CatchER<sup>+</sup> with a morphology fluorescence probe to confirm that the changes being seen are not convoluted from neuronal dendritic movement during imaging. Moreover, designing CatchER<sup>+</sup> for viral infection into mouse models to examine whole mouse brain and hippocampal responses



with WT and relevant mutants in response to stimuli would expand the understanding of the effects of ER  $\text{Ca}^{2+}$  dynamics in related disorders.

## **6.4 Materials and Methods**

### ***6.4.2 Generation of primary hippocampal neuron cultures and transfection***

Mice were kept in standard housing with littermates, provided with food and water ad libitum and maintained on a 12:12 (light-dark) cycle. Primary neuron culture was approved by the Georgia State University Institutional Animal Care and Use Committee. Primary hippocampal neurons of mixed sex were isolated from P0-1 mice as previously described<sup>[395]</sup>. At day in-vitro 11, neurons were transfected with Lipofectamine 2000 (Thermo Fisher Scientific) as described previously<sup>[396]</sup> and imaged 1-2 days later.

### ***6.4.3 Epifluorescence imaging of CatchER<sup>+</sup>***

CatchER<sup>+</sup> was transiently transfected into cells grown on coverslips and cultured for 48 hr at 37°C. Cells were washed twice with 2 mL of artificial cerebrospinal fluid (ACSF) buffer (124 mM NaCl, 3 mM KCl, 1.8 mM  $\text{CaCl}_2$ , 2 mM  $\text{MgCl}_2$ , 10 mM HEPES, 10 mM D-Glucose, pH=7.4). The coverslips were mounted on a Warner Instruments low profile open diamond bath imaging chamber. The cells were illuminated with 488 nm and the fluorescence at an emission wavelength 510 nm was recorded in real-time as the concentration of ER/SR  $\text{Ca}^{2+}$  was perturbed with 4-cmc, CPA, or ATP. All experiments were performed at room temperature on a Leica DM6100B inverted microscope with a Hamamatsu cooled EM-CCD camera and illuminated with a Till Polychrome V monochromator and a xenon lamp.

#### ***6.4.4 HILO imaging of CatchER<sup>+</sup>***

HILO microscopy was accomplished based on a Nikon TiE inverted microscope. Briefly, a fiber coupled 488 nm laser (Oxxius) was collimated and introduced into the optical train of the microscope. The laser was then focused at the back focal plane of a 100X TIRF objective (N.A. 1.49, Nikon) by using an achromatic optical lens (Thorlabs) with 200 mm focal length. The laser collimation system and focusing lens were both mounted a mechanic translation stage (Thorlabs) so that its optical axis of incident laser could be laterally shifted to change the incident angle of the laser at the cell-coverslip interface. The HILO imaging condition was achieved by operating at sub-critical angles of the total internal reflection. Since the thickness of cells, as well as the depth of ER structure, varies among individual cells, the best HILO imaging conditions were achieved by carefully tuning the incident angle of the excitation laser. Moreover, the epifluorescence images used for comparing with HILO imaging was taken by setting the incident angle at 0 degrees. Large scale data analysis was done with a self-written MATLAB script.

## 7 Major Conclusions and Significance

### 7.1 CaSR Significance and Conclusions

The research we have done on CaSR address key gaps in our understanding of extracellular signaling and the CaSR structure. The discovery of the parathyroid CaSR by Dr. Ed Brown et al. in 1993 revealed the source for  $\text{Ca}^{2+}$  homeostasis and extracellular  $\text{Ca}^{2+}$  signaling<sup>[22]</sup>. Our research into the structure of CaSR ECD exposes the crucial role of  $\text{Ca}^{2+}$  binding sites of the CaSR ECD in diseases of  $[\text{Ca}^{2+}]_o$  sensing and also revealed the binding of a drug TNCA in the main binding pocket of CaSR, thus opening a new research path of drug design previously untapped. More than 400 mutations have been found in the CaSR for a variety of diseases and disorders, over half of these are related to disorders of  $\text{Ca}^{2+}$  dysfunction. Inactivating human mutations with familial hypocalciuric hypercalcemia (FHH) and neonatal severe hyperparathyroidism (NSHPT) reduce CaSR's sensitivity to  $[\text{Ca}^{2+}]_o$ , whereas activating mutations of autosomal dominant hypocalcemia (ADH) cause heightened sensitivity of  $[\text{Ca}^{2+}]_o$  and  $[\text{Mg}^{2+}]_o$ <sup>[397, 398]</sup>. Studies have reported that these disease-associated mutations alter either the CaSR's responses to  $[\text{Ca}^{2+}]_o$  and  $[\text{Mg}^{2+}]_o$  by shifting of the responsiveness of CaSR or altering the cooperativity<sup>[399]</sup>. CaSR has also been shown as a critical regulator for renal fibrosis<sup>[255, 400-406]</sup>. Remarkably, CaSR calcilytic R-568 showed in mouse models to inhibit renal fibrosis<sup>[403]</sup> Our determined crystal structure of human CaSR ECD exposed significant insights on the regulation and structural foundation of CaSR diseases as well as the potential for drug development<sup>[287]</sup>. We initially optimized expression of CaSR ECD in order to use this purified protein for crystallization studies. We optimized expression by removing the 7TMD, ICD, and cys-rich region from the CaSR ECD. We then removed the flag tag for staining as to not further perturb the CaSR structure. Additionally, we expressed the CaSR ECD in a mammalian expression system lacking GnT1 so that CaSR ECD would not be glycosylated with

complex glycans and instead only with mannose glycans leading to easier deglycosylation using Endo-F1. We then ordered new Sepharose beads to use exclusively for mCaSR hist-tag purification. Doing all of these steps allowed us to get a crystal formation under 200 mM  $Mg^{2+}$  and 10 mM  $Ca^{2+}$  with 2.1 Å resolution. We found in our determined CaSR ECD structure two confirmed  $Mg^{2+}$  binding sites, two of which overlap with our predicted  $Ca^{2+}$  binding sites, and then a novel drug binding site in the hinge region thought to be the main  $Ca^{2+}$  binding site based on mutation studies (Table 2.3). The hinge TNCA binding site consists of residues S147, A168, S170, Y218, and E297. Four of these residues overlap exactly with our predicted  $Ca^{2+}$  binding site. The dimerization binding site of  $Mg^{2+}$ , which is possible to also be  $Ca^{2+}$  since with weak binding  $Ca^{2+}$  did not show on the crystal structure, are residues E228, E231, S240 and E341 from the other monomer. Two of these residues overlap a binding site on the modeled structure. Lastly, a new  $Mg^{2+}$  site was found that was not predicted using our modeled structure and also found in another crystal paper which came out after ours, and these residues are I81, S84, L87, and L88. With all of these binding sites known we can then be poised to examine the disease mutations at these sites and find I81M (FHH), L87I (lung carcinoma), L87R (thyroid neoplasm), Y218S (FHH), Y218C (FHH), E228Q (ADH), E228K (ADH), E297D (ADH), and E297K (FHH). There are many more mutations affecting the residues directly around each residue number as well as in the region of the binding pockets in general. Inactivating and activating mutations are primarily distributed in the TNCA binding site at the hinge region as well as the dimerization interface binding site of  $Mg^{2+}$ . We found that the residues of E297 and Y218 were critical for CaSR function since mutation of these residues to Ile and Lys, respectively, lead to a complete loss of CaSR function in cell imaging. The E228 residue mutation to Ile led to a loss of CaSR signaling function only able to be overcome by higher  $[Ca^{2+}]_o$  or TNCA treatment.

Additionally, we use a multitude of methods for analyzing the CaSR; bacterial expression (bCaSR), mammalian expression (mCaSR), and cellular imaging, cell population, binding studies, ELISA, and crystallography. We utilized a bacterial *E. coli* expression system for the CaSR ECD which has been optimized to have a higher yield and less degradation by removing the cys-rich domain, the signal peptide region, and mutating 4 Cys residues to Ala in order to prevent incorrect disulfide bond formation and thus give us a structure correctly formed. The benefits of bCaSR are that there are no post-translational modifications like glycosylation, there is quicker cell growth, in addition to being economical. We then used the SHuffle expression cell line in order to prevent incorrect disulfide bonds from occurring. Using this methodology, we were able to get consistent CaSR ECD expression and purification as confirmed by CD studies. Then we further created mutations to disturb the binding sites or related disease mutations in order to correlate our functional studies in the cell to binding studies using fluorimetry. We were able to make mutations S272A to disturb hinge region binding, E228K/Q for ADH mutations affecting the dimerization site, R66H FHH related mutation affecting the bicarbonate binding site, and D216N cancer mutation near the hinge site. We found that mutation of R66H, E228K, and E228Q led to a loss of CaSR expression and a complete loss of purification capacity. S272A and D216N both successfully purified but their Trp fluorimetry results saw a decrease in  $\text{Ca}^{2+}$  binding induced conformational effects and using  $\text{Tb}^{3+}$ /FRET with S272A we saw disturbance of  $\text{Tb}^{3+}$  cooperative binding effects with no apparent binding pattern and high precipitation showing a detrimental effect of the mutation on CaSR stability.

While CaSR is an important therapeutic target there has so far only been one FDA approved positive allosteric modulator named cinacalcet for treatment of hyperthyroidism. There is still a pressing need for discovery of additional calcimimetics since cinacalcet causes adverse side effects

of nausea and vomiting in 15–20% of patients, reduction of male testosterone levels in 15–30% of patients and needing a twice-daily dosage schedule is often problematic. The long-term safety and efficacy of the calcimimetics are also unclear. A recent trial in humans using cinacalcet showed a slight, but statistically insignificant, improvement in cardiovascular disorders, a significant cause of death in the dialysis population, which may be mitigated by further development of this class of drugs. So far no CaSR calcilytics have been FDA approved since all have failed in animal trials for the adverse effects of usage, this is still a critical target for future drug studies since antagonists of CaSR have the potential to treat osteoporosis or forms of hypoparathyroidism<sup>[407, 408]</sup>.

The revealed Trp derivative TNCA as a co-agonist improves CaSR activation through  $\text{Ca}^{2+}$  by increasing oscillation frequency and by  $\text{Mg}^{2+}$  by decreasing the  $\text{EC}_{50}$  of  $[\text{Mg}^{2+}]_o$ <sup>[287]</sup>. These results give us hope that TNCA can be used for further drug development. TNCA binds at the hinge pocket adjacent to the proposed  $\text{Ca}^{2+}$  site, here TNCA either acts as a cooperative regulator or as a competitive binding partner. Due to limitations of biopsy and lack of imaging agents, the biodistribution of CaSR expression during biological and pathological states are not currently defined. The first major gap in understanding human diseases is non-invasive mapping CaSR's expression in both physiological and pathological states. Our initial drug studies here reveal that TNCA as a lead drug target is possible, and further drug design and collaborations need to be done to provide more dramatic drug compounds to synthesize for testing. Our initial lead drug design led us to find a couple of compounds which act as calcimimetics and calcilytics, but none yet which are more effective than cinacalcet or NPS2-143, respectively.

The CaSR studies is an ever-growing and furthering field. Our future work in this research includes more disease related mutations of the CaSR ECD to see effects on the functionality in response to mutation as well as drug recoveries. Additionally, more lead drug target studies where

TNCA based compounds can be made to find a potential CaSR therapeutic. The full-length CaSR has also yet to be crystallized and crystallization of full-length human CaSR would greatly help in identifying potential therapeutic directions since cinacalcet and many other designed CaSR drugs are thought to be targeted to the CaSR TMD.

## 7.2 Calcium Sensors Significance and Conclusions

The discovery of  $\text{Ca}^{2+}$  binding dyes such as Fura-2 and then the additional discovery of fluorescent proteins spearheaded the  $\text{Ca}^{2+}$  imaging field. While GECIs based on fluorescent protein scaffold are critical in  $\text{Ca}^{2+}$  imaging today, there is still an ever-growing need for new sensor colors, kinetic rates, binding modalities, and organelle/location targeting. Currently, only our CatchER is available on the market which can bind a single  $\text{Ca}^{2+}$  per EGFP backbone, this capability gives CatchER fast kinetics as well as being able to quantitate the signal as 1:1 binding using min/max experiments. Our sensor is targeted to the ER/SR through KDEL and calreticulin retention sequences but can also be targeted to the cytosol upon removal of those regions. CatchER does have drawbacks of being bright at 30°C but dim at the commonly used 37°C for cell culture and animal models. Therefore, we modified CatchER through thermostability, and fluorescence mutations reported by others to create the improved CatchER<sup>+</sup> which still has 1:1 binding and fast kinetics in the ns-ms range.

In collaboration with Dr. Zorzato in an attempt to further comprehend the  $\text{Ca}^{2+}$  dynamics involved within the ER/SR in skeletal muscle cells during E-C coupling at the junctional face membrane, we created a fusion of CatchER<sup>+</sup> with the newly discovered JP45 which colocalizes with RyR1. This new construct has JP45 at the N-terminus of CatchER<sup>+</sup> so that CatchER<sup>+</sup> remain inside the ER/SR, we named this construct CatchER<sup>+</sup>-JP45.

The adaptability of  $\text{Ca}^{2+}$  as an intracellular messenger is modulated by the distribution of CaBP and  $\text{Ca}^{2+}$  regulating protein throughout the cell as well as its spatial and temporal properties.  $\text{Ca}^{2+}$  signaling is shown to be in differential microdomains. These microdomains of  $\text{Ca}^{2+}$  equip regions of the cell to have dynamic  $\text{Ca}^{2+}$  signaling differences localized to that region of the cell which do not necessitate full cell signaling for local processes.  $\text{Ca}^{2+}$  microdomains and regions of high calcium gradients are present more frequently in areas of  $\text{Ca}^{2+}$  signaling usually under rapid conditions for example near calcium channels for  $\text{Ca}^{2+}$  influx or near RyR1 for E-C coupling of skeletal muscle contraction. Many of these microdomains are present in the major  $\text{Ca}^{2+}$  storage organelles of the ER/SR and mitochondria. There have been many studies indicating that  $\text{Ca}^{2+}$  dysregulation in the ER/SR and the cell as a whole for homeostasis have significant effects on diseases affecting the whole body.  $\text{Ca}^{2+}$  dysregulation from ER/SR proteins such as RyR, IP<sub>3</sub>R and the SERCA pump alone have been attributed to Malignant hyperthermia (MH), Central core disease of muscle (CCD), Multiminicore disease with external ophthalmoplegia (MMDO), Catecholaminergic polymorphic ventricular tachycardia (CPVT), spinocerebellar ataxia 15 and 29 (SCA15/29, acrokeratosis verruciformis (AKV) and Darier disease (DD). Additionally  $\text{Ca}^{2+}$  dysfunction in the neuronal system alone has been linked to many neurodegenerative disorders including Alzheimer's disease (AD), bipolar disorder (BPD), amyotrophic lateral sclerosis (ALS), Huntington's disease (HD), schizophrenia, spinocerebellar ataxias, Parkinson's disease (PD), epilepsy, and fragile X syndrome (FXS) [146-163].

As such, there is a critical need to understand how disease states affect  $\text{Ca}^{2+}$  dynamics and signaling in the ER/SR in a global and microdomain regions as well as the whole cell in multiple body systems. Additionally, understanding how  $\text{Ca}^{2+}$  microdomains are precisely arranged to assist in cellular function will aid us in comprehending disease states and treating them. In order



to achieve this, our sensor CatchER<sup>+</sup> along with HILO microscopy can examine the sources of Ca<sup>2+</sup> microdomains and then further examine these regions for targets of microdomain placement. We have found that CatchER<sup>+</sup> with HILO imaging can elucidate the differential Ca<sup>2+</sup> dynamics throughout the subcellular regions of the ER as indicated by the variance in release and recovery rates throughout the ER in a single cell. By targeting our sensor to JP45, we could examine the microdomain specifically in the junctional zone of the SR. CatchER<sup>+</sup>-JP45 can be used to monitor the Ca<sup>2+</sup> flux in this microdomain in skeletal muscle cells in neuromuscular diseases associated with dysfunctional proteins. We find that not only does CatchER<sup>+</sup>-JP45 distribute in specific areas of the ER/SR but that the response kinetics and dynamics are differential to global CatchER<sup>+</sup>. We are therefore ideally placed to target our sensor to other proteins thought to be in microdomain regions and examine the effects of Ca<sup>2+</sup> signaling in these regions under normal and disease states. In order to more fully understand these microdomains, we looked towards transfection of CatchER<sup>+</sup> into hippocampal neurons using HILO imaging to examine the differential ER responses thought to occur throughout the neuronal structure where expression of the ER can vary from the soma to dendrites and dendritic spines. We found that not only does the ER present with regions of signaling and non-signaling Ca<sup>2+</sup> dynamics but that different regions of the same neuron ER have an increase or decrease response to 100 μM DHPG activation of the mGluR1/5 which potentiate LTD.

Our research so far with CatchER<sup>+</sup> and CatchER<sup>+</sup>-JP45 show that our sensor can be utilized in multiple cell types including C2C12, HEK293, HeLa, Cos-7 and cultured neurons to monitor ER/SR receptor-mediated Ca<sup>2+</sup> responses in response to agonist or antagonist additions. We can further continue our research by making mouse models expressing CatchER<sup>+</sup>, targeting CatchER<sup>+</sup>

to other organelles such as the mitochondria, and developing other CatchER<sup>+</sup> color variants using RFP, YFP, and CFP backbones to apply a Ca<sup>2+</sup> binding site to.

## 8 APPENDICES

### Appendix A – Optimizations

#### *Removal of TNCA from mCaSR*

When we elucidated the crystal structure for CaSR we also saw and TNCA bound in the hinge region of the ECD. We need to remove that ligand in order to accomplish accurate binding studies on the mCaSR. Thus, we used varying concentrations of Phe on the mCaSR to see which concentration could displace TNCA. 150 mM Phe was the most proficient at TNCA removal (Figure 8.1).

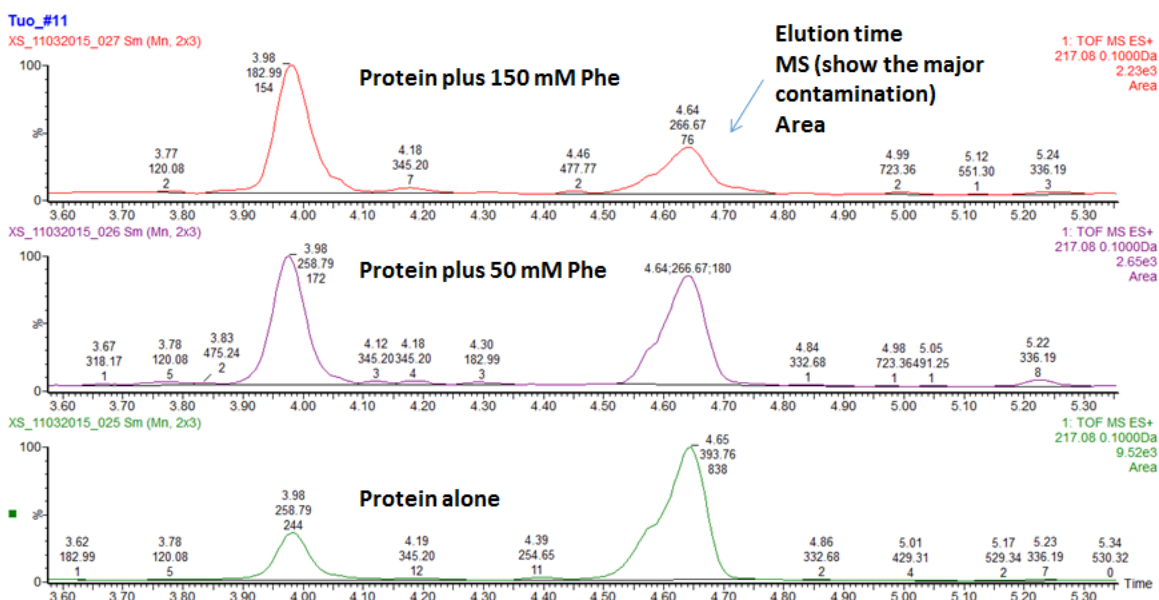


**Figure 8.1 – TOF MS of mCaSR TNCA peak being competed out by Phe. Left peaks are Phe, right peaks are TNCA.**

We did the next expression batch of mCaSR ECD using 150 mM Phe. We initially did Phe removal with multiple concentrations and at room temp but decided that the previous method for MS analysis of Phe removal of TNCA was too harsh. Therefore, we elected to wash the column/mCaSR with 150 mM Phe for 5-10 CVs after the protein was loaded O/N onto the column.

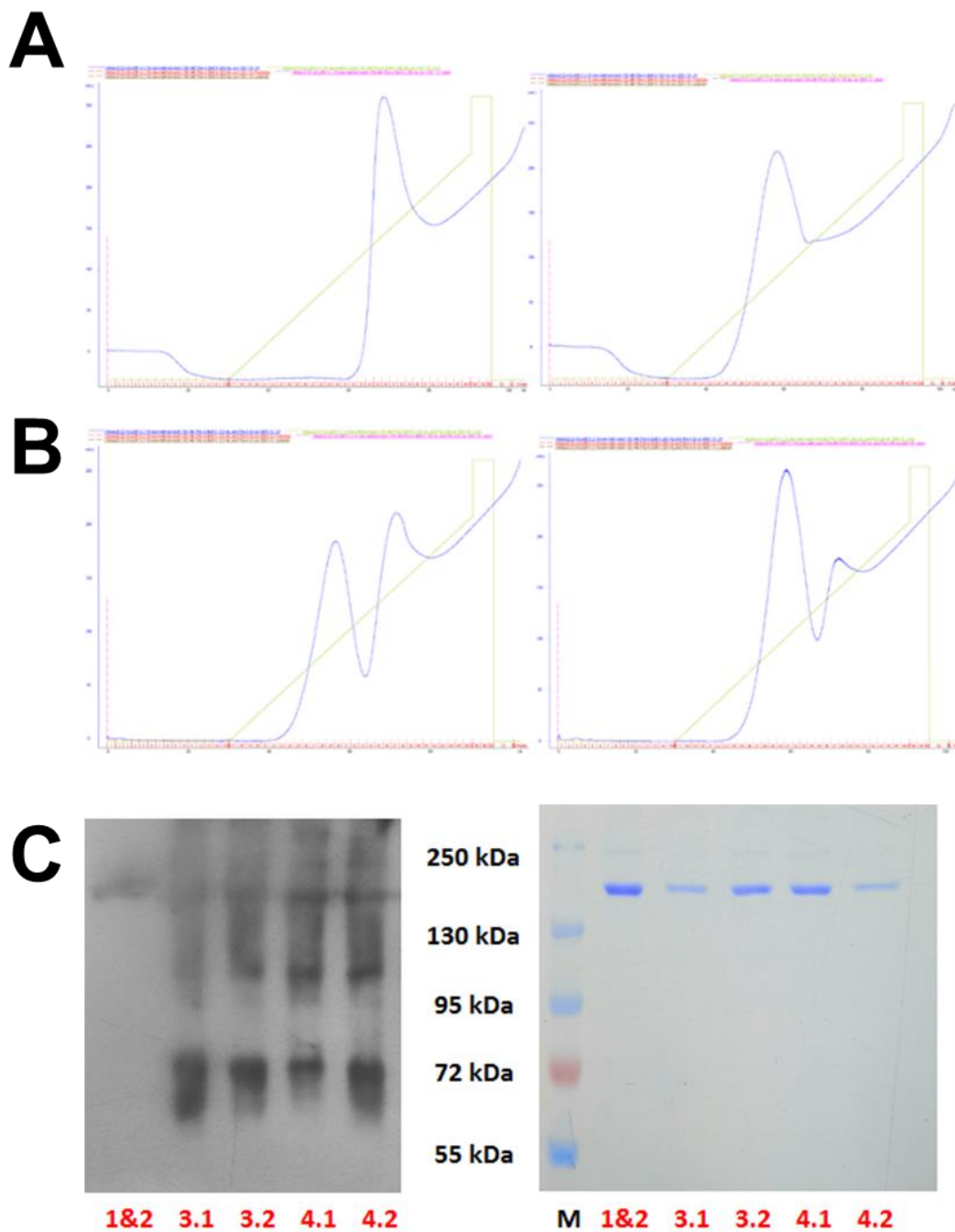


**Figure 8.2 – Expression and purification of mCaSR using Phe wash.**  
**(A)** 150 mM Phe only in buffer A pre-wash not in run of program buffer A or B. **(B)** 150 mM Phe in buffer A and B throughout purification. **(C)** Western blot done with ADD antibody and SDS gel stained with Coomassie Blue.

We did 150 mM Phe wash in Buffer A as to not shock the protein which is in mammalian buffer. We also decided to do half of the purifications with Phe in Buffer A and B throughout, and half with Phe only in the pre-running Buffer A and none in the elution (Figure 8.2). We saw that having Phe only in buffer A led to a single mCaSR peak (Figure 8.2A) whereas having Phe throughout the whole purification led to a doublet mCaSR peak (Figure 8.2B). Upon doing coomassie blue and western blot gels we see that all of the peaks are the same kDa since TNCA is such a small MW we do not expect to see changes on the gel. Mass spectrometry was performed on these peaks but no TNCA was found in any of the peaks, while this may be true in actuality this could also mean that the concentrations of the TNCA are just too low to detect but that TNCA is still present. As such, using hCaSR for TNCA studies will be more ideal since we know there is no TNCA bound in hCaSR.

### *Identifying CaSR Disease Mutations*

Utilizing the CaSR database (CaSRdb) and the Catalogue Of Somatic Mutations In Cancer (COSMIC) database which collects known cancer disease mutations from scientific publications<sup>[409, 410]</sup>. We were able to extract all of the currently listed disease mutations known by 2017 to affect CaSR utilizing these two databases. These were then outlined in a table sorted by the amino acid sequence and the type of mutation as well as the effect this mutation had (Table 8.1).

**Table 8.1 – CaSR disease mutations using CaSRdb and COSMIC.**

<u>Domain</u>	<u>Amino Acid Mutation</u>	<u>AA#</u>	<u>Histology</u>	<u>CDS Mutation</u>	<u>Primary Tissue</u>	<u>Pubmed Id</u>
ECD	M1R	1	FHH			
ECD	p.A2E	2	Carcinoma	c.5C>A	Skin	21984974

ECD	p.C6R	6	Malignant melanoma	c.16T>C	Soft tissue	26168399
ECD	p.C6*	6	Ewings sarcoma	c.18C>A	Bone	25186949
ECD	C7ins/fsX47	7	FHH			
ECD	p.V9I	9	Carcinoma	c.25G>A	Large intestine	25344691
ECD	p.L10I	10	Carcinoma	c.28C>A	Endometrium	-
ECD	L11S	11	FHH			
ECD	L13P	13	FHH			
ECD	T14A	14	FHH/Polymorphisms			
ECD	p.W15*	15	Malignant melanoma	c.45G>A	Skin	26214590
ECD	Y20H	20	FHH/Polymorphisms			
ECD	G21R	21	FHH			
ECD	p.P22L	22	Malignant melanoma	c.65C>T	Skin	-
ECD	p.D23N	23	Carcinoma	c.67G>A	Lung	-
ECD	p.R25L	25	Carcinoma	c.74G>T	Ovary	-
ECD	R25X	25	FHH			
ECD	Q27R	27	FHH			
ECD	p.K28K	28	Malignant melanoma	c.84G>A	Skin	-
ECD	p.K28N	28	Malignant melanoma	c.84G>C	Skin	-
ECD	K29E	29	ADH			
ECD	p.G30R	30	Malignant melanoma	c.88G>A	Skin	-
ECD	p.G30R	30	Carcinoma	c.88G>A	Skin	25303977
ECD	p.G30E	30	Malignant melanoma	c.89G>A	Skin	-

ECD	p.G30E	30	Carcinoma	c.89G>A	Skin	25303977
ECD	p.D31N	31	Carcinoma	c.91G>A	Stomach	-
ECD	p.I33I	33	Chondrosarcoma	c.99C>A	Bone	23770606
ECD	p.I33I	33	Malignant melanoma	c.99C>T	Skin	-
ECD	p.I33I	33	Malignant melanoma	c.99C>T	Skin	-
ECD	p.G36V	36	Carcinoma	c.107G>T	Large intestine	25344691
ECD	p.P39S	39	Malignant melanoma	c.115C>T	Skin	-
ECD	p.P39S	39	Malignant melanoma	c.115C>T	Skin	-
ECD	p.P39S	39	Malignant melanoma	c.115C>T	Skin	26214590
ECD	p.P39S	39	Carcinoma	c.115C>T	Skin	25759019
ECD	<b>P39A</b>	<b>39</b>	<b>FHH</b>			
ECD	<b>I40F</b>	<b>40</b>	<b>FHH</b>			
ECD	p.F42F	42	Malignant melanoma	c.126T>C	Skin	-
ECD	<b>F42S</b>	<b>42</b>	<b>FHH</b>			
ECD	<b>K47N</b>	<b>47</b>	<b>ADH</b>			
ECD	p.S53L	53	Malignant melanoma	c.158C>T	Skin	26343386
ECD	<b>S53P</b>	<b>53</b>	<b>FHH</b>			
ECD	<b>P55L</b>	<b>55</b>	<b>FHH</b>			
ECD	<b>C60F</b>	<b>60</b>	<b>FHH</b>			
ECD	<b>R62M</b>	<b>62</b>	<b>FHH</b>			
ECD	p.F65F	65	Malignant melanoma	c.195C>T	Skin	-
ECD	p.R66H	66	Carcinoma	c.197G>A	Ovary	21720365

ECD	<b>R66C</b>	<b>66</b>	<b>FHH</b>			
ECD	<b>R66H</b>	<b>66</b>	<b>FHH</b>			
ECD	p.R69C	69	Carcinoma	c.205C>T	Endometrium	-
ECD	p.R69H	69	Carcinoma	c.206G>A	Lung	-
ECD	p.R69H	69	Carcinoma	c.206G>A	Salivary gland	27103403
ECD	p.F76C	76	Carcinoma	c.227T>G	Endometrium	-
ECD	p.E80K	80	Carcinoma	c.238G>A	Breast	-
ECD	<b>I81M</b>	<b>81</b>	<b>FHH</b>			
ECD	p.P85L	85	Carcinoma	c.254C>T	Stomach	25042771
ECD	p.A86A	86	Malignant melanoma	c.258C>T	Skin	-
ECD	p.L87I	87	Carcinoma	c.259C>A	Lung	22980975
ECD	p.L87R	87	Other	c.260T>G	Thyroid	-
ECD	p.P89S	89	Malignant melanoma	c.265C>T	Skin	-
ECD	p.T92M	92	Carcinoma	c.275C>T	Large intestine	-
ECD	p.L93L	93	Glioma	c.279G>A	Central nervous system	-
ECD	<b>G94X</b>	<b>94</b>	<b>FHH</b>			
ECD	<b>G94R</b>	<b>94</b>	<b>FHH</b>			
ECD	p.R96K	96	Malignant melanoma	c.287G>A	Skin	-
ECD	p.R96R	96	Malignant melanoma	c.288G>A	Skin	-
ECD	p.I97T	97	Carcinoma	c.290T>C	Liver	-
ECD	p.I97T	97	Carcinoma	c.290T>C	Liver	-
ECD	<b>T100I</b>	<b>100</b>	<b>FHH</b>			



ECD	p.C101C	101	Carcinoma	c.303C>T	Pancreas	-
ECD	p.T103S	103	Carcinoma	c.308C>G	Breast	-
ECD	p.T103T	103	Carcinoma	c.309C>T	Skin	25303977
ECD	p.V104I	104	Carcinoma	c.310G>A	Kidney	-
ECD	p.K106K	106	Malignant melanoma	c.318G>A	Skin	-
ECD	p.A107T	107	Carcinoma	c.319G>A	Skin	25303977
ECD	A116T	116	ADH			
ECD	A116P	116	ADH			
ECD	p.N118fs*6	118	Carcinoma	c.350delA	Large intestine	-
ECD	N118K	118	ADH			
ECD	p.I120M	120	Carcinoma	c.360T>G	Esophagus	-
ECD	p.S122Y	122	Carcinoma	c.365C>A	Endometrium	-
ECD	p.S122Y	122	Carcinoma	c.365C>A	Endometrium	-
ECD	A124K	124	ADH			
ECD	L125P	125	ADH			
ECD	L125F	125	ADH			
ECD	E127K	127	ADH			
ECD	E127G	127	ADH			
ECD	E127A	127	ADH			
ECD	p.F128L	128	Carcinoma	c.382T>C	Stomach	-
ECD	F128L	128	ADH			
ECD	C129Y	129	ADH			

ECD	<b>C129F</b>	<b>129</b>	<b>ADH</b>			
ECD	<b>C129S</b>	<b>129</b>	<b>ADH</b>			
ECD	<b>C129R</b>	<b>129</b>	<b>ADH</b>			
ECD	<b>p.N130I</b>	<b>130</b>	<b>Carcinoma</b>	<b>c.389A&gt;T</b>	Large intestine	24755471
ECD	<b>p.N130I</b>	<b>130</b>	<b>Carcinoma</b>	<b>c.389A&gt;T</b>	Large intestine	24755471
ECD	<b>C131Y</b>	<b>131</b>	<b>ADH</b>			
ECD	<b>C131F</b>	<b>131</b>	<b>ADH</b>			
ECD	<b>C131W</b>	<b>131</b>	<b>ADH</b>			
ECD	<b>p.P136L</b>	<b>136</b>	<b>Malignant melanoma</b>	<b>c.407C&gt;T</b>	Skin	26214590
ECD	<b>S137P</b>	<b>137</b>	<b>FHH/Dominant Neg</b>			
ECD	<b>p.T138T</b>	<b>138</b>	<b>Malignant melanoma</b>	<b>c.414G&gt;A</b>	Skin	-
ECD	<b>T138M</b>	<b>138</b>	<b>FHH</b>			
ECD	<b>G143R</b>	<b>143</b>	<b>FHH</b>			
ECD	<b>G143E</b>	<b>143</b>	<b>FHH</b>			
ECD	<b>p.G146G</b>	<b>146</b>	<b>Carcinoma</b>	<b>c.438C&gt;T</b>	Large intestine	-
ECD	<b>p.G148D</b>	<b>148</b>	<b>Malignant melanoma</b>	<b>c.443G&gt;A</b>	NS	24265153
ECD	<b>p.V149I</b>	<b>149</b>	<b>Carcinoma</b>	<b>c.445G&gt;A</b>	Large intestine	22810696
ECD	<b>p.S150S</b>	<b>150</b>	<b>Malignant melanoma</b>	<b>c.450C&gt;T</b>	Skin	-
ECD	<b>T151M</b>	<b>151</b>	<b>ADH</b>			
ECD	<b>T151R</b>	<b>151</b>	<b>ADH</b>			
ECD	<b>G158R</b>	<b>158</b>	<b>FHH</b>			
ECD	<b>L159P</b>	<b>159</b>	<b>FHH</b>			

ECD	<b>Y161C</b>	<b>161</b>	<b>FHH</b>			
ECD	p.I162M	162	Carcinoma	c.486T>G	Large intestine	-
ECD	p.P163S	163	Carcinoma	c.487C>T	Lung	-
ECD	p.P163S	163	Malignant melanoma	c.487C>T	Skin	-
ECD	<b>P163R</b>	<b>163</b>	<b>FHH</b>			
ECD	<b>Q164X</b>	<b>164</b>	<b>FHH</b>			
ECD	<b>V165del/fsX188</b>	<b>165</b>	<b>FHH</b>			
ECD	<b>S166G</b>	<b>166</b>	<b>FHH</b>			
ECD	p.S169F	169	Malignant melanoma	c.506C>T	Skin	22842228
ECD	p.S171G	171	Carcinoma	c.511A>G	Lung	-
ECD	<b>S171N</b>	<b>171</b>	<b>FHH</b>			
ECD	p.R172K	172	Malignant melanoma	c.515G>A	Skin	22842228
ECD	<b>R172G</b>	<b>172</b>	<b>FHH</b>			
ECD	<b>L173P</b>	<b>173</b>	<b>FHH</b>			
ECD	<b>L174R</b>	<b>174</b>	<b>FHH</b>			
ECD	p.N176N	176	Carcinoma	c.528C>T	Lung	-
ECD	<b>N178D</b>	<b>178</b>	<b>FHH</b>			
ECD	<b>F180C</b>	<b>180</b>	<b>FHH</b>			
ECD	p.S182T	182	Carcinoma	c.544T>A	Lung	22510280
ECD	p.F183Y	183	Carcinoma	c.548T>A	Lung	-
ECD	p.L184F	184	Malignant melanoma	c.550C>T	Skin	-
ECD	p.R185*	185	Malignant melanoma	c.553C>T	Skin	-

ECD	p.R185Q	185	Malignant melanoma	c.554G>A	Skin	-
ECD	p.R185Q	185	Carcinoma	c.554G>A	Skin	25759019
ECD	<b>R185X</b>	<b>185</b>	<b>FHH</b>			
ECD	<b>R185Q</b>	<b>185</b>	<b>FHH and Dominant Negative</b>			
ECD	p.T186T	186	Carcinoma	c.558C>A	Lung	20505728
ECD	p.E191E	191	Ewings sarcoma	c.573G>A	Bone	25186949
ECD	<b>E191K</b>	<b>191</b>	<b>ADH</b>			
ECD	<b>A194T</b>	<b>194</b>	<b>FHH</b>			
ECD	p.A196T	196	Malignant melanoma	c.586G>A	Skin	26286987
ECD	p.M197I	197	Malignant melanoma	c.591G>A	Skin	-
ECD	p.A198V	198	Other	c.593C>T	Liver	-
ECD	p.A198V	198	Other	c.593C>T	Liver	-
ECD	p.D199N	199	Malignant melanoma	c.595G>A	Skin	24838835
ECD	p.D199H	199	Carcinoma	c.595G>C	Lung	22941189
ECD	p.I200I	200	Malignant melanoma	c.600C>T	NS	23890154
ECD	p.I201I	201	Carcinoma	c.603C>T	Endometrium	-
ECD	p.F204F	204	Malignant melanoma	c.612C>T	Skin	26343386
ECD	p.F204F	204	Malignant melanoma	c.612C>T	Skin	26286987
ECD	p.F204F	204	Malignant melanoma	c.612C>T	Skin	26286987
ECD	p.F204F	204	Malignant melanoma	c.612C>T	Skin	26286987
ECD	p.F204F	204	Malignant melanoma	c.612C>T	Skin	26286987
ECD	p.R205C	205	Carcinoma	c.613C>T	Endometrium	-

ECD	p.R205C	205	Carcinoma	c.613C>T	Liver	-
ECD	p.R205C	205	Carcinoma	c.613C>T	Liver	-
ECD	p.R205C	205	Lymphoid neoplasm	c.613C>T	Hematopoietic and lymphoid	-
ECD	p.R205H	205	Carcinoma	c.614G>A	Stomach	-
ECD	p.R205L	205	Carcinoma	c.614G>T	Esophagus	26873401
ECD	p.R205R	205	Carcinoma	c.615C>T	Esophagus	26873401
ECD	p.W206*	206	Malignant melanoma	c.617G>A	Skin	-
ECD	W208S	208	FHH			
ECD	I212S	212	FHH			
ECD	I212T	212	FHH			
ECD	D215G	215	FHH			
ECD	p.D216N	216	Malignant melanoma	c.646G>A	Soft tissue	26168399
ECD	p.D216D	216	Glioma	c.648C>T	Central nervous system	-
ECD	p.D216D	216	Carcinoma	c.648C>T	Endometrium	-
ECD	p.D216D	216	Glioma	c.648C>T	Central nervous system	23917401
ECD	p.D216D	216	Carcinoma	c.648C>T	Stomach	-
ECD	p.D217G	217	Pulmonary blastoma	c.650A>G	Pleura	24909177
ECD	Y218S	218	FHH			
ECD	Y218C	218	FHH			
ECD	p.R220W	220	Malignant melanoma	c.658C>T	Skin	22842228
ECD	p.R220W	220	Carcinoma	c.658C>T	Upper aerodigestive tract	27693639

ECD	p.R220Q	220	Carcinoma	c.659G>A	Breast	22722193
ECD	R220W	220	FHH			
ECD	R220P	220	FHH			
ECD	R220Q	220	FHH			
ECD	P221L	221	ADH			
ECD	P221Q	221	FHH			
ECD	P221S	221	FHH			
ECD	p.G222G	222	Malignant melanoma	c.666G>A	Skin	26286987
ECD	p.G222G	222	Malignant melanoma	c.666G>A	Skin	26286987
ECD	p.G222G	222	Malignant melanoma	c.666G>A	Skin	26286987
ECD	p.G222G	222	Malignant melanoma	c.666G>A	Skin	26286987
ECD	p.I223fs*34	223	Carcinoma	c.663delG	Large intestine	-
ECD	K225T	225	FHH			
ECD	p.F226F	226	Malignant melanoma	c.678C>T	Skin	-
ECD	p.F226F	226	Malignant melanoma	c.678C>T	Skin	-
ECD	p.F226F	226	Malignant melanoma	c.678C>T	Skin	26214590
ECD	p.R227*	227	Carcinoma	c.679C>T	Endometrium	-
ECD	p.R227*	227	Malignant melanoma	c.679C>T	Skin	22842228
ECD	p.R227*	227	Carcinoma	c.679C>T	Stomach	-
ECD	p.R227*	227	Carcinoma	c.679C>T	Large intestine	25344691
ECD	p.R227*	227	Malignant melanoma	c.679C>T	Skin	26343386
ECD	p.R227Q	227	Carcinoma	c.680G>A	Lung	22980975

ECD	p.R227Q	227	Malignant melanoma	c.680G>A	NS	23890154
ECD	<b>R227Q</b>	227	<b>FHH</b>			
ECD	<b>R227L</b>	227	<b>FHH/Dominant Neg</b>			
ECD	<b>E228Q</b>	228	<b>ADH</b>			
ECD	<b>E228K</b>	228	<b>ADH</b>			
ECD	p.E232K	232	Malignant melanoma	c.694G>A	Skin	22842228
ECD	p.E232G	232	Carcinoma	c.695A>G	Endometrium	-
ECD	p.R233R	233	Malignant melanoma	c.699G>A	Skin	-
ECD	p.I237I	237	Carcinoma	c.711C>T	Large intestine	25344691
ECD	p.E241V	241	Carcinoma	c.722A>T	Liver	-
ECD	<b>E241K</b>	241	<b>ADH</b>			
ECD	p.S244F	244	Malignant melanoma	c.731C>T	Skin	-
ECD	p.S244F	244	Carcinoma	c.731C>T	Skin	25303977
ECD	p.Q245K	245	Malignant melanoma	c.733C>A	Skin	-
ECD	p.Q245Q	245	Carcinoma	c.735G>A	Large intestine	22810696
ECD	<b>Q245R</b>	245	<b>ADH</b>			
ECD	p.D248N	248	Carcinoma	c.742G>A	Urinary tract	-
ECD	p.D248H	248	Carcinoma	c.742G>C	Urinary tract	-
ECD	p.D248H	248	Malignant melanoma	c.742G>C	Soft tissue	26168399
ECD	<b>E250K</b>	250	<b>FHH</b>			
ECD	p.E251E	251	Malignant melanoma	c.753G>A	Skin	26214590
ECD	p.T263M	263	Carcinoma	c.788C>T	Liver	-

ECD	p.T263M	263	Carcinoma	c.788C>T	Liver	25822088
ECD	<b>T263M</b>	<b>263</b>	<b>FHH</b>			
ECD	p.A264T	264	Carcinoma	c.790G>A	Prostate	26000489
ECD	p.I267I	267	Malignant melanoma	c.801C>T	Skin	21499247
ECD	p.I267I	267	Malignant melanoma	c.801C>T	Skin	-
ECD	p.I267I	267	Malignant melanoma	c.801C>T	Skin	-
ECD	<b>V268del/fsX2 73</b>	<b>268</b>	<b>FHH</b>			
ECD	p.F270L	270	Carcinoma	c.808T>C	Liver	-
ECD	p.F270L	270	Carcinoma	c.808T>C	Liver	-
ECD	p.F270L	270	Carcinoma	c.808T>C	Liver	25822088
ECD	<b>S271F</b>	<b>271</b>	<b>FHH</b>			
ECD	<b>P274S</b>	<b>274</b>	<b>FHH/Polymorphisms</b>			
ECD	p.D275N	275	NS	c.823G>A	NS	22722201
ECD	p.L276F	276	Malignant melanoma	c.826C>T	Skin	-
ECD	p.P278L	278	Carcinoma	c.833C>T	Skin	25303977
ECD	p.E282E	282	Malignant melanoma	c.846G>A	Skin	-
ECD	p.E282D	282	Carcinoma	c.846G>C	Cervix	-
ECD	<b>I283T</b>	<b>283</b>	<b>FHH</b>			
ECD	p.R285R	285	Carcinoma	c.853C>A	Stomach	-
ECD	p.R285W	285	Carcinoma	c.853C>T	Endometrium	-
ECD	<b>R285W</b>	<b>285</b>	<b>FHH/Polymorphisms</b>			
ECD	p.R286C	286	Lymphoid neoplasm	c.856C>T	Hematopoietic and lymphoid	23415222



ECD	p.R286C	286	Carcinoma	c.856C>T	Biliary tract	-
ECD	p.I288I	288	Malignant melanoma	c.864C>T	Skin	-
ECD	p.T289T	289	Carcinoma	c.867G>T	Prostate	-
ECD	p.G290S	290	Malignant melanoma	c.868G>A	Skin	-
ECD	p.G290S	290	Carcinoma	c.868G>A	Skin	25303977
ECD	A295T	295	FHH			
ECD	p.S296R	296	Malignant melanoma	c.886A>C	Skin	-
ECD	S296N	296	FHH			
ECD	E297D	297	ADH			
ECD	E297K	297	FHH			
ECD	p.A300T	300	Carcinoma	c.898G>A	Skin	25759019
ECD	p.A300A	300	Glioma	c.900C>T	Central nervous system	-
ECD	p.A300A	300	Glioma	c.900C>T	Central nervous system	23917401
ECD	p.S302F	302	Carcinoma	c.905C>T	Upper aerodigestive tract	25275298
ECD	p.S303F	303	Malignant melanoma	c.908C>T	Skin	-
ECD	p.S303F	303	Malignant melanoma	c.908C>T	NS	23890154
ECD	p.S303S	303	Malignant melanoma	c.909C>T	Skin	26343386
ECD	p.I305I	305	Carcinoma	c.915C>T	Endometrium	-
ECD	p.F311V	311	Other	c.931T>G	Thyroid	-
ECD	p.G316S	316	Adenoma	c.946G>A	Prostate	23265383
ECD	p.F320I	320	Carcinoma	c.958T>A	Esophagus	26873401

ECD	p.F320F	320	Carcinoma	c.960C>T	Breast	-
ECD	p.F320F	320	Malignant melanoma	c.960C>T	Skin	-
ECD	p.F320F	320	Malignant melanoma	c.960C>T	Skin	-
ECD	p.F320F	320	Malignant melanoma	c.960C>T	Skin	-
ECD	p.F320F	320	Ewings sarcoma	c.960C>T	Bone	25186949
ECD	p.F320F	320	Malignant melanoma	c.960C>T	Skin	-
ECD	p.F320F	320	Malignant melanoma	c.960C>T	Skin	26214590
ECD	p.A321T	321	Carcinoma	c.961G>A	Lung	22980975
ECD	A321P	321	FHH			
ECD	K323X	323	FHH			
ECD	p.A324T	324	Carcinoma	c.970G>A	Skin	25303977
ECD	p.G325R	325	Carcinoma	c.973G>A	Kidney	-
ECD	p.I327I	327	Malignant melanoma	c.981C>T	Skin	-
ECD	p.G329S	329	Malignant melanoma	c.985G>A	Skin	-
ECD	p.R331W	331	Carcinoma	c.991C>T	Large intestine	22895193
ECD	p.R331R	331	Malignant melanoma	c.993G>A	Skin	-
ECD	p.E332K	332	Malignant melanoma	c.994G>A	Skin	26214590
ECD	p.E332K	332	Malignant melanoma	c.994G>A	Skin	26343386
ECD	p.E332K	332	Carcinoma	c.994G>A	Skin	25759019
ECD	p.L334P	334	Carcinoma	c.1001T>C	Stomach	24816253
ECD	K335_V337del	335	FHH			
ECD	P339T	339	FHH			

ECD	p.R340R	340	Malignant melanoma	c.1020G>A	Skin	-
ECD	p.R340R	340	Malignant melanoma	c.1020G>A	Skin	-
ECD	p.R340S	340	Carcinoma	c.1020G>T	Lung	22980975
ECD	p.S342F	342	Malignant melanoma	c.1025C>T	Skin	-
ECD	p.H344L	344	Carcinoma	c.1031A>T	Breast	-
ECD	p.E350K	350	Malignant melanoma	c.1048G>A	Skin	-
ECD	p.E350K	350	Carcinoma	c.1048G>A	Skin	25303977
ECD	p.E350K	350	Malignant melanoma	c.1048G>A	NS	24265153
ECD	p.E350K	350	Carcinoma	c.1048G>A	Skin	25759019
ECD	p.E350V	350	Carcinoma	c.1049A>T	Lung	-
ECD	<b>F351V</b>	<b>351</b>	<b>FHH</b>			
ECD	p.W352fs*6	352	Carcinoma	c.1050_1051 insT	Large intestine	24755471
ECD	<b>W352X</b>	<b>352</b>	<b>FHH</b>			
ECD	p.E353K	353	Malignant melanoma	c.1057G>A	Skin	-
ECD	p.E353K	353	Malignant melanoma	c.1057G>A	Skin	26214590
ECD	<b>E354A</b>	<b>354</b>	<b>ADH</b>			
ECD	p.E362K	362	Malignant melanoma	c.1084G>A	Skin	-
ECD	p.G366R	366	Malignant melanoma	c.1096G>A	Skin	-
ECD	p.G376D	376	Carcinoma	c.1127G>A	Liver	-
ECD	p.E378K	378	Malignant melanoma	c.1132G>A	Skin	22842228
ECD	p.E378K	378	Carcinoma	c.1132G>A	Skin	25303977
ECD	p.E378K	378	Malignant melanoma	c.1132G>A	Skin	26214590

ECD	p.E378K	378	Lymphoid neoplasm	c.1132G>A	Hematopoietic and lymphoid	24531327
ECD	p.E379K	379	Malignant melanoma	c.1135G>A	Skin	-
ECD	p.G381V	381	Carcinoma	c.1142G>T	Prostate	26000489
ECD	p.G381G	381	Adenoma	c.1143C>T	Large intestine	23204322
ECD	p.G381G	381	Carcinoma	c.1143C>T	Large intestine	25957691
ECD	p.G381G	381	Carcinoma	c.1143C>T	Large intestine	25957691
ECD	p.D382N	382	Malignant melanoma	c.1144G>A	NS	24265153
ECD	p.S385R	385	Carcinoma	c.1155C>A	Breast	-
ECD	p.S387N	387	Malignant melanoma	c.1160G>A	Skin	-
ECD	p.S388*	388	Carcinoma	c.1163C>A	Large intestine	24755471
ECD	p.S388L	388	Malignant melanoma	c.1163C>T	Skin	-
ECD	p.S388L	388	Carcinoma	c.1163C>T	Large intestine	24755471
ECD	p.A390V	390	Malignant melanoma	c.1169C>T	Skin	22842228
ECD	p.R392*	392	Carcinoma	c.1174C>T	Ovary	-
ECD	p.R392*	392	Carcinoma	c.1174C>T	Stomach	-
ECD	p.R392*	392	Carcinoma	c.1174C>T	Stomach	-
ECD	p.R392Q	392	Malignant melanoma	c.1175G>A	Skin	-
ECD	p.R392Q	392	Carcinoma	c.1175G>A	Stomach	-
ECD	<b>R392X</b>	<b>392</b>	<b>FHH</b>			
ECD	p.P393S	393	Malignant melanoma	c.1177C>T	Skin	-
ECD	p.P393L	393	Malignant melanoma	c.1178C>T	Skin	-
ECD	p.C395F	395	Lymphoid neoplasm	c.1184G>T	Hematopoietic and lymphoid	26608593

ECD	<b>C395R</b>	<b>395</b>	<b>FHH</b>			
ECD	<b>G397R</b>	<b>397</b>	<b>FHH</b>			
ECD	p.E399D	399	Malignant melanoma	c.1197G>C	Soft tissue	26168399
ECD	p.V404V	404	Carcinoma	c.1212C>T	Endometrium	-
ECD	p.V404V	404	Malignant melanoma	c.1212C>T	Skin	-
ECD	p.V404V	404	Malignant melanoma	c.1212C>T	Skin	-
ECD	p.T406>?	406	Carcinoma	c.1218_1219 CC>AG	Lung	22980975
ECD	p.R415W	415	Carcinoma	c.1243C>T	Endometrium	-
ECD	p.S417F	417	Malignant melanoma	c.1250C>T	Skin	-
ECD	<b>N419S</b>	<b>419</b>	<b>ADH</b>			
ECD	<b>A423K</b>	<b>423</b>	<b>FHH</b>			
ECD	p.V424I	424	Carcinoma	c.1270G>A	Stomach	-
ECD	<b>I427S</b>	<b>427</b>	<b>FHH</b>			
ECD	p.H429Y	429	Ewings sarcoma	c.1285C>T	Bone	25186949
ECD	p.H429H	429	Carcinoma	c.1287C>T	Large intestine	25344691
ECD	p.A430T	430	Carcinoma	c.1288G>A	Large intestine	-
ECD	p.Q432*	432	Carcinoma	c.1294C>T	Stomach	-
ECD	<b>D433H</b>	<b>433</b>	<b>FHH</b>			
ECD	p.Y435F	435	Ewings sarcoma	c.1304A>T	Bone	25186949
ECD	p.P439T	439	Glioma	c.1315C>A	Central nervous system	-
ECD	p.G440E	440	Carcinoma	c.1319G>A	Skin	25303977
ECD	p.R441fs*21	441	Carcinoma	c.1318delG	Lung	22980975

ECD	p.L443I	443	Carcinoma	c.1327C>A	Lung	22980975
ECD	<b>T445A</b>	<b>445</b>	<b>FHH/Polymorphisms</b>			
ECD	p.G447D	447	Carcinoma	c.1340G>A	Large intestine	22895193
ECD	p.G447G	447	Carcinoma	c.1341C>T	Endometrium	-
ECD	p.S448S	448	Malignant melanoma	c.1344C>T	Skin	-
ECD	p.E456K	456	Malignant melanoma	c.1366G>A	Skin	-
ECD	p.A457V	457	Carcinoma	c.1370C>T	Pancreas	-
ECD	p.A457V	457	Carcinoma	c.1370C>T	Pancreas	-
ECD	p.A457A	457	Carcinoma	c.1371G>A	Large intestine	24755471
ECD	p.R465W	465	Carcinoma	c.1393C>T	Prostate	22722839
ECD	<b>R465W</b>	<b>465</b>	<b>FHH</b>			
ECD	<b>R465Q</b>	<b>465</b>	<b>FHH</b>			
ECD	p.G474V	474	Carcinoma	c.1421G>T	Lung	23856246
ECD	p.G474G	474	Carcinoma	c.1422G>A	Skin	25303977
ECD	p.E475fs*3	475	Carcinoma	c.1419delG	Large intestine	25344691
ECD	p.E475K	475	Carcinoma	c.1423G>A	Breast	22722193
ECD	p.E475D	475	Carcinoma	c.1425G>C	Ovary	21720365
ECD	<b>V477A</b>	<b>477</b>	<b>FHH</b>			
ECD	p.L485L	485	Carcinoma	c.1455G>C	Urinary tract	-
ECD	p.V486E	486	Malignant melanoma	c.1457T>A	Soft tissue	26168399
ECD	p.G487G	487	Malignant melanoma	c.1461G>A	Skin	-
ECD	p.S490F	490	Malignant melanoma	c.1469C>T	Skin	-

ECD	p.I491V	491	Carcinoma	c.1471A>G	Liver	-
ECD	p.P498L	498	Malignant melanoma	c.1493C>T	Skin	22842228
ECD	p.D500N	500	Malignant melanoma	c.1498G>A	Skin	-
ECD	p.I503I	503	Malignant melanoma	c.1509C>T	Skin	-
ECD	p.I503I	503	Malignant melanoma	c.1509C>T	Skin	-
ECD	p.G509G	509	Carcinoma	c.1527G>A	Lung	22941188
ECD	<b>G509R</b>	<b>509</b>	<b>FHH</b>			
ECD	p.V513I	513	Carcinoma	c.1537G>A	Large intestine	22810696
ECD	p.G518E	518	Malignant melanoma	c.1553G>A	Skin	-
ECD	p.I528I	528	Malignant melanoma	c.1584C>T	Skin	-
ECD	<b>W530G</b>	<b>530</b>	<b>FHH</b>			
ECD	p.R535K	535	Carcinoma	c.1604G>A	Breast	-
ECD	p.R535M	535	Carcinoma	c.1604G>T	Large intestine	-
ECD	p.R535M	535	Carcinoma	c.1604G>T	Skin	25303977
ECD	p.P538H	538	Other	c.1613C>A	Liver	-
ECD	p.D545Y	545	Carcinoma	c.1633G>T	Large intestine	23856246
ECD	p.D545Y	545	Carcinoma	c.1633G>T	Large intestine	24755471
ECD	p.D545Y	545	Carcinoma	c.1633G>T	Large intestine	24755471
ECD	p.D545Y	545	Carcinoma	c.1633G>T	Large intestine	24755471
ECD	<b>G549R</b>	<b>549</b>	<b>FHH</b>			
ECD	p.T550T	550	Carcinoma	c.1650C>T	Skin	25303977
ECD	p.R551K	551	Malignant melanoma	c.1652G>A	Skin	-

ECD	<b>R551K</b>	<b>551</b>	<b>FHH</b>			
ECD	<b>G553R</b>	<b>553</b>	<b>FHH</b>			
ECD	<b>I555V</b>	<b>555</b>	<b>FHH</b>			
ECD	<b>E556K</b>	<b>556</b>	<b>ADH</b>			
ECD	p.G557E	557	Carcinoma	c.1670_1671 GG>AA	Skin	25303977
ECD	<b>G557E</b>	<b>557</b>	<b>FHH</b>			
ECD	p.E558K	558	Malignant melanoma	c.1672G>A	Skin	24838835
ECD	p.E558*	558	Carcinoma	c.1672G>T	Lung	22980975
ECD	p.E558G	558	Carcinoma	c.1673A>G	Large intestine	25344691
ECD	p.E558E	558	Malignant melanoma	c.1674G>A	Skin	26286987
ECD	p.E558E	558	Malignant melanoma	c.1674G>A	Skin	26286987
ECD	p.E558E	558	Malignant melanoma	c.1674G>A	Skin	26286987
ECD	p.P559A	559	Carcinoma	c.1675C>G	Large intestine	25344691
ECD	<b>C562Y</b>	<b>562</b>	<b>FHH</b>			
ECD	p.E564K	564	Malignant melanoma	c.1690G>A	Skin	-
ECD	p.E564G	564	Carcinoma	c.1691A>G	Large intestine	25344691
ECD	p.C565R	565	Carcinoma	c.1693T>C	Liver	-
ECD	p.C565R	565	Carcinoma	c.1693T>C	Liver	-
ECD	<b>C565G</b>	<b>565</b>	<b>FHH</b>			
ECD	<b>C568Y</b>	<b>568</b>	<b>FHH</b>			
ECD	p.P569S	569	Malignant melanoma	c.1705C>T	Skin	-
ECD	p.P569L	569	Malignant melanoma	c.1706C>T	Skin	-



ECD	p.G571E	571	Malignant melanoma	c.1712G>A	NS	23890154
ECD	p.G571G	571	Malignant melanoma	c.1713G>A	Skin	-
ECD	p.E572V	572	Malignant melanoma	c.1715A>T	Skin	-
ECD	<b>Y573X</b>	<b>573</b>	<b>FHH</b>			
ECD	p.D575N	575	Malignant melanoma	c.1723G>A	Skin	-
ECD	p.D578N	578	Carcinoma	c.1732G>A	Skin	25303977
ECD	p.A581A	581	Carcinoma	c.1743C>T	Skin	25303977
ECD	<b>C582Y</b>	<b>582</b>	<b>FHH</b>			
ECD	<b>C582F</b>	<b>582</b>	<b>FHH</b>			
ECD	p.N583D	583	Malignant melanoma	c.1747A>G	Skin	-
ECD	<b>N583X</b>	<b>583</b>	<b>FHH</b>			
ECD	p.C585F	585	Carcinoma	c.1754G>T	Ovary	-
ECD	<b>F589L</b>	<b>589</b>	<b>ADH</b>			
ECD	p.W590fs*37	590	Carcinoma	c.1769delG	Large intestine	25344691
ECD	<b>S591C</b>	<b>591</b>	<b>FHH</b>			
ECD	<b>H595Y</b>	<b>595</b>	<b>FHH</b>			
ECD	p.S597S	597	Malignant melanoma	c.1791C>T	Skin	26214590
ECD	p.K601K	601	Malignant melanoma	c.1803G>A	Skin	-
ECD	p.E602D	602	Carcinoma	c.1806G>C	Lung	22980975
ECD	p.I603T	603	Carcinoma	c.1808T>C	Lung	-
ECD	p.I603I	603	Malignant melanoma	c.1809C>T	Skin	-
ECD	p.E604K	604	Glioma	c.1810G>A	Central nervous system	-

ECD	<b>E604K</b>	<b>604</b>	<b>ADH</b>			
ECD	<b>S607X</b>	<b>607</b>	<b>FHH</b>			
ECD	p.T609T	609	Malignant melanoma	c.1827G>A	Skin	-
ECD	p.E610K	610	Adenoma	c.1828G>A	Prostate	23265383
ECD	p.E610K	610	Malignant melanoma	c.1828G>A	Skin	22842228
ECD	p.E610K	610	Malignant melanoma	c.1828G>A	Skin	-
ECD	p.E610E	610	Malignant melanoma	c.1830G>A	Skin	-
ECD	<b>E610G</b>	<b>610</b>	<b>ADH</b>			
ECD	<b>F612S</b>	<b>612</b>	<b>ADH</b>			
TMD	p.G613R	613	Malignant melanoma	c.1837G>A	Skin	22842228
TMD	p.G613E	613	Carcinoma	c.1838_1839 GG>AA	Skin	25303977
TMD	p.G613G	613	Malignant melanoma	c.1839G>A	Skin	26343386
TMD	p.I614I	614	Malignant melanoma	c.1842C>T	Skin	-
TMD	p.I614I	614	Malignant melanoma	c.1842C>T	Skin	-
TMD	p.I614I	614	Malignant melanoma	c.1842C>T	NS	23890154
TMD	p.A615T	615	Osteosarcoma	c.1843G>A	Bone	25512523
TMD	<b>L616V</b>	<b>616</b>	<b>ADH</b>			
TMD	p.L618F	618	Malignant melanoma	c.1852C>T	Skin	-
TMD	p.L618F	618	Carcinoma	c.1852C>T	Liver	-
TMD	p.L618F	618	Carcinoma	c.1852C>T	Liver	25822088
TMD	p.F619S	619	Malignant melanoma	c.1856T>C	Skin	-
TMD	p.F619S	619	Malignant melanoma	c.1856T>C	Skin	-

TMD	p.V621fs*6	621	Carcinoma	c.1861delG	Large intestine	-
TMD	p.V621M	621	Hematopoietic neoplasm	c.1861G>A	Hematopoietic and lymphoid	21909114
TMD	p.V621M	621	Glioma	c.1861G>A	Central nervous system	24140581
TMD	<b>G623D</b>	<b>623</b>	<b>FHH</b>			
TMD	p.F625F	625	Malignant melanoma	c.1875C>T	Skin	-
TMD	p.F625F	625	Malignant melanoma	c.1875C>T	Skin	-
TMD	p.F625F	625	Malignant melanoma	c.1875C>T	Skin	-
ICL	p.F637F	637	Carcinoma	c.1911C>T	Endometrium	-
ICL	p.F637F	637	Malignant melanoma	c.1911C>T	Skin	-
ICL	p.R638C	638	Malignant melanoma	c.1912C>T	Skin	-
ICL	p.R638C	638	Carcinoma	c.1912C>T	Large intestine	-
ICL	<b>R638L</b>	<b>638</b>	<b>FHH</b>			
ICL	p.N639K	639	Carcinoma	c.1917C>A	Breast	-
ICL	p.V643I	643	Carcinoma	c.1927G>A	Prostate	-
ICL	p.V643A	643	Malignant melanoma	c.1928T>C	Skin	22842228
ICL	<b>R648X</b>	<b>648</b>	<b>FHH</b>			
ICL	p.E649Q	649	Carcinoma	c.1945G>C	Ovary	-
TMD	<b>L650P</b>	<b>650</b>	<b>FHH</b>			
TMD	p.L653F	653	Carcinoma	c.1957C>T	Large intestine	22895193
TMD	p.L654L	654	Malignant melanoma	c.1962C>T	Skin	-
TMD	p.L655H	655	Carcinoma	c.1964T>A	Kidney	23856246
TMD	<b>S657Y</b>	<b>657</b>	<b>FHH</b>			

TMD	<b>C661Y</b>	<b>661</b>	<b>FHH</b>			
TMD	p.S665F	665	Carcinoma	c.1994C>T	Upper aerodigestive tract	-
TMD	p.S665F	665	Carcinoma	c.1994C>T	Upper aerodigestive tract	24292195
TMD	<b>L666ins/fsX707</b>	<b>666</b>	<b>FHH</b>			
TMD	<b>L666P</b>	<b>666</b>	<b>FHH</b>			
TMD	p.I669I	669	Carcinoma	c.2007C>T	Large intestine	22810696
TMD	p.G670W	670	Carcinoma	c.2008G>T	Prostate	-
TMD	<b>G670E</b>	<b>670</b>	<b>FHH</b>			
TMD	<b>G670R</b>	<b>670</b>	<b>FHH</b>			
ECL	p.E671K	671	Carcinoma	c.2011G>A	Skin	-
ECL	p.P672T	672	Carcinoma	c.2014C>A	Lung	-
ECL	p.W675*	675	Malignant melanoma	c.2024G>A	Skin	-
ECL	p.W675*	675	Carcinoma	c.2024G>A	Skin	25303977
ECL	p.R678H	678	Carcinoma	c.2033G>A	Ovary	21720365
ECL	p.L679M	679	Carcinoma	c.2035C>A	Endometrium	-
ECL	<b>R680H</b>	<b>680</b>	<b>FHH</b>			
ECL	<b>R680C</b>	<b>680</b>	<b>FHH</b>			
ECL	<b>Q681H</b>	<b>681</b>	<b>ADH</b>			
TMD	p.P682L	682	Carcinoma	c.2045C>T	Large intestine	-
TMD	p.A683V	683	Malignant melanoma	c.2048C>T	Skin	22842228
TMD	p.G685D	685	Malignant melanoma	c.2054G>A	Skin	-

TMD	<b>I686V</b>	<b>686</b>	<b>ADH</b>			
TMD	p.S687G	687	Carcinoma	c.2059A>G	Stomach	-
TMD	p.F688F	688	Malignant melanoma	c.2064C>T	Skin	-
TMD	p.F688F	688	Malignant melanoma	c.2064C>T	Skin	-
TMD	p.V689M	689	Carcinoma	c.2065G>A	Large intestine	-
TMD	<b>V689M</b>	<b>689</b>	<b>FHH</b>			
TMD	p.L690F	690	Carcinoma	c.2068C>T	Stomach	-
TMD	p.L696L	696	Carcinoma	c.2086C>T	Lung	22980975
TMD	p.N700S	700	Malignant melanoma	c.2099A>G	Skin	22842228
ICL	p.N700N	700	Malignant melanoma	c.2100C>T	Skin	-
ICL	p.R701C	701	Malignant melanoma	c.2101C>T	Skin	-
ICL	p.R701L	701	Carcinoma	c.2102G>T	Endometrium	-
ICL	p.A708A	708	Carcinoma	c.2124C>A	Lung	-
ICL	p.K709N	709	Carcinoma	c.2127G>T	Stomach	-
ICL	p.T712I	712	Carcinoma	c.2135C>T	Kidney	-
ICL	<b>W718X</b>	<b>718</b>	<b>FHH</b>			
ICL	p.W719C	719	Carcinoma	c.2157G>C	Liver	-
ICL	p.G720R	720	Malignant melanoma	c.2158G>A	Skin	-
ICL	p.G720G	720	Malignant melanoma	c.2160G>A	Skin	-
ICL	p.L723M	723	Carcinoma	c.2167C>A	Breast	-
TMD	p.F725F	725	Carcinoma	c.2175C>T	Large intestine	-
TMD	p.F725F	725	Malignant melanoma	c.2175C>T	Skin	-

TMD	p.L726L	726	Carcinoma	c.2178G>A	Endometrium	-
TMD	L727Q	727	ADH			
TMD	V728I	728	FHH			
TMD	p.T732A	732	Carcinoma	c.2194A>G	Breast	-
TMD	p.F733F	733	Malignant melanoma	c.2199C>T	Skin	-
TMD	M734R	734	FHH			
TMD	p.I738I	738	Carcinoma	c.2214C>A	Endometrium	-
TMD	W742R	742	FHH			
ECL	p.A746A	746	Carcinoma	c.2238G>A	Stomach	-
ECL	p.P747L	747	Malignant melanoma	c.2240C>T	Skin	-
ECL	P747ins/fsX776	747	FHH			
ECL	p.P748S	748	Malignant melanoma	c.2242C>T	Skin	-
ECL	P748L	748	FHH			
ECL	P748H	748	FHH			
ECL	P748R	748	FHH			
ECL	p.S749fs*28	749	Carcinoma	c.2244delG	Large intestine	-
ECL	p.Y751C	751	Carcinoma	c.2252A>G	Pancreas	26806338
ECL	p.R752H	752	Carcinoma	c.2255G>A	Prostate	26000489
ECL	E755D	755	FHH/Polymorphisms			
ECL	p.I760I	760	Malignant melanoma	c.2280C>T	Skin	-
ECL	p.I760I	760	Malignant melanoma	c.2280C>T	Skin	-
ECL	p.I761S	761	Malignant melanoma	c.2282T>G	Skin	22622578

ECL	<b>I761del</b>	<b>761</b>	<b>FHH</b>			
ECL	p.I763F	763	Carcinoma	c.2287A>T	Lung	22510280
ECL	<b>C765W</b>	<b>765</b>	<b>FHH</b>			
ECL	p.E767K	767	Carcinoma	c.2299G>A	Endometrium	-
ECL	p.E767K	767	Carcinoma	c.2299G>A	Cervix	-
ECL	<b>E767K</b>	<b>767</b>	<b>ADH</b>			
TMD	p.A772T	772	Malignant melanoma	c.2314G>A	Skin	24838835
TMD	p.A772A	772	Carcinoma	c.2316C>T	Lung	22980975
TMD	<b>L773R</b>	<b>773</b>	<b>ADH</b>			
TMD	p.F775F	775	Malignant melanoma	c.2325C>T	Skin	-
TMD	p.I777I	777	Glioma	c.2331C>T	Central nervous system	-
TMD	<b>F788C</b>	<b>778</b>	<b>ADH</b>			
TMD	<b>G778D</b>	<b>778</b>	<b>FHH</b>			
TMD	p.T780T	780	Malignant melanoma	c.2340C>A	Soft tissue	26168399
TMD	p.L782L	782	Carcinoma	c.2346G>A	Large intestine	24755471
TMD	p.A784S	784	Carcinoma	c.2350G>T	Cervix	-
TMD	p.I786I	786	Carcinoma	c.2358C>A	Biliary tract	-
TMD	p.I786M	786	Carcinoma	c.2358C>G	Esophagus	26873401
TMD	p.F788Y	788	Carcinoma	c.2363T>A	Kidney	-
TMD	<b>F788L</b>	<b>788</b>				
TMD	p.A791D	791	Carcinoma	c.2372C>A	Upper aerodigestive tract	-

ICL	p.R795Q	795	Carcinoma	c.2384G>A	Endometrium	-
ICL	<b>R795del/fsX836</b>	795	<b>FHH</b>			
ICL	<b>R795W</b>	795	<b>FHH/Dominant Neg</b>			
ICL	p.K796*	796	Malignant melanoma	c.2386A>T	Skin	-
ICL	p.P798L	798	Glioma	c.2393C>T	Central nervous system	-
ICL	p.P798L	798	Carcinoma	c.2393C>T	Esophagus	-
ICL	<b>P798T</b>	798	<b>FHH</b>			
ICL	p.E799K	799	Malignant melanoma	c.2395G>A	Skin	-
ICL	<b>E799K</b>	799	<b>ADH</b>			
ICL	p.N800N	800	Carcinoma	c.2400C>T	Pancreas	-
ICL	<b>N802I</b>	802	<b>ADH</b>			
ICL	p.A804A	804	Carcinoma	c.2412C>A	Stomach	24308032
ICL	<b>A804D</b>	804	<b>FHH</b>			
TMD	<b>F806S</b>	806	<b>ADH</b>			
TMD	p.I807T	807	Adenoma	c.2420T>C	Small intestine	26806338
TMD	p.T808A	808	Carcinoma	c.2422A>G	Breast	-
TMD	<b>F809L</b>	809	<b>FHH</b>			
TMD	<b>M811V</b>	811	<b>ADH</b>			
TMD	p.I813V	813	Carcinoma	c.2437A>G	Endometrium	-
TMD	p.I816I	816	Malignant melanoma	c.2448C>T	Skin	-
TMD	p.V817I	817	Glioma	c.2449G>A	Central nervous system	-
TMD	p.V817I	817	Malignant melanoma	c.2449G>A	NS	24265153



TMD	<b>V817I</b>	<b>817</b>	<b>FHH</b>			
TMD	p.W818L	818	Carcinoma	c.2453G>T	Prostate	-
TMD	p.S820F	820	Malignant melanoma	c.2459C>T	Skin	-
TMD	<b>S820F</b>	<b>820</b>	<b>ADH</b>			
TMD	<b>F821L</b>	<b>821</b>	<b>ADH</b>			
TMD	p.P823S	823	Malignant melanoma	c.2467C>T	Skin	-
TMD	p.A824T	824	Carcinoma	c.2470G>A	Large intestine	-
TMD	p.A824A	824	Malignant melanoma	c.2472C>T	Skin	-
TMD	<b>A824S</b>	<b>824</b>	<b>ADH</b>			
TMD	<b>A826T</b>	<b>826</b>	<b>FHH/Polymorphisms</b>			
TMD	<b>T828N</b>	<b>828</b>	<b>ADH</b>			
ECL	p.G830D	830	Carcinoma	c.2489G>A	Endometrium	22923510
ECL	<b>G830S</b>	<b>830</b>	<b>ADH</b>			
ECL	<b>F832L</b>	<b>830</b>	<b>ADH</b>			
ECL	<b>F832S</b>	<b>832</b>	<b>ADH</b>			
ECL	<b>S834del/fsX836</b>	<b>834</b>	<b>FHH</b>			
ECL	<b>A835T</b>	<b>835</b>	<b>ADH</b>			
ECL	p.V836I	836	Malignant melanoma	c.2506G>A	Skin	-
ECL	<b>V836L</b>	<b>836</b>	<b>ADH</b>			
TMD	<b>A843E</b>	<b>843</b>	<b>ADH</b>			
TMD	<b>A844T</b>	<b>844</b>	<b>ADH</b>			
TMD	<b>S845N</b>	<b>845</b>	<b>ADH</b>			

TMD	<b>L849P</b>	<b>849</b>	<b>FHH</b>			
TMD	p.A850V	850	Carcinoma	c.2549C>T	Large intestine	22895193
TMD	<b>A850ins/fsX9 81</b>	<b>850</b>	<b>FHH</b>			
TMD	p.C851G	851	Malignant melanoma	c.2551T>G	Skin	-
TMD	<b>C851S</b>	<b>851</b>	<b>FHH/Polymorphisms</b>			
TMD	p.K856K	856	Malignant melanoma	c.2568G>A	Skin	-
ICD	p.P864S	864	Carcinoma	c.2590C>T	Kidney	25401301
ICD	p.P864L	864	Carcinoma	c.2591C>T	Skin	25303977
ICD	p.R866H	866	Carcinoma	c.2597G>A	Large intestine	24755471
ICD	p.E870K	870	Carcinoma	c.2608G>A	Breast	22722193
ICD	p.E870E	870	Carcinoma	c.2610G>A	Lung	22980975
ICD	p.E871K	871	Malignant melanoma	c.2611G>A	Skin	-
ICD	p.E871E	871	Malignant melanoma	c.2613G>A	Skin	26214590
ICD	p.R873C	873	Carcinoma	c.2617C>T	Lung	22941188
ICD	p.R873H	873	Carcinoma	c.2618G>A	Large intestine	25344691
ICD	p.R873H	873	Carcinoma	c.2618G>A	Large intestine	24755471
ICD	p.T876T	876	Carcinoma	c.2628C>T	Large intestine	24755471
ICD	<b>T876 Alu ins</b>	<b>876</b>	<b>FHH</b>			
ICD	p.H879Y	879	Malignant melanoma	c.2635C>T	Skin	26343386
ICD	p.A880T	880	Carcinoma	c.2638G>A	Endometrium	-
ICD	p.F881F	881	Malignant melanoma	c.2643C>T	Skin	-
ICD	<b>F881L</b>	<b>881</b>	<b>FHH/Dominant Neg</b>			

ICD	p.A884V	884	Malignant melanoma	c.2651C>T	NS	23890154
ICD	p.R886W	886	Glioma	c.2656C>T	Central nervous system	-
ICD	p.R886Q	886	Carcinoma	c.2657G>A	Breast	-
ICD	<b>R886W</b>	<b>886</b>	<b>FHH</b>			
ICD	<b>R886P</b>	<b>886</b>	<b>FHH</b>			
ICD	p.A887V	887	Carcinoma	c.2660C>T	Lung	22941189
ICD	p.T888T	888	Malignant melanoma	c.2664G>T	Soft tissue	26168399
ICD	p.R890C	890	Carcinoma	c.2668C>T	Ovary	-
ICD	p.R890H	890	Carcinoma	c.2669G>A	Stomach	-
ICD	p.R890R	890	Carcinoma	c.2670C>T	Lung	-
ICD	p.R891G	891	Carcinoma	c.2671C>G	Lung	-
ICD	p.R891H	891	Carcinoma	c.2672G>A	Endometrium	-
ICD	p.R891P	891	Carcinoma	c.2672G>C	Lung	-
ICD	p.N893N	893	Carcinoma	c.2679C>T	Large intestine	24755471
ICD	p.V894I	894	Carcinoma	c.2680G>A	Breast	-
ICD	p.V894V	894	Malignant melanoma	c.2682C>T	Skin	-
ICD	p.S895S	895	Malignant melanoma	c.2685C>T	Skin	26343386
ICD	<b>S895-V1075del</b>	<b>895</b>	<b>ADH</b>			
ICD	p.R896C	896	Carcinoma	c.2686C>T	Large intestine	-
ICD	<b>R896H</b>	<b>896</b>	<b>FHH</b>			
ICD	<b>K897ins/fsX979</b>	<b>897</b>	<b>ADH</b>			
ICD	p.R898W	898	Carcinoma	c.2692C>T	Large intestine	25344691

ICD	p.R898Q	898	Carcinoma	c.2693G>A	Lung	22980975
ICD	p.R898R	898	Carcinoma	c.2694G>T	Lung	-
ICD	<b>R898Q</b>	<b>898</b>	<b>ADH</b>			
ICD	p.L902V	902	Carcinoma	c.2704C>G	Lung	-
ICD	p.G903R	903	Malignant melanoma	c.2707G>A	Skin	-
ICD	p.G907E	907	Malignant melanoma	c.2720G>A	Skin	-
ICD	p.P910T	910	Carcinoma	c.2728C>A	Endometrium	-
ICD	p.S911fs*28	911	Carcinoma	c.2726delC	Large intestine	-
ICD	p.S911fs*28	911	Carcinoma	c.2726delC	Large intestine	25344691
ICD	p.S911fs*28	911	Carcinoma	c.2726delC	Large intestine	24755471
ICD	p.S912F	912	Malignant melanoma	c.2735C>T	Skin	22842228
ICD	p.S912F	912	Carcinoma	c.2735C>T	Skin	25303977
ICD	p.P923L	923	Carcinoma	c.2767_2768 CC>TT	Skin	21984974
ICD	p.P923L	923	Carcinoma	c.2768C>T	Large intestine	-
ICD	p.Q926Q	926	Glioma	c.2778G>A	Central nervous system	-
ICD	<b>Q926R</b>	<b>926</b>	<b>FHH</b>			
ICD	p.P927P	927	Carcinoma	c.2781C>T	Large intestine	22810696
ICD	<b>Q930del/fsX9 38</b>	<b>930</b>	<b>ADH</b>			
ICD	p.P935S	935	Carcinoma	c.2803C>T	Large intestine	-
ICD	p.P935S	935	Carcinoma	c.2803C>T	Biliary tract	-
ICD	p.P935L	935	Carcinoma	c.2804C>T	Large intestine	-
ICD	p.Q940K	940	Carcinoma	c.2818C>A	Skin	25303977

ICD	E942K	942	ADH			
ICD	p.R955Q	955	Malignant melanoma	c.2864G>A	Skin	22842228
ICD	p.R955Q	955	Lymphoid neoplasm	c.2864G>A	Hematopoietic and lymphoid	26189108
ICD	p.R955Q	955	Carcinoma	c.2864G>A	Large intestine	-
ICD	p.R955L	955	Malignant melanoma	c.2864G>T	Soft tissue	26168399
ICD	p.Q958L	958	Carcinoma	c.2873A>T	Stomach	23525077
ICD	p.R961K	961	Carcinoma	c.2882G>A	Lung	22980975
ICD	p.I967V	967	Carcinoma	c.2899A>G	Liver	-
ICD	p.S970S	970	Carcinoma	c.2910C>T	Prostate	22722839
ICD	p.S970S	970	Carcinoma	c.2910C>T	Stomach	25042771
ICD	p.G971S	971	Carcinoma	c.2911G>A	Esophagus	-
ICD	p.G971S	971	Carcinoma	c.2911G>A	Stomach	-
ICD	p.T972M	972	Carcinoma	c.2915C>T	Stomach	-
ICD	p.T974T	974	Malignant melanoma	c.2922C>T	Skin	-
ICD	p.F979S	979	Carcinoma	c.2936T>C	Endometrium	-
ICD	p.D980H	980	Carcinoma	c.2938G>C	Lung	-
ICD	p.Q983E	983	Carcinoma	c.2947C>G	Breast	-
ICD	p.Q983R	983	Carcinoma	c.2948A>G	Large intestine	25344691
ICD	A986S	986	FHH/Polymorphisms			
ICD	A988V	988	ADH			
ICD	A988G	988	ADH			
ICD	p.R990R	990	Malignant melanoma	c.2970G>A	Skin	-

ICD	p.R990R	990	Malignant melanoma	c.2970G>A	Skin	-
ICD	p.R990R	990	Malignant melanoma	c.2970G>A	NS	23890154
ICD	p.R990R	990	Malignant melanoma	c.2970G>A	Skin	26343386
ICD	R990G	990	ADH/Polymorphisms			
ICD	p.N991S	991	Carcinoma	c.2972A>G	Skin	25303977
ICD	p.T993M	993	Carcinoma	c.2978C>T	Esophagus	25839328
ICD	p.T993M	993	Carcinoma	c.2978C>T	Biliary tract	-
ICD	H994Y	994	ADH			
ICD	p.S997F	997	Carcinoma	c.2990C>T	Skin	25303977
ICD	p.S997S	997	Malignant melanoma	c.2991C>T	Skin	21499247
ICD	p.S997S	997	Malignant melanoma	c.2991C>T	Skin	-
ICD	D1005N	1005	FHH			
ICD	p.T1006M	1006	Carcinoma	c.3017C>T	Large intestine	24755471
ICD	p.T1006M	1006	Carcinoma	c.3017C>T	Esophagus	26873401
ICD	Q1011E	1011	FHH/Polymorphisms			
ICD	p.P1015L	1015	Carcinoma	c.3044C>T	Endometrium	-
ICD	p.C1018C	1018	Carcinoma	c.3054C>T	Large intestine	-
ICD	p.E1020K	1020	Malignant melanoma	c.3058G>A	Skin	-
ICD	p.D1022N	1022	Malignant melanoma	c.3064G>A	Skin	-
ICD	p.L1025M	1025	Glioma	c.3073C>A	Central nervous system	-
ICD	p.T1026T	1026	Carcinoma	c.3078C>T	Stomach	-
ICD	p.V1027I	1027	Osteosarcoma	c.3079G>A	Bone	25512523

ICD	p.E1029K	1029	Malignant melanoma	c.3085G>A	NS	23890154
ICD	p.L1032R	1032	Carcinoma	c.3095T>G	Lung	22980975
ICD	p.G1034E	1034	Malignant melanoma	c.3101G>A	Skin	-
ICD	p.R1041W	1041	Carcinoma	c.3121C>T	Ovary	21720365
ICD	p.R1041W	1041	Adenoma	c.3121C>T	Prostate	23265383
ICD	p.R1041W	1041	Carcinoma	c.3121C>T	Prostate	22502944
ICD	p.R1041Q	1041	Carcinoma	c.3122G>A	Prostate	26000489
ICD	p.P1042L	1042	Malignant melanoma	c.3125C>T	NS	23890154
ICD	p.V1044V	1044	Malignant melanoma	c.3132G>A	Skin	-
ICD	p.E1045K	1045	Carcinoma	c.3133G>A	Liver	-
ICD	p.E1045K	1045	Carcinoma	c.3133G>A	Liver	25822088
ICD	p.E1048*	1048	Carcinoma	c.3142G>T	Small intestine	27900363
ICD	p.L1050*	1050	Carcinoma	c.3149T>A	Stomach	22037554
ICD	p.S1051P	1051	Carcinoma	c.3151T>C	Large intestine	-
ICD	p.P1052S	1052	Malignant melanoma	c.3154C>T	Skin	-
ICD	p.V1056M	1056	Carcinoma	c.3166G>A	Large intestine	23856246
ICD	p.V1056M	1056	Carcinoma	c.3166G>A	Large intestine	24755471
ICD	p.S1061G	1061	Carcinoma	c.3181A>G	Liver	-
ICD	p.V1063A	1063	Carcinoma	c.3188T>C	Large intestine	22895193
ICD	p.G1066R	1066	Carcinoma	c.3196G>C	Urinary tract	-
ICD	p.G1066D	1066	Carcinoma	c.3197G>A	Upper aerodigestive tract	26934577
ICD	p.S1069N	1069	Carcinoma	c.3206G>A	Large intestine	25344691

ICD	p.N1074N	1074	Glioma	c.3222C>T	Central nervous system	-
ICD	p.V1076V	1076	Malignant melanoma	c.3228G>A	Skin	-
ICD	p.N1077D	1077	Carcinoma	c.3229A>G	Lung	22980975
ICD	X1079QextX 1087	1079	FHH			
ICD	p.?		Carcinoma	c.1378- 1G>T	Large intestine	25344691
ICD	p.?		Carcinoma	c.1733- 1G>C	Upper aerodigestive tract	21798897
ICD	p.?		Carcinoma	c.1733- 1G>C	Upper aerodigestive tract	23619168
ICD	p.?		Lymphoid neoplasm	c.186-1G>A	Hematopoietic and lymphoid	26437031

ECD – Extracellular domain (dark purple), TMD – Transmembrane domain (brown), ICD – Intracellular domain (red), ECL – Extracellular loops (light purple), ICL – Intracellular loops (pink), AA – Amino acids, FHH – Familial hypocalciuric hypercalcemia or NSHPT mutations (cyan), ADH – Autosomal dominant hypocalcemia mutations (magenta), COSMIC cancer missense mutations (light blue) and non-missense mutations (dark blue). No data in gray.

### *PCR of CaSR Mutations*

To begin in making the disease mutation of bCaSR and hCaSR we designed the primers for the mutations we were interested in creating (Figure 3.5). Our CaSR structure competitor did many mutations previously for the analysis of their binding site locations. The Geng et al. mutations are as follows; for the dimerization site L159P, W458A, R172G, D215G, R227L, R551K, and G557E<sup>[284]</sup>. For the binding Sites, T145I, S147A, S170A, Y218S, E297K, I81M, T100I, N102I, R66H, R69E, and S417L<sup>[284]</sup>. We have also analyzed S170, Y218, E297 for the TNCA/proposed Ca<sup>2+</sup> binding site I pocket, as well as now looking into I81M for the Mg<sup>2+</sup> binding site I pocket .



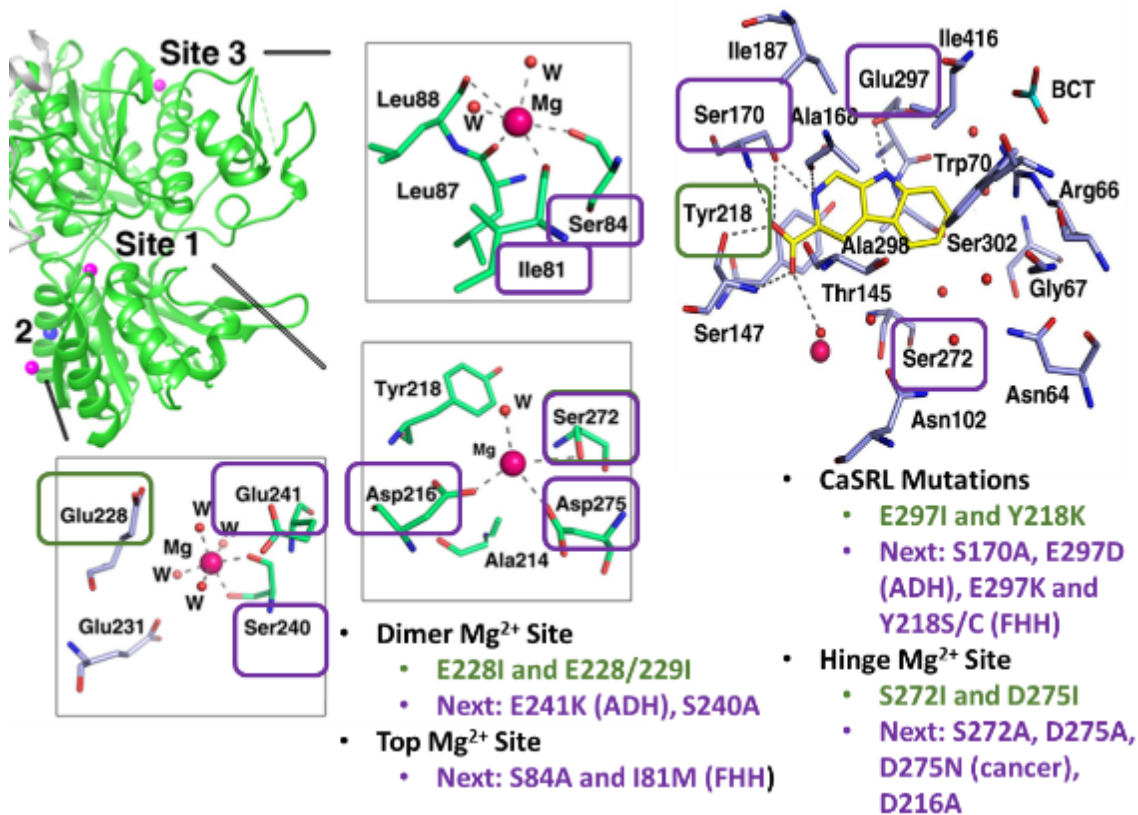


**Figure 8.3– CaSR disease mutations for ECD.**

**Green are mutations already done previously. Purple are planned mutations and if they have disease relevance they are noted in parentheses.**

Initially we made these mutations with the noted  $T_m$  based on previous primer design methods. After running PCR there were little to no colonies after transformation into Dh5 $\alpha$ . The colonies that did present were not correct once amplified using miniprep and run for sequencing. We investigated further how to optimize the primer design. We found that primers should be between 14-28 bp long, the previous primers are too long since the previous method was 25-45 bp. The GC content should be 40-60%, ideally around 50% GC. The  $T_m$  should be between 55-65°C, where the previous protocol was a  $T_m \geq 78^\circ C$ . Therefore, the primers were redesigned to meet these parameters for our planned mutation sites (Figure 3.5).

Of the new primers ordered all had colony growth on their plates this time around. All of these PCR were done using the pfu kit for PCR. There seems to be a double band pattern showing for all the samples in the DNA gel. After running sequencing, we confirmed that the reason was that the samples were contaminated with template DNA as all the sequencing matched the template and no mutations were successful. Next time the DNA needs to be treated with newly ordered PNK in order to remove the template DNA before running the DNA gel and doing miniprep, since the old PNK seems to be expired. We repeated the PCR again exactly as before, but all samples were either too low of a concentration to sequence or the sequence had no mutation present.

Further, repeated with only 5 mutations to simplify the protocol and using the KOD Hot Start that others use. For those 5 mutations, all of them had colonies on their plates to did miniprep and sent to sequencing. Again, the mutations either did not have enough DNA sample or no mutation was seen. With the lack of successful mutations once again, we turned to different primer approach of not having the primers be complementary. Since complementary primers have a higher risk of binding to each other instead of the parent DNA leading to a failed PCR reaction .

Initially we just did 5 mutations with the new primers to keep it simple; R69L (Anion site), I81M (FHH Mg<sup>2+</sup> top site), E228Q (ADH Dimer Site), E241K (ADH Dimer Site), D275N (Hinge Site). First did phosphorylation of primers using T4 PNK. Then did PCR using pfu DNA polymerase protocol with 20 ng/μL of CaSR pcDNA at 30 cycles with an 8.5 minute extension time. After PCR did DpnI parent DNA digestion followed by transformation into XL10 Gold competent cells using 20 μL of PCR product. The next day only 1 plate grew colonies out of 5. So, we repeated mutation on D275N and R69L, for D275N did 4 different temperatures than before. Initially did Ta of 60.8°C for D275N and this time did 65, 55, 50, and 45°C. For R69L did one at 50°C versus 55°C before. Same protocol as before besides temperature change. Additionally, did

transformation with 2  $\mu$ L and 20  $\mu$ L of PCR product to see which was most effective. Still no correct mutations after doing miniprep and sequencing on these colonies. Also saw no apparent difference in using 2 or 20  $\mu$ L of PCR product for transformation, will continue to use 2  $\mu$ L for saving of product and reduction of salts.

Since the new primers saw no success, we decided to go back to the last time we were able to get a successful point mutation on CaSR pcDNA to look at the protocol differences. Back then we used KOD DNA polymerase versus pfu DNA polymerase and the primers we used were around 35-45 bp long. So, we decided to look up which polymerase is better for larger plasmids such as CaSR pcDNA which is 8662 bp long. In the PCR paper by Munteanu et al. has a comparison of pfu and KOD Hot Start DNA Polymerase on large plasmids for site-directed mutagenesis<sup>[411]</sup>. Their plasmid total size to test which is better is 16 kbp, which is relevant to our CaSR mutagenesis since the CaSR plasmid is 6.8 kb for bCaSR and 8.7 kb for hCaSR. Pfu DNA polymerase can do up to 10 kb but loses efficacy the larger the plasmid, while KOD can do up to 21 kb plasmids. They found that KOD was able to give results at just 8 cycles of PCR, with more cycles up to 30 give even better results. Pfu, on the other hand, was unable to give results for their large plasmid.

**Table 8.2 – hCaSR disease mutation primers designed.**

Primer Name	Sequence	Primer Name	Sequence
pcDNA R66C For CaSR	GAA TGT ATC AGG TAT AAT TTC TGT GGG	pcDNA E241K For CaSR	CG GGG ATT GAG AAA TTC CGA AAG GAA
pcDNA R66C Rev CaSR	CTGTAACCAGCGAAACCCACAGAA	pcDNA E241K Rev CaSR	AT ATC CCT TTC CTC AGC TTC CTT TCG
pcDNA R66H For CaSR	GAA TGT ATC AGG TAT AAT TTC CAT GGG	pcDNA E241K For CaSR	GAT ATC TGC ATC GAC TTC AGT AAA CTC
pcDNA R66H Rev CaSR	TG TAA CCA GCG AAA CCC ATG GAA	pcDNA E241K Rev CaSR	ATC AGA GTA CTG GGA GAT GAG TTT ACT
pcDNA R69L For CaSR	GG TAT AAT TTC CGT GGG TTT CTC TGG	pcDNA H254A For CaSR	AT GAG GAA GAG ATC CAG GCT GTG
pcDNA R69L Rev CaSR	C AAA TAT CAT AGC CTG TAA CCA GAG AAA	pcDNA H254A Rev CaSR	G AAT CAC CTC TAC CAC AGC CTG
pcDNA I81M For CaSR	ATG ATA TTT GCC ATA GAG GAG ATG AAC	pcDNA S272A For CaSR	GTC ATC GTG GTT TTC TCC GCT GGC
pcDNA I81M Rev CaSR	GGC TGG GCT GCT GTT CAT CTC	pcDNA S272A Rev CaSR	G CTC AAG ATC TGG GCC AGC GGA
pcDNA S84A For CaSR	GCC ATA GAG GAG ATA AAC AGC GCC CCA	pcDNA D275N For CaSR	TG GTT TTC TCC AGT GGC CCA AAT CTT
pcDNA S84A Rev CaSR	TT GGG AAG AAG GGC TGG GGC GCT	pcDNA D275N Rev CaSR	TC CTT GAT GAG GGG CTC AAG ATT TGG
pcDNA D216N For CaSR	GTG GGC ACA ATT GCA GCT GAT AAC GAC	pcDNA S296A For CaSR	GC AAG ATC TGG CTG GCC GCC GAG
pcDNA D216N Rev CaSR	CC CGG CCG CCC ATA GTC GTT ATC	pcDNA S296A Rev CaSR	T GGC CCA GGC CTC GGC GGC
pcDNA Y218S For CaSR	C ACA ATT GCA GCT GAT GAC GAC TCT GGG	pcDNA E297K For CaSR	AAG ATC TGG CTG GCC AGC AAG GCC
pcDNA Y218S Rev CaSR	AAT CCC CCG CCG CCC AGA GTC	pcDNA E297K Rev CaSR	A GGA GCT GCC CCA GGC CTT GCT
pcDNA Y218C For CaSR	C ACA ATT GCA GCT GAT GAC GAC TGT GGG	pcDNA E297D For CaSR	TC TGG CTG GCC AGC GAC GCC
pcDNA Y218C Rev CaSR	AAT CCC CCG CCG CCC ACA GTC	pcDNA E297D Rev CaSR	GA GCT GGC CCA GGC GTC GC
pcDNA Y218C For CaSR	CG GGG ATT GAG AAA TTC CGA CAG GAA		
pcDNA Y218C Rev CaSR	AT ATC CCT TTC CTC AGC TTC CTG TCG		

They also referenced a 2009 paper by Laible and Boonrod for primer design<sup>[412]</sup>. This paper recommends primers of 25-45 bp with more than 40% GC content where the primer ends in a G or C on both ends.

We used this method of primer design to design new primers to continue the mutations of CaSR pcDNA using KOD DNA polymerase (Table 8.2). Next, we choose 3 mutations to initially try these primers and the KOD DNA polymerase technique; S272A (hinge site), D275N (hinge site), and E297D (hinge site, ADH). We did two temperatures for each primer with one being the temperature listed on the IDT primer sheets and the other being 5 degrees lower than the  $T_m$ . Phosphorylation of primers using T4 PNK as before per protocol. Then we did PCR using KOD DNA Polymerase following their protocol which has 5  $\mu$ L of 10x KOD buffer, 5  $\mu$ L of 1x 2 mM dNTPs each, 5  $\mu$ L of 10 mM MgCl<sub>2</sub>, 30.6  $\mu$ L filtered water, 1.5  $\mu$ L of 10  $\mu$ M Sense (5') Primer (5 pmol/ $\mu$ L), 1.5  $\mu$ L of 10  $\mu$ M Antisense (3') Primer (5 pmol/ $\mu$ L), 1  $\mu$ L of 200 ng/ $\mu$ L template DNA, and 0.4  $\mu$ L of KOD DNA polymerase (2.5 U/ $\mu$ L) with a total volume of 50  $\mu$ L. Then we did thermocycling conditions per the KOD protocol slightly increased to 30 cycles for the larger plasmid size.

After PCR we did DpnI parent DNA digestion using 0.5  $\mu$ L DpnI enzyme and 5  $\mu$ M cutsmart buffer added directly to PCR product and incubated at 37°C for 1 hour then heat inactivated at 80°C for 20 mins. Finally, we took 2  $\mu$ L of the PCR product for transformation into XL10 Gold cells. We were able to get 18 colonies on the 6 plates and used those for miniprep and sent the DNA for sequencing. So far for hCaSR S272A, E297K, and R66H have been successfully cloned. Unfortunately, our microscope was having issues, so we temporarily switched gears to bCaSR mutations while the microscope was being repaired. We designed the bCaSR primers using the

same method we had found to be successful for the hCaSR mutations and ordered them as outlined in Table 8.3.

**Table 8.3 – bCaSR ECD disease mutation primers designed.**

R66C F	65.64545	GCTATAATTTT <b>TGT</b> GGC TTC CGCTGGCTGCAGG	E228Q R	62.08857	GGTTCTTCGGC TTC TTG ACGAAATTTTCAATAC
R66C R	65.64545	CCTGCAGCCAGCG GAA GCC ACA AAAATTATAGC	E228K F	60.91714	GTATTGAAAAATTCGT <b>AAA</b> GAA GCCGAAGAACGC
R66H F	65.64545	GCTATAATTTT <b>CAT</b> GGC TTC CGCTGGCTGCAGG	E228K R	60.91714	GGTTCTTCGGC TTC TTT ACGAAATTTTCAATAC
R66H R	65.64545	CCTGCAGCCAGCG GAA GCC ATG AAAATTATAGC	E241K F	59.59412	CAATCGATTCAGT <b>AAA</b> CTGATCTCACAGTATTC
R69L F	65.81111	C GT GGC TTC <b>TTG</b> TGGCTGCAGGCCATG	E241K R	59.59412	GAATACTGTGAGATCAG TTT ACTGAAATCGATTG
R69L R	65.81111	CATGGCCTGCAGCCA CAA GAA GCC ACG	H254A F	64.41765	GAAGAA GAA ATC CAG <b>GCT</b> GTCGTGGAAATGATTC
I81M F	61.91818	GATCTTCGCAATCGAAGAA <b>ATG</b> AAT AGC TCT CC	H254A R	64.41765	GAATCACTCCACGAC AGC CTG GAT TTC TTCTTC
I81M R	61.91818	GG AGA GCT ATT CAT TTCTTCGATTCGGAAGATC	S272A F	64.244	GTTGTCTTT <b>TCG</b> <b>GCC</b> GGC CCG GAT C
S84A F	64.29259	GAA ATC AAT AGC <b>GCC</b> CCGGCACTGCTG	S272A R	64.244	G ATC CGG GCC GGC CGA AAAGACAAC
S84A R	64.29259	CAGCAGTGCCGG GGC GCT ATT GAT TTC	D275N F	62.29091	G AGC GGC CCG <b>AAT</b> CTGGAACCG
D216N F	62.85	CC ATC GCA GCA GAT <b>AAC</b> GAT TAC GGTCCG	D275N R	62.29091	CGGTTCCAG ATT CGG GCC GCT C
D216N R	62.85	CGACC GTA ATC GAT TGC TGC GAT GG	S296A F	64.11905	GG CTG GCC <b>GCT</b> GAA GCCTGG G
Y218S F	62.50833	GCA GAT GAC GAT <b>AGC</b> GGTCGTCGG	S296A R	64.11905	C CCAGGC TTC AGC GGC CAG CC
Y218S R	62.50833	CGGACGACC GCT ATC GTC ATC TGC	E297K F	64.244	GG CTG GCC AGT <b>AAA</b> GCCTGGGCATC
Y218C F	62.50833	GCA GAT GAC GAT <b>TGC</b> GGTCGTCGG	E297K R	64.244	GATGCCAAGGC TTT ACT GGC CAG CC
Y218C R	62.50833	CGGACGACC GCA ATC GTC ATC TGC	E297D F	64.11905	G CTG GCC AGT <b>GAC</b> GCCTGGGC
			E297D R	64.11905	GCCAGGC GTC ACT GGC CAG C

We made mutations for bCaSR so far of R66H (Anion/pH for FHH), D216N (Anion/pH for disrupt/cancer), E241K (Dimer for ADH), S272A (Hinge Mg for disruption), E297K (Hinge for FHH/NSHPT), H254A (pH for disrupt), E228Q (Dimer for ADH), and E228K (Dimer for ADH), these mutations were successfully made using the primers in Table 8.3 and the KOD DNA Polymerase protocol as described earlier. For large plasmids we have found KOD works effectually but for smaller plasmids pfu works more efficiently.

The successful mutations made for bCaSR and hCaSR are outlined in Table 3.1, where planned mutations to be made indicated in the third column in black, successfully made hCaSR mutations are shown in blue, made bCaSR mutations are in red, and mutations made for hCaSR and bCaSR are in green.

Previously the mutations have been unsuccessful but with research we found the correct primer formation and PCR protocols to successfully produce bCaSR and hCaSR mutants. Using the correct DNA polymerase for the size of the plasmid and protein for site-directed mutagenesis is critical. Although the primers and protocol are optimized this does not necessitate that the mutations will effectively work during PCR. There are many factors influencing primers and PCR, most notably temperature, cycles of run, and primer design. Thus, looking at alternative reasons and going back to protocols when we were successful is key. By doing this we have found out the KOD DNA polymerase is better for larger plasmids and that primer design can also matter for plasmid size. Using the new primers and KOD polymerase resulted in a successful mutation.

We were able to PCR three mutations for hCaSR and bCaSR of E297K (FHH), S272A, R66H (FHH). With the maintenance of our epifluorescence microscope for almost a year we focused on bCaSR mutation binding assays. We were able to purify each mutant and the WT for bCaSR, although R66H both times had such a low concentration of protein through purification that binding studies were not possible. The WT bCaSR and E297K and S272A mutants went forward with binding studies. We first optimized our binding study protocols where we did not utilize EGTA since the  $\text{Ca}^{2+}$  present was negligible and adding EGTA can lead to saturation or pH changes. Also increasing the amount of titration added from 1-2  $\mu\text{L}$  to  $\sim 4 \mu\text{L}$  helped to significantly reduce error, by keeping the volume closer to 4-5  $\mu\text{L}$  we can also reduce dilution effects of the bCaSR.

These tables outline the primers and mutations as well as the results for our CaSR mutations and the Geng at al. mutations for comparison of mutations made and the results (Table 8.4-Table 8.5).

**Table 8.4 – bCaSR and hCaSR ECD disease mutations and primers made.**

Binding Sites	Binding Residues	Disease Mutations ( <b>bCaSR/hCaSR</b> /primers to be PCR)
New Site	I81, S84, L87, L88, L91	<b>FHH/NSHPT:</b> I81M <b>Disruption:</b> S84A
TNCA Site	S147, A168, S170, Y218, E297	<b>FHH/NSHPT:</b> Y218S, Y218C, <b>E297K (reduced bCaSR expression)</b> <b>Disruption:</b> Y218K (loss of all function), Y218Q (reduced activity), E297I (loss of all function)
Hinge Site	A214, D216, Y218, S272, D275	<b>Disruption:</b> S272I (loss of all function), D275I (loss of all function), <b>S272A (LOF Ca<sup>2+</sup> binding Trp and loss of cooperativity and LOF Tb<sup>3+</sup>/Trp)</b> <b>Cancer:</b> D275N
Anion Site	R66, R69, W70, R415, I416, S417	<b>FHH/NSHPT:</b> R66C, <b>R66H (loss of bCaSR expression)</b> <b>Disruption:</b> R69L
Dimer Site	E228, E229, E231, E232, S240, E241	<b>ADH:</b> <b>E228Q (loss of bCaSR expression), E228K (loss of bCaSR expression), E241K (reduced bCaSR expression)</b> <b>Disruption:</b> E224I (to be tested), E228I (reduced Mg function TNCA recovers)
pH/pKa Effects	N/A	<b>Disrupt pH/pKa:</b> R69L, <b>D215I (to be tested), D215G (FHH), H254A (reduced bCaSR expression), S296A</b> <b>Cancer:</b> <b>D216N (LOF of Ca<sup>2+</sup> Trp binding), S296A</b>

Geng et al. showed that Trp acts as agonist shifting EC<sub>50</sub> to 1 mM IP1 accumulation and that at higher Ca<sup>2+</sup> higher Trp induced Ca<sup>2+</sup> release with 2.5 mM being much higher than 0.5 and 1.5 mM showing that basal Ca<sup>2+</sup> first activates similar to what we observed with TNCA. Geng et al. showed that Trp induces oscillation in the presence of 1.5 mM Ca<sup>2+</sup> at 2-20 mM Trp. They also showed that SO<sub>4</sub> leads to less sensitive CaSR to [Ca<sup>2+</sup>]<sub>o</sub> from 2.2 to 2.7 mM for IP1 accumulation.

Table 8.5 –hCaSR ECD disease mutation made by Geng et al. and observations.

Binding Sites	Binding Residues	Geng et al Mutations (hCaSR) (WT IP1 100% & EC <sub>50</sub> 1.5 mM and [Ca <sup>2+</sup> ] <sub>i</sub> oscillation EC <sub>50</sub> 1.6 mM) ( <b>LOF = loss of function</b> )
New Site	I81, S84, L87, L88, L91	<b>FHH/NSHPT: I81M</b> ([Ca <sup>2+</sup> ] <sub>i</sub> oscillation EC <sub>50</sub> 2.5 mM and IP1 20% & EC <sub>50</sub> 2.5 mM)
TNCA Site	S147, A168, S170, Y218, E297	<b>FHH/NSHPT: Y218S</b> (IP1 20% & EC <sub>50</sub> 4.5 mM), <b>E297K</b> (IP1 10% & EC <sub>50</sub> 5.5 mM)
		<b>Disruption: S170A</b> (IP1 LOF 0% & EC <sub>50</sub> none), <b>S147A</b> (IP1 LOF 50% & EC <sub>50</sub> 5 mM)
Hinge Site	A214, D216, Y218, S272, D275	<b>FHH/NSHPT: Y218S</b> (IP1 20% & EC <sub>50</sub> 4.5 mM)
Anion Site	R66, R69, W70, R415, I416, S417	<b>FHH/NSHPT: R66H</b> (40% IP1 & EC <sub>50</sub> 4.5 mM and [Ca <sup>2+</sup> ] <sub>i</sub> oscillation EC <sub>50</sub> 4 mM)
		<b>Disruption: R69E</b> (LOF 20% IP1 & EC <sub>50</sub> 3.5 mM and [Ca <sup>2+</sup> ] <sub>i</sub> oscillation EC <sub>50</sub> 4 mM) and <b>S417L</b> (LOF 10% IP1 & EC <sub>50</sub> 4.5 mM and [Ca <sup>2+</sup> ] <sub>i</sub> oscillation EC <sub>50</sub> 2.5 mM).
Dimer Site	E228, E229, E231, E232, S240, E241	<b>FHH/cancer: G557E</b> (lower dimer Ca <sup>2+</sup> site, IP1 85% & EC <sub>50</sub> 3.2 mM, [Ca <sup>2+</sup> ] <sub>i</sub> oscillation EC <sub>50</sub> 3 mM LOF), <b>R227L</b> (IP1 75% & EC <sub>50</sub> 5 mM)
pH/pKa Effects	N/A	<b>FHH/NSHPT: D215G</b> (dimer interface LOF IP1 50% & EC <sub>50</sub> 5.5 mM)
Homodimer Interface		<b>FHH/NSHPT: L159P</b> (IP1 50% & EC <sub>50</sub> 4 mM), <b>R172G</b> (IP1 60% & EC <sub>50</sub> 4 mM), <b>R551K</b> (IP1 80% & EC <sub>50</sub> 4 mM)
		<b>Disruption: W458A</b> (LOF IP1 50% & EC <sub>50</sub> 2.3 mM)
Internal Inactive Ca <sup>2+</sup> site	T100, N102, T145, G146	<b>FHH/NSHPT: T100I</b> (LOF IP1 0% & EC <sub>50</sub> 1 mM)
		<b>Disruption: T145I</b> (IP1 LOF 20% & EC <sub>50</sub> 4.2 mM), <b>N102I</b> (LOF [Ca <sup>2+</sup> ] <sub>i</sub> oscillation EC <sub>50</sub> 3.1 mM and IP1 25% & EC <sub>50</sub> 4 mM)
Glycosylation Mutations		N386Q, S402N and/or N468Q says does not change IP1 function



### ***Perfusion Drug Treatment Over Small Volume Diffusion Method***

Since the ATP  $\Delta F$  change for Cos-7, and other cell lines, was relatively weaker than other drugs such as 4-cmc and CPA we wanted to investigate different methods of adding the drug as well as increasing concentrations. So, in and we tried three different methods. First, 100  $\mu\text{M}$  ATP small volume addition which is 60  $\mu\text{L}$  of 1.25 mM ATP added on to cells, 200  $\mu\text{M}$  ATP perfusion large volume, and lastly 5 mM perfusion of ATP. There is a low response, around 10-20%, to the small volume 100  $\mu\text{M}$  ATP and a similar response to 200  $\mu\text{M}$  ATP perfusion large volume, but there was a much greater response to 5 mM perfusion of ATP, around 25-30%. In we replaced the 200  $\mu\text{M}$  ATP perfusion with 2.5 mM ATP perfusion, but unfortunately the signal constantly decreases the whole trial telling us the cells were not good and therefore null. The next three dishes were done just with the 100  $\mu\text{M}$  ATP small volume and then with 5 mM ATP perfusion in order to compare the differences between the concentrations (Figure 8.4). Doing this technique, over 10 dishes, we were able to see that the small volume addition of 60  $\mu\text{L}$  of 1.25 mM ATP only caused a release of around 5-15% whereas the 5 mM ATP perfusion led to a 25-35% release. Thus using 0.5-5 mM perfusion would be more ideal for future trials in order to see the release better for analysis and then we would know if the recovery curve was from true change as opposed to a reaction to diffusion of the small volume technique as previously used. This perfusion technique can be used for future cell imaging experiments.

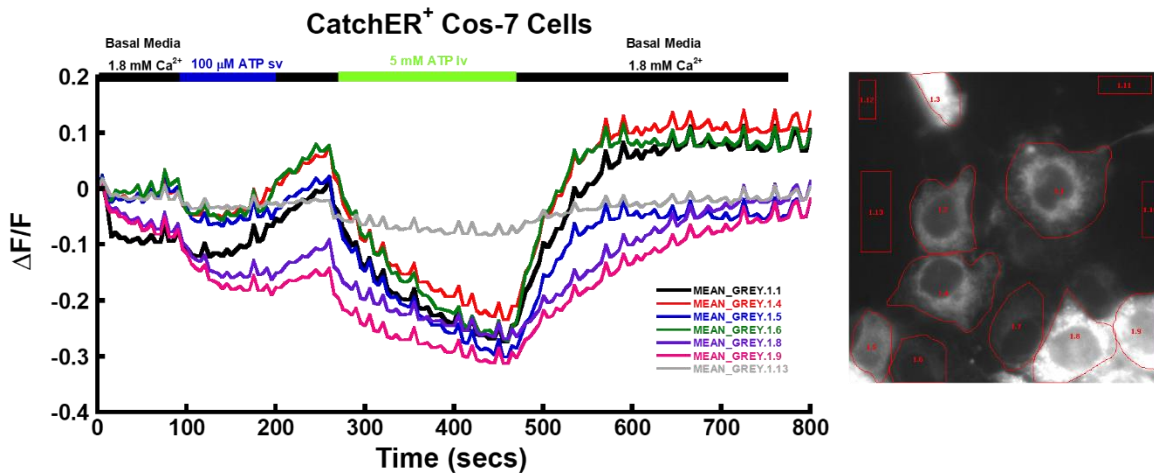


**Figure 8.4 -CatchER<sup>+</sup> in Cos-7 cells small volume versus perfusion systems.** Cos-7 cells transfected with CatchER<sup>+</sup> are treated with 100  $\mu\text{M}$  small volume (sv) ATP at 60  $\mu\text{L}$  of 1.25 mM ATP then washed with buffer. Next the cells are treated with perfusion of 3-5 mL large volume (lv) of 5 mM ATP to mimic the concentrations actually added using sv of  $\geq 1.25$  mM then washed with buffer.

The results were repeated in C2C12 myoblast cells but some of the cells had issues compared to the previous results where they elicited no response, this is probably due to do the perfusion method of 200  $\mu\text{M}$  4-cmc over the small volume method which adds a small amount of higher concentrated compound (2-100  $\mu\text{L}$  of  $\sim 1$ -20 mM) depending on the volume adding and the volume of the chamber estimating the amount being added directly on the cells can be anywhere from 1-20 mM in actuality. This is further confirmed by the fact the doing perfusion large volume method elicited almost no response compared to the concentrated small volume method, for what should be the same ending concentration of 200  $\mu\text{M}$  4-cmc. When the small volume method was returned, we see a typical response of between 15-35% change. Based on our previous epifluorescence test of ATP perfusion concentrations we just need to increase the perfusion concentration to see the same response as the small volume since the actual concentration being added to the cells in much higher before diffusion.

### *Neuron Imaging*

We were able to image one transfected neuron with CatchER<sup>+</sup> and 3 dishes with transfected glial cells. Since we were not initially experienced in identifying neurons, we often accidentally imaged glial cells that we thought were neurons but weren't. The neuron we circled the soma (center) versus dendrites (extended parts) to compare the signaling difference between the two since the ER spans the soma and dendrites but being so far translocated might respond differently. We circled both soma and full dendrites to observe if there were any differences in the ER signaling in the different regions. We did see a difference between the soma and dendrites here, but multiple trials need to be performed with multiple compounds and control to confirm if results are true. Initially we used DHPG an mGluR1/5 agonist which activates ER Ca<sup>2+</sup> release through the IP<sub>3</sub>R, the decrease in response was seen after addition of DHPG with the soma being slower than the dendrites to respond with about a 10-20% release, much higher than what we see for ATP release of around 5-15%.

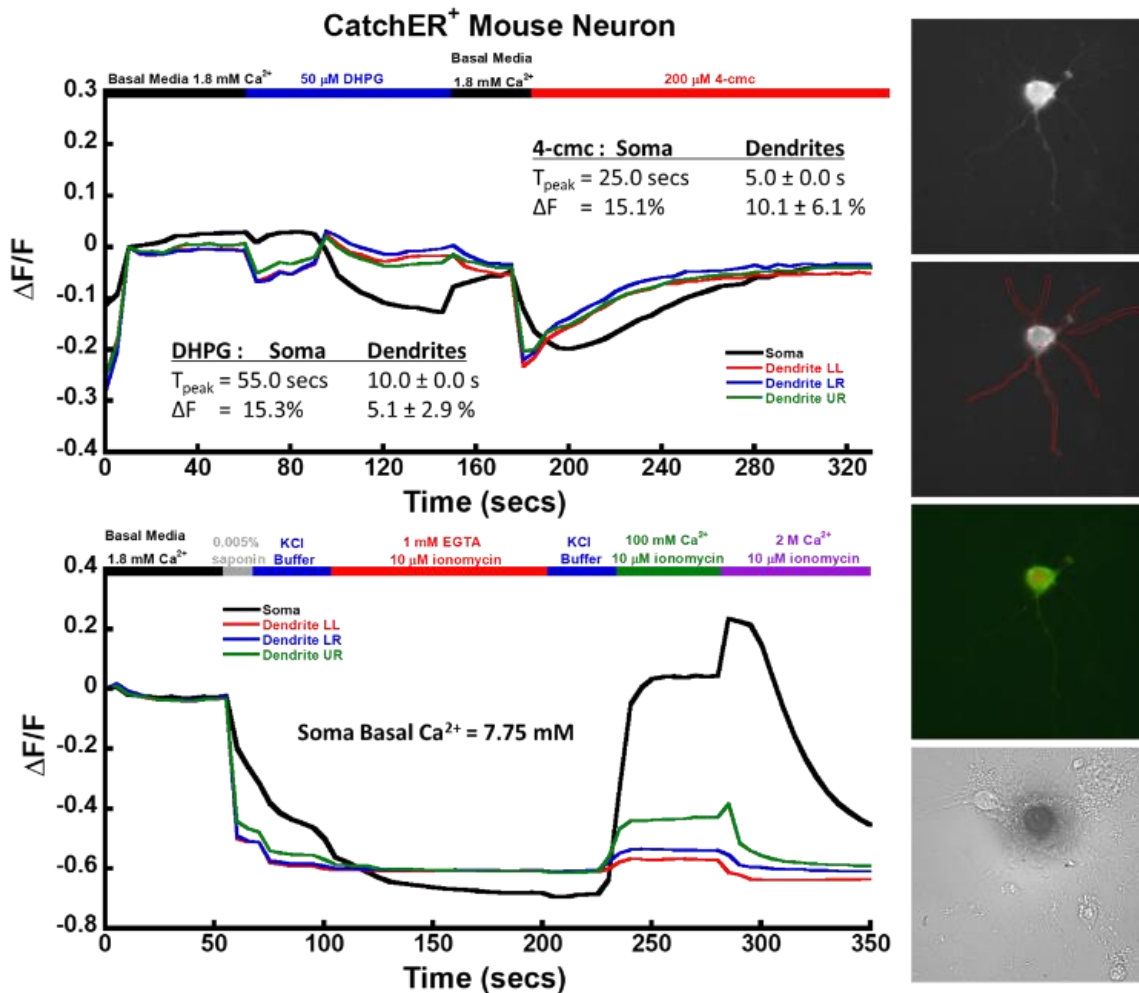


**Figure 8.5 – CatchER<sup>+</sup> in mouse hippocampal neurons.**  
**Top – 50  $\mu$ M DHPG and 200  $\mu$ M of 4-cmc was added to initiate a release of  $Ca^{2+}$  from the ER through the IP<sub>3</sub>R/mGluR1 and RyR, respectively. Bottom – Min/Max of neurons. 0.005% saponin was added to permeabilize the cells, followed by 1 mM EGTA with 10  $\mu$ M ionomycin (min) and 100 mM – 2M  $Ca^{2+}$  with 10  $\mu$ M ionomycin (max). Far Right – Neuron at 488 nm excitation showing CatchER<sup>+</sup>, the same cell showing circles of soma and dendrites, overlay of 550 nm and 488 nm, and then bright field.**

We also tested 4-cmc for comparison to our other CatchER<sup>+</sup> imaging, and then min/max at the end to try and get a basal  $Ca^{2+}$  level for calibration. The 4-cmc response was similar to 4-cmc release in other cell types with around 20-30% release. The soma was able to recover the max signal past the baseline for the min/max experiment while the dendrites were not able to achieve a maximum signal higher than the basal signal indicating a high starting  $Ca^{2+}$  concentration in neurons. The

glial cells responded similarly to other cell lines in response to 4-cmc and min/max, with the basal  $\text{Ca}^{2+}$  levels still being much higher than other cell lines. This could be because the cells were too stressed after 2 drugs and permeabilization to achieve a maximum signal, or it could be because the ER basal  $\text{Ca}^{2+}$  levels in glial cells and neurons are substantially higher. More studies need to be done to confirm.

A second batch of neurons was plated and transfected with CatchER<sup>+</sup> for 9 dishes, and then one dish was transfected with GFP as a control. We decided to do 4 trials with 50  $\mu\text{M}$  DHPG wash and 200  $\mu\text{M}$  4-cmc and the other 5 trials with 15  $\mu\text{M}$  CPA and then 10 mM Caffeine all done in the basal media that the neurons are cultured in to prevent shock of Ringer's buffer.

Unfortunately, this time the soma and dendrites did not respond differentially like in the previous neuron imaging we did. We were able to better identify neurons though, so no glial cells were imaged and only neurons. The response to the 50  $\mu\text{M}$  DHPG was very small and in some cases negligible with the average being 5-10% release (Figure 8.6). 4-cmc release shows a very quick response for release in 0-10 seconds releasing 25-35% (Figure 8.6). Initially, the release of CPA and Caffeine seemed very large, but after subtracting the background there was no change at all.

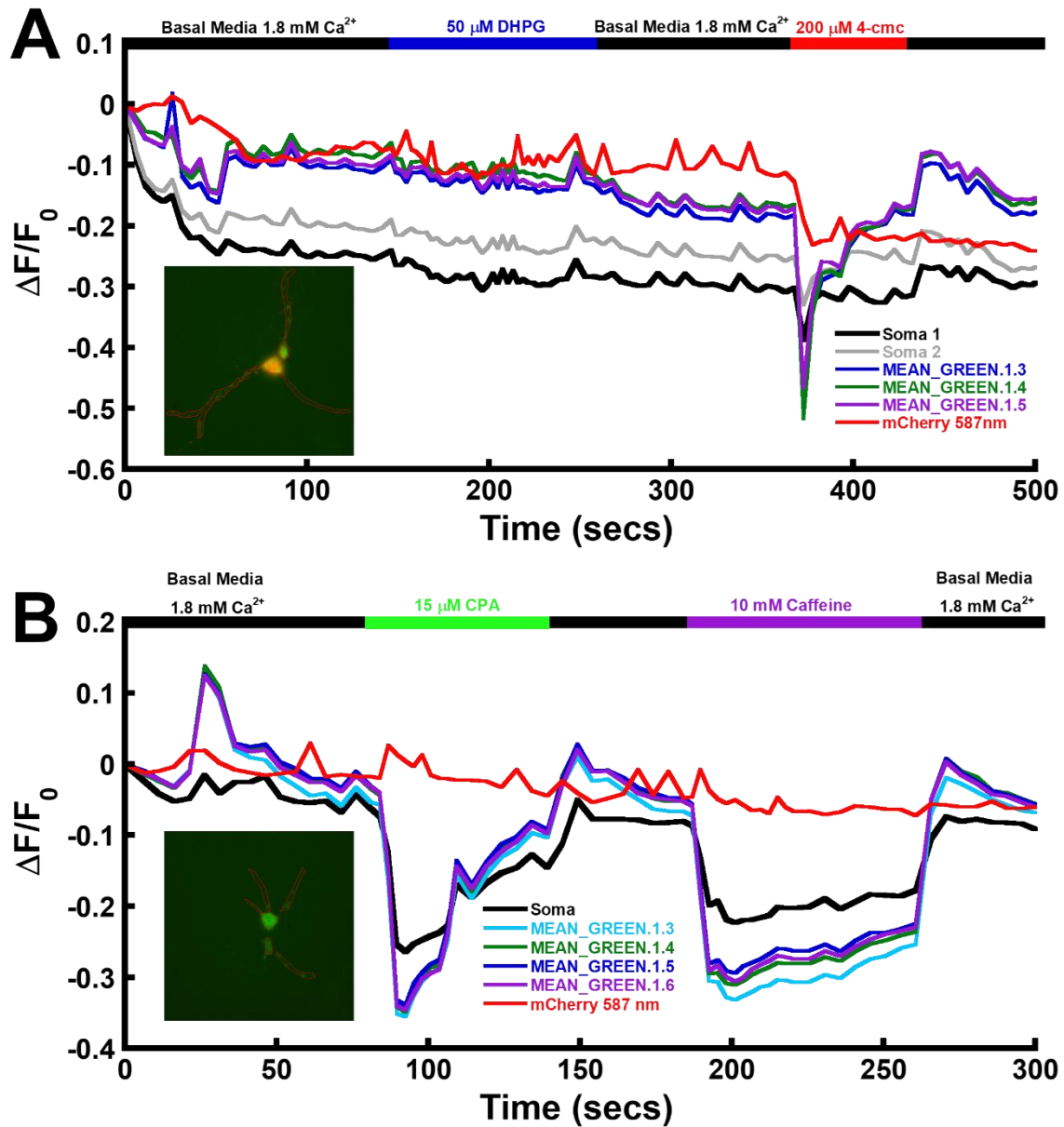


**Figure 8.6 – CatchER<sup>+</sup> in mouse hippocampal neurons.**

**A** – 50 μM DHPG (blue), 200 μM of 4-cmc (red) was added to initiate a release of Ca<sup>2+</sup> from the ER through the IP<sub>3</sub>R/mGluR1 and RyR, respectively. The neurons were washed between with neurobasal medium (black) to equilibrate. **B** – 15 μM CPA (green), and 10 mM Caffeine (purple) was added to initiate a release of Ca<sup>2+</sup> from the ER through inhibiting SERCA pump and activating the IP<sub>3</sub>R/mGluR1, respectively. The neurons were washed between with neurobasal medium (black) to equilibrate.

We noticed when doing the imaging there was a high background coming from the basal media where the background and dendrite fluorescence intensity were both near 20,000 and soma was

40,000-60,000. This led to not being able to visualize the dendrite signal and barely being able to differentiate the soma signal. The GFP transfected neuron was done also with 50  $\mu\text{M}$  DHPG, 200  $\mu\text{M}$  4-cmc, 15  $\mu\text{M}$  CPA, and 10 mM Caffeine in basal media the whole time (Figure 8.7).

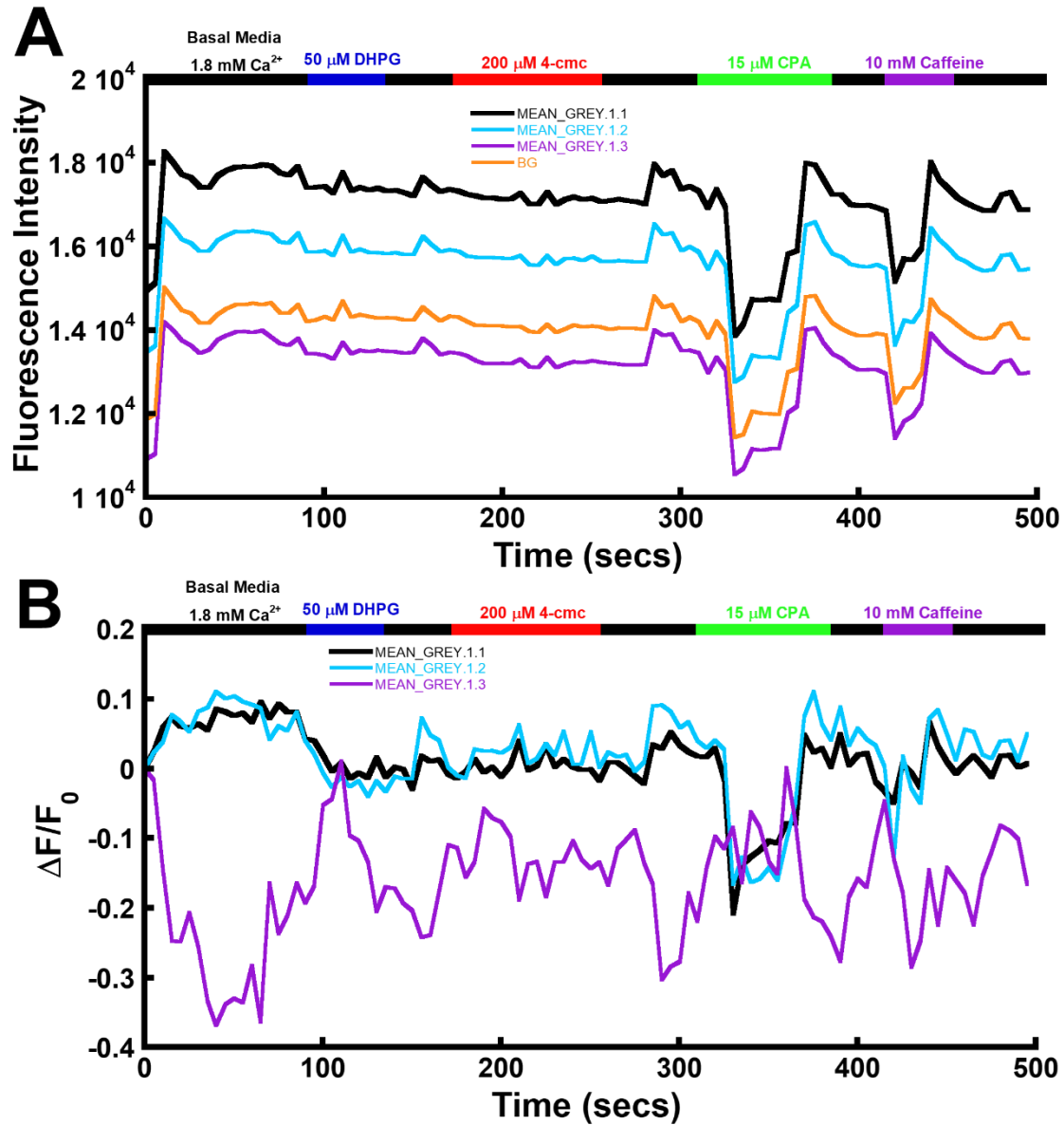


**Figure 8.7 – GFP in mouse hippocampal neurons.**

**A&B –** 50  $\mu\text{M}$  DHPG (blue), 200  $\mu\text{M}$  of 4-cmc (red), 15  $\mu\text{M}$  CPA (green), and 10 mM Caffeine (purple) was added to initiate a release of  $\text{Ca}^{2+}$  from the ER through the  $\text{IP}_3\text{R}/\text{mGluR1}$  and RyR, SERCA pump, and  $\text{IP}_3\text{R}$ , respectively. The neurons were washed between with neurobasal medium (black) to equilibrate. Data is shown as raw (A) or normalized with background signal subtracted (B).

It was during this trial that the background fluorescence was very apparent because while there was no change in fluorescence with DHPG and 4-cmc additions there was a change in fluorescence in CPA and Caffeine responses (Figure 8.7). This led us to see that the basal media was contributing to the background fluorescence and causing false results. This led us to further investigate the reason for this background fluorescence in the basal media (NEUROBASAL medium, ThermoFisher Cat# 21103049) and what buffers others use for cell imaging neurons. We found an article by Samtleben et al. which specifically talking about imaging ER  $Ca^{2+}$  in hippocampal neurons<sup>[413]</sup>. They use a buffer called artificial cerebrospinal fluid buffer (ACSF) for their imaging<sup>[413]</sup>. When we consulted with Dr. Mabb on using this buffer she said that the lab she was in previously had used an ACSF buffer they called E4 (124 mM NaCl, 3 mM KCl, 1.8 mM  $CaCl_2$ , 2 mM  $MgCl_2$ , 10 mM HEPES, 10 mM D-Glucose, pH=7.4). The basal media has many components needed for growth several of which could be contributing to the fluorescence at 488 nm, most notably riboflavin which is excitable at 488 nm (Table 8.6).

**Table 8.6 – Components of NEUROBASAL medium.**

Components	Concentration (mM)
Glycine	0.4
L-Alanine	0.02247191
L-Arginine hydrochloride	0.39810428
L-Asparagine-H <sub>2</sub> O	0.005533333
L-Cysteine	0.2603306
L-Histidine hydrochloride-H <sub>2</sub> O	0.2
L-Isoleucine	0.8015267



L-Leucine	0.8015267
L-Lysine hydrochloride	0.7978142
L-Methionine	0.20134228
L-Phenylalanine	0.4
L-Proline	0.06747826
L-Serine	0.4
L-Threonine	0.79831934
L-Tryptophan	0.078431375
L-Tyrosine	0.39779004
L-Valine	0.8034188
Choline chloride	0.028571429
D-Calcium pantothenate	0.008385744
Folic Acid	0.009070295
Niacinamide	0.032786883
Pyridoxal hydrochloride	0.019607844
Riboflavin	0.00106383
Thiamine hydrochloride	0.011869436
Vitamin B12	5.02E-06
i-Inositol	0.04
Calcium Chloride (CaCl <sub>2</sub> ) (anhyd.)	1.8018018
Ferric Nitrate (Fe(NO <sub>3</sub> ) <sub>3</sub> ·9H <sub>2</sub> O)	2.48E-04
Magnesium Chloride (anhydrous)	0.8136842

Potassium Chloride (KCl)	5.3333335
Sodium Bicarbonate (NaHCO <sub>3</sub> )	26.190475
Sodium Chloride (NaCl)	51.724136
Sodium Phosphate monobasic (NaH <sub>2</sub> PO <sub>4</sub> - H <sub>2</sub> O)	0.9057971
Zinc sulfate (ZnSO <sub>4</sub> -7H <sub>2</sub> O)	6.74E-04
D-Glucose (Dextrose)	25
HEPES	10.92437
Phenol Red	0.021519661
Sodium Pyruvate	0.22727273

Thus, for our next batch we decided to use the ACSF buffer over the neurobasal media for cell imaging to prevent background fluorescence contributing to signal change disturbances. We additionally decided to use an inline buffer heater to heat the ACSF buffer to 37°C so that the temperature change of buffers doesn't also affect the neurons during imaging. We received neurons but unfortunately the plates had no viable individual transfected neurons after an hour of searching so we used an area on the plate which had clumps of cells to test the buffer exchange between neurobasal media and ACSF buffer to make sure the ACSF buffer didn't affect the cell quality and to not waste a dish of neurons for imaging (Figure 8.8). We can see upon addition of the ACSF buffer the background fluorescence decreases dramatically but the cell quality is not affected (Figure 8.8). Thus, we can do our future trials in ACSF without risk to the neurons.

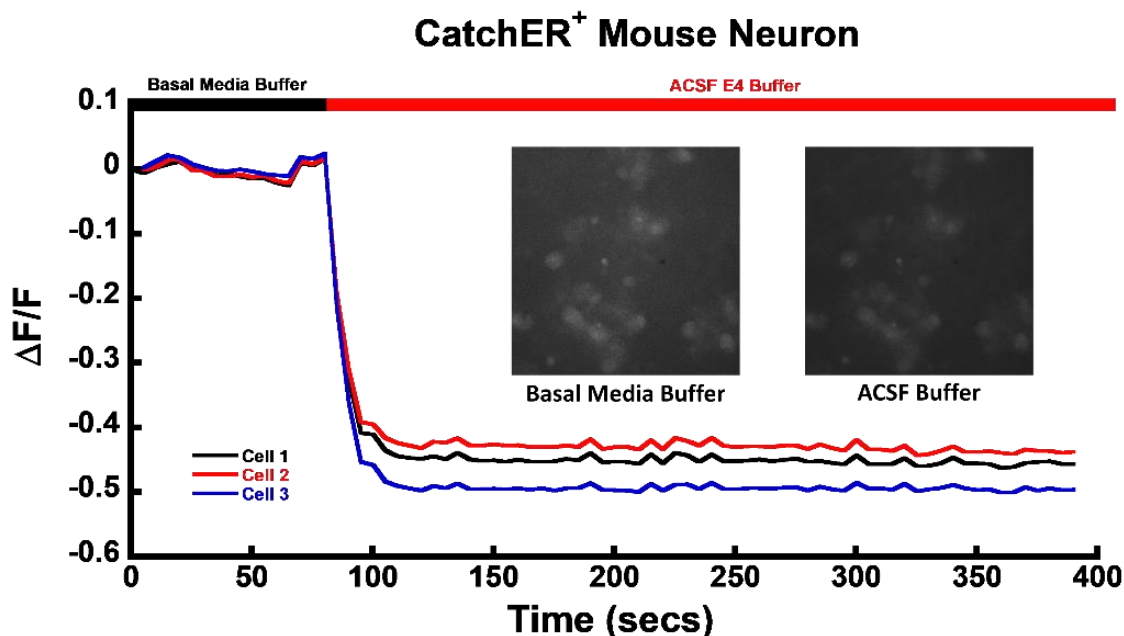


**Figure 8.8 – ACSF buffer on mouse hippocampal neurons.**

An area of neurons transfected with CatchER<sup>+</sup> (insert left) were imaged in neurobasal media and then washed with ACSF buffer leading to a large decrease in fluorescence signal from the removal of background fluorescence in neurobasal media. The decrease in background fluorescence can also be seen in cell image of ACSF buffer (insert right) where the background is notably darker than the neurobasal media.

The next batch of neurons can be successfully done using the inline heater and ACSF buffer so we may get concrete results and push forward on the neuron imaging with CatchER<sup>+</sup>. Simultaneously, the development of the HILO imaging technique on CatchER<sup>+</sup> in other cells types has been thoroughly investigated and perfected opening up the possibility of trying neurons in the HILO imaging methodology. Since neurons present with a vast and dynamic ER structure with differing signaling possibly occurring throughout the neuron body and dendrites the HILO imaging system could help to investigate microdomains of Ca<sup>2+</sup> signaling present.

We were able to see a response to all of the compounds but had a multitude of issues which had to be remedied until the results could be confirmed as accurate. Firstly, the neurobasal media had fluorescent compounds in the media which excited at 488 nm, the same wavelength of CatchER<sup>+</sup>,

and caused high background signal which disrupted the accuracy of the treatment signals. This background fluorescence was corrected by instead utilizing ACSF media for imaging which we showed decreases the fluorescence without disruption to neuron quality. We also used small volume addition of the reagents and buffers instead of utilizing an inline heated perfusion system, so we switched to that methodology for future experiments.

We were able to successfully image hippocampal neurons which were obtained from post-natal mice using our fluorescence ER  $\text{Ca}^{2+}$  sensor, CatchER<sup>+</sup>, in epifluorescence, HILO, confocal, and STORM imaging systems. We initially imaged CatchER<sup>+</sup> in neurons on an epifluorescence 40x Leica microscope in neurobasal media activating the ER response using 200  $\mu\text{M}$  4-cmc to activate the RyR  $\text{Ca}^{2+}$  release, 50  $\mu\text{M}$  DHPG or 10 mM Caffeine to activate mGluR1/5 to indirectly activate the IP<sub>3</sub>R  $\text{Ca}^{2+}$  release, and lastly with 15  $\mu\text{M}$  CPA to inhibit SERCA pump refilling (Figure 8.5-Figure 8.7). We were able to see a response to all of these compounds but had a multitude of issues which had to be remedied until the results could be confirmed as accurate. Firstly, the neurobasal media had fluorescent compounds in the media which excited at 488 nm, the same wavelength of CatchER<sup>+</sup>, and caused high background signal which disrupted the accuracy of the treatment signals (Table 8.6). This background fluorescence was corrected by instead utilizing ACSF media for imaging which we showed decreases the fluorescence without disruption to neuron quality (Figure 8.8). We also used small volume addition of the reagents and buffers instead of utilizing an inline heated perfusion system, so we switched to that methodology for future experiments. Additionally, the resolution of our 40x objective and the overall fluorescence overlap of epifluorescence led us to change to HILO imaging technique with a 100x objective on a Nikon microscope in order to see micro changes throughout the neuron and be able to visualize the soma, dendrites, and dendritic spines accurately.

### *CatchER<sup>+</sup> STORM Imaging in Neurons*

In order to analyze the microdomain area differences we see through our HILO imaging and correlate these differences to protein expression, whether it be ER or PM proteins, we needed to be able to confirm the protein expression in these areas with the signals we are seeing. Ideally, we would want to first image the single neuron on the HILO microscope and then treat the same sample with fixing and antibody staining in order to see the protein expression on that same exact neuron. We are currently optimizing the protocol in order to not only treat the same sample for staining after HILO imaging, but also the best way to find the exact same neuron. In order to implement this eventually optimized procedure we first needed to optimize the best staining and imaging technique to visualize these proteins along the neuron such as mGluR1/5, IP<sub>3</sub>R, RyR and/or CatchER<sup>+</sup>.

We have previously shown the staining and imaging of fixed cells transfected with CatchER<sup>+</sup> using confocal microscopy as well as direct STORM (dSTORM) imaging. Both of these techniques can visualize the protein expression but in order to image staining accurately in smaller regions of interest, such as neuron dendrites and dendritic spines, the dSTORM method will be more accurate since the dSTORM method images based on photon by photon response as opposed to confocal imaging the full fluorescence signal and helps to reduce the background noise over confocal imaging. Currently our STORM imaging can only do one probe at a time, unfortunately, but the system is being improved to include a two-color imaging system. Thus, confocal currently holds the benefit of multicolor imaging but with lower accuracy and resolution, as well as higher S/N ratio of STORM.

Before optimizing the STORM imaging technique for CatchER<sup>+</sup> in other cell types and eventually neurons we began imaging neurons with epifluorescence and confocal imaging (Figure 8.9).

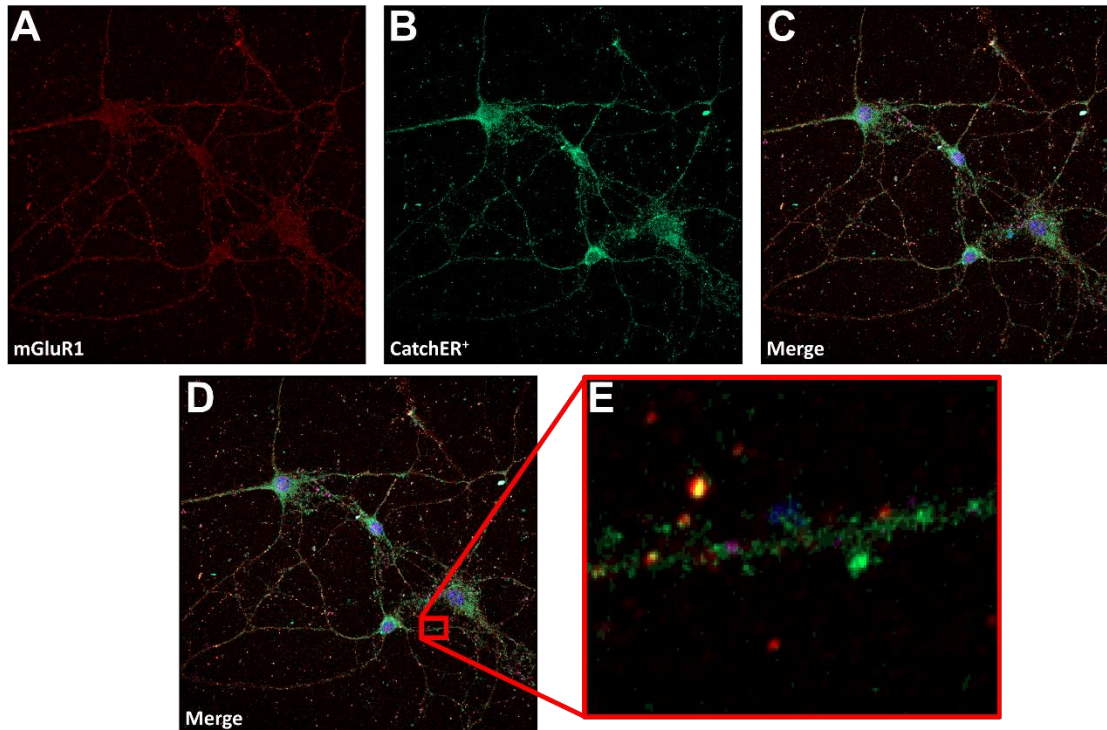


**Figure 8.9 – Confocal imaging of hippocampal neurons with mGluR1 and CatchER<sup>+</sup>. Neurons were transfected with CatchER<sup>+</sup> (B) and stained with mGluR1 antibody (A) and the two signals were merged together (C&D) and then a dendritic region with dendritic spines were enlarged (E) for further in dept visualization.**

As mentioned, we are able to see the neuron soma, dendrites, and dendritic spines but the resolution at the dendritic spine level gets more difficult to discern from background signal. We can see the red staining of mGluR1 (Figure 8.9A), the green color of the CatchER<sup>+</sup> transfected into the neurons (Figure 8.9B) and the merging of these two channels to see the ER signal versus mGluR1 signal (Figure 8.9C&D). We further zoomed in on the merge channel to a region of the dendrite with visible dendritic spines and are able to see one spine has CatchER<sup>+</sup> ER expression and mGluR1 expression seen by the orange color overlap of red and green in Figure 8.9E and further along the

dendrite we see another spine with ER expression but no mGluR1 present. This implies that one of the spines is having mGluR1 and IP<sub>3</sub>R activation present while the other spine has no mGluR1 signaling occurring since there is no expression.

We can see the dendrite and dendritic spines in Figure 8.9E but there are also background mGluR1 staining signal shown by the red points away from the dendrites. These red points could be mGluR1 signal from other neurons not transfected with CatchER<sup>+</sup> but is more likely just background signal. The issue with this background signal is that the red areas are not much smaller than the dendritic spine staining we observed and brings forth the issue of if the red signal seen in Figure 8.9E on the left spine is true signal or background signal.

This is where the advantages of STORM imaging can come into play over confocal imaging. Since STORM imaging is photon by photon signal from photo switchable fluorescence probes with the brighter the photon signal being further from the background and multiple photons measured in the same region over a length of time, we can then eliminate background signal and visualize the true signal versus background signal. This technique would eliminate the possibility of background signal being interpreted as true signal.

We first tested C2C12 cells with CatchER<sup>+</sup> using dSTORM, conjugated secondary antibody in the lab, and the standard STORM fixing protocol which worked seamlessly (Figure 5.21). Therefore, we attempted the same protocol on the next batch of neurons plated on the 18x18 mm slides for STORM imaging and were able to obtain five dishes. We planned to use two dishes for control staining with GFP primary antibody (Figure 8.10) as a control compared to CatchER<sup>+</sup> signal, the next dishes were one each of mGluR1 (Figure 8.11A-C), mGluR5 (Figure 8.11D-F), and IP<sub>3</sub>R (Figure 8.12) primary antibodies.

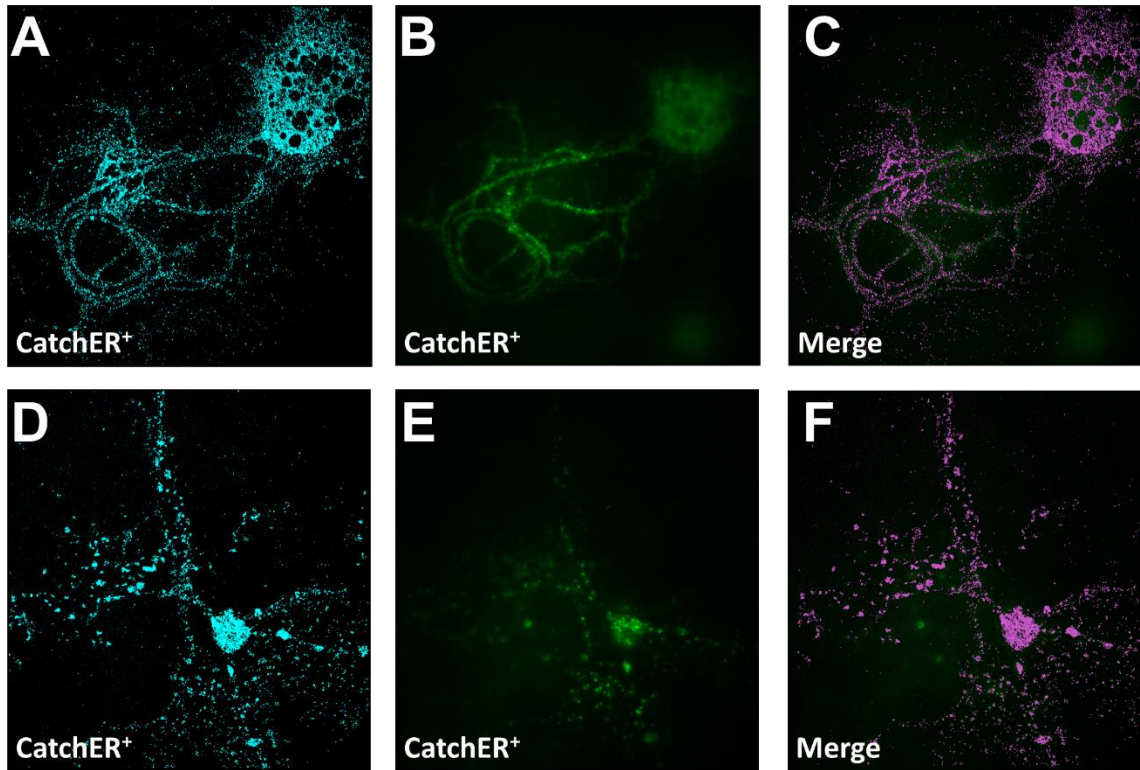


**Figure 8.10 – STORM imaging of mouse hippocampal neurons with CatchER<sup>+</sup>.** Neurons were transfected with CatchER<sup>+</sup> (488 nm, B&E, green) and stained with GFP antibody (647 nm, A&D, blue and magenta). The CatchER<sup>+</sup> signal was first imaged using fluorescence at 488 nm and then the corresponding STORM signal was collected at 647 nm with the merged image (C&F) where 488 nm signal is green, and 647 nm signal is magenta. All samples were done with 647 secondary antibodies conjugated in lab (non-commercial).

The main difference in our CatchER<sup>+</sup> STORM imaging in C2C12 cells versus our first batch of neurons is our permeabilization method in which we utilized 0.005% saponin instead of 0.1% Triton-X100. We first washed each dish with 1 mL of PBS once and then fixed the with 400  $\mu$ L of fixing solution (3% paraformaldehyde (PFA), 0.1% glutaraldehyde (GA) in PBS) at RT for 10 mins, no shaking. The sample is reduced with 2 mL of 0.1% NaBH<sub>4</sub>, prepared immediately before use, and shaking for 7 mins at RT. The sample is then washed 3 times with 1.5 mL of PBS for 7 mins each time while shaking at RT. Before adding antibody, the sample is blocked using 1.5 mL of blocking buffer (3% BSA and 0.1% Triton-X100 (0.005% saponin for neurons)) for 20 mins



while shaking at RT. Then add 1.5 mL of primary antibody (2 ug/mL) in blocking buffer, incubate for 30 mins at RT or O/N at 4°C (while shaking for at least 30 mins). Then wash 3 times with 1.5 mL of washing buffer (0.2% BSA and 0.05% Triton-X100 (no Triton-X100 or saponin for neurons)) for 15 mins each time while shaking at RT.

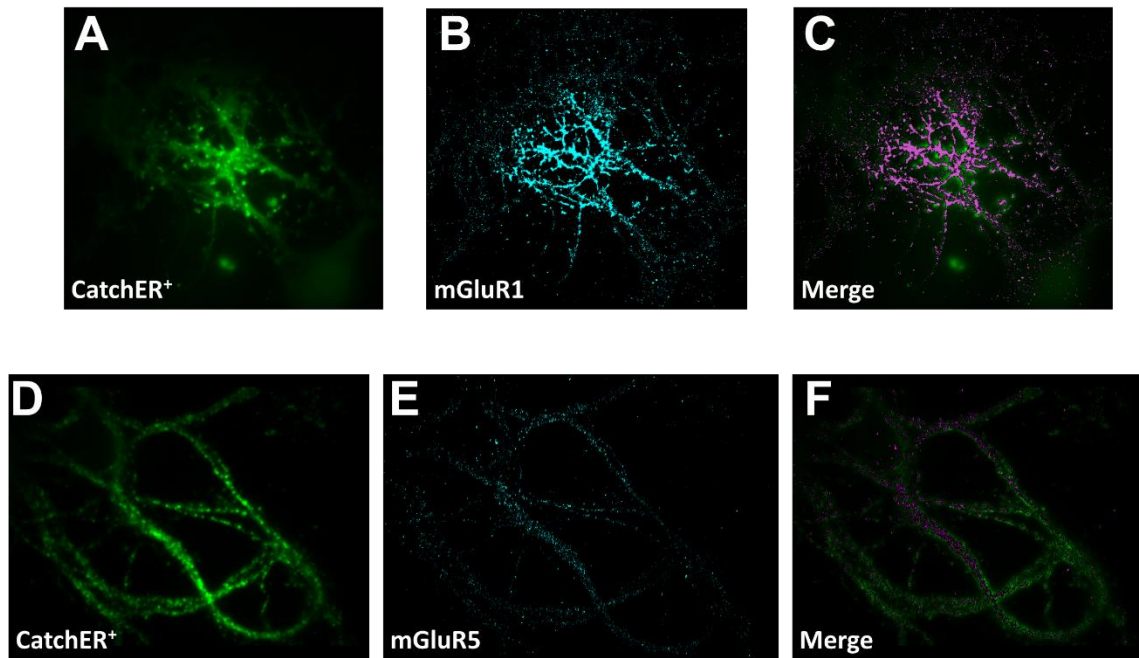


**Figure 8.11 – STORM imaging of neurons with mGluR1/5 and CatchER<sup>+</sup>.** Neurons were transfected with CatchER<sup>+</sup> (488 nm, A&D, green) and stained with either mGluR1 (B&C) or mGluR5 (E&F) antibody (647 nm, blue and magenta). The CatchER<sup>+</sup> signal was first imaged using fluorescence at 488 nm and then the corresponding STORM signal was collected at 647 nm with the merged image (C&F) where 488 nm signal is green, and 647 nm signal is magenta. All samples were done with 647 secondary antibodies conjugated in lab (non-commercial).

Next, add 1.5 mL of secondary antibody (2 ug/mL) dilution in blocking buffer and incubate for 30 mins at RT while shaking and covered with foil to protect fluorophore from light. Wash 3 times with 1.5 mL of washing buffer for 10 mins each time while shaking at RT and covered with foil to protect fluorophore from light. Wash once with 1.5 mL of PBS for 5 mins and covered with foil to protect fluorophore from light.

We saw for the CatchER<sup>+</sup> signal at 488 nm (Figure 8.10A&D) versus the GFP antibody with secondary STORM antibody at 647 nm (Figure 8.10B&E) had almost exact overlap when merged together (Figure 8.10C&F) showing that the STORM technique accurately stains the antibody we are interested in observing. The mGluR1 primary antibody (Figure 8.11B) had a strong STORM signal and when overlapped (Figure 8.11C) with the CatchER<sup>+</sup> 488 nm signal (Figure 8.11A) we can see that the expression of mGluR1 seems to be highly expressed throughout the ER of the neuron. While this data may be the true signal change, we did find it unusual that there would be such high expression.



**Figure 8.12 – STORM imaging of mouse hippocampal neurons with IP<sub>3</sub>R and CatchER<sup>+</sup>.**

Neurons were transfected with CatchER<sup>+</sup> (488 nm, A, green) and stained with IP<sub>3</sub>R antibody (647 nm, B&C, blue and magenta). The CatchER<sup>+</sup> signal was first imaged using fluorescence at 488 nm and then the corresponding STORM signal was collected at 647 nm with the merged image (C) where 488 nm signal is green, and 647 nm signal is magenta. All samples were done with 647 secondary antibodies conjugated in lab (non-commercial).

mGluR5, on the other hand, had much lower expression when stained with primary antibody with the STORM secondary antibody at 647 nm (Figure 8.11E) in comparison to the CatchER<sup>+</sup> 488 nm signal (Figure 8.11D) image and is even more apparent when merged together (Figure 8.11F). Lastly, IP<sub>3</sub>R expression is lower similar to mGluR5 expression (Figure 8.12). The CatchER<sup>+</sup> 488 nm image shows expected ER expression (Figure 8.12A) while the IP<sub>3</sub>R primary antibody with secondary 647 nm antibody (Figure 8.12B) has much lighter expression as seen in the merged

image (Figure 8.12C). These data suggests that the IP<sub>3</sub>R expression is much lower than mGluR1/5 and actually more expressed evenly throughout the dendrites and soma.

The issue we came upon with our first batch of neuronal STORM imaging was that the negative control (not shown) had high background fluorescence for the secondary antibody even though no primary antibody was present. We did not know if this was an issue with our permeabilization method (0.005% saponin) or due to using in lab conjugated secondary antibody as opposed to commercially purchased secondary antibody.

Our STORM imaging of mouse hippocampal post-natal neurons in order to correlate the protein expression on these neurons to the responses we see in the HILO imaging are so far inconclusive. The first batch of STORM imaging were promising but with only a small field of view and only one color of STORM imaging available these results are not very telling in that they show that the mGluR1/5 and IP<sub>3</sub>R proteins are present but without the dual color system as in confocal imaging cannot quantify pertinent information (Figure 8.10-Figure 8.12). The next batch of neurons for STORM was too confluent to see any expression of the antibodies without background disruption and was therefore unsuccessful. Further trials of dual color STORM or confocal imaging need to be performed so we can correlate the protein expression to the signaling response we see in response to compound treatment.

## **Appendix B – ArcKR Neuron Mutation**

Since we have been able to consistently get neuron imaging results using HILO microscopy, ACSF buffer, and CatchER<sup>+</sup> transfected using WT hippocampal neurons then we are perfectly placed to try our methodology on mutant post-natal mouse hippocampal neurons. The activity-regulated cytoskeleton-associated (Arc) protein is thought to be master regulator of synaptic plasticity in the

brain as well as through regulation of endocytosis of AMPA receptors<sup>[414-418]</sup>. Arc protein synthesis dysfunction has been shown to be a factor in such neurological disorders as Alzheimer's disease (AD), autism, amnesia and fragile X syndrome (FXS)<sup>[419]</sup>. mGluR type I activation with DHPG to induce long term depression (LTD) of the neuron synaptic plasticity leads to increase in Arc translation and a decrease in postsynaptic AMPA receptors expression. Therefore, increased levels of Arc could lead to sustained LTD. Arc is degraded by ubiquitination pathway by the K267/268 ubiquitination site, so disruption of the Arc degradation could lead to enhanced sustained LTD upon DHPG activation of mGluR1/5. To test this hypothesis the Mabb lab designed an Arc protein mutation at residues K268/269 to 268R (ArcKR mutant) which disrupts the ubiquitination site on the Arc protein. This ArcKR mutant can be compared to the WT Arc for the effects on disrupted ubiquitination on long term depression effects in hippocampal neurons. We are interested in the effect that this mutant ArcKR will have in response to DHPG activation of mGluR1/5 and ER Ca<sup>2+</sup> signaling differences.

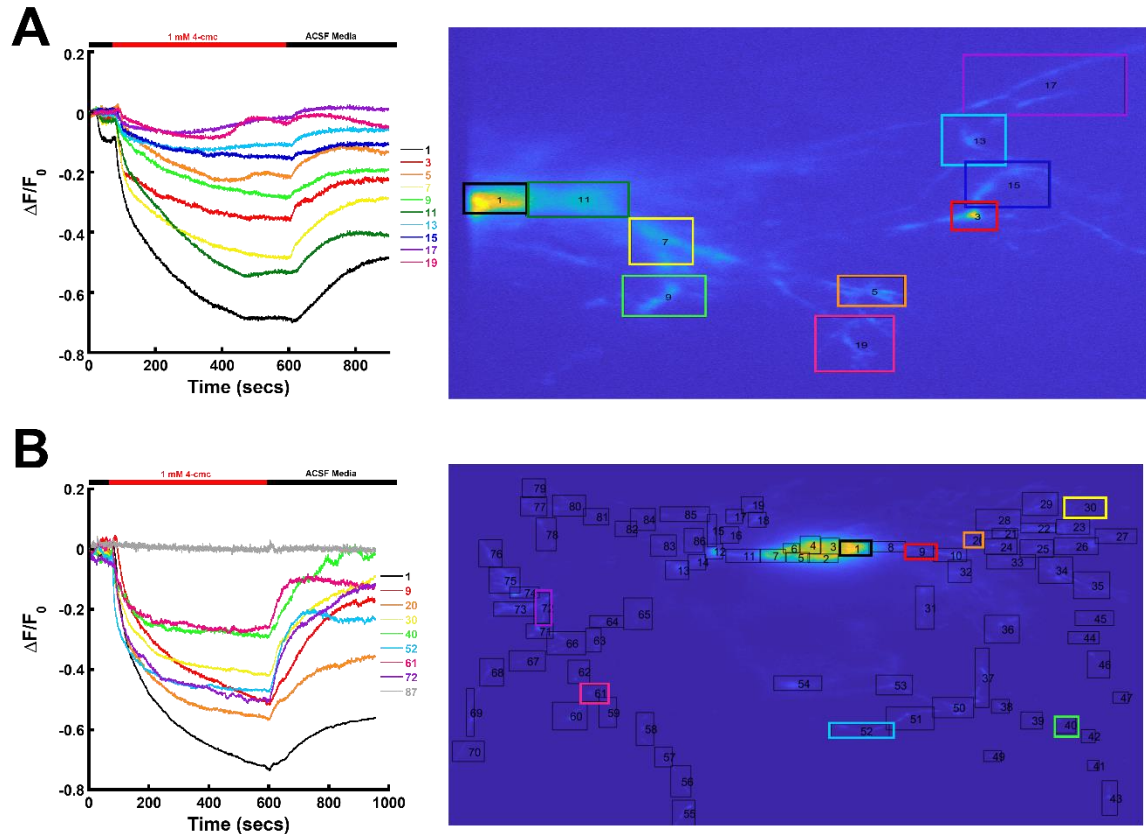


**Figure 8.13 – ArcKR and WT mouse hippocampal neurons 4-cmc responses.** The response to the perfusion of 1 mM 4-cmc is shown through the  $\Delta F/F_0$  plot with a heat map of CatchER<sup>+</sup> transfected into the mouse hippocampal neuron WT (A) and ArcKR mutant (B). The color of the lines correspond with the regions highlighted by boxes in the heat map.

We looked at 5 trials of WT Arc with CatchER<sup>+</sup> with four trials being 100  $\mu$ M DHPG (Figure 8.14) and one trial being 1 mM 4-cmc for a control (Figure 8.13). Then we also investigated 9 trials of ArcKR transfected with CatchER<sup>+</sup> with eight trials being 100  $\mu$ M DHPG (Figure 8.15- Figure 8.16) and one trial being 1 mM 4-cmc for a control of the ER response (Figure 8.13).

The 4-cmc response between the WT and ArcKR mutant were similar with a release between 10-50%, there was a slight difference in the rate of release, the ArcKR mutant seemed to reach a plateau of signal for the lower release (~20%) whereas the WT has a more consistent decrease

without a plateau effect seen (Figure 8.13). More trials need to be done with 4-cmc on the WT and ArcKR mutant on the same conditions and time course to confirm these differences.

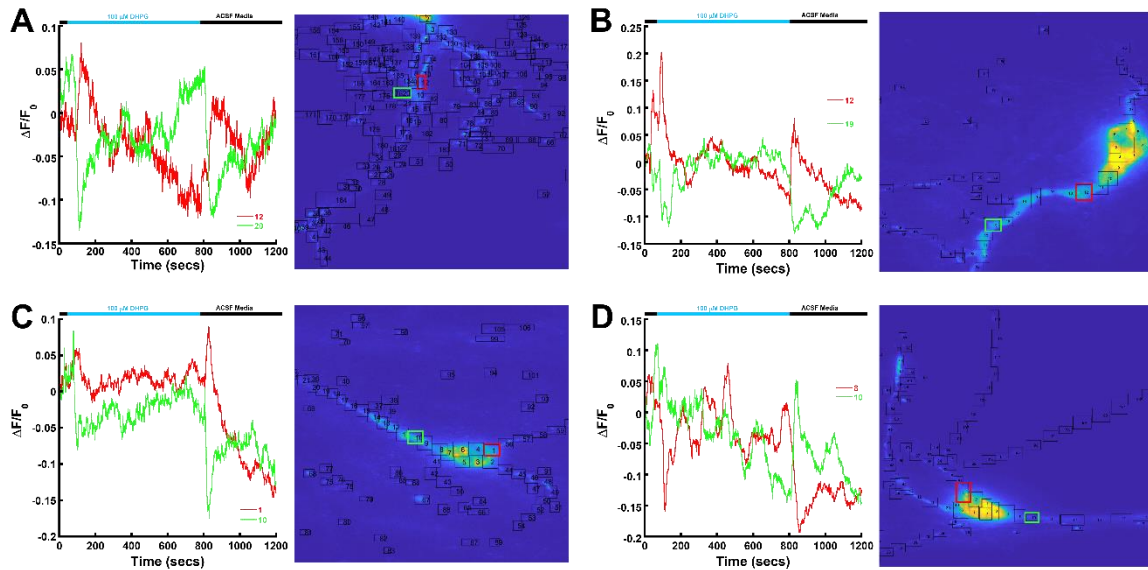


**Figure 8.14 – WT mouse hippocampal neurons DHPG representative responses. A-D – The response to the perfusion of 100  $\mu$ M DHPG is shown through the  $\Delta F/F_0$  plot with a heat map of CatchER<sup>+</sup> transfected into the WT mouse hippocampal neuron. The color of the lines correspond with the regions highlighted by boxes in the heat map.**

WT Arc is what all of our previous neuron trials have been under since WT Arc is naturally occurring in the mouse hippocampal neurons. We still repeated 4 trials of WT with CatchER<sup>+</sup> treated with 100  $\mu$ M DHPG (Figure 8.14) the same day as our ArcKR mutant trials to confirm that any signal differences between WT and ArcKR are directly correlated by the mutant of ArcKR and not because the sample batch of neurons, mice, or CatchER<sup>+</sup> transfection had an effect on the signaling. We see a similar response as we have seen with 100  $\mu$ M DHPG treatments in our past experiments (Figure 8.14). The 100  $\mu$ M DHPG leads to a release in Ca<sup>2+</sup> from the ER, shown by a decrease in the CatchER<sup>+</sup> signal, in a majority of regions of the neuron and that some regions of the neurons actually exhibit an increase in the ER Ca<sup>2+</sup> response implicating an influx of Ca<sup>2+</sup> into the ER (Figure 8.14). Additionally, we again see the effect of the washing with ACSF buffer leads

to the same response as DHPG as previously discussed (Figure 8.14). After the DHPG and wash treatments the WT neurons are able to fully recover in most regions and mostly recover in the others, rarely do we see a neuron, dendrites or dendritic spines have no recovery at all since most have at least a partial recovery (Figure 8.14).

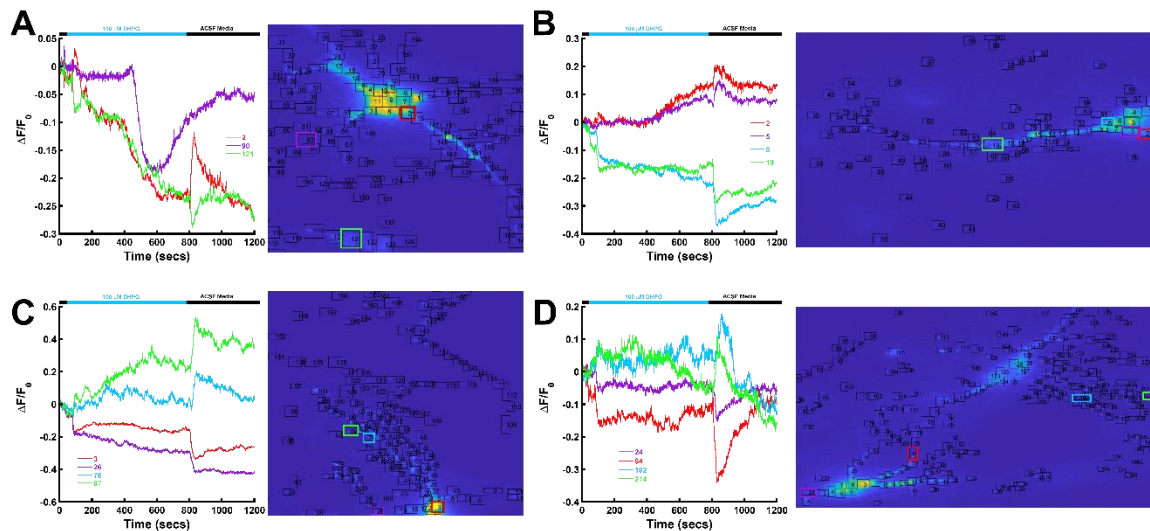


**Figure 8.15 – ArcKR neurons DHPG responses for trials 3, 4, 6, and 8.**

**A-D – The response to the perfusion of 100  $\mu$ M DHPG is shown through the  $\Delta F/F_0$  plot with a heat map of CatchER<sup>+</sup> transfected into the ArcKR mutant mouse hippocampal neuron. The color of the lines correspond with the regions highlighted by boxes in the heat map. Eight trials were done trial 3 (A), 4 (B), 6 (C), 8 (D), 9, and 11-13.**

We did 8 trials of ArcKR mutant mouse hippocampal neurons with CatchER<sup>+</sup> transfection and 100  $\mu$ M DHPG treatment (Figure 8.15-Figure 8.16). Only one of the trials had an obvious out of character response and that was trial 3 (Figure 8.15A) midway through the DHPG treatment when the sample is not being disturbed in any way with buffer or DHPG some regions the neurons saw ~20% curved release similar to what we see with 4-cmc. None of the other 7 trials saw this effect so was probably an issue in this particular dish sample. The video of the experiment shows the issue might be from focus changes although that would hypothetically affect all of the regions and not just a few. Besides this outlier on some regions in trial 3 the rest of the trials were all similar



to each other with some similarities and differences to the WT neurons. The main similarities seen between the WT and ArcKR experiments was, firstly, the trend we see of a release of  $\text{Ca}^{2+}$  from the ER and an uptake of  $\text{Ca}^{2+}$  to the ER in different regions of the neurons and, secondly, the response to DHPG and to ACSF buffer wash (Figure 8.14-Figure 8.16).

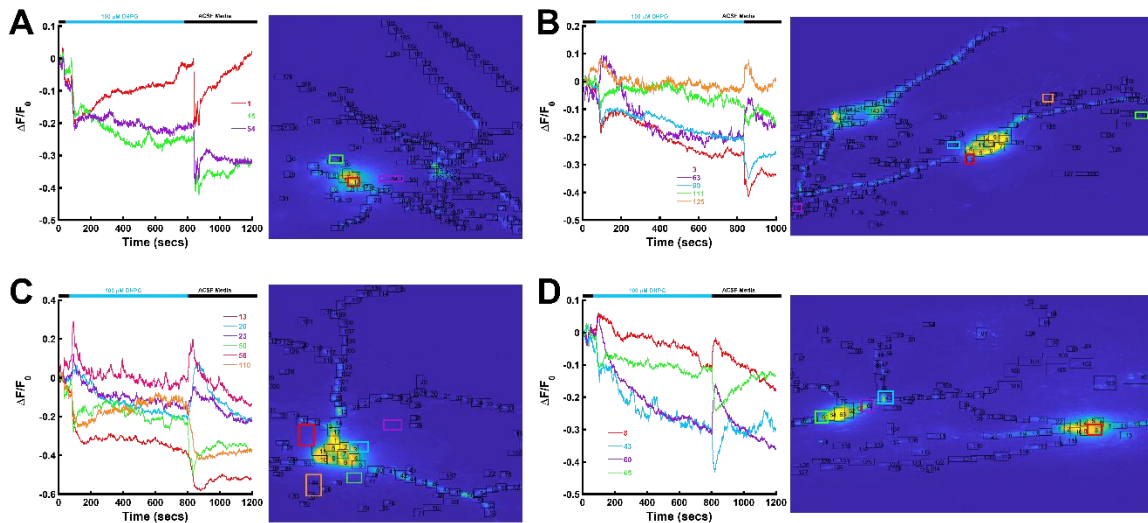


**Figure 8.16 – ArcKR neurons DHPG representative responses for trials 9 and 11-13. A-D – The response to the perfusion of 100  $\mu\text{M}$  DHPG is shown through the  $\Delta\text{F}/\text{F}_0$  plot with a heat map of  $\text{CatchER}^+$  transfected into the ArcKR mutant mouse hippocampal neuron. The color of the lines correspond with the regions highlighted by boxes in the heat map. Eight trials were done trial 3, 4, 6, 8, 9 (A), 11 (B), 12 (D), and 13 (C).**

The most striking response difference was the lack of recovery in the ArcKR mutant neurons in compared to the WT neurons (Figure 8.15-Figure 8.16). Where the WT neurons had a complete or mostly complete recovery to the baseline after DHPG treatment, the ArcKR neurons only saw a very minor recovery or a complete plateau with little to no recovery of signal. Then when the ACSF buffer was added to wash away the DHPG the neurons were much more differential with some of the washes having recovery to the DHPG plateau before wash or some also having little to no recovery and leading to another signal plateau (Figure 8.15-Figure 8.16). Additionally, many of the trials had a progressive overall decrease in signal throughout the whole experiment, this



trend is generally not seen for the WT neurons which mostly stay flat in comparison (Figure 8.14- Figure 8.16).

Further research needs to be done on mutant hippocampal neurons of interest in comparison to the WT using CatchER<sup>+</sup> with 50  $\mu$ M and 100  $\mu$ M DHPG, 4-cmc, and CPA to confirm that the DHPG mediated mGluR1/5 activation is the cause of upregulation of Arc transcription as well as the cause of LTD. CPA and 4-cmc can show that the ER release is not effected by Arc except from the DHPG activation of mGluR1/5.

## REFERENCES

1. Berridge, M.J., M.D. Bootman, and P. Lipp, *Calcium--a life and death signal*. Nature, 1998. **395**(6703): p. 645-8.
2. Carafoli, E. and J. Krebs, *Why Calcium? How Calcium Became the Best Communicator*. J Biol Chem, 2016. **291**(40): p. 20849-20857.
3. Permyakov, E. and R.H. Kretsinger, *Calcium Binding Proteins*. 2011, Hoboken, UNITED STATES: John Wiley & Sons, Incorporated.
4. Jimenez-Moreno, R., et al., *Sarcoplasmic reticulum Ca(2+) depletion in adult skeletal muscle fibres measured with the biosensor DIER*. Pflugers Archiv-European Journal of Physiology, 2010. **459**(5): p. 725-735.
5. Ryu, S.Y., et al., *Mitochondrial ryanodine receptors and other mitochondrial Ca(2+) permeable channels*. Febs Letters, 2010. **584**(10): p. 1948-1955.
6. Santo-Domingo, J. and N. Demaurex, *Calcium uptake mechanisms of mitochondria*. Biochimica Et Biophysica Acta-Bioenergetics, 2010. **1797**(6-7): p. 907-912.
7. Bhattacharya, S., C.G. Bunick, and W.J. Chazin, *Target selectivity in EF-hand calcium binding proteins*. Biochimica Et Biophysica Acta-Molecular Cell Research, 2004. **1742**(1-3): p. 69-79.
8. Berridge, M.J., *Elementary and global aspects of calcium signalling*. Journal of Experimental Biology, 1997. **200**(2): p. 315-319.
9. Marx, S.O., et al., *PKA phosphorylation dissociates FKBP12.6 from the calcium release channel (ryanodine receptor): Defective regulation in failing hearts*. Cell, 2000. **101**(4): p. 365-376.
10. Betzenhauser, M.J. and A.R. Marks, *Ryanodine receptor channelopathies*. Pflugers Archiv-European Journal of Physiology, 2010. **460**(2): p. 467-480.
11. Brini, M., et al., *Calcium in health and disease*. Met Ions Life Sci, 2013. **13**: p. 81-137.
12. Kretsinger, R.H., *Calcium-binding proteins*. Annu Rev Biochem, 1976. **45**: p. 239-66.
13. Kawasaki, H. and R.H. Kretsinger, *Structural and functional diversity of EF-hand proteins: Evolutionary perspectives*. Protein Sci, 2017. **26**(10): p. 1898-1920.
14. Chazin, W.J., *Relating form and function of EF-hand calcium binding proteins*. Acc Chem Res, 2011. **44**(3): p. 171-9.
15. Gerke, V. and S.E. Moss, *Annexins: from structure to function*. Physiol Rev, 2002. **82**(2): p. 331-71.
16. Bjarnadottir, T.K., et al., *Comprehensive repertoire and phylogenetic analysis of the G protein-coupled receptors in human and mouse*. Genomics, 2006. **88**(3): p. 263-73.
17. Mombaerts, P., *Genes and ligands for odorant, vomeronasal and taste receptors*. Nat Rev Neurosci, 2004. **5**(4): p. 263-78.
18. Joost, P. and A. Methner, *Phylogenetic analysis of 277 human G-protein-coupled receptors as a tool for the prediction of orphan receptor ligands*. Genome Biol, 2002. **3**(11): p. RESEARCH0063.
19. Harmar, A.J., *Family-B G-protein-coupled receptors*. Genome Biol, 2001. **2**(12): p. REVIEWS3013.
20. Brauner-Osborne, H., P. Wellendorph, and A.A. Jensen, *Structure, pharmacology and therapeutic prospects of family C G-protein coupled receptors*. Curr Drug Targets, 2007. **8**(1): p. 169-84.

21. Brown, E.M., M. Pollak, and S.C. Hebert, *The extracellular calcium-sensing receptor: its role in health and disease*. *Annu Rev Med*, 1998. **49**: p. 15-29.
22. Brown, E.M., et al., *Cloning and characterization of an extracellular Ca(2+)-sensing receptor from bovine parathyroid*. *Nature*, 1993. **366**(6455): p. 575-80.
23. Zhang, C., et al., *Identification of an L-phenylalanine binding site enhancing the cooperative responses of the calcium-sensing receptor to calcium*. *J Biol Chem*, 2014. **289**(8): p. 5296-309.
24. Zhang, C., et al., *Role of Ca<sup>2+</sup> and L-Phe in regulating functional cooperativity of disease-associated "toggle" calcium-sensing receptor mutations*. *PLoS One*, 2014. **9**(11): p. e113622.
25. Parekh, A.B., *Decoding cytosolic Ca<sup>2+</sup> oscillations*. *Trends Biochem Sci*, 2011. **36**(2): p. 78-87.
26. Pinto, M.C., et al., *Studying complex system: calcium oscillations as attractor of cell differentiation*. *Integr Biol (Camb)*, 2016. **8**(2): p. 130-48.
27. Smedler, E. and P. Uhlen, *Frequency decoding of calcium oscillations*. *Biochim Biophys Acta*, 2014. **1840**(3): p. 964-9.
28. Uhlen, P. and N. Fritz, *Biochemistry of calcium oscillations*. *Biochem Biophys Res Commun*, 2010. **396**(1): p. 28-32.
29. Wettschureck, N. and S. Offermanns, *Mammalian G proteins and their cell type specific functions*. *Physiol Rev*, 2005. **85**(4): p. 1159-204.
30. Martin, C., et al., *Partial cloning and differential expression of ryanodine receptor/calcium-release channel genes in human tissues including the hippocampus and cerebellum*. *Neuroscience*, 1998. **85**(1): p. 205-16.
31. Awad, S.S., et al., *Differential expression of ryanodine receptor Ryr2 mRNA in the non-pregnant and pregnant human myometrium*. *Biochem J*, 1997. **322** ( Pt 3): p. 777-83.
32. Nakashima, Y., et al., *Molecular cloning and characterization of a human brain ryanodine receptor*. *FEBS Lett*, 1997. **417**(1): p. 157-62.
33. Zhang, Y., et al., *Characterization of cDNA and genomic DNA encoding SERCA1, the Ca(2+)-ATPase of human fast-twitch skeletal muscle sarcoplasmic reticulum, and its elimination as a candidate gene for Brody disease*. *Genomics*, 1995. **30**(3): p. 415-24.
34. Brandl, C.J., et al., *Adult forms of the Ca<sup>2+</sup>ATPase of sarcoplasmic reticulum. Expression in developing skeletal muscle*. *J Biol Chem*, 1987. **262**(8): p. 3768-74.
35. Brandl, C.J., et al., *Two Ca<sup>2+</sup> ATPase genes: homologies and mechanistic implications of deduced amino acid sequences*. *Cell*, 1986. **44**(4): p. 597-607.
36. Dally, S., et al., *Ca<sup>2+</sup>-ATPases in non-failing and failing heart: evidence for a novel cardiac sarco/endoplasmic reticulum Ca<sup>2+</sup>-ATPase 2 isoform (SERCA2c)*. *Biochem J*, 2006. **395**(2): p. 249-58.
37. Gelebart, P., et al., *Identification of a new SERCA2 splice variant regulated during monocytic differentiation*. *Biochem Biophys Res Commun*, 2003. **303**(2): p. 676-84.
38. Ruiz-Perez, V.L., et al., *ATP2A2 mutations in Darier's disease: variant cutaneous phenotypes are associated with missense mutations, but neuropsychiatric features are independent of mutation class*. *Hum Mol Genet*, 1999. **8**(9): p. 1621-30.
39. MacLennan, D.H., et al., *Amino-acid sequence of a Ca<sup>2+</sup> + Mg<sup>2+</sup>-dependent ATPase from rabbit muscle sarcoplasmic reticulum, deduced from its complementary DNA sequence*. *Nature*, 1985. **316**(6030): p. 696-700.

40. Zarain-Herzberg, A., D.H. MacLennan, and M. Periasamy, *Characterization of rabbit cardiac sarco(endo)plasmic reticulum Ca<sup>2+</sup>(+)-ATPase gene*. J Biol Chem, 1990. **265**(8): p. 4670-7.
41. de la Bastie, D., et al., *Function of the sarcoplasmic reticulum and expression of its Ca<sup>2+</sup>(+)-ATPase gene in pressure overload-induced cardiac hypertrophy in the rat*. Circ Res, 1990. **66**(2): p. 554-64.
42. Guntjeski-Hamblin, A.M., J. Greeb, and G.E. Shull, *A novel Ca<sup>2+</sup> pump expressed in brain, kidney, and stomach is encoded by an alternative transcript of the slow-twitch muscle sarcoplasmic reticulum Ca-ATPase gene. Identification of cDNAs encoding Ca<sup>2+</sup> and other cation-transporting ATPases using an oligonucleotide probe derived from the ATP-binding site*. J Biol Chem, 1988. **263**(29): p. 15032-40.
43. Lytton, J. and D.H. MacLennan, *Molecular cloning of cDNAs from human kidney coding for two alternatively spliced products of the cardiac Ca<sup>2+</sup>-ATPase gene*. J Biol Chem, 1988. **263**(29): p. 15024-31.
44. Martin, V., et al., *Three novel sarco/endoplasmic reticulum Ca<sup>2+</sup>-ATPase (SERCA) 3 isoforms. Expression, regulation, and function of the membranes of the SERCA3 family*. J Biol Chem, 2002. **277**(27): p. 24442-52.
45. Bobe, R., et al., *Identification, expression, function, and localization of a novel (sixth) isoform of the human sarco/endoplasmic reticulum Ca<sup>2+</sup>ATPase 3 gene*. J Biol Chem, 2004. **279**(23): p. 24297-306.
46. Burk, S.E., et al., *cDNA cloning, functional expression, and mRNA tissue distribution of a third organellar Ca<sup>2+</sup> pump*. J Biol Chem, 1989. **264**(31): p. 18561-8.
47. Wuytack, F., et al., *A sarco/endoplasmic reticulum Ca(2+)-ATPase 3-type Ca<sup>2+</sup> pump is expressed in platelets, in lymphoid cells, and in mast cells*. J Biol Chem, 1994. **269**(2): p. 1410-6.
48. Wuytack, F., et al., *The SERCA3-type of organellar Ca<sup>2+</sup> pumps*. Biosci Rep, 1995. **15**(5): p. 299-306.
49. Bobe, R., et al., *The rat platelet 97-kDa Ca<sup>2+</sup>ATPase isoform is the sarcoendoplasmic reticulum Ca<sup>2+</sup>ATPase 3 protein*. J Biol Chem, 1994. **269**(2): p. 1417-24.
50. Bobe, R., et al., *How many Ca(2)+ATPase isoforms are expressed in a cell type? A growing family of membrane proteins illustrated by studies in platelets*. Platelets, 2005. **16**(3-4): p. 133-50.
51. Brandom, B.W., et al., *Ryanodine receptor type 1 gene variants in the malignant hyperthermia-susceptible population of the United States*. Anesth Analg, 2013. **116**(5): p. 1078-86.
52. Davis, M., et al., *Malignant hyperthermia associated with exercise-induced rhabdomyolysis or congenital abnormalities and a novel RYR1 mutation in New Zealand and Australian pedigrees*. Br J Anaesth, 2002. **88**(4): p. 508-15.
53. Galli, L., et al., *Mutations in the RYR1 gene in Italian patients at risk for malignant hyperthermia: evidence for a cluster of novel mutations in the C-terminal region*. Cell Calcium, 2002. **32**(3): p. 143-51.
54. Gillard, E.F., et al., *Polymorphisms and deduced amino acid substitutions in the coding sequence of the ryanodine receptor (RYR1) gene in individuals with malignant hyperthermia*. Genomics, 1992. **13**(4): p. 1247-54.

55. Kim, J.H., et al., *Exome sequencing reveals novel rare variants in the ryanodine receptor and calcium channel genes in malignant hyperthermia families*. *Anesthesiology*, 2013. **119**(5): p. 1054-65.
56. Levano, S., et al., *Increasing the number of diagnostic mutations in malignant hyperthermia*. *Hum Mutat*, 2009. **30**(4): p. 590-8.
57. Loke, J.C., et al., *Detection of a novel ryanodine receptor subtype 1 mutation (R328W) in a malignant hyperthermia family by sequencing of a leukocyte transcript*. *Anesthesiology*, 2003. **99**(2): p. 297-302.
58. Lynch, P.J., et al., *Identification of heterozygous and homozygous individuals with the novel RYR1 mutation Cys35Arg in a large kindred*. *Anesthesiology*, 1997. **86**(3): p. 620-6.
59. Manning, B.M., et al., *Identification of novel mutations in the ryanodine-receptor gene (RYR1) in malignant hyperthermia: genotype-phenotype correlation*. *Am J Hum Genet*, 1998. **62**(3): p. 599-609.
60. Monnier, N., et al., *Correlations between genotype and pharmacological, histological, functional, and clinical phenotypes in malignant hyperthermia susceptibility*. *Hum Mutat*, 2005. **26**(5): p. 413-25.
61. Monnier, N., et al., *Presence of two different genetic traits in malignant hyperthermia families: implication for genetic analysis, diagnosis, and incidence of malignant hyperthermia susceptibility*. *Anesthesiology*, 2002. **97**(5): p. 1067-74.
62. Murayama, T., et al., *Divergent Activity Profiles of Type I Ryanodine Receptor Channels Carrying Malignant Hyperthermia and Central Core Disease Mutations in the Amino-Terminal Region*. *PLoS One*, 2015. **10**(6): p. e0130606.
63. Quane, K.A., et al., *Detection of a novel mutation at amino acid position 614 in the ryanodine receptor in malignant hyperthermia*. *Br J Anaesth*, 1997. **79**(3): p. 332-7.
64. Rueffert, H., et al., *Identification of a novel mutation in the ryanodine receptor gene (RYR1) in patients with malignant hyperthermia*. *Hum Mutat*, 2001. **17**(3): p. 238.
65. Rueffert, H., et al., *Mutation screening in the ryanodine receptor 1 gene (RYR1) in patients susceptible to malignant hyperthermia who show definite IVCT results: identification of three novel mutations*. *Acta Anaesthesiol Scand*, 2002. **46**(6): p. 692-8.
66. Sambuughin, N., et al., *North American malignant hyperthermia population: screening of the ryanodine receptor gene and identification of novel mutations*. *Anesthesiology*, 2001. **95**(3): p. 594-9.
67. Sei, Y., et al., *Malignant hyperthermia in North America: genetic screening of the three hot spots in the type I ryanodine receptor gene*. *Anesthesiology*, 2004. **101**(4): p. 824-30.
68. Tammaro, A., et al., *Novel missense mutations and unexpected multiple changes of RYR1 gene in 75 malignant hyperthermia families*. *Clin Genet*, 2011. **79**(5): p. 438-47.
69. Vukcevic, M., et al., *Functional properties of RYR1 mutations identified in Swedish patients with malignant hyperthermia and central core disease*. *Anesth Analg*, 2010. **111**(1): p. 185-90.
70. Gillard, E.F., et al., *A substitution of cysteine for arginine 614 in the ryanodine receptor is potentially causative of human malignant hyperthermia*. *Genomics*, 1991. **11**(3): p. 751-5.
71. Moroni, I., et al., *Ryanodine receptor gene point mutation and malignant hyperthermia susceptibility*. *J Neurol*, 1995. **242**(3): p. 127-33.
72. Quane, K.A., et al., *Mutations in the ryanodine receptor gene in central core disease and malignant hyperthermia*. *Nat Genet*, 1993. **5**(1): p. 51-5.

73. Keating, K.E., et al., *Detection of a novel RYR1 mutation in four malignant hyperthermia pedigrees*. Hum Mol Genet, 1994. **3**(10): p. 1855-8.
74. Phillips, M.S., et al., *The substitution of Arg for Gly2433 in the human skeletal muscle ryanodine receptor is associated with malignant hyperthermia*. Hum Mol Genet, 1994. **3**(12): p. 2181-6.
75. Quane, K.A., et al., *Detection of a novel common mutation in the ryanodine receptor gene in malignant hyperthermia: implications for diagnosis and heterogeneity studies*. Hum Mol Genet, 1994. **3**(3): p. 471-6.
76. Keating, K.E., et al., *Detection of a novel mutation in the ryanodine receptor gene in an Irish malignant hyperthermia pedigree: correlation of the IVCT response with the affected and unaffected haplotypes*. J Med Genet, 1997. **34**(4): p. 291-6.
77. Manning, B.M., et al., *Novel mutations at a CpG dinucleotide in the ryanodine receptor in malignant hyperthermia*. Hum Mutat, 1998. **11**(1): p. 45-50.
78. Brandt, A., et al., *Screening of the ryanodine receptor gene in 105 malignant hyperthermia families: novel mutations and concordance with the in vitro contracture test*. Hum Mol Genet, 1999. **8**(11): p. 2055-62.
79. Barone, V., et al., *Mutation screening of the RYR1 gene and identification of two novel mutations in Italian malignant hyperthermia families*. J Med Genet, 1999. **36**(2): p. 115-8.
80. Chamley, D., et al., *Malignant hyperthermia in infancy and identification of novel RYR1 mutation*. Br J Anaesth, 2000. **84**(4): p. 500-4.
81. Brown, R.L., et al., *A novel ryanodine receptor mutation and genotype-phenotype correlation in a large malignant hyperthermia New Zealand Maori pedigree*. Hum Mol Genet, 2000. **9**(10): p. 1515-24.
82. Gencik, M., et al., *Novel mutation in the RYR1 gene (R2454C) in a patient with malignant hyperthermia*. Hum Mutat, 2000. **15**(1): p. 122.
83. Sambuughin, N., et al., *Single-amino-acid deletion in the RYR1 gene, associated with malignant hyperthermia susceptibility and unusual contraction phenotype*. Am J Hum Genet, 2001. **69**(1): p. 204-8.
84. Sambuughin, N., et al., *Identification and functional characterization of a novel ryanodine receptor mutation causing malignant hyperthermia in North American and South American families*. Neuromuscul Disord, 2001. **11**(6-7): p. 530-7.
85. McWilliams, S., et al., *Novel skeletal muscle ryanodine receptor mutation in a large Brazilian family with malignant hyperthermia*. Clin Genet, 2002. **62**(1): p. 80-3.
86. Oyamada, H., et al., *Novel mutations in C-terminal channel region of the ryanodine receptor in malignant hyperthermia patients*. Jpn J Pharmacol, 2002. **88**(2): p. 159-66.
87. Tamaro, A., et al., *Scanning for mutations of the ryanodine receptor (RYR1) gene by denaturing HPLC: detection of three novel malignant hyperthermia alleles*. Clin Chem, 2003. **49**(5): p. 761-8.
88. Guis, S., et al., *Multiminicore disease in a family susceptible to malignant hyperthermia: histology, in vitro contracture tests, and genetic characterization*. Arch Neurol, 2004. **61**(1): p. 106-13.
89. Shepherd, S., et al., *RYR1 mutations in UK central core disease patients: more than just the C-terminal transmembrane region of the RYR1 gene*. J Med Genet, 2004. **41**(3): p. e33.
90. Marchant, C.L., et al., *Mutation analysis of two patients with hypokalemic periodic paralysis and suspected malignant hyperthermia*. Muscle Nerve, 2004. **30**(1): p. 114-7.

91. Migita, T., et al., *Functional analysis of ryanodine receptor type 1 p.R2508C mutation in exon 47*. J Anesth, 2009. **23**(3): p. 341-6.
92. Miyoshi, H., et al., *Several Ryanodine Receptor Type 1 Gene Mutations of p.Arg2508 Are Potential Sources of Malignant Hyperthermia*. Anesth Analg, 2015. **121**(4): p. 994-1000.
93. Murayama, T., et al., *Genotype-Phenotype Correlations of Malignant Hyperthermia and Central Core Disease Mutations in the Central Region of the RYR1 Channel*. Hum Mutat, 2016. **37**(11): p. 1231-1241.
94. Johannsen, S., et al., *Functional characterization of the RYR1 mutation p.Arg4737Trp associated with susceptibility to malignant hyperthermia*. Neuromuscul Disord, 2016. **26**(1): p. 21-5.
95. Zhang, Y., et al., *A mutation in the human ryanodine receptor gene associated with central core disease*. Nat Genet, 1993. **5**(1): p. 46-50.
96. Quane, K.A., et al., *Mutation screening of the RYR1 gene in malignant hyperthermia: detection of a novel Tyr to Ser mutation in a pedigree with associated central cores*. Genomics, 1994. **23**(1): p. 236-9.
97. Lynch, P.J., et al., *A mutation in the transmembrane/luminal domain of the ryanodine receptor is associated with abnormal Ca<sup>2+</sup> release channel function and severe central core disease*. Proc Natl Acad Sci U S A, 1999. **96**(7): p. 4164-9.
98. Scacheri, P.C., et al., *A novel ryanodine receptor gene mutation causing both cores and rods in congenital myopathy*. Neurology, 2000. **55**(11): p. 1689-96.
99. Monnier, N., et al., *Familial and sporadic forms of central core disease are associated with mutations in the C-terminal domain of the skeletal muscle ryanodine receptor*. Hum Mol Genet, 2001. **10**(22): p. 2581-92.
100. Tilgen, N., et al., *Identification of four novel mutations in the C-terminal membrane spanning domain of the ryanodine receptor 1: association with central core disease and alteration of calcium homeostasis*. Hum Mol Genet, 2001. **10**(25): p. 2879-87.
101. Ferreira, A., et al., *A recessive form of central core disease, transiently presenting as multi-minicore disease, is associated with a homozygous mutation in the ryanodine receptor type 1 gene*. Ann Neurol, 2002. **51**(6): p. 750-9.
102. Jungbluth, H., et al., *Autosomal recessive inheritance of RYR1 mutations in a congenital myopathy with cores*. Neurology, 2002. **59**(2): p. 284-7.
103. Quinlivan, R.M., et al., *Central core disease: clinical, pathological, and genetic features*. Arch Dis Child, 2003. **88**(12): p. 1051-5.
104. Romero, N.B., et al., *Dominant and recessive central core disease associated with RYR1 mutations and fetal akinesia*. Brain, 2003. **126**(Pt 11): p. 2341-9.
105. Zorzato, F., et al., *Clinical and functional effects of a deletion in a COOH-terminal luminal loop of the skeletal muscle ryanodine receptor*. Hum Mol Genet, 2003. **12**(4): p. 379-88.
106. Davis, M.R., et al., *Principal mutation hotspot for central core disease and related myopathies in the C-terminal transmembrane region of the RYR1 gene*. Neuromuscul Disord, 2003. **13**(2): p. 151-7.
107. Gambelli, S., et al., *Inheritance of a novel RYR1 mutation in a family with myotonic dystrophy type 1*. Clin Genet, 2007. **71**(1): p. 93-4.
108. Kossugue, P.M., et al., *Central core disease due to recessive mutations in RYR1 gene: is it more common than described?* Muscle Nerve, 2007. **35**(5): p. 670-4.
109. von der Hagen, M., et al., *Novel RYR1 missense mutation causes core rod myopathy*. Eur J Neurol, 2008. **15**(4): p. e31-2.

110. Monnier, N., et al., *Null mutations causing depletion of the type 1 ryanodine receptor (RYR1) are commonly associated with recessive structural congenital myopathies with cores*. Hum Mutat, 2008. **29**(5): p. 670-8.
111. Duarte, S.T., et al., *Dominant and recessive RYR1 mutations in adults with core lesions and mild muscle symptoms*. Muscle Nerve, 2011. **44**(1): p. 102-8.
112. Gu, M., et al., *Novel RYR1 missense mutations in six Chinese patients with central core disease*. Neurosci Lett, 2014. **566**: p. 32-5.
113. Fattahi, Z., et al., *Improved diagnostic yield of neuromuscular disorders applying clinical exome sequencing in patients arising from a consanguineous population*. Clin Genet, 2017. **91**(3): p. 386-402.
114. Monnier, N., et al., *A homozygous splicing mutation causing a depletion of skeletal muscle RYR1 is associated with multi-minicore disease congenital myopathy with ophthalmoplegia*. Hum Mol Genet, 2003. **12**(10): p. 1171-8.
115. Jungbluth, H., et al., *Minicore myopathy with ophthalmoplegia caused by mutations in the ryanodine receptor type 1 gene*. Neurology, 2005. **65**(12): p. 1930-5.
116. Clarke, N.F., et al., *Recessive mutations in RYR1 are a common cause of congenital fiber type disproportion*. Hum Mutat, 2010. **31**(7): p. E1544-50.
117. Borko, L., et al., *Structural insights into the human RyR2 N-terminal region involved in cardiac arrhythmias*. Acta Crystallogr D Biol Crystallogr, 2014. **70**(Pt 11): p. 2897-912.
118. Priori, S.G., et al., *Mutations in the cardiac ryanodine receptor gene (hRyR2) underlie catecholaminergic polymorphic ventricular tachycardia*. Circulation, 2001. **103**(2): p. 196-200.
119. Laitinen, P.J., et al., *Mutations of the cardiac ryanodine receptor (RyR2) gene in familial polymorphic ventricular tachycardia*. Circulation, 2001. **103**(4): p. 485-90.
120. Priori, S.G., et al., *Clinical and molecular characterization of patients with catecholaminergic polymorphic ventricular tachycardia*. Circulation, 2002. **106**(1): p. 69-74.
121. Bauce, B., et al., *Screening for ryanodine receptor type 2 mutations in families with effort-induced polymorphic ventricular arrhythmias and sudden death: early diagnosis of asymptomatic carriers*. J Am Coll Cardiol, 2002. **40**(2): p. 341-9.
122. Laitinen, P.J., H. Swan, and K. Kontula, *Molecular genetics of exercise-induced polymorphic ventricular tachycardia: identification of three novel cardiac ryanodine receptor mutations and two common calsequestrin 2 amino-acid polymorphisms*. Eur J Hum Genet, 2003. **11**(11): p. 888-91.
123. Choi, G., et al., *Spectrum and frequency of cardiac channel defects in swimming-triggered arrhythmia syndromes*. Circulation, 2004. **110**(15): p. 2119-24.
124. Bagattin, A., et al., *Gene symbol: RYR2. Disease: Effort-induced polymorphic ventricular arrhythmias*. Hum Genet, 2004. **114**(4): p. 404.
125. Bagattin, A., et al., *Gene symbol: RYR2. Disease: Effort-induced polymorphic ventricular arrhythmias*. Hum Genet, 2004. **114**(4): p. 405.
126. Tester, D.J., et al., *Targeted mutational analysis of the RyR2-encoded cardiac ryanodine receptor in sudden unexplained death: a molecular autopsy of 49 medical examiner/coroner's cases*. Mayo Clin Proc, 2004. **79**(11): p. 1380-4.
127. Tester, D.J., et al., *Spectrum and prevalence of cardiac ryanodine receptor (RyR2) mutations in a cohort of unrelated patients referred explicitly for long QT syndrome genetic testing*. Heart Rhythm, 2005. **2**(10): p. 1099-105.



128. Jiang, D., et al., *Loss of luminal Ca<sup>2+</sup> activation in the cardiac ryanodine receptor is associated with ventricular fibrillation and sudden death*. Proc Natl Acad Sci U S A, 2007. **104**(46): p. 18309-14.
129. Di Pino, A., et al., *A novel RyR2 mutation in a 2-year-old baby presenting with atrial fibrillation, atrial flutter, and atrial ectopic tachycardia*. Heart Rhythm, 2014. **11**(8): p. 1480-3.
130. Xiao, Z., et al., *Enhanced Cytosolic Ca<sup>2+</sup> Activation Underlies a Common Defect of Central Domain Cardiac Ryanodine Receptor Mutations Linked to Arrhythmias*. J Biol Chem, 2016. **291**(47): p. 24528-24537.
131. Tiso, N., et al., *Identification of mutations in the cardiac ryanodine receptor gene in families affected with arrhythmogenic right ventricular cardiomyopathy type 2 (ARVD2)*. Hum Mol Genet, 2001. **10**(3): p. 189-94.
132. van de Leemput, J., et al., *Deletion at ITPR1 underlies ataxia in mice and spinocerebellar ataxia 15 in humans*. PLoS Genet, 2007. **3**(6): p. e108.
133. Hara, K., et al., *Total deletion and a missense mutation of ITPR1 in Japanese SCA15 families*. Neurology, 2008. **71**(8): p. 547-51.
134. Huang, L., et al., *Missense mutations in ITPR1 cause autosomal dominant congenital nonprogressive spinocerebellar ataxia*. Orphanet J Rare Dis, 2012. **7**: p. 67.
135. Shadrina, M.I., et al., *ITPR1 gene p.Val1553Met mutation in Russian family with mild Spinocerebellar ataxia*. Cerebellum Ataxias, 2016. **3**: p. 2.
136. Gerber, S., et al., *Recessive and Dominant De Novo ITPR1 Mutations Cause Gillespie Syndrome*. Am J Hum Genet, 2016. **98**(5): p. 971-980.
137. McEntagart, M., et al., *A Restricted Repertoire of De Novo Mutations in ITPR1 Cause Gillespie Syndrome with Evidence for Dominant-Negative Effect*. Am J Hum Genet, 2016. **98**(5): p. 981-992.
138. Klar, J., et al., *Abolished InsP3R2 function inhibits sweat secretion in both humans and mice*. J Clin Invest, 2014. **124**(11): p. 4773-80.
139. Odermatt, A., et al., *The mutation of Pro789 to Leu reduces the activity of the fast-twitch skeletal muscle sarco(endo)plasmic reticulum Ca<sup>2+</sup> ATPase (SERCA1) and is associated with Brody disease*. Hum Genet, 2000. **106**(5): p. 482-91.
140. Sakuntabhai, A., et al., *Spectrum of novel ATP2A2 mutations in patients with Darier's disease*. Hum Mol Genet, 1999. **8**(9): p. 1611-9.
141. Jacobsen, N.J., et al., *ATP2A2 mutations in Darier's disease and their relationship to neuropsychiatric phenotypes*. Hum Mol Genet, 1999. **8**(9): p. 1631-6.
142. Sakuntabhai, A., et al., *Mutations in ATP2A2, encoding a Ca<sup>2+</sup> pump, cause Darier disease*. Nat Genet, 1999. **21**(3): p. 271-7.
143. Tsuruta, D., et al., *Three-base deletion mutation c.120\_122delGTT in ATP2A2 leads to the unique phenotype of comedonal Darier disease*. Br J Dermatol, 2010. **162**(3): p. 687-9.
144. Nellen, R.G., et al., *Mendelian Disorders of Cornification Caused by Defects in Intracellular Calcium Pumps: Mutation Update and Database for Variants in ATP2A2 and ATP2C1 Associated with Darier Disease and Hailey-Hailey Disease*. Hum Mutat, 2017. **38**(4): p. 343-356.
145. Dhitavat, J., et al., *Acrokeratosis verruciformis of Hopf is caused by mutation in ATP2A2: evidence that it is allelic to Darier's disease*. J Invest Dermatol, 2003. **120**(2): p. 229-32.
146. Alexianu, M.E., et al., *The role of calcium-binding proteins in selective motoneuron vulnerability in amyotrophic lateral sclerosis*. Ann Neurol, 1994. **36**(6): p. 846-58.

147. Atherton, J., et al., *Calpain cleavage and inactivation of the sodium calcium exchanger-3 occur downstream of Abeta in Alzheimer's disease*. *Aging Cell*, 2014. **13**(1): p. 49-59.
148. Bano, D., et al., *Neurodegenerative processes in Huntington's disease*. *Cell Death Dis*, 2011. **2**: p. e228.
149. Bezprozvanny, I. and M.R. Hayden, *Deranged neuronal calcium signaling and Huntington disease*. *Biochem Biophys Res Commun*, 2004. **322**(4): p. 1310-7.
150. Vyleta, N.P. and S.M. Smith, *Spontaneous glutamate release is independent of calcium influx and tonically activated by the calcium-sensing receptor*. *J Neurosci*, 2011. **31**(12): p. 4593-606.
151. Cali, T., D. Ottolini, and M. Brini, *Mitochondria, calcium, and endoplasmic reticulum stress in Parkinson's disease*. *Biofactors*, 2011. **37**(3): p. 228-40.
152. Cali, T., D. Ottolini, and M. Brini, *Calcium signaling in Parkinson's disease*. *Cell Tissue Res*, 2014. **357**(2): p. 439-54.
153. Supnet, C. and I. Bezprozvanny, *The dysregulation of intracellular calcium in Alzheimer disease*. *Cell Calcium*, 2010. **47**(2): p. 183-9.
154. Ermolyuk, Y.S., et al., *Differential triggering of spontaneous glutamate release by P/Q-, N- and R-type Ca<sup>2+</sup> channels*. *Nat Neurosci*, 2013. **16**(12): p. 1754-1763.
155. Ganguly, G., et al., *Proteinopathy, oxidative stress and mitochondrial dysfunction: cross talk in Alzheimer's disease and Parkinson's disease*. *Drug Des Devel Ther*, 2017. **11**: p. 797-810.
156. Gardoni, F. and C. Bellone, *Modulation of the glutamatergic transmission by Dopamine: a focus on Parkinson, Huntington and Addiction diseases*. *Front Cell Neurosci*, 2015. **9**: p. 25.
157. Giacomello, M., et al., *Neuronal Ca(2+) dyshomeostasis in Huntington disease*. *Prion*, 2013. **7**(1): p. 76-84.
158. Grosskreutz, J., L. Van Den Bosch, and B.U. Keller, *Calcium dysregulation in amyotrophic lateral sclerosis*. *Cell Calcium*, 2010. **47**(2): p. 165-74.
159. Kawahara, Y., et al., *Human spinal motoneurons express low relative abundance of GluR2 mRNA: an implication for excitotoxicity in ALS*. *J Neurochem*, 2003. **85**(3): p. 680-9.
160. LaFerla, F.M., *Calcium dyshomeostasis and intracellular signalling in Alzheimer's disease*. *Nat Rev Neurosci*, 2002. **3**(11): p. 862-72.
161. Magi, S., et al., *Intracellular Calcium Dysregulation: Implications for Alzheimer's Disease*. *Biomed Res Int*, 2016. **2016**: p. 6701324.
162. Pieri, M., et al., *Over-expression of N-type calcium channels in cortical neurons from a mouse model of Amyotrophic Lateral Sclerosis*. *Exp Neurol*, 2013. **247**: p. 349-58.
163. Prell, T., J. Lautenschlager, and J. Grosskreutz, *Calcium-dependent protein folding in amyotrophic lateral sclerosis*. *Cell Calcium*, 2013. **54**(2): p. 132-43.
164. Guergueltcheva, V., et al., *Autosomal-recessive congenital cerebellar ataxia is caused by mutations in metabotropic glutamate receptor 1*. *Am J Hum Genet*, 2012. **91**(3): p. 553-64.
165. Watson, L.M., et al., *Dominant Mutations in GRM1 Cause Spinocerebellar Ataxia Type 44*. *Am J Hum Genet*, 2017. **101**(3): p. 451-458.
166. Huentelman, M.J., et al., *Association of SNPs in EGR3 and ARC with Schizophrenia Supports a Biological Pathway for Schizophrenia Risk*. *PLoS One*, 2015. **10**(10): p. e0135076.

167. Chuang, Y.A., et al., *Rare mutations and hypermethylation of the ARC gene associated with schizophrenia*. Schizophr Res, 2016. **176**(2-3): p. 106-113.
168. Devon, R.S., et al., *The genomic organisation of the metabotropic glutamate receptor subtype 5 gene, and its association with schizophrenia*. Mol Psychiatry, 2001. **6**(3): p. 311-4.
169. Gratacos, M., et al., *Identification of new putative susceptibility genes for several psychiatric disorders by association analysis of regulatory and non-synonymous SNPs of 306 genes involved in neurotransmission and neurodevelopment*. Am J Med Genet B Neuropsychiatr Genet, 2009. **150B**(6): p. 808-16.
170. Fatemi, S.H., et al., *Metabotropic glutamate receptor 5 upregulation in children with autism is associated with underexpression of both Fragile X mental retardation protein and GABAA receptor beta 3 in adults with autism*. Anat Rec (Hoboken), 2011. **294**(10): p. 1635-45.
171. Pretto, D.I., et al., *Reduced excitatory amino acid transporter 1 and metabotropic glutamate receptor 5 expression in the cerebellum of fragile X mental retardation gene 1 premutation carriers with fragile X-associated tremor/ataxia syndrome*. Neurobiol Aging, 2014. **35**(5): p. 1189-97.
172. Devon, R.S. and D.J. Porteous, *Physical mapping of a glutamate receptor gene in relation to a balanced translocation associated with schizophrenia in a large Scottish family*. Psychiatr Genet, 1997. **7**(4): p. 165-9.
173. Shimomura, O., F.H. Johnson, and Y. Saiga, *Extraction, purification and properties of aequorin, a bioluminescent protein from the luminous hydromedusan, Aequorea*. J Cell Comp Physiol, 1962. **59**: p. 223-39.
174. Prasher, D.C., et al., *Primary structure of the Aequorea victoria green-fluorescent protein*. Gene, 1992. **111**(2): p. 229-33.
175. Chalfie, M., et al., *Green fluorescent protein as a marker for gene expression*. Science, 1994. **263**(5148): p. 802-5.
176. Inouye, S. and F.I. Tsuji, *Aequorea green fluorescent protein. Expression of the gene and fluorescence characteristics of the recombinant protein*. FEBS Lett, 1994. **341**(2-3): p. 277-80.
177. Ormo, M., et al., *Crystal structure of the Aequorea victoria green fluorescent protein*. Science, 1996. **273**(5280): p. 1392-5.
178. Yang, F., L.G. Moss, and G.N. Phillips, Jr., *The molecular structure of green fluorescent protein*. Nat Biotechnol, 1996. **14**(10): p. 1246-51.
179. Yang, T.T., L. Cheng, and S.R. Kain, *Optimized codon usage and chromophore mutations provide enhanced sensitivity with the green fluorescent protein*. Nucleic Acids Res, 1996. **24**(22): p. 4592-3.
180. Heim, R., D.C. Prasher, and R.Y. Tsien, *Wavelength mutations and posttranslational autoxidation of green fluorescent protein*. Proc Natl Acad Sci U S A, 1994. **91**(26): p. 12501-4.
181. Heim, R. and R.Y. Tsien, *Engineering green fluorescent protein for improved brightness, longer wavelengths and fluorescence resonance energy transfer*. Curr Biol, 1996. **6**(2): p. 178-82.
182. Tsien, R.Y., *The green fluorescent protein*. Annu Rev Biochem, 1998. **67**: p. 509-44.

183. Cubitt, A.B., L.A. Woollenweber, and R. Heim, *Understanding structure-function relationships in the Aequorea victoria green fluorescent protein*. *Methods Cell Biol*, 1999. **58**: p. 19-30.
184. Patterson, G.H., et al., *Use of the green fluorescent protein and its mutants in quantitative fluorescence microscopy*. *Biophys J*, 1997. **73**(5): p. 2782-90.
185. Wachter, R.M., et al., *Structural basis of spectral shifts in the yellow-emission variants of green fluorescent protein*. *Structure*, 1998. **6**(10): p. 1267-77.
186. Llopis, J., et al., *Measurement of cytosolic, mitochondrial, and Golgi pH in single living cells with green fluorescent proteins*. *Proc Natl Acad Sci U S A*, 1998. **95**(12): p. 6803-8.
187. Griesbeck, O., et al., *Reducing the environmental sensitivity of yellow fluorescent protein. Mechanism and applications*. *J Biol Chem*, 2001. **276**(31): p. 29188-94.
188. Nagai, T., et al., *A variant of yellow fluorescent protein with fast and efficient maturation for cell-biological applications*. *Nat Biotechnol*, 2002. **20**(1): p. 87-90.
189. Matz, M.V., et al., *Fluorescent proteins from nonbioluminescent Anthozoa species*. *Nat Biotechnol*, 1999. **17**(10): p. 969-73.
190. Baird, G.S., D.A. Zacharias, and R.Y. Tsien, *Biochemistry, mutagenesis, and oligomerization of DsRed, a red fluorescent protein from coral*. *Proc Natl Acad Sci U S A*, 2000. **97**(22): p. 11984-9.
191. Campbell, R.E., et al., *A monomeric red fluorescent protein*. *Proc Natl Acad Sci U S A*, 2002. **99**(12): p. 7877-82.
192. Shaner, N.C., et al., *Improving the photostability of bright monomeric orange and red fluorescent proteins*. *Nat Methods*, 2008. **5**(6): p. 545-51.
193. Shaner, N.C., et al., *Improved monomeric red, orange and yellow fluorescent proteins derived from Discosoma sp. red fluorescent protein*. *Nat Biotechnol*, 2004. **22**(12): p. 1567-72.
194. Tsien, R.Y., *New calcium indicators and buffers with high selectivity against magnesium and protons: design, synthesis, and properties of prototype structures*. *Biochemistry*, 1980. **19**(11): p. 2396-404.
195. Tsien, R.Y., *A non-disruptive technique for loading calcium buffers and indicators into cells*. *Nature*, 1981. **290**(5806): p. 527-528.
196. Grynkiewicz, G., M. Poenie, and R.Y. Tsien, *A new generation of Ca<sup>2+</sup> indicators with greatly improved fluorescence properties*. *J Biol Chem*, 1985. **260**(6): p. 3440-50.
197. Eberhard, M. and P. Erne, *Calcium binding to fluorescent calcium indicators: calcium green, calcium orange and calcium crimson*. *Biochem Biophys Res Commun*, 1991. **180**(1): p. 209-15.
198. Hurley, T.W., M.P. Ryan, and R.W. Brinck, *Changes of cytosolic Ca<sup>2+</sup> interfere with measurements of cytosolic Mg<sup>2+</sup> using mag-fura-2*. *Am J Physiol*, 1992. **263**(2 Pt 1): p. C300-7.
199. Kao, J.P., A.T. Harootunian, and R.Y. Tsien, *Photochemically generated cytosolic calcium pulses and their detection by fluo-3*. *J Biol Chem*, 1989. **264**(14): p. 8179-84.
200. Wahl, M., M.J. Lucherini, and E. Gruenstein, *Intracellular Ca<sup>2+</sup> measurement with Indo-1 in substrate-attached cells: advantages and special considerations*. *Cell Calcium*, 1990. **11**(7): p. 487-500.
201. Gee, K.R., et al., *Chemical and physiological characterization of fluo-4 Ca(2+)-indicator dyes*. *Cell Calcium*, 2000. **27**(2): p. 97-106.

202. Miriel, V.A., et al., *Local and cellular Ca<sup>2+</sup> transients in smooth muscle of pressurized rat resistance arteries during myogenic and agonist stimulation*. J Physiol, 1999. **518** ( Pt 3): p. 815-24.
203. Chambers, J., et al., *Melanin-concentrating hormone is the cognate ligand for the orphan G-protein-coupled receptor SLC-1*. Nature, 1999. **400**(6741): p. 261-5.
204. Altimimi, H.F. and P.P. Schnetkamp, *Na<sup>+</sup>-dependent inactivation of the retinal cone/brain Na<sup>+</sup>/Ca<sup>2+</sup>-K<sup>+</sup> exchanger NCKX2*. J Biol Chem, 2007. **282**(6): p. 3720-9.
205. Daniel, H., A. Rancillac, and F. Crepel, *Mechanisms underlying cannabinoid inhibition of presynaptic Ca<sup>2+</sup> influx at parallel fibre synapses of the rat cerebellum*. J Physiol, 2004. **557**(Pt 1): p. 159-74.
206. Casas, J., et al., *Overexpression of cytosolic group IVA phospholipase A2 protects cells from Ca<sup>2+</sup>-dependent death*. J Biol Chem, 2006. **281**(9): p. 6106-16.
207. Zenisek, D., et al., *Imaging calcium entry sites and ribbon structures in two presynaptic cells*. J Neurosci, 2003. **23**(7): p. 2538-48.
208. Rehberg, M., et al., *A new non-disruptive strategy to target calcium indicator dyes to the endoplasmic reticulum*. Cell Calcium, 2008. **44**(4): p. 386-99.
209. Brochet, D.X., et al., *Ca<sup>2+</sup> blinks: rapid nanoscopic store calcium signaling*. Proc Natl Acad Sci U S A, 2005. **102**(8): p. 3099-104.
210. Etter, E.F., et al., *Near-membrane [Ca<sup>2+</sup>] transients resolved using the Ca<sup>2+</sup> indicator FFP18*. Proc Natl Acad Sci U S A, 1996. **93**(11): p. 5368-73.
211. Kao, J.P. and R.Y. Tsien, *Ca<sup>2+</sup> binding kinetics of fura-2 and azo-1 from temperature-jump relaxation measurements*. Biophys J, 1988. **53**(4): p. 635-9.
212. Klein, M.G., et al., *Simultaneous recording of calcium transients in skeletal muscle using high- and low-affinity calcium indicators*. Biophys J, 1988. **53**(6): p. 971-88.
213. Baylor, S.M. and S. Hollingworth, *Fura-2 calcium transients in frog skeletal muscle fibres*. J Physiol, 1988. **403**: p. 151-92.
214. Wokosin, D.L., C.M. Loughrey, and G.L. Smith, *Characterization of a range of fura dyes with two-photon excitation*. Biophys J, 2004. **86**(3): p. 1726-38.
215. Shirakawa, H. and S. Miyazaki, *Blind spectral decomposition of single-cell fluorescence by parallel factor analysis*. Biophys J, 2004. **86**(3): p. 1739-52.
216. Patel, S., et al., *Inducible nitric-oxide synthase attenuates vasopressin-dependent Ca<sup>2+</sup> signaling in rat hepatocytes*. J Biol Chem, 2002. **277**(37): p. 33776-82.
217. Mironov, S.L., M.V. Ivannikov, and M. Johansson, *[Ca<sup>2+</sup>]<sub>i</sub> signaling between mitochondria and endoplasmic reticulum in neurons is regulated by microtubules. From mitochondrial permeability transition pore to Ca<sup>2+</sup>-induced Ca<sup>2+</sup> release*. J Biol Chem, 2005. **280**(1): p. 715-21.
218. Thomas, D., et al., *A comparison of fluorescent Ca<sup>2+</sup> indicator properties and their use in measuring elementary and global Ca<sup>2+</sup> signals*. Cell Calcium, 2000. **28**(4): p. 213-23.
219. Lohr, C., *Monitoring neuronal calcium signalling using a new method for ratiometric confocal calcium imaging*. Cell Calcium, 2003. **34**(3): p. 295-303.
220. Park, M.K., O.H. Petersen, and A.V. Tepikin, *The endoplasmic reticulum as one continuous Ca(2+) pool: visualization of rapid Ca(2+) movements and equilibration*. EMBO J, 2000. **19**(21): p. 5729-39.
221. Hofer, A.M. and I. Schulz, *Quantification of intraluminal free [Ca] in the agonist-sensitive internal calcium store using compartmentalized fluorescent indicators: some considerations*. Cell Calcium, 1996. **20**(3): p. 235-42.

222. Hofer, A.M., et al., *Spatial distribution and quantitation of free luminal [Ca] within the InsP3-sensitive internal store of individual BHK-21 cells: ion dependence of InsP3-induced Ca release and reloading*. FASEB J, 1995. **9**(9): p. 788-98.
223. Hofer, A.M., C. Fasolato, and T. Pozzan, *Capacitative Ca<sup>2+</sup> entry is closely linked to the filling state of internal Ca<sup>2+</sup> stores: a study using simultaneous measurements of ICRAC and intraluminal [Ca<sup>2+</sup>]*. J Cell Biol, 1998. **140**(2): p. 325-34.
224. Launikonis, B.S., et al., *Confocal imaging of [Ca<sup>2+</sup>] in cellular organelles by SEER, shifted excitation and emission ratioing of fluorescence*. J Physiol, 2005. **567**(Pt 2): p. 523-43.
225. Zhao, M., S. Hollingworth, and S.M. Baylor, *Properties of tri- and tetracarboxylate Ca<sup>2+</sup> indicators in frog skeletal muscle fibers*. Biophys J, 1996. **70**(2): p. 896-916.
226. Brain, K.L. and M.R. Bennett, *Calcium in sympathetic varicosities of mouse vas deferens during facilitation, augmentation and autoinhibition*. J Physiol, 1997. **502** ( Pt 3): p. 521-36.
227. Tanaka, K., et al., *Ca<sup>2+</sup> requirements for cerebellar long-term synaptic depression: role for a postsynaptic leaky integrator*. Neuron, 2007. **54**(5): p. 787-800.
228. Peshenko, I.V. and A.M. Dizhoor, *Ca<sup>2+</sup> and Mg<sup>2+</sup> binding properties of GCAP-1. Evidence that Mg<sup>2+</sup>-bound form is the physiological activator of photoreceptor guanylyl cyclase*. J Biol Chem, 2006. **281**(33): p. 23830-41.
229. Valant, P.A., P.N. Adjei, and D.H. Haynes, *Rapid Ca<sup>2+</sup> extrusion via the Na<sup>+</sup>/Ca<sup>2+</sup> exchanger of the human platelet*. J Membr Biol, 1992. **130**(1): p. 63-82.
230. Vergara, J., et al., *Imaging of calcium transients in skeletal muscle fibers*. Biophys J, 1991. **59**(1): p. 12-24.
231. Coatesworth, W. and S. Bolsover, *Spatially organised mitochondrial calcium uptake through a novel pathway in chick neurones*. Cell Calcium, 2006. **39**(3): p. 217-25.
232. Bruce, J.I., et al., *Modulation of [Ca<sup>2+</sup>]<sub>i</sub> signaling dynamics and metabolism by perinuclear mitochondria in mouse parotid acinar cells*. J Biol Chem, 2004. **279**(13): p. 12909-17.
233. Garcia-Chacon, L.E., et al., *Extrusion of Ca<sup>2+</sup> from mouse motor terminal mitochondria via a Na<sup>+</sup>-Ca<sup>2+</sup> exchanger increases post-tetanic evoked release*. J Physiol, 2006. **574**(Pt 3): p. 663-75.
234. Micu, I., et al., *Real-time measurement of free Ca<sup>2+</sup> changes in CNS myelin by two-photon microscopy*. Nat Med, 2007. **13**(7): p. 874-9.
235. Marks, K.M., M. Rosinov, and G.P. Nolan, *In vivo targeting of organic calcium sensors via genetically selected peptides*. Chem Biol, 2004. **11**(3): p. 347-56.
236. Blum, R., O.H. Petersen, and A. Verkhratsky, *Ca<sup>2+</sup> Imaging of Intracellular Organelles: Endoplasmic Reticulum*. Neuromethods, 2010. **43**: p. 137-147.
237. Jaepel, J. and R. Blum, *Capturing ER calcium dynamics*. Eur J Cell Biol, 2011. **90**(8): p. 613-9.
238. Palmer, A.E. and R.Y. Tsien, *Measuring calcium signaling using genetically targetable fluorescent indicators*. Nat Protoc, 2006. **1**(3): p. 1057-65.
239. Miyawaki, A., et al., *Fluorescent indicators for Ca<sup>2+</sup> based on green fluorescent proteins and calmodulin*. Nature, 1997. **388**(6645): p. 882-7.
240. Porumb, T., et al., *A calmodulin-target peptide hybrid molecule with unique calcium-binding properties*. Protein Eng, 1994. **7**(1): p. 109-15.

241. Baird, G.S., D.A. Zacharias, and R.Y. Tsien, *Circular permutation and receptor insertion within green fluorescent proteins*. Proc Natl Acad Sci U S A, 1999. **96**(20): p. 11241-6.
242. Nagai, T., et al., *Circularly permuted green fluorescent proteins engineered to sense Ca<sup>2+</sup>*. Proc Natl Acad Sci U S A, 2001. **98**(6): p. 3197-202.
243. Nakai, J., M. Ohkura, and K. Imoto, *A high signal-to-noise Ca(2+) probe composed of a single green fluorescent protein*. Nat Biotechnol, 2001. **19**(2): p. 137-41.
244. Palmer, A.E., et al., *Ca<sup>2+</sup> indicators based on computationally redesigned calmodulin-peptide pairs*. Chem Biol, 2006. **13**(5): p. 521-30.
245. Tallini, Y.N., et al., *Imaging cellular signals in the heart in vivo: Cardiac expression of the high-signal Ca<sup>2+</sup> indicator GCaMP2*. Proc Natl Acad Sci U S A, 2006. **103**(12): p. 4753-8.
246. Zhao, Y., et al., *An expanded palette of genetically encoded Ca(2+)(+) indicators*. Science, 2011. **333**(6051): p. 1888-91.
247. Brown, E.M. and R.J. MacLeod, *Extracellular calcium sensing and extracellular calcium signaling*. Physiol Rev, 2001. **81**(1): p. 239-297.
248. Tfelt-Hansen, J. and E.M. Brown, *The calcium-sensing receptor in normal physiology and pathophysiology: a review*. Crit Rev Clin Lab Sci, 2005. **42**(1): p. 35-70.
249. Conigrave, A.D., et al., *L-amino acid sensing by the calcium-sensing receptor: a general mechanism for coupling protein and calcium metabolism?* Eur J Clin Nutr, 2002. **56**(11): p. 1072-80.
250. Chang, W., et al., *Expression and signal transduction of calcium-sensing receptors in cartilage and bone*. Endocrinology, 1999. **140**(12): p. 5883-93.
251. Cheng, I., et al., *Identification and localization of the extracellular calcium-sensing receptor in human breast*. J Clin Endocrinol Metab, 1998. **83**(2): p. 703-7.
252. Chattopadhyay, N., P.M. Vassilev, and E.M. Brown, *Calcium-sensing receptor: roles in and beyond systemic calcium homeostasis*. Biol Chem, 1997. **378**(8): p. 759-68.
253. Riccardi, D., *Wellcome Prize Lecture. Cell surface, ion-sensing receptors*. Exp Physiol, 2002. **87**(4): p. 403-11.
254. Quinn, S.J., et al., *CaSR-mediated interactions between calcium and magnesium homeostasis in mice*. Am J Physiol Endocrinol Metab, 2013. **304**(7): p. E724-33.
255. Li, X., et al., *Etelcalcetide (AMG 416), a peptide agonist of the calcium-sensing receptor, preserved cortical bone structure and bone strength in subtotal nephrectomized rats with established secondary hyperparathyroidism*. Bone, 2017. **105**: p. 163-172.
256. Cohen, A. and S.J. Silverberg, *Calcimimetics: therapeutic potential in hyperparathyroidism*. Curr Opin Pharmacol, 2002. **2**(6): p. 734-9.
257. Nemeth, E.F., et al., *Calcilytic compounds: potent and selective Ca<sup>2+</sup> receptor antagonists that stimulate secretion of parathyroid hormone*. J Pharmacol Exp Ther, 2001. **299**(1): p. 323-31.
258. Nemeth, E.F., *The search for calcium receptor antagonists (calcilytics)*. J Mol Endocrinol, 2002. **29**(1): p. 15-21.
259. Huang, Y., et al., *Identification and dissection of Ca(2+)-binding sites in the extracellular domain of Ca(2+)-sensing receptor*. J Biol Chem, 2007. **282**(26): p. 19000-10.
260. Higgins, D.G., *CLUSTAL V: multiple alignment of DNA and protein sequences*. Methods Mol Biol, 1994. **25**: p. 307-18.
261. Kopp, J. and T. Schwede, *Automated protein structure homology modeling: a progress report*. Pharmacogenomics, 2004. **5**(4): p. 405-16.

262. Schwede, T., et al., *SWISS-MODEL: An automated protein homology-modeling server*. Nucleic Acids Res, 2003. **31**(13): p. 3381-5.
263. Marti-Renom, M.A., et al., *Comparative protein structure modeling of genes and genomes*. Annu Rev Biophys Biomol Struct, 2000. **29**: p. 291-325.
264. Yang, W., et al., *Design of a calcium-binding protein with desired structure in a cell adhesion molecule*. J Am Chem Soc, 2005. **127**(7): p. 2085-93.
265. Deng, H., et al., *Predicting calcium-binding sites in proteins - a graph theory and geometry approach*. Proteins, 2006. **64**(1): p. 34-42.
266. Kirberger, M., et al., *Statistical analysis of structural characteristics of protein Ca<sup>2+</sup>-binding sites*. J Biol Inorg Chem, 2008. **13**(7): p. 1169-81.
267. Wang, X., et al., *Towards predicting Ca<sup>2+</sup>-binding sites with different coordination numbers in proteins with atomic resolution*. Proteins, 2009. **75**(4): p. 787-98.
268. Zhao, K., et al., *Predicting Ca<sup>2+</sup>-binding sites using refined carbon clusters*. Proteins, 2012. **80**(12): p. 2666-79.
269. Huang, Y., et al., *Multiple Ca(2+)-binding sites in the extracellular domain of the Ca(2+)-sensing receptor corresponding to cooperative Ca(2+) response*. Biochemistry, 2009. **48**(2): p. 388-98.
270. Kunishima, N., et al., *Structural basis of glutamate recognition by a dimeric metabotropic glutamate receptor*. Nature, 2000. **407**(6807): p. 971-7.
271. Monn, J.A., et al., *Synthesis and pharmacological characterization of C4-disubstituted analogs of 1S,2S,5R,6S-2-aminobicyclo[3.1.0]hexane-2,6-dicarboxylate: identification of a potent, selective metabotropic glutamate receptor agonist and determination of agonist-bound human mGlu2 and mGlu3 amino terminal domain structures*. J Med Chem, 2015. **58**(4): p. 1776-94.
272. Herraiz, T., J. Galisteo, and C. Chamorro, *L-tryptophan reacts with naturally occurring and food-occurring phenolic aldehydes to give phenolic tetrahydro-beta-carboline alkaloids: activity as antioxidants and free radical scavengers*. J Agric Food Chem, 2003. **51**(8): p. 2168-73.
273. Hannan, F.M., et al., *Identification of 70 calcium-sensing receptor mutations in hyper- and hypo-calcaemic patients: evidence for clustering of extracellular domain mutations at calcium-binding sites*. Hum Mol Genet, 2012. **21**(12): p. 2768-78.
274. Hannan, F.M. and R.V. Thakker, *Calcium-sensing receptor (CaSR) mutations and disorders of calcium, electrolyte and water metabolism*. Best Pract Res Clin Endocrinol Metab, 2013. **27**(3): p. 359-71.
275. Quinn, S.J., M. Bai, and E.M. Brown, *pH Sensing by the calcium-sensing receptor*. J Biol Chem, 2004. **279**(36): p. 37241-9.
276. Ray, K., et al., *Identification of the cysteine residues in the amino-terminal extracellular domain of the human Ca(2+) receptor critical for dimerization. Implications for function of monomeric Ca(2+) receptor*. J Biol Chem, 1999. **274**(39): p. 27642-50.
277. Minami, H., et al., *Direct determination of silicon in powdered aluminium oxide by use of slurry sampling with in situ fusion graphite-furnace atomic-absorption spectrometry*. Fresenius J Anal Chem, 2001. **370**(7): p. 855-9.
278. Tsuchiya, D., et al., *Structural views of the ligand-binding cores of a metabotropic glutamate receptor complexed with an antagonist and both glutamate and Gd<sup>3+</sup>*. Proc Natl Acad Sci U S A, 2002. **99**(5): p. 2660-5.



279. Geng, Y., et al., *Structural mechanism of ligand activation in human GABA(B) receptor*. Nature, 2013. **504**(7479): p. 254-9.
280. Nemeth, E.F. and W.G. Goodman, *Calcimimetic and Calcilytic Drugs: Feats, Flops, and Futures*. Calcif Tissue Int, 2016. **98**(4): p. 341-58.
281. Conigrave, A.D., S.J. Quinn, and E.M. Brown, *L-amino acid sensing by the extracellular Ca<sup>2+</sup>-sensing receptor*. Proc Natl Acad Sci U S A, 2000. **97**(9): p. 4814-9.
282. Ferre, S., J.G. Hoenderop, and R.J. Bindels, *Sensing mechanisms involved in Ca<sup>2+</sup> and Mg<sup>2+</sup> homeostasis*. Kidney Int, 2012. **82**(11): p. 1157-66.
283. Silve, C., et al., *Delineating a Ca<sup>2+</sup> binding pocket within the venus flytrap module of the human calcium-sensing receptor*. J Biol Chem, 2005. **280**(45): p. 37917-23.
284. Geng, Y., et al., *Structural mechanism of ligand activation in human calcium-sensing receptor*. Elife, 2016. **5**.
285. Zhang, C., et al., *Direct determination of multiple ligand interactions with the extracellular domain of the calcium-sensing receptor*. J. Biol. Chem., 2014. **289**(48): p. 33529-42.
286. Meng, L., et al., *Enzymatic basis for N-glycan sialylation: structure of rat alpha2,6-sialyltransferase (ST6GAL1) reveals conserved and unique features for glycan sialylation*. J Biol Chem, 2013. **288**(48): p. 34680-98.
287. Zhang, C., et al., *Structural basis for regulation of human calcium-sensing receptor by magnesium ions and an unexpected tryptophan derivative co-agonist*. Sci Adv, 2016. **2**(5): p. e1600241.
288. Otwinowski, Z. and W. Minor, *Processing of X-ray diffraction data collected in oscillation mode*. Methods Enzymol, 1997. **276**: p. 307-26.
289. Adams, P.D., et al., *PHENIX: a comprehensive Python-based system for macromolecular structure solution*. Acta Crystallogr D Biol Crystallogr, 2010. **66**(Pt 2): p. 213-21.
290. Emsley, P., et al., *Features and development of Coot*. Acta Crystallogr D Biol Crystallogr, 2010. **66**(Pt 4): p. 486-501.
291. Winn, M.D., et al., *Overview of the CCP4 suite and current developments*. Acta Crystallogr D Biol Crystallogr, 2011. **67**(Pt 4): p. 235-42.
292. Rask-Andersen, M., S. Masuram, and H.B. Schioth, *The druggable genome: Evaluation of drug targets in clinical trials suggests major shifts in molecular class and indication*. Annu Rev Pharmacol Toxicol, 2014. **54**: p. 9-26.
293. Santos, R., et al., *A comprehensive map of molecular drug targets*. Nat Rev Drug Discov, 2017. **16**(1): p. 19-34.
294. Hauser, A.S., et al., *Trends in GPCR drug discovery: new agents, targets and indications*. Nat Rev Drug Discov, 2017. **16**(12): p. 829-842.
295. Hauser, A.S., et al., *Pharmacogenomics of GPCR Drug Targets*. Cell, 2018. **172**(1-2): p. 41-54 e19.
296. Sriram, K. and P.A. Insel, *G Protein-Coupled Receptors as Targets for Approved Drugs: How Many Targets and How Many Drugs?* Mol Pharmacol, 2018. **93**(4): p. 251-258.
297. Chen, P., et al., *Population pharmacokinetics analysis of AMG 416, an allosteric activator of the calcium-sensing receptor, in subjects with secondary hyperparathyroidism receiving hemodialysis*. J Clin Pharmacol, 2015. **55**(6): p. 620-8.
298. Walter, S., et al., *Pharmacology of AMG 416 (Velcalcetide), a novel peptide agonist of the calcium-sensing receptor, for the treatment of secondary hyperparathyroidism in hemodialysis patients*. J Pharmacol Exp Ther, 2013. **346**(2): p. 229-40.

299. Harada, K., et al., *Pharmacology of Parsabiv((R)) (etelcalcetide, ONO-5163/AMG 416), a novel allosteric modulator of the calcium-sensing receptor, for secondary hyperparathyroidism in hemodialysis patients*. Eur J Pharmacol, 2019. **842**: p. 139-145.
300. Silva, B.C. and J.P. Bilezikian, *Parathyroid hormone: anabolic and catabolic actions on the skeleton*. Curr Opin Pharmacol, 2015. **22**: p. 41-50.
301. Gowen, M., et al., *Antagonizing the parathyroid calcium receptor stimulates parathyroid hormone secretion and bone formation in osteopenic rats*. J Clin Invest, 2000. **105**(11): p. 1595-604.
302. Stockigt, J., et al., *The Pictet-Spengler reaction in nature and in organic chemistry*. Angew Chem Int Ed Engl, 2011. **50**(37): p. 8538-64.
303. Ray, K., et al., *Calindol, a positive allosteric modulator of the human Ca(2+) receptor, activates an extracellular ligand-binding domain-deleted rhodopsin-like seven-transmembrane structure in the absence of Ca(2+)*. J Biol Chem, 2005. **280**(44): p. 37013-20.
304. Keller, A.N., et al., *Identification of Global and Ligand-Specific Calcium Sensing Receptor Activation Mechanisms*. Mol Pharmacol, 2018. **93**(6): p. 619-630.
305. Xu, C., B. Bailly-Maitre, and J.C. Reed, *Endoplasmic reticulum stress: cell life and death decisions*. J Clin Invest, 2005. **115**(10): p. 2656-64.
306. Lindholm, D., H. Wootz, and L. Korhonen, *ER stress and neurodegenerative diseases*. Cell Death Differ, 2006. **13**(3): p. 385-92.
307. Kim, I., W. Xu, and J.C. Reed, *Cell death and endoplasmic reticulum stress: disease relevance and therapeutic opportunities*. Nat Rev Drug Discov, 2008. **7**(12): p. 1013-30.
308. Papp, S., et al., *Is all of the endoplasmic reticulum created equal? The effects of the heterogeneous distribution of endoplasmic reticulum Ca<sup>2+</sup>-handling proteins*. J Cell Biol, 2003. **160**(4): p. 475-9.
309. Berridge, M.J., *The endoplasmic reticulum: a multifunctional signaling organelle*. Cell Calcium, 2002. **32**(5-6): p. 235-49.
310. Petersen, O.H., A. Tepikin, and M.K. Park, *The endoplasmic reticulum: one continuous or several separate Ca(2+) stores?* Trends Neurosci, 2001. **24**(5): p. 271-6.
311. Durham, W.J., et al., *Diseases associated with altered ryanodine receptor activity*. Subcell Biochem, 2007. **45**: p. 273-321.
312. Lorenzon, N.M. and K.G. Beam, *Calcium channelopathies*. Kidney Int, 2000. **57**(3): p. 794-802.
313. Blayney, L.M. and F.A. Lai, *Ryanodine receptor-mediated arrhythmias and sudden cardiac death*. Pharmacol Ther, 2009. **123**(2): p. 151-77.
314. Gyorke, S., *Molecular basis of catecholaminergic polymorphic ventricular tachycardia*. Heart Rhythm, 2009. **6**(1): p. 123-9.
315. Foggia, L. and A. Hovnanian, *Calcium pump disorders of the skin*. Am J Med Genet C Semin Med Genet, 2004. **131C**(1): p. 20-31.
316. Brini, M. and E. Carafoli, *Calcium pumps in health and disease*. Physiol Rev, 2009. **89**(4): p. 1341-78.
317. Bezprozvanny, I., *Calcium signaling and neurodegenerative diseases*. Trends Mol Med, 2009. **15**(3): p. 89-100.
318. Berridge, M.J., *Calcium hypothesis of Alzheimer's disease*. Pflugers Arch, 2010. **459**(3): p. 441-9.

319. Zhang, S., et al., *Inositol 1,4,5-trisphosphate receptor subtype-specific regulation of calcium oscillations*. *Neurochem Res*, 2011. **36**(7): p. 1175-85.
320. Brini, M., et al., *Ca<sup>2+</sup> signaling in HEK-293 and skeletal muscle cells expressing recombinant ryanodine receptors harboring malignant hyperthermia and central core disease mutations*. *J Biol Chem*, 2005. **280**(15): p. 15380-9.
321. Li, Y., et al., *Enrichment of endoplasmic reticulum with cholesterol inhibits sarcoplasmic-endoplasmic reticulum calcium ATPase-2b activity in parallel with increased order of membrane lipids: implications for depletion of endoplasmic reticulum calcium stores and apoptosis in cholesterol-loaded macrophages*. *J Biol Chem*, 2004. **279**(35): p. 37030-9.
322. Querfurth, H.W., et al., *Expression of ryanodine receptors in human embryonic kidney (HEK293) cells*. *Biochem J*, 1998. **334** ( Pt 1): p. 79-86.
323. Tong, J., T.V. McCarthy, and D.H. MacLennan, *Measurement of resting cytosolic Ca<sup>2+</sup> concentrations and Ca<sup>2+</sup> store size in HEK-293 cells transfected with malignant hyperthermia or central core disease mutant Ca<sup>2+</sup> release channels*. *J Biol Chem*, 1999. **274**(2): p. 693-702.
324. Hattori, M., et al., *Distinct roles of inositol 1,4,5-trisphosphate receptor types 1 and 3 in Ca<sup>2+</sup> signaling*. *J Biol Chem*, 2004. **279**(12): p. 11967-75.
325. Lytton, J., et al., *Functional comparisons between isoforms of the sarcoplasmic or endoplasmic reticulum family of calcium pumps*. *J Biol Chem*, 1992. **267**(20): p. 14483-9.
326. Treves, S., et al., *Functional properties of EGFP-tagged skeletal muscle calcium-release channel (ryanodine receptor) expressed in COS-7 cells: sensitivity to caffeine and 4-chloro-m-cresol*. *Cell Calcium*, 2002. **31**(1): p. 1-12.
327. Tarroni, P., et al., *Expression of the ryanodine receptor type 3 calcium release channel during development and differentiation of mammalian skeletal muscle cells*. *J Biol Chem*, 1997. **272**(32): p. 19808-13.
328. Bennett, D.L., et al., *Expression and function of ryanodine receptors in nonexcitable cells*. *J Biol Chem*, 1996. **271**(11): p. 6356-62.
329. Powell, J.A., et al., *IP(3) receptor function and localization in myotubes: an unexplored Ca(2+) signaling pathway in skeletal muscle*. *J Cell Sci*, 2001. **114**(Pt 20): p. 3673-83.
330. Kirberger, M., et al., *Statistical analysis of structural characteristics of protein Ca(2+)-binding sites*. *Journal of Biological Inorganic Chemistry*, 2008. **13**(7): p. 1169-1181.
331. Tang, S., et al., *Design and application of a class of sensors to monitor Ca<sup>2+</sup> dynamics in high Ca<sup>2+</sup> concentration cellular compartments*. *Proc Natl Acad Sci U S A*, 2011. **108**(39): p. 16265-70.
332. Zhang, Y., et al., *Structural basis for a hand-like site in the calcium sensor CatchER with fast kinetics*. *Acta Crystallogr D Biol Crystallogr*, 2013. **69**(Pt 12): p. 2309-19.
333. Zhuo, Y., et al., *Effect of Ca(2+)(+) on the steady-state and time-resolved emission properties of the genetically encoded fluorescent sensor CatchER*. *J Phys Chem B*, 2015. **119**(6): p. 2103-11.
334. Reddish, F.N., et al., *Monitoring ER/SR Calcium Release with the Targeted Ca<sup>2+</sup> Sensor CatchER*. *J Vis Exp*, 2017(123).
335. Zou, J., et al., *Developing sensors for real-time measurement of high Ca<sup>2+</sup> concentrations*. *Biochemistry*, 2007. **46**(43): p. 12275-88.
336. Tang, S., et al., *Design and application of a class of sensors to monitor Ca(2+) dynamics in high Ca(2+) concentration cellular compartments*. *Proceedings of the National Academy of Sciences of the United States of America*, 2011. **108**(39): p. 16265-16270.

337. Tokunaga, M., N. Imamoto, and K. Sakata-Sogawa, *Highly inclined thin illumination enables clear single-molecule imaging in cells*. Nat Meth, 2008. **5**(2): p. 159-161.
338. Axelrod, D., *Chapter 7: Total Internal Reflection Fluorescence Microscopy*. 2008.
339. Poteser, M., et al., *Live-cell imaging of ER-PM contact architecture by a novel TIRFM approach reveals extension of junctions in response to store-operated Ca<sup>2+</sup>-entry*. Scientific Reports, 2016. **6**: p. 35656.
340. Jensen, E.C., *Types of imaging, Part 2: an overview of fluorescence microscopy*. Anat Rec (Hoboken), 2012. **295**(10): p. 1621-7.
341. Lauterbach, M.A., et al., *Fast Calcium Imaging with Optical Sectioning via HiLo Microscopy*. PLoS One, 2015. **10**(12): p. e0143681.
342. Tokunaga, M., N. Imamoto, and K. Sakata-Sogawa, *Highly inclined thin illumination enables clear single-molecule imaging in cells*. Nature Methods, 2008. **5**: p. 159.
343. MacMillan, D., C. Kennedy, and J.G. McCarron, *ATP inhibits Ins(1,4,5)P<sub>3</sub>-evoked Ca<sup>2+</sup> release in smooth muscle via P2Y<sub>1</sub> receptors*. J Cell Sci, 2012. **125**(Pt 21): p. 5151-8.
344. Sandow, A., *Excitation-contraction coupling in muscular response*. Yale J Biol Med, 1952. **25**(3): p. 176-201.
345. Fill, M. and J.A. Copello, *Ryanodine receptor calcium release channels*. Physiol Rev, 2002. **82**(4): p. 893-922.
346. Calderon-Velez, J.C. and L.C. Figueroa-Gordon, *[Excitation-contraction coupling in skeletal muscle: questions remaining after 50 years of research]*. Biomedica, 2009. **29**(1): p. 140-60.
347. van de Linde, S., et al., *Direct stochastic optical reconstruction microscopy with standard fluorescent probes*. Nat Protoc, 2011. **6**(7): p. 991-1009.
348. Rust, M.J., M. Bates, and X. Zhuang, *Sub-diffraction-limit imaging by stochastic optical reconstruction microscopy (STORM)*. Nat Methods, 2006. **3**(10): p. 793-5.
349. Bates, M., T.R. Blosser, and X. Zhuang, *Short-range spectroscopic ruler based on a single-molecule optical switch*. Phys Rev Lett, 2005. **94**(10): p. 108101.
350. Higley, M.J. and B.L. Sabatini, *Calcium signaling in dendritic spines*. Cold Spring Harb Perspect Biol, 2012. **4**(4): p. a005686.
351. Platt, S.R., *The role of glutamate in central nervous system health and disease--a review*. Vet J, 2007. **173**(2): p. 278-86.
352. Rosenmund, C., Y. Stern-Bach, and C.F. Stevens, *The tetrameric structure of a glutamate receptor channel*. Science, 1998. **280**(5369): p. 1596-9.
353. Laube, B., et al., *Molecular determinants of agonist discrimination by NMDA receptor subunits: analysis of the glutamate binding site on the NR2B subunit*. Neuron, 1997. **18**(3): p. 493-503.
354. Furukawa, H., et al., *Subunit arrangement and function in NMDA receptors*. Nature, 2005. **438**(7065): p. 185-92.
355. Lipton, S.A., *Failures and successes of NMDA receptor antagonists: molecular basis for the use of open-channel blockers like memantine in the treatment of acute and chronic neurologic insults*. NeuroRx, 2004. **1**(1): p. 101-10.
356. Liu, Y. and J. Zhang, *Recent development in NMDA receptors*. Chin Med J (Engl), 2000. **113**(10): p. 948-56.
357. Kleckner, N.W. and R. Dingledine, *Requirement for glycine in activation of NMDA-receptors expressed in Xenopus oocytes*. Science, 1988. **241**(4867): p. 835-7.

358. Moriyoshi, K., et al., *Molecular cloning and characterization of the rat NMDA receptor*. Nature, 1991. **354**(6348): p. 31-7.
359. Cull-Candy, S., S. Brickley, and M. Farrant, *NMDA receptor subunits: diversity, development and disease*. Curr Opin Neurobiol, 2001. **11**(3): p. 327-35.
360. Li, F. and J.Z. Tsien, *Memory and the NMDA receptors*. N Engl J Med, 2009. **361**(3): p. 302-3.
361. Dingledine, R., et al., *The glutamate receptor ion channels*. Pharmacol Rev, 1999. **51**(1): p. 7-61.
362. Paoletti, P. and J. Neyton, *NMDA receptor subunits: function and pharmacology*. Curr Opin Pharmacol, 2007. **7**(1): p. 39-47.
363. Lu, B., et al., *alpha7 nicotinic acetylcholine receptor signaling inhibits inflammasome activation by preventing mitochondrial DNA release*. Mol Med, 2014. **20**: p. 350-8.
364. Itier, V. and D. Bertrand, *Neuronal nicotinic receptors: from protein structure to function*. FEBS Lett, 2001. **504**(3): p. 118-25.
365. Catterall, W.A., et al., *International Union of Pharmacology. XLVIII. Nomenclature and structure-function relationships of voltage-gated calcium channels*. Pharmacol Rev, 2005. **57**(4): p. 411-25.
366. Yamakage, M. and A. Namiki, *Calcium channels--basic aspects of their structure, function and gene encoding; anesthetic action on the channels--a review*. Can J Anaesth, 2002. **49**(2): p. 151-64.
367. Brauchi, S., et al., *A hot-sensing cold receptor: C-terminal domain determines thermosensation in transient receptor potential channels*. J Neurosci, 2006. **26**(18): p. 4835-40.
368. Eccles, R., *Nasal physiology and disease with reference to asthma*. Agents Actions Suppl, 1989. **28**: p. 249-61.
369. Philippaert, K., et al., *Steviol glycosides enhance pancreatic beta-cell function and taste sensation by potentiation of TRPM5 channel activity*. Nat Commun, 2017. **8**: p. 14733.
370. Vriens, J., B. Nilius, and T. Voets, *Peripheral thermosensation in mammals*. Nat Rev Neurosci, 2014. **15**(9): p. 573-89.
371. Siegel, G.J., *Basic neurochemistry : molecular, cellular, and medical aspects*. 6th ed. 1999, Philadelphia: Lippincott Williams & Wilkins. xxi, 1183.
372. Jensen, T.P., L.E. Buckby, and R.M. Empson, *Expression of plasma membrane Ca<sup>2+</sup> ATPase family members and associated synaptic proteins in acute and cultured organotypic hippocampal slices from rat*. Brain Res Dev Brain Res, 2004. **152**(2): p. 129-36.
373. Carafoli, E., *Calcium pump of the plasma membrane*. Physiol Rev, 1991. **71**(1): p. 129-53.
374. Strehler, E.E. and D.A. Zacharias, *Role of alternative splicing in generating isoform diversity among plasma membrane calcium pumps*. Physiol Rev, 2001. **81**(1): p. 21-50.
375. Carafoli, E., et al., *Generation, control, and processing of cellular calcium signals*. Crit Rev Biochem Mol Biol, 2001. **36**(2): p. 107-260.
376. Yu, S.P. and D.W. Choi, *Na(+)-Ca<sup>2+</sup> exchange currents in cortical neurons: concomitant forward and reverse operation and effect of glutamate*. Eur J Neurosci, 1997. **9**(6): p. 1273-81.
377. DiPolo, R. and L. Beauge, *Sodium/calcium exchanger: influence of metabolic regulation on ion carrier interactions*. Physiol Rev, 2006. **86**(1): p. 155-203.

378. Burette, A. and R.J. Weinberg, *Perisynaptic organization of plasma membrane calcium pumps in cerebellar cortex*. J Comp Neurol, 2007. **500**(6): p. 1127-35.
379. Valenzuela, J.I. and F. Perez, *Diversifying the secretory routes in neurons*. Front Neurosci, 2015. **9**: p. 358.
380. Breit, M., et al., *Spine-to-Dendrite Calcium Modeling Discloses Relevance for Precise Positioning of Ryanodine Receptor-Containing Spine Endoplasmic Reticulum*. Sci Rep, 2018. **8**(1): p. 15624.
381. Holcman, D., et al., *Single particle trajectories reveal active endoplasmic reticulum luminal flow*. Nat Cell Biol, 2018. **20**(10): p. 1118-1125.
382. Liu, X., et al., *Atlastin-1 regulates morphology and function of endoplasmic reticulum in dendrites*. Nat Commun, 2019. **10**(1): p. 568.
383. Summerville, J.B., et al., *The effects of ER morphology on synaptic structure and function in Drosophila melanogaster*. J Cell Sci, 2016. **129**(8): p. 1635-48.
384. Wu, Y., et al., *Contacts between the endoplasmic reticulum and other membranes in neurons*. Proc Natl Acad Sci U S A, 2017. **114**(24): p. E4859-E4867.
385. Xu, L.H., et al., *Critical Role of Endoplasmic Reticulum Stress in Chronic Intermittent Hypoxia-Induced Deficits in Synaptic Plasticity and Long-Term Memory*. Antioxid Redox Signal, 2015. **23**(9): p. 695-710.
386. Harris, K.M., *Calcium from internal stores modifies dendritic spine shape*. Proc Natl Acad Sci U S A, 1999. **96**(22): p. 12213-5.
387. Harris, K.M., *Structure, development, and plasticity of dendritic spines*. Curr Opin Neurobiol, 1999. **9**(3): p. 343-8.
388. Harris, K.M., J.C. Fiala, and L. Ostroff, *Structural changes at dendritic spine synapses during long-term potentiation*. Philos Trans R Soc Lond B Biol Sci, 2003. **358**(1432): p. 745-8.
389. Park, M., et al., *Plasticity-induced growth of dendritic spines by exocytic trafficking from recycling endosomes*. Neuron, 2006. **52**(5): p. 817-30.
390. Bartol, T.M., et al., *Computational reconstitution of spine calcium transients from individual proteins*. Front Synaptic Neurosci, 2015. **7**: p. 17.
391. Kwon, S.K., Y. Hirabayashi, and F. Polleux, *Organelle-Specific Sensors for Monitoring Ca(2+) Dynamics in Neurons*. Front Synaptic Neurosci, 2016. **8**: p. 29.
392. Henderson, M.J., et al., *A Low Affinity GCaMP3 Variant (GCaMPer) for Imaging the Endoplasmic Reticulum Calcium Store*. PLoS One, 2015. **10**(10): p. e0139273.
393. Choi, Y.M., et al., *Regional interaction of endoplasmic reticulum Ca<sup>2+</sup> signals between soma and dendrites through rapid luminal Ca<sup>2+</sup> diffusion*. J Neurosci, 2006. **26**(47): p. 12127-36.
394. Solovyova, N., et al., *Ca(2+) dynamics in the lumen of the endoplasmic reticulum in sensory neurons: direct visualization of Ca(2+)-induced Ca(2+) release triggered by physiological Ca(2+) entry*. EMBO J, 2002. **21**(4): p. 622-30.
395. Wall, M.J., et al., *The Temporal Dynamics of Arc Expression Regulate Cognitive Flexibility*. Neuron, 2018. **98**(6): p. 1124-1132 e7.
396. Mabb, A.M., et al., *Triad3A regulates synaptic strength by ubiquitination of Arc*. Neuron, 2014. **82**(6): p. 1299-316.
397. Thakker, R.V., *Diseases associated with the extracellular calcium-sensing receptor*. Cell Calcium, 2004. **35**(3): p. 275-82.

398. Kinoshita, Y., et al., *Functional activities of mutant calcium-sensing receptors determine clinical presentations in patients with autosomal dominant hypocalcemia*. J Clin Endocrinol Metab, 2014. **99**(2): p. E363-8.
399. Zhang, C.M., N.; Hannan, F.; Nesbit, M.; Thakker, R.; Hamelberg, D.; Brown, E.; Yang, J., *Role of Ca<sup>2+</sup> and L-Phe in Regulating Functional Cooperativity of Disease-Associated "Toggle" Calcium-Sensing Receptor Mutations*. PLoS One, 2014.
400. Wu, M., et al., *Calcium-sensing receptor activation attenuates collagen expression in renal proximal tubular epithelial cells*. Am J Physiol Renal Physiol, 2019.
401. Shimizu, T., et al., *Down-regulation of magnesium transporting molecule, claudin-16, as a possible cause of hypermagnesiuria with the development of tubulo-interstitial nephropathy*. Magnes Res, 2018. **31**(1): p. 11-23.
402. Yiu, A.J., et al., *Melamine induces Ca(2+)-sensing receptor activation and elicits apoptosis in proximal tubular cells*. Am J Physiol Cell Physiol, 2017. **313**(1): p. C27-C41.
403. Chen, N.X., et al., *Calcimimetics inhibit renal pathology in rodent nephronophthisis*. Kidney Int, 2011. **80**(6): p. 612-9.
404. Koleganova, N., et al., *Interstitial fibrosis and microvascular disease of the heart in uremia: amelioration by a calcimimetic*. Lab Invest, 2009. **89**(5): p. 520-30.
405. Wang, X., et al., *Effect of calcium-sensing receptor activation in models of autosomal recessive or dominant polycystic kidney disease*. Nephrol Dial Transplant, 2009. **24**(2): p. 526-34.
406. Ogata, H., et al., *Beneficial effects of calcimimetics on progression of renal failure and cardiovascular risk factors*. J Am Soc Nephrol, 2003. **14**(4): p. 959-67.
407. Kiefer, L., S. Leiris, and R.H. Dodd, *Novel calcium sensing receptor ligands: a patent survey*. Expert Opin Ther Pat, 2011. **21**(5): p. 681-98.
408. Frolik, C.A., et al., *Anabolic and catabolic bone effects of human parathyroid hormone (1-34) are predicted by duration of hormone exposure*. Bone, 2003. **33**(3): p. 372-9.
409. Pidasheva, S., et al., *CASRdb: calcium-sensing receptor locus-specific database for mutations causing familial (benign) hypocalciuric hypercalcemia, neonatal severe hyperparathyroidism, and autosomal dominant hypocalcemia*. Hum Mutat, 2004. **24**(2): p. 107-11.
410. Tate, J.G., et al., *COSMIC: the Catalogue Of Somatic Mutations In Cancer*. Nucleic Acids Res, 2019. **47**(D1): p. D941-D947.
411. Munteanu, B., M. Braun, and K. Boonrod, *Improvement of PCR reaction conditions for site-directed mutagenesis of big plasmids*. J Zhejiang Univ Sci B, 2012. **13**(4): p. 244-7.
412. Laible, M. and K. Boonrod, *Homemade site directed mutagenesis of whole plasmids*. J Vis Exp, 2009(27).
413. Samtleben, S., et al., *Direct imaging of ER calcium with targeted-esterase induced dye loading (TED)*. J Vis Exp, 2013(75): p. e50317.
414. Lyford, G.L., et al., *Arc, a growth factor and activity-regulated gene, encodes a novel cytoskeleton-associated protein that is enriched in neuronal dendrites*. Neuron, 1995. **14**(2): p. 433-45.
415. Link, W., et al., *Somatodendritic expression of an immediate early gene is regulated by synaptic activity*. Proc Natl Acad Sci U S A, 1995. **92**(12): p. 5734-8.
416. Mabb, A.M. and M.D. Ehlers, *Arc ubiquitination in synaptic plasticity*. Semin Cell Dev Biol, 2018. **77**: p. 10-16.

417. Shepherd, J.D. and M.F. Bear, *New views of Arc, a master regulator of synaptic plasticity*. Nature Neuroscience, 2011. **14**: p. 279.
418. Waung, M.W., et al., *Rapid translation of Arc/Arg3.1 selectively mediates mGluR-dependent LTD through persistent increases in AMPAR endocytosis rate*. Neuron, 2008. **59**(1): p. 84-97.
419. Gautam, A., R. Wadhwa, and M.K. Thakur, *Involvement of hippocampal Arc in amnesia and its recovery by alcoholic extract of Ashwagandha leaves*. Neurobiol Learn Mem, 2013. **106**: p. 177-84.